Optimization of ultra-thin Cu(In,Ga)Se2 based solar cells with alternative back-contacts

Fabien Mollica

Thèse de Doctorat de l'Université Pierre et Marie Curie

École Doctorale 397 - Physique et Chimie des Matériaux

Optimization of ultra-thin Cu(In,Ga)Se_2 based solar cells with alternative back-contacts

---

Présentée par **Fabien MOLLICA**

Soutenue publiquement le 21 Decembre 2016 devant un jury composé de :

Rapporteurs	**M. SIMON Jean-Jacques**
	M. ABOU-RAS Daniel
Examinateurs	**Mme EDOFF Marika**
	Mme SIEBENTRITT Susanne
	M. BARREAU Nicolas
	Mme LABERTY-ROBERT Christel
Encadrante de thèse	**Mme JUBAULT Marie**
Directrice de thèse	**Mme NAGHAVI Negar**

This study was carried out in the framework of the ANR Progelec program ANR-12-PGRE-0003 under the UltraCIS^{M} project. Additionnal financial support was received from the ANRT under CIFRE agreement 2013/1005.

Contents

Abstract

In the past three years, record efficiency of Cu(In,Ga)Se_2 (CIGS) based solar cells has improved from 20% up to 22.6%. These results show that CIGS absorber is ideal for thin-film solar cells, even if lower manufacture cost can improve its competitiveness. The fabrication of devices with thinner CIGS absorbers is a way to increase the throughput of a factory and to reduce material consumption. The present PhD thesis aims to develop cells with a CIGS thickness below 500 nm instead of the conventional 2.0-2.5 µm. However, previous studies have reported reduced cell performance of ultra-thin CIGS. We carefully analyzed this effect by the comparison between simulations and sample characterizations: it is attributed, on one hand, to a lack of light absorption in the CIGS layer and, on the other hand, to an increased impact of the back-contact (high recombination and low reflectivity). To resolve these problems, we demonstrated theoretically and experimentally that the use of an alternative back-contact, other than molybdenum, such as a transparent conducting oxide coupled with a metallic light reflector, improves the cell efficiency. To achieve these results, an optimization of the CIGS deposition on ZnO:Al and SnO_2:F back-contact was necessary. Moreover, we proved that a porous insulating oxide layer inserted between the CIGS and the back-contact has a passivating effect and removes some parasitic resistances. Finally, we achieved an efficiency of 10.7% for a 480-nm-thick CIGS solar cell with a SnO_2:F back-contact passivated with a porous Al_2O_3 layer and 9.2% for a 260-nm-thick CIGS solar cell with a SnO_2:F back-contact.

Résumé

En quelques années, l'efficacité des cellules solaires à base de Cu(In,Ga)Se_2 (CIGS) est passée de 20% à 22,6%. La rapidité de ce développement montre que le CIGS est un matériau idéal pour les technologies solaires en couches minces. Pourtant, le coût de production cette technologie doit encore être abaissé pour une meilleure compétitivité de la filiaire. Industriellement, un module avec une couche de CIGS plus fine augmenterait le taux de production et réduirait sa consommation en métaux. Ce travail de thèse vise à réduire l'épaisseur du CIGS d'un standard de 2.0-2.5 µm à une épaisseur inférieure à 500 nm sans altérer les performances électriques. Cependant, comme rapporté dans la littérature, nous avons observé une diminution des rendements de conversion, ce que nous avons analysé en détail en comparant simulations et caractérisations d'échantillons. Celle-ci est causée à la fois par une faible absorption de la lumière dans la couche de CIGS et par un impact important du contact arrière (fortes recombinaisons et faible réflectivité). Pour dépasser ces limites, nous démontrons à la fois théoriquement et expérimentalement que le contact arrière en molybdène peut être remplacé par un oxyde transparent conducteur couplé à un miroir métallique. De meilleurs rendements sont obtenues avec une telle architecture. Pour atteindre ce résultat, nous avons optimisé le dépôt de CIGS sur SnO_2 :F et ZnO :Al. De plus, nous prouvons qu'une couche d'oxyde perforée, insérée entre le CIGS et le contact arrière, a un effet passivant et réduit l'influence des courants parallèles. Au final, nous avons fabriqué un dispositif avec un CIGS de 480 nm, passivé par une couche perforée d'alumine, sur contact arrière en SnO_2 :F, atteignant un rendement de 10.7%, ainsi qu'un dispositif avec un CIGS de 260 nm sur contact arrière en SnO_2 :F atteignant un rendement de 9.2%.

Remerciements

Je remercie chaleureusement ma directrice de thèse Negar Naghavi et mon encadrante de thèse Marie Jubault. Negar, également responsable du projet ANR UltraCIS^M, a su orienter au mieux le projet, grâce à son écoute et parfois son inflexibilité. Cela me forçait à étayer mes arguments et à réfléchir aux implications de mes propositions. Marie apportait aussi de nombreuses idées, rendant les réunions très constructives. Je les remercie également pour toutes les relectures d'articles/abstracts, leurs écoutes attentives de mes présentations interminables et les encouragements quotidiens.

Je voudrais remercier Negar et EDF m'avoir fait confiance en me choisissant pour ce projet. L'IRDEP, qui m'a accueilli pendant cette thèse, est un cadre exceptionnel pour effectuer de la recherche de haute qualité. Je remercie donc Daniel Lincot et Matthieu Versavel, qui font vivre cette structure. De plus, les discussions avec Daniel et Matthieu ont toujours été très enrichissantes.

Je remercie particulièrement les rapporteurs, Daniel Abou-Ras et Jean-Jacques Simon, pour avoir examiné attentivement la thèse. Enfin je remercie l'exceptionnel jury de soutenance pour avoir lu en détail le manuscrit : Marika Edoff, Susanne Siebentritt, Nicolas Barreau et la présidente de jury Christel Laberty-Robert. Les questions, très précises, posées lors de la soutenance ont montrés un intérêt certain pour le travail effectué.

Je remercie également Marie Jubault et Frédérique Donsanti pour m'avoir formé aux réacteurs de dépôts sous vide. Je ne crois pas avoir cassé quelque chose (à par moi-même) ! Mais je n'aurais jamais été à la hauteur concernant le remontage des cellules d'effusions... Merci à tous ceux qui s'occupent des différentes étapes de fabrication des cellules solaires avec la tâche difficile de les standardiser et les optimiser : Samuel R., Laurent M., Thibaud H., Jessica L., Kim N., Nicolas L., Benoît R. Et je remercie fortement Enrique L. pour les nombreuses caractérisations électriques et pour l'attention particulière qu'il portait à mes échantillons spéciaux. Je remercie aussi le pôle Bâtiment F pour les caractérisations avancées : Laurent L., Daniel O. et Gilbert H. En particulier, Laurent L. pour toutes les discussions que l'on a pu avoir sur l'interprétation des résultats et Daniel O. pour l'analyse statistique des plans d'expériences.

Je remercie tous les partenaires du projet UltraCISM. J'ai eu la chance de collaborer avec le C2N : Julie Goffard pour les nombreux deals d'échantillons sur la thématique nanostructure, sa bonne humeur et sa motivation, ainsi Stéphane Collin et Andréa Cattoni pour les nombreuses discussions très constructives. J'ai pu travailler avec l'ILV sur les caractérisations avancées des matériaux, Anaïs Loubat, Murielle Bouttemy et Arnaud Etcheberry, avec qui il était très agréable de travailler (et qui sont très patients quand je suis en retard !). Les caractérisations étaient toujours très minutieuses. Mes échantillons ont également été suivis attentivement par Patrick Chapon et Céline Eypert de la société Horiba Jobin-Yvon.

Merci également à tous ceux qui m'ont aidé, de près ou de loin, ont pris le temps de répondre à mes questions ou qui m'ont débloqué sur un problème : Corentin B. (process de lift-off), Romain B. (question sur la DRX), Elisabeth C. (dissolutions en tout genre), Aurélien D. (four de recuits), Pierre-Philippe G. (plans après-thèses), Thibaud H. (blind test Madonna), Jessica L. (images MEB), Laurent M. (aide GD-OES), Stephan B. (images MEB), Laurent L. (pour le temps passé sur mes échantillons un peu spéciaux), Nicolas L. (référent paillasse en folie), Javier M (discussions sur le TiO2), Dac-Trunc N. (aide PL), Daniel O. (plans d'expériences), Jorge P. (expert Lyx et râleur pro), Jean R. (substrat de SnO2 :F), Nathanaëlle S. (ALD), Frédérique D. (expert en chef coévaporation et ALD), Bertrand T. (jonction Schottky), Myriam P. (pour ta patience infinie pour mes trèèès nombreuses questions variées, pour la litho et les solutions de gravures), Cathy B. (travail sur le contact arrière), Loraine D. (travail sur le contact arrière), Torben K. (trucs et astuces coévaporation). Un gros merci à Sophie G. à qui j'ai dû donner des petites sueurs froides, Mireille O. par ta patience avec moi, et Claire V. pour les séances de gym !

Enfin, je voudrais remercier les anciens/nouveaux co-thésard Julien, Charlène, Thomas, Valentin, Jean, Amélie, Sébastien, Harold, Ombline, Jorge, Mishael, Solange, Linda, Thibaud, Torben, Cathy, Loraine, Serena, Tarik pour les foots, les footings, les bières au Patio, les bouteilles de vins sur le canal de la Villette, le maintien en vie de mes plantes, les recherches de mes lunettes perdues au labo,.... Et je remercie tout le labo pour les bons moments informels au café ou ailleurs ! Je remercie du fond du cœur mes parents, mes frères et toute ma famille pour leur soutien inconditionnel ! Je pense aussi à tous mes amis qui m'ont aidé en toutes circonstances.

Enfin, je remercie la RATP pour les 1575h de moments de grâces passés dans les transports...

Liste des symboles

FF	Fill Factor
J_{SC}	Short-circuit current density
V_{OC}	Open-circuit voltage
ALD	Atomic-Layer Deposition
BC	Back-Contact
CBD	Chemical Bath Deposition
CGI	[Cu]/([Ga]+[In]) as atomic ratio
CIGS	Copper Indium Galium Didelenide - $Cu(In,Ga)Se_2$
EDS	Energy Dispersive Spectroscopy
EQE	External Quantum Efficiency
GD-OES	Glow-Discharge Optical Emission Spectroscopy
GGI	[Ga]/([Ga]+[In]) ratio
I(V)	Current-Voltage
IQE	Internal Quantum Efficiency
IR	Infrared
ITO	Tin-doped indium oxide
LCOE	Levelized Cost of Electricity
nano-AES	nano-Auger Electron Spectroscopy
OVC	Ordered Vacancy Compound
PDT	Post Deposition Treatment
PL	Photoluminescence

PV	Photovoltaic
QNR	Quasi Neutral Region
RTM	Ray Transfer Matrix
SCR	Space Charge Region
SEM	Scanning Electron Microscopy
SQL	Shockley-Queisser Limit
TCO	Transparent Conducting Oxide
TRPL	Time-Resolved Photoluminescence
XPS	X-ray Photoelectron Spectroscopy
XRD	X-Ray Diffraction
XRF	X-Ray Fluorescence

General introduction

Renewable energies are essential to meet the Paris Agreement 2015 that aimed at responding to the threat of climate change [1]. Photovoltaic (PV) technologies are a key component of decarbonized electricity that exploits the sun power and becomes competitive against other source of energy.

Photovoltaics today are dominated by crystalline silicon technology. Among the alternatives, Cu(In,Ga)Se_2 (CIGS) thin-film solar cells are most advanced and most efficient [2]. They are already well developed with current record conversion efficiencies for 0.5 cm^2 large cells of 22.6% [3] and for production size modules of 16.5%. To be more competitive, the CIGS module cost, calculated by the levelized cost of electricity, has to be further reduced by a decrease in the module fabrication cost, an up-scaling of the production, an improvement of the module efficiency while maintaining similar module price and lower degradation rate [4].

The present PhD thesis aims to reduce the module fabrication cost and increase the module efficiency by reducing the CIGS absorber thickness. This strategy would (1) increase the throughput of a manufactory by reducing the CIGS deposition time, (2) reduce the material consumption, especially indium and gallium identified as critical raw materials by an European Commission Report in 2014 [5] and (3) increase the power conversion efficiency of the device by minimizing the electrical losses in the CIGS absorber.

However, previous studies have reported that thinning down the CIGS absorber thickness from 2 - 2.5 μm in the conventional of high-efficiency cells to below 500 nm in ultra-thin CIGS cells negatively impacts the cell efficiency[6]. The CIGS absorption coefficient is insufficient to guaranty a light absorption for less than 500 nm thickness. Moreover, the absorption of the molybdenum layer is substantial and the charge carrier recombination at the back-contact is increased. A change of paradigm is necessary: we need to make the materials look “electrically thin but optically thick”.

In this PhD thesis, we aimed to develop an appropriate back-interface for ultra-thin CIGS solar cell that allows for an efficient charge-carrier generation and collection.

In **Chapter 1**, we provide the context into which this PhD thesis is inserted: a description of the PV market and of the need for lower CIGS module cost, and also the physics of CIGS cells. This overview is completed by the state of the art of ultra-thin CIGS solar cells.

In **Chapter 2**, we discuss the mechanisms that limit the efficiency of ultra-thin CIGS cells fabricated in our laboratory. For this purpose, we have fabricated solar cells on Mo back-contact with different CIGS thicknesses (**Section 2.3**) and different compositions (**Section 2.4**). The samples were analyzed by combining materials characterizations of the CIGS, electrical characterizations of the solar cells, and simulation of the device performances (SCAPS model and a generation-collection model). Moreover, alternative back-contacts can require different CIGS growth conditions. The impact of the growth conditions on the performance of ultra-thin CIGS cells on Mo back-contact is discussed in **Section 2.5**.

Then, in **Chapters 3 to 5**, we detail alternative back-contacts that compensate the identified losses: a more reflective back-contact (**Chapter 3**), a passivating back-contact (**Chapter 4**) or the combination of both (**Chapter 5**).

In **Chapter 3**, we replace the molybdenum back-contact by a transparent conducting oxide (TCO). After a state of the art on the CIGS deposition on TCO (**Section 3.2**), the chosen TCO substrates (ZnO:Al and SnO_2:F) were analyzed to determine the required CIGS deposition recipes (**Section 3.3**). In **Section 3.4** we optimize the CIGS deposition on TCO back-contact: the CIGS and its interface with the TCO were characterized (**Section 3.4.2**) as well as the cell performances (**Section 3.4.3**). Later, we show that a reflector placed behind the glass substrate can enhance the light absorption in the CIGS absorber (**Section 3.5**).

The **Chapter 4** deals with the control of the electrical losses at the back-contact. A perforated oxide layer inserted between the Mo and the CIGS layer can reduce the charge carrier recombination (**Section 4.2**). Therefore we explored the passivation effect of Al_2O_3 or TiO_2 layers on Mo-substrates (**Section 4.3**). The resulting cells are characterized for different CIGS growth condition (**Section 4.4**). We also performed in-depth characterizations of the interface by photoluminescence measurements (**Section 4.5**).

As a perspective, in **Chapter 5**, the reflective and the passivated back-interface are combined to reach high efficiency. In **Section 5.2,** we fabricate and characterize a sample that contains a TCO back-contact with a perforated passivation Al_2O_3 layer. In **Section 5.3,** we fabricate and characterize a sample with a Cu reflector encapsulated between the Mo and the Al_2O_3 layers, while the electrical contact between the CIGS and the Mo layer is made by openings in the Cu/Al_2O_3 stack.

1. Overview of the photovoltaic market and motivation of this study

1.1. Introduction to the current PV market

1.1.1. The need in PV system

Te present PhD thesis is dedicated to the photovoltaic (PV) energy and, more largely, to the development of the PV industry. It is therefore important to make a brief overview of the energy sector and of the position of photovoltaics in the energy market.

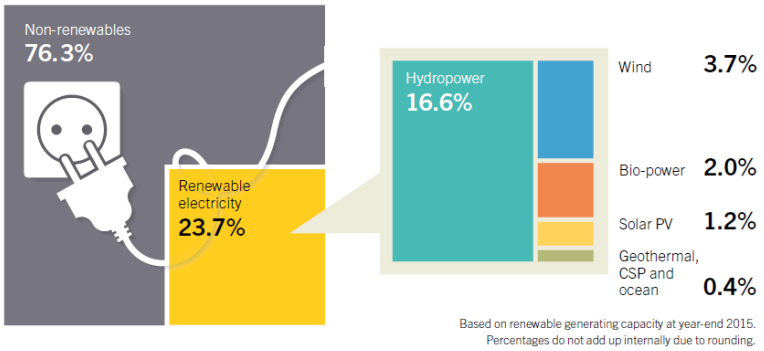

Figure 1.1.: Estimated renewable energy share of global electricity production, end-2015. From [7].

In 2014, the world energy demand rose to 13 800 million tonnes of oil equivalent, according to the International Energy Agency (IEA) [8]. As observed in Fig. 1.1 from [7], a large part (76.3%) of the energy is produced by non-renewable resources of energy such as oil, coal, or uranium. In the global energy production share, the solar PV had produced only 1.2% of the electricity in 2015. The PV market is therefore still under-developed compared with the other technologies.

However, the PV market is rapidly rising, as given in Fig. 1.2 presenting the global installed capacity of solar PV system from 2005 to 2015. In 2015, the total PV

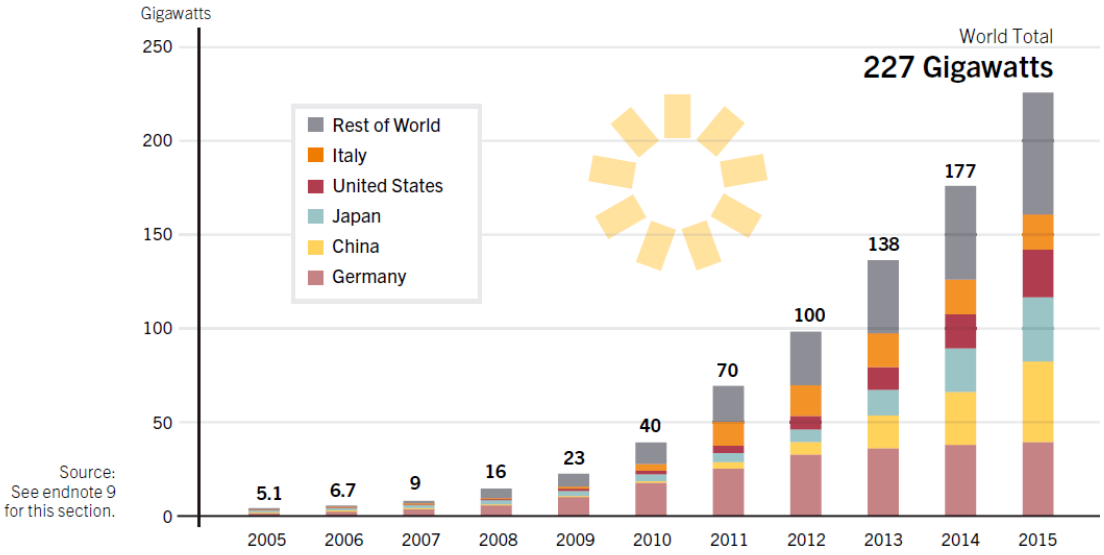

Figure 1.2.: Solar PV global capacity, by country/region. From [7].

global capacity was about 230 GW and the capacity rose of around 25% from one year to the other [7].

The development of the PV market is driven by two main forces: (1) the need in renewable energy to tackle the issue of the greenhouse gas emission and its effects on the global warming; (2) the rapid decrease in the PV system cost making the technology competitive against the other sources of energy.

1.1.1.1. Tackle the issue of the greenhouse gas emission

The COP21 stood in Paris at the end of 2015 and aimed to find responses to the threat of climate change. The Paris Agreement was adopted by consensus by 195 countries. The objective (a) of the Article 2 was adopted as following [1]:

(a) *Holding the increase in the global average temperature to well below 2°C above pre-industrial levels and to pursue efforts to limit the temperature increase to 1.5°C above pre-industrial levels, recognizing that this would significantly reduce the risks and impacts of climate change;*

In anticipation to the COP21, the IPCC (Intergovernmental Panel on Climate Change) has released a report providing a clear scientific view on the current state of knowledge in climate change and its potential environmental and socio-economic impacts. The report 3, chapter 7 [9] deals with the impact of the energy sector on the mitigation of climate change. It has been shown that 430-530 ppm CO_2eq. concentration in the atmosphere for 2100 would lead to an end-of-century median temperature change between 1.7 to 2°C compared to the pre-industrial time.

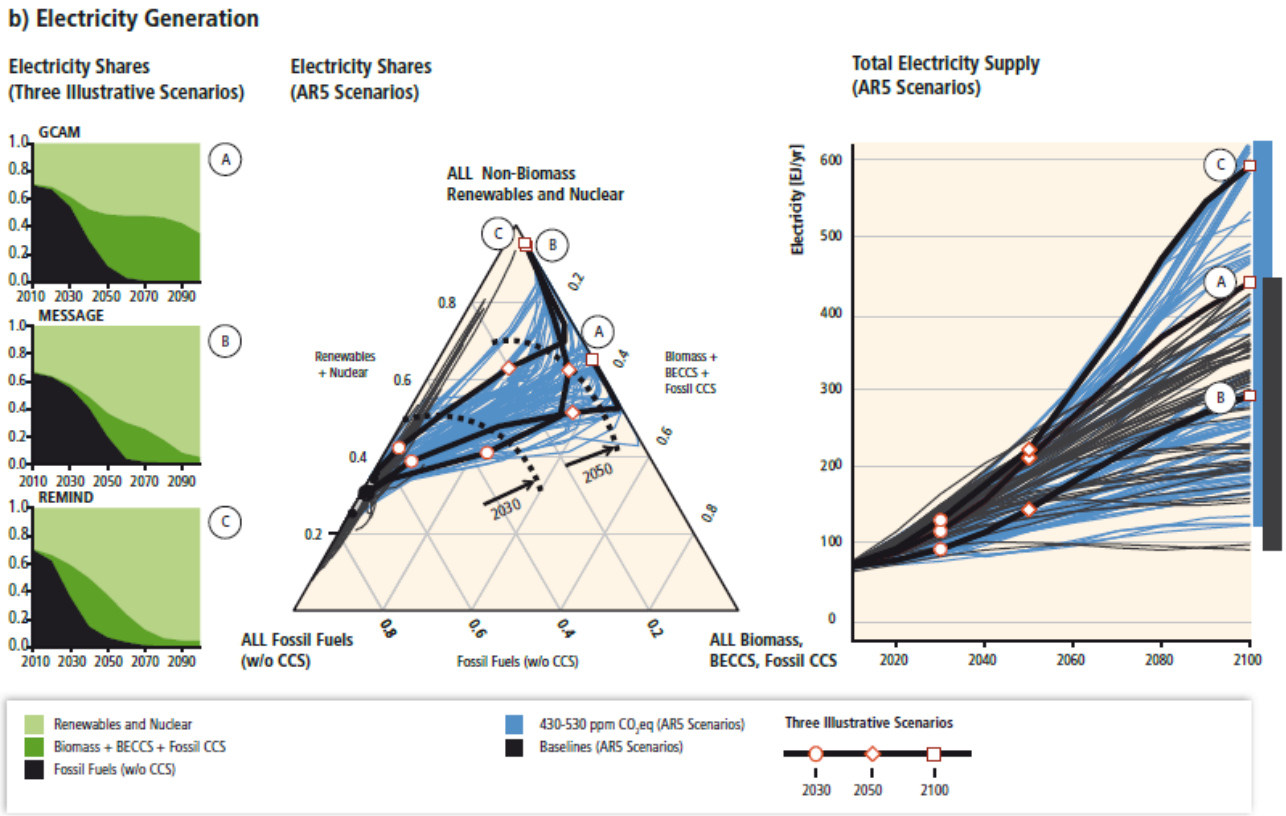

Figure 1.3.: Transition pathways for the electricity supply: 2010 to 2100 for baseline mitigation scenarios (430-530 ppm CO_2eq). The pathway of three illustrative scenarios (cases A, B and C) are highlighted for comparison. From [9].

In order to achieve the Paris Agreement objectives, a change of paradigm in the energy sector is absolutely necessary. A decarbonizing electricity generation is a key component of a cost-effective mitigation strategies. An energy transition pathway has to be plan to achieve this objective. Examples of electricity generation transition from 2010 to 2100 corresponding to different scenarios are presented in Fig. 1.3. As observed on the electricity share (left figure), the fossil fuel has to be cut-off in the next decades while renewable energy production has to largely rise. According to the total energy supply data (right figure), those strategies do not necessarily demand a reduction of the electricity production. The PV, as a key player in the renewable energy, is expected to have a role in this strategy.

1.1.1.2. Competitiveness of the PV technology

In 2015, the average price for a PV module was around 55 € / kWp [10]. A reduction of the component cost, an increase of the module efficiency and an increase of the production volume are expected. In the following decades, of the PV module price will decrease further to 23-38 € / kWp [11].

The Fig. 1.4 presents the cost of electricity from new solar power plants in Europe. These results indicate that in the future, power produced from large-scale solar PV plants will be cheaper than power produced from any conventional technology in large parts of Europe (that typically ranges between 5 and 10 ct-€/kWh). Cost competitiveness will thus be achieved under optimal conditions before 2025, and full cost competitiveness even under non-optimal conditions by 2050 at the latest [9].

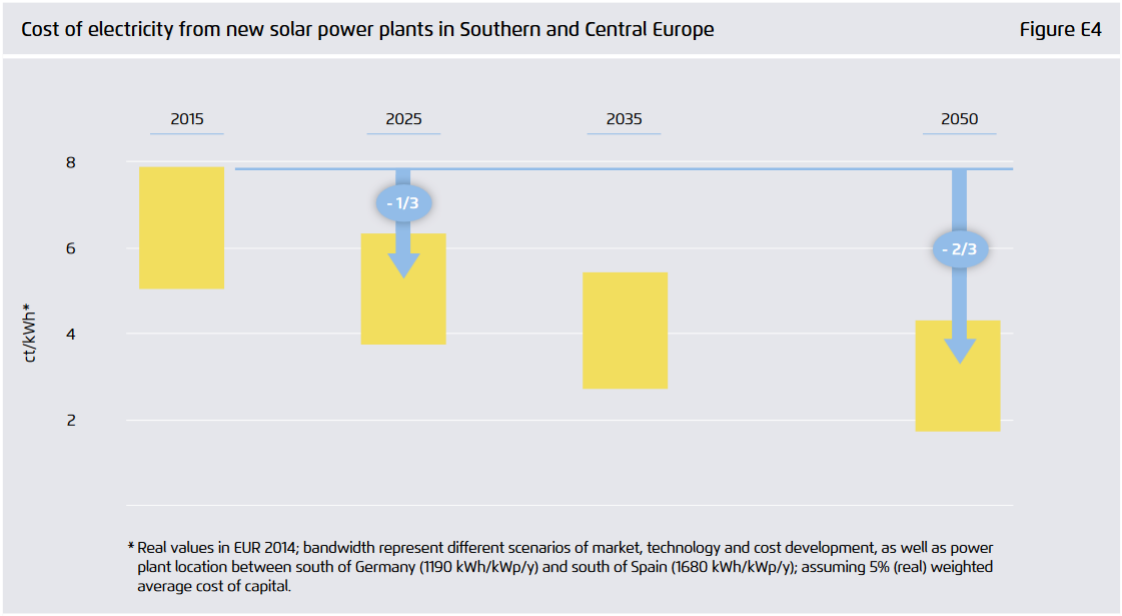

Figure 1.4.: Learning curve of the solar PV module price. From [11].

Moreover the cost competitiveness depends on the region around the world. A power purchase agreement for a 800 MW-solar farm in Dubai was recently signed for only 3 ct-$/kWh (may 2016) [12].

1.1.2. Commercial PV technologies

Several PV technologies are currently commercially available. The most noticeable are the crystalline or multi-crystalline silicon technologies (c-Si) and the thin film based technologies including the cadmium-telluride (CdTe) modules, amorphous silicon modules (a-Si) and copper indium gallium diselenide module (CIGS). The present PhD thesis is focused on CIGS based solar cells.

The position of CIGS modules in the PV market is presented in Fig. 1.5. The thin film technology represent only 7% on the PV module production in 2015 and the CIGS module production represents approximately half of this production. It corresponds to 1250 MWp produced in 2015 and has rapidly grown since 2010. In 2016, the major CIGS industries are Solar Frontier, Hanergy, Solopower, Stion, Silva Power, Avancis, Manz and more.

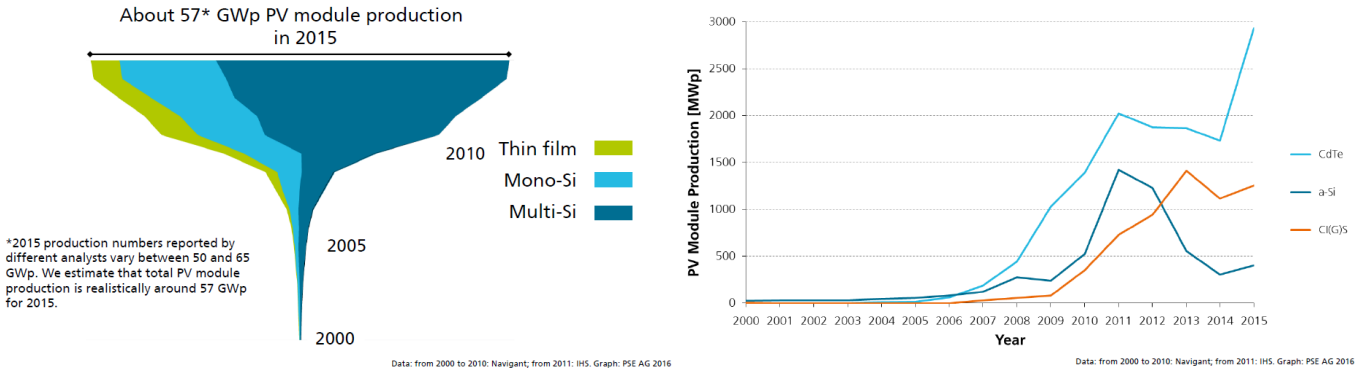

Figure 1.5.: PV module production: (left) thin-film module compared the c-Si module and (right) CIGS module compared to the other thin-film technologies. From [10].

CIGS technology exhibits still lower efficiency than c-Si technology (17.5% for the CIGS best modules compared with 22.9% for the best mono-Si modules [10]). However, it presents some advantages compared with the c-Si technology [2]:

- a lower energy pay-back time: the energy consumed to fabricate a module is produced in approximately 2 years for a 13.0% efficiency mono-Si module of 2013 and 1 year for a 11.5 % efficiency CIGS module of 2013 under AM1.5G illumination. [13];
- a lower carbon footprint and a lower impact on air pollution over a life cycle of the module (lower NO_x and SO_x production) [9];
- a levelized cost of electricity (LCOE)) equivalent to that of c-Si (approximately 0.05-0.07 €/kWh) [4, 14];
- a better behavior of the module for non-standard conditions: lower temperature coefficient, higher shading tolerance, good low light performance;
- the possibility to adapt the technology to light-weight or even flexible substrate [15].

Moreover, there is still potential for LCOE reduction by (1) reduction of the module fabrication cost, (2) up-scaling the production, (3) increasing the module efficiency while maintaining similar module price and (4) reducing the degradation rate.

In this PhD thesis, we will work on the reduction of the CIGS solar cell fabrication cost.

1.2. Description of the CIGS solar cells

1.2.1. Introduction

The configuration and the composition of the current Cu(In,Ga)Se_2 (CIGS) devices are the product of a long development. In 1975, the Bell laboratory demonstrated conversion efficiency of 12% for a $CuInSe_2$/CdS solar cell [16]. The best cells have reached today efficiencies higher than 20% (see Tab. 1.1) after several breakthroughs such as:

- Optimization of the pn junction, especially when using of a thin CdS buffer layer deposited by chemical bath;
- the control of the CIGS band-gap profile across the CIGS layer perpendicular to the substrate;
- Advanced and multistage deposition methods such as the Three-stage coevaporation process or sputtered metallic precursor followed by a selenization or sulfurization;
- the control of the alkali content in the CIGS layer;
- the optimization of the front window layers (optical transparency, electrical conduction and mobility.

A record efficiency of 22.6% for a 0.5 cm^2 cell was achieved in 2016 by ZSW [3].

We will present in the following the main aspects of the device structure and the material properties.

1.2.2. CIGS solar cell architecture

1.2.2.1. Structure of a standard CIGS solar cell

The standard CIGS solar cells refers to a cell structure which is commonly fabricated in different laboratories and industries, and is schematized in Fig. 1.6. The cell is basically composed of a p-type Cu(In,Ga)Se_2 layer, which act as the main light absorber, in contact with a n-type CdS layer to form a p-n junction. At the front-side, a transparent electrode generally based on a ZnO/ZnO:Al bilayer, collects the electrons. At the rear-side, a molybdenum electrode collects the holes. This configuration is called substrate configuration: the light enters into the cell from the last layer deposited (ZnO:Al).

The role and the particularities of each layer are detailed in this section. This structure is nevertheless not frozen and is perpetually adapted to specific issues or improved to reach high efficiencies.

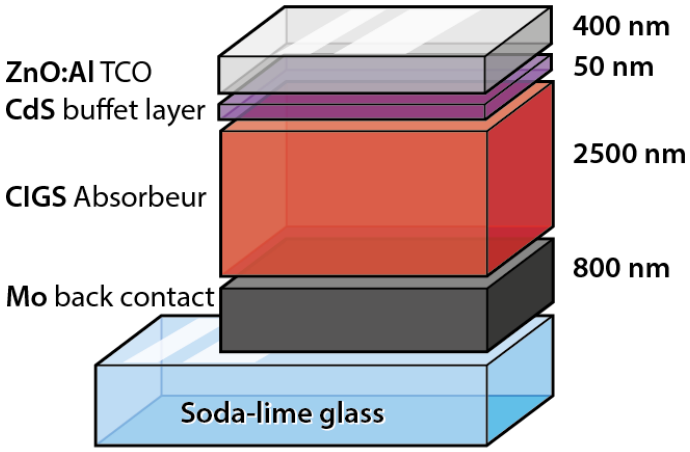

Figure 1.6.: Schematics of a standard Cu(In,Ga)Se_2 solar cell.

1.2.2.2. Substrates

The substrate generally used for the deposition of the different layers is a soda-lime glass. This substrate is particularly well adapted for the following reasons:

- its low cost (4 US$/m^2 in 2015 for the stack EVA, front and back glasses in a CIGS module for a total module cost of 78.22 US$/m^2 [4]);
- its stability at high temperature because of its glass transition at 550-600°C. The formation of the CIGS generally requires a substrate temperature of larger than 350°C [17]. Usually, an increase of the CIGS deposition temperature leads to an increase of the conversion efficiency [17].
- a thermal expansion of 9-9.5 ppm/K that matches with the Mo and CIGS layers;
- its Na impurities. It has been demonstrated that Na diffuses from the glass to the CIGS layer at high temperature and has a beneficial impact on the CIGS. This effect was first observed by Hedström *et al.* [18] and will be detailed in the CIGS description (sec. 1.2.2.4).

More recently, interest has grown in flexible substrates: polyimide substrate [19, 20], metallic substrate [21] or ultra-thin glass [22].

1.2.2.3. Mo back-contact

The back-contact is generally a molybdenum layer for the following reasons:

- its high electron affinity (~ 4.5 eV) permitting an ohmic contact with the CIGS, supported by the formation of a thin $MoSe_2$ interfacial layer at high temperature [23, 24];

- the adhesion of the CIGS layer on Mo;
- its permeability for alkali element permitting a diffusion of Na from the soda-lime glass substrate though canals between the Mo grains [25]. Na also favors the formation of the $MoSe_2$ layer [26, 27].

The required Mo layer is a result of the optimization of the DC magnetron sputtering deposition parameters: the conductance of the Mo film increases for lower Ar pressures, whereas its adherence to glass and the Na diffusion is favored for higher pressure.

Other thin metal films were tested to replace the Mo back-contact, but only W and Ta have been proven to give a similar efficiency than Mo back-contact [28].

1.2.2.4. CIGS absorber

$Cu(In,Ga)Se_2$ is a quaternary I-III-VI semi-conductor, a solid solution of the ternary $CuInSe_2$ and $CuGaSe_2$ compounds. In and Ga atoms occupy the same atomic sites. The CIGS crystallizes in a tetragonal chalcopyrite structure, derived from the cubic sphalerite structure (Fig. 1.7).

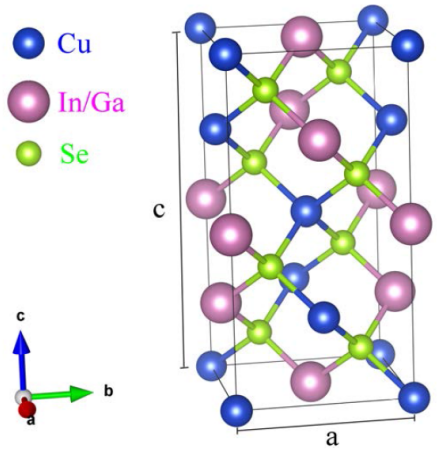

Figure 1.7.: Unit cell of chalcopyrite of stoichiometric $Cu(In,Ga)Se_2$. a and c are the lattice constants. From [29].

Substitution of In by Ga in the structure enlarge the primitive cell: from $CuInSe_2$ to $CuGaSe_2$ the lattice constants a and c varies from 5.780 to 5.607 Å and from 11.604 to 10.983 Å respectively [30]. The structure also exhibits a distortion ($c/a \neq 2$) which depends on the In and Ga ratio in the CIGS structure.

One consequence of this structure variation is the variation of the CIGS band-gap as a function of the Ga content. From $CuInSe_2$ to CuGaSe, the band-gap varies from approximately 1.01 eV to 1.63 eV [31, 32]. For the following, the composition

GGI = [Ga]/([Ga]+[In]) is introduced. The band-gap energy as a function of GGI is [32]:

$$E_g(GGI) = 1.01 + 0.626 \cdot GGI - 0.167 \cdot GGI \cdot (1 - GGI) \tag{1.1}$$

The most efficient devices are obtained when the CIGS band-gap ranges from 1.15 to 1.25 eV [33].

The CIGS is usually sub-stoichiometric with a Cu-poor ([Cu]/([Ga]+[In]<1) composition with an intrinsic p-type conduction [34, 35]. The reported doping level is $5 \cdot 10^{15}$ - $5 \cdot 10^{16}$ cm^{-3}. The acceptor Cu vacancy state (V_{cu}^{-}), the donor Cu substitution state ($In_{Cu}^{2+}$and Ga_{Cu}^{2+}) and the donor Se vacancy state (V_{Se}^{2+}) have a very low formation and form shallow states [36]. V_{Cu}^{-} and (In_{Cu}^{2+}, Ga_{Cu}^{2+}) are strongly correlated, and their concentrations remains close to 2:1 forming a neutral defect pair. A small variation of this ratio is responsible for the p-type conductivity of the CIGS. However, particularly in Cu-poor conditions, CIGS contains a large number of (In_{Cu}^{2+}, Ga_{Cu}^{2+}) defects that enhances the charge carrier recombination. The growth in Cu-rich composition prevents the formation of such defects [37].

Na incorporation in the CIGS layer in adequate concentration has been shown to be beneficial for the cell performance [38, 39, 18]. In small concentrations, Na occupies Cu and In sites [40]. The donor defect In_{Cu} is easily eliminated by the substitution $Na_{(In_{Cu})}$. As a consequence, the effective hole density is increased, and the recombination reduced.

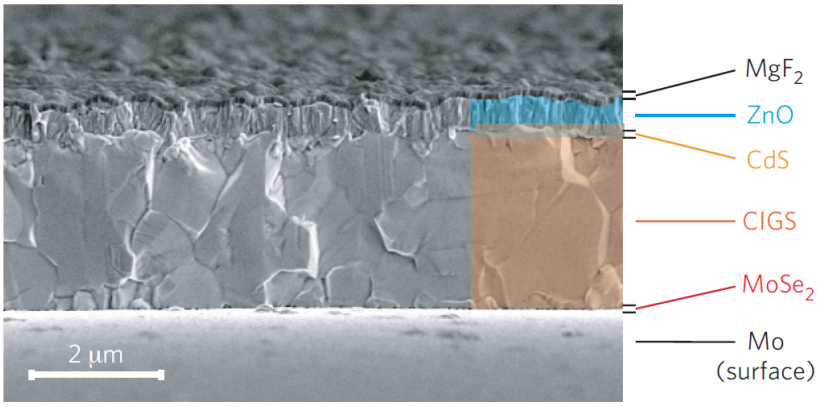

Figure 1.8.: Cross sectional SEM image of a complete CIGS device on polyimide with a conversion efficiency greater than 18%. From [41].

CIGS thin films usually exhibit large grains with average grain sizes of few micrometers. Fig. 1.8 shows the typical morphology of a CIGS layer, with many grain boundaries across the CIGS thickness. Surprisingly, the grain boundaries seem to have a minor impact on the cell performance [42]. Although, random grain

boundaries [43], twin grain boundaries, dislocations, stacking faults, and micro-strains have been extensively studied, and the reason of their low impact on the cell efficiency is still under debate. A low surface recombination velocity at the grain boundaries below 10^4 cm/s was measured by various methods such as electron-beam-induced current (EBIC) [44, 45] as well as time-resolved photoluminescence (TRPL) [46]. The properties depends on the local reconstruction of the grain boundary. It has been observed a local composition variation such as Cu enrichment or deficiency anticorrelated with In variation, a removal of the Se vacancy, an oxygen enrichment or the presence of Na. These changes can lead to a deep defect density [47, 48] or to the formation of a small potential barrier at the conduction-band limiting the recombination at the grain boundaries [49].

The CIGS properties are often correlated to the deposition technique of the CIGS. The most important CIGS deposition technique is the physical vapor deposition of the metallic element at high temperature [3], which is the technique used in this study. We should also mentioned the sputtering of metallic precursors followed by an annealing at high temperature under Se or S atmosphere [50]; or a non-vacuum process such as the electro-deposition of metallic or oxide precursors followed by an annealing at high temperature under Se or S atmosphere [51].

1.2.2.5. CdS buffer layer

The CdS layer is deposited on the surface of the CIGS layer. The deposition technique is generally the chemical bath deposition that exploits the precipitation of a CdS layer of controlled composition. The CdS is an n-type semi-conductor forming an heterojunction with the p-type CIGS. However, the role of the CdS layer is more complex and is associated to a passivation of the CIGS surface, a chemical intermixing at the interface and a protecting role on the absorber surface during the sputtering of the window layer [34].

For Cu-poor CIGS materials, a formation of a thin Cu deficiency layer at the CIGS/CdS interface, called ordered vacancy compound (OVC), has been reported [52]. This layer wider the band-gap close to the interface. The valence energy band offset repels the holes and reduces the recombination at the CIGS/CdS contact [37, 34].

However, the CdS has a too low band-gap (2.4 eV) for a use at the front-window which causes optical losses. Moreover the use of toxic Cd-compounds limits the development of the industries. Other buffer layers are therefore investigated such as Zn(O,S) [53].

1.2.2.6. ZnO/ZnO:Al front electrode

Before the deposition of the front-contact, a thin intrinsic ZnO layer is sputtered on the surface of the CdS. Its main role is to prevent shunt paths in the device because

of its high resistivity [54]. The ZnO layer is intrinsically doped and permits the electron conduction through the conduction-band.

The front-contact is fabricated using a transparent conducting oxide (TCO). Aluminum doped zinc oxide (ZnO:Al) deposited by sputtering is commonly used. Optimization of the ZnO:Al layer is a balance between its transparency to the sun spectrum and its conductivity to avoid resistive loss.

A low index materials such as MgF_2 can be evaporated at the surface of the ZnO:Al to reduce the light reflection at the air/ZnO:Al interface.

1.2.2.7. Cell efficiency for various device fabrication process

High cell efficiency was achieved with various substrate, CIGS deposition techniques or buffer/front-contact materials. Tab. 1.1, inspired by [57], gives an overview of the efficiency of different CIGS devices. For comparison with other solar cells technologies, the reader can refer to the record efficiency table of M. Green *et al.* [58].

The CIGS based solar cells are a complex structure. It is important to understand the physical issues involved in the devices and how to use them for an accurate cell analysis.

1.2.3. Physics of the CIGS solar cells

The basic optical and electrical principles of the CIGS devices will be discussed in this section. We will report the points that are the most relevant for our study. Our guideline is to see how the charge-carriers are generated in the CIGS and what are the mechanisms to collect them. This overview gives the opportunity to discuss the light absorption in the CIGS that limits the charge generation and the recombination that limits the charge lifetime. We also set a collection model that will be used in the next chapters.

1.2.3.1. The Mo/CIGS/CdS/ZnO heterojunction

The Mo/CIGS/CdS/ZnO/ZnO:Al structure is an hererojunction, *i.e.* a junction between semiconductors of different band-gaps. In Fig. 1.9 we have simulated the band-diagram on SCAPS (VERSION 3.2.01 software created by Prof. Burgelman *et al.* from university of Gent [59, 60], see sec. 2.2.4.1) using the materials parameters used by Chirilă *et al.* [41]. We observe in this diagram that the valence and conduction-band (E_V and E_C) show discontinuities due to the variation of band-gap, electron affinity and doping concentration for the different layers. A positive conduction-band offset and a negative valence-band offset are achieved at the CIGS/CdS interface. This reduces the recombination at the interface.

Table 1.1.: Overview of the efficiency of CIGS based solar cells or mini-modules fabricated with different processes. This list is not exhaustive and just aimed to highlight the diversity of the solar device fabrication. ⋆: efficiency externally certified. ▷: PDT ◇: PI = Polyimide. ○: SS = Stainless Steel.

Institute or Company	Substrate /back-contact	CIGS deposition	Buffer / Intrisic layer	Front-contact	Efficiency	Reference
Solar Frontier	Glass/Mo	Sputtering, selenization, sulfurization, KF PDT▷	CBD-Zn(O,S) / ALD-(Zn,Mg)O	ZnO:Al	22.8 %	[50]
ZSW	Glass/Mo	Coevaporation, RbF PDT▷	? / ZnO or (Zn,Mg)O	ZnO:Al	22.6 % ⋆	[3]
Empa	PI◇/Mo	Coevaporation NaF + KF PDT▷	CBD-CdS / ZnO	ZnO:Al	20.4 % ⋆	[19]
Miasolé	SS○/Mo:Na	Sputtering, selenization	sputtered-CdS / NaN	ZnO:Al	17% large area ⋆	[21]
Nexcis	Glass/Mo	Electrodepostion, selenization	CBD-CdS / ZnO	ZnO:Al	17.3 % ⋆	[51]
Nakada	Glass/ITO	Coevaporation	CBD-CdS / ZnO	ZnO:Al	15.2 % no MgF_2	[55]
Avancis	Glass/SiN/Mo	Sputtering, Rapid thermal processing, S and Se	sputtered-In_xN_y:Na / ZnO	ZnO:Al	17.9% 30x30 cm^2 ⋆	[56]

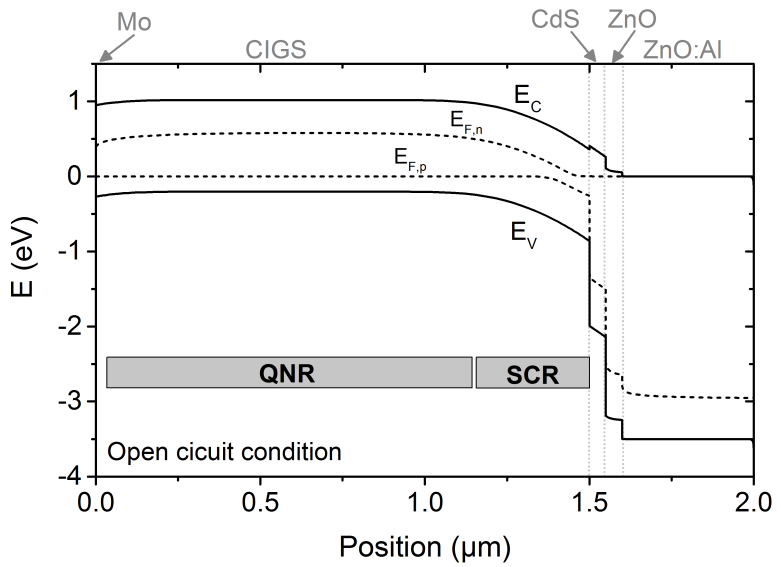

Figure 1.9.: Band-diagram for the Mo/Cu($In_{0.7}Ga_{0.3}$)Se_2/CdS/ZnO/ZnO:Al heterojunction simulated for open circuit condition under illumination. Simulation was performed on SCAPS according to the materials parameters described in [41].

The heterojunction is between the CIGS layer, which is poorly p-doped ($4 \cdot 10^{15}$ cm^{-3}), and the CdS layer, which is highly n-doped (10^{18} cm^{-3}). Diffusion of charges at the interface leads to positive charges in the n-region and negative charges in the p-region. Due to the neutrality condition at the CIGS/CdS interface, an electric field is implemented across a distance of approximately 300 nm in the CIGS layer according to the Poisson equation. This region, deficient in free carriers, is called Space Charge Region (SCR). In the CIGS region that extends from the SCR to the back contact is called Quasi-Neutral Region (QNR): the free majority carrier density is close to the net doping density ($p \sim N_a$). This region is therefore almost neutral.

1.2.3.2. Charges generation

Photo-carriers are generated in the CIGS layer from photons emitted by the sun. The solar spectrum is described by the black body emission given by the Stefan-Boltzmann radiation law at a temperature of 5800 K. The solar spectrum on earth also takes into account the absorption of various species present in the earth atmosphere for an angle of incident of 48°. It results in the AM1.5 solar spectrum presented in Fig. 1.10 with an energy onto a surface normal to the sun of 1000 W/m^2.

When a photon is absorbed by the CIGS, an electron-hole pair is photogenerated. The experimental absorption coefficient measured for the CIGS is presented in Fig. 1.11a (see Appendix B). As the CIGS is a direct band-gap semiconductor, the absorption coefficient of the photons with energy above its band-gap is high (from 10^7 to 10^8 m^{-1} in the visible region). We have calculated the charge carrier

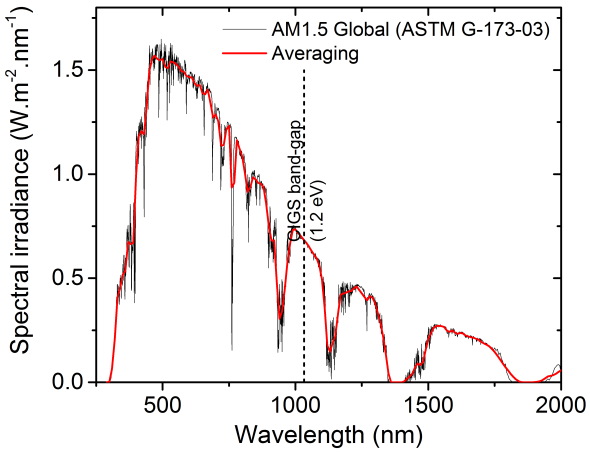

Figure 1.10.: AM1.5 solar spectrum. In red: averaging used for photocurrent calculations.

generation density for a 1000 nm thick CIGS (using the Ray Transfer Matrix method detailed in sec. 2.2.4.2 and Appendix C). The result is presented in Fig. 1.11b. A majority of the charge carriers are generated in a CIGS region of approximately 400 nm. We also observe that the reflection at the back contact creates some interference shapes.

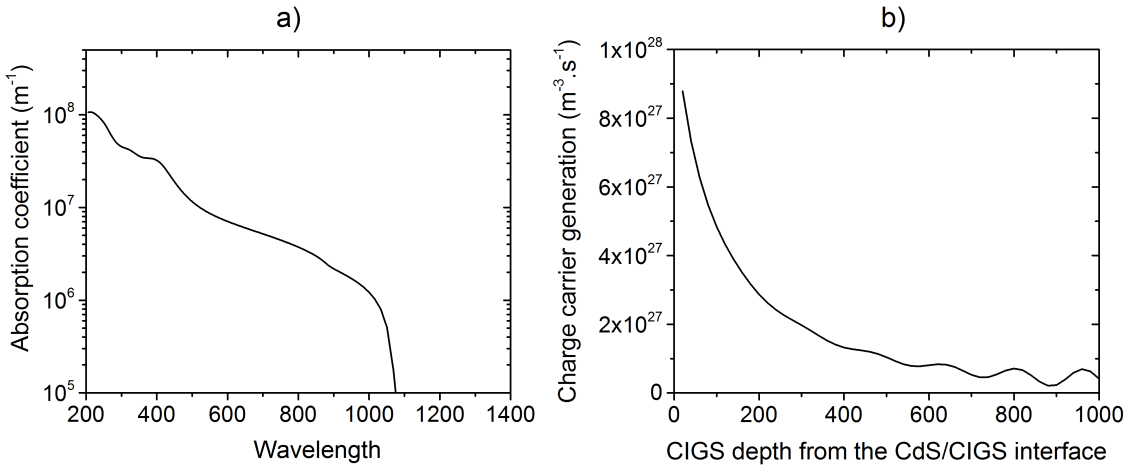

Figure 1.11.: Photon absorption in the CIGS layer: a) absorption coefficient of a CIGS with a band-gap of 1.2 eV calculated from ellipsometric measurements (seeAppendix B) and b) charge carrier generation density profile in a 1000 nm thick CIGS layer simulated by ray transfer matrix method (see sec. 2.2.4.2and Appendix C).

The electron-hole pairs are generated in identical energy distribution than the absorbed photons (corresponding to the solar spectrum). The system is brought out of equilibrium with an excess of electrons in the conduction-band and an excess of holes

in the valence-band. Therefore, electron and hole concentrations are defined by two quasi-Fermi levels. The difference between both quasi-Fermi levels corresponds to the generated chemical potential.

1.2.3.3. Charges collection

Electrons are collected at the CIGS/CdS interface and holes are collected at the Mo interface. Considering an infinite lifetime of the charge carriers in the CIGS and energy selective contacts, the carrier would freely diffuse before the adequate contact is reached. However, those conditions are not valid in a CIGS device.

The separation of the electrons and the holes can be assisted by two mechanisms:

- from an electric field. This is the main driving force acting on the charges in the SCR. The electric field implemented in the SCR (between the CIGS/CdS junction to approximately 300 nm in the CIGS) leads to a drift of the electron to the CIGS/CdS contact and of the holes to the QNR.
- from diffusion when the charge carrier concentration is not the same along the CIGS thickness. This is represented by a chemical potential variation. According to the SCAPS calculations in Fig. 1.9, the chemical potential variations are small in the CIGS bulk. Therefore the current diffusion is low.

From these principles and inspired from previous studies [34, 61, 62, 63, 64], we set a simple minority carrier collection model to describe our cells. We simulate a collection function ($f_c(z)$) which is the probability to collect a charge generated at a distance z of the CdS/CIGS interface along the thickness d of the CIGS layer. The minority charge carriers act differently in the SCR and in the QNR:

SCR — The collection of electrons is almost perfect due the electric-field. However, we assumed a collection function below 1 to simulated the drift-loss or the tunneling assisted recombination [61, 37]. To illustrate this effect, a factor h is used with $0 < h < 1$.

QNR — The electrons diffuse without preferential direction before their recombination (radiative recombination or defect-related recombination in the bulk or at the interface) or their collection when they reach the SCR border. Different models of collection function can be used. The Gärtner model [65] is usually used for thick CIGS solar cells [61, 66, 62]. The collection function in the Quasi Neutral Region depends on the electron diffusion length (L_n) and a neglects the recombination at the back contact (which can be either due to low electron recombination velocity at the back interface or thick CIGS $d \gg L_n$). This leads to $f_c^{QNR} = \exp\left(-\left(z-w\right)/L_n\right)$ and $f_c^{SCR} = 1$.

The electron diffusion length L_n in the CIGS is estimated at approximately 1-2 µm [61, 67] which is larger than the CIGS thickness in ultra-thin CIGS cells. Therefore the influence of the back-contact has to be

taken into consideration with a more accurate model and is described by R. Scheer and H.W. Schock [63, 34]. The collection function $f_c(z)$ depends on the electron back contact recombination velocity ($S_{n,BC}$), the electron diffusion length in the CIGS (L_n), the depletion width w and the electron diffusion coefficient D_n.

Finally, the collection function is $z-$position dependent and is detailed in Eq. F.1.

$$\begin{cases} f_c^{SCR} = h \\ f_c^{QNR} = h.\dfrac{\left(\frac{1}{L_n}\right)\cosh\left(\frac{z-d}{L_n}\right)-\left(\frac{S_{n,BC}}{D_n}\right)\sinh\left(\frac{z-d}{L_n}\right)}{\left(\frac{S_{n,BC}}{D_n}\right)\cosh\left(\frac{d-w}{L_n}\right)-\left(\frac{1}{L_n}\right)\sinh\left(\frac{d-w}{L_n}\right)} \end{cases} \tag{1.2}$$

This model will be useful for the estimation of the back-contact surface recombination velocity.

1.2.3.4. Non-ideality and recombination mechanisms

The current voltage curve I(V) of an ideal cell can be expressed as Eq. 1.3:

$$J_{light}(V) = J_{diode}(V) - J_{ph}(V) \tag{1.3}$$

where J_{ph} is the photocurrent generated by the cell and J_{diode} is the diode current also called dark current . The diode current is expressed by: $J_{diode} = J_0(\exp(qV/kT)-1)$ with J_0 the saturation current, q the charge of electron, k the Boltzmann constant and T the temperature. This equation is based on the superposition principle that assumes that the photocurrent is simply added to the diode current. The J_{diode} is due to the radiative recombination current that cannot be avoided and corresponds to the emission of a black-body at the cell temperature.

However the I(V) curves of a real CIGS device differs to Eq. 1.3 because of:

- **A voltage-dependent photocurrent.** This can be due to either a cross-over effect or from a violation of the superposition principle [34] as presented in Fig. 1.12. The cross-over effect is commonly observed in CIGS solar cells. One explanation is the presence of an electron barrier at the CdS/CIGS interface which is reduced under illumination [68]. The violation of the superposition principle is a decrease of the photocurrent for an increase of the applied bias. It can be due to small electron diffusion length that limits the collection in the QNR. For increasing applied bias, the SCR is shorter and the collection is lower [34]. As a consequence, we express $J_{ph}(V) = J_{SC} \cdot f_c(V)$ with $f_c(V)$ the voltage dependent collection function.

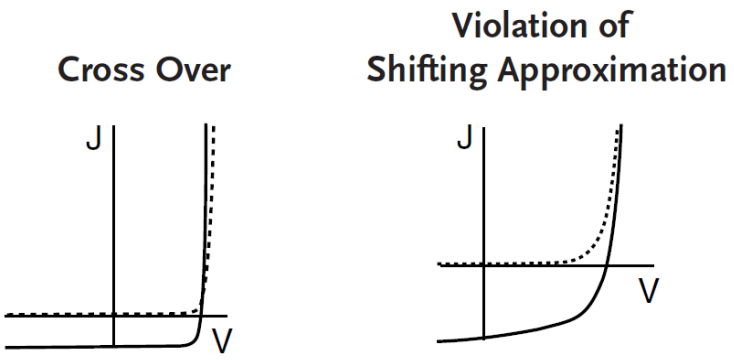

Figure 1.12.: Effect of a voltage-dependent photocurrent on the I(V) curve: (left) cross over effect, (right) violation of the shifting approximation. from [34].

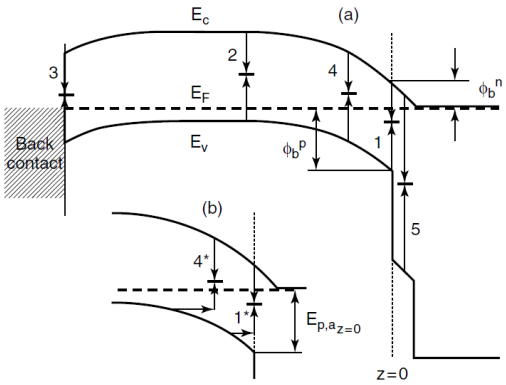

Figure 1.13.: a) Schematic presentation of the most critical recombination paths in a CIGS solar cell. Recombination (1) at the absorber surface, (2) in the absorber bulk, (3) at the absorber back contact, and (4) in the absorber space charge region. b) Sketch of tunneling enhanced recombination (1∗) for interface and (4∗) SCR recombination. From [34].

- **Non-ideal diodes and recombination current.** The real diode current is the sum of different recombination currents in the cells with different activation energies (schematized in Fig. 1.13). To express this effect, we insert an ideality factor or diode factor n in the current diode: $J_{diode} = J_0(\exp(qV/nkT) - 1)$. Moreover, the saturation current J_0 is increased. Defect-related recombination are mainly concerned. The defect-related recombination can be described as an electron-hole pair recombination *via* a single defect at an energy E_d between the valence- and the conduction-band of the CIGS, with a density N_d (Schockley-Read-Hall recombination). The energy released is transferred to a phonon. Recombinations occur in different regions and exhibits different voltage dependence behavior (reflected by the ideality factor n):

  1. *in the SCR*: this region is under the influence of the electric field of the junction which varies with the applied bias. For a mid-gap defect, the activation energy is $E_g/2$ and leads to an ideality factor of 2. The ideality

factor of 2 can also be seen as a symmetric variation of the quasi-Fermi level with respect to the defect level for applied bias [34]. However, for intermediate energy defect ($E_d < E_g/2$), which is the case for some defect in the CIGS, the ideality factor can lay between 1 and 2 but there total recombination rate would be small. Accordingly, even with a combination of shallow and deep defects, the diode ideality factor

2. *in the QNR*: in this region, the recombination can be related to defects in the CIGS bulk and back-contact. The current recombination depends on the collection function that governs the minority carriers concentration. Only the quasi-Fermi level for electron varies with the applied bias for low and medium voltages. As a consequence the ideality factor observed for this recombination is 1.

3. *at the front interface*: the recombination depends on the conduction-band offset ($\triangle E_c$) between the CIGS and the CdS and the defects at the interface. For $\triangle E_c < 0$ (*i.e.* spike between the CIGS and the CdS), the activation energy is equal to the CIGS band-gap at the interface leading to an ideality factor of 1. For $\triangle E_c > 0$ (*i.e.* cliff between the CIGS and the CdS), the activation energy is reduced by $\triangle E_c$ leading to an ideality factor between 1 and 2. If the Fermi level is pinned closed to the valence band by a sufficient acceptor interface charge density, the band-gap at the interface is smaller than the band-gap of the material. As a consequence, the activation energy is smaller and the ideality factor is higher than 1.

4. *Tunneling enhanced recombination*: holes can be transfer by tunneling to a defect in the SCR or at the interface where the valence band is bent. For example, tunneling enhanced recombination at the front interface can happen when the CIGS is highly doped leading to a strong band-bending close to the CIGS/CdS interface [37]. The tunneling recombination increase the ideality factor and can even lead to a cell ideality factor higher than 2.

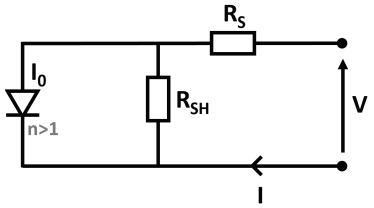

Figure 1.14.: Schematics of the series resistance (R_S) and the shunt resistance (R_{SH}) in the equivalent circuit of the solar cell.

- **Parasitic resistance.** A solar cell is not a perfect diode and a series resistance (R_S) and a shunt resistance (R_{SH}) as schematized in Fig. 1.14 has to be taken into account. The electrodes layers and the interfaces (CIGS/Mo, CdS/ZnO

and ZnO/ZnO:Al) are resistive. Moreover some shunt paths can be created through the CIGS.

Finally, the equation modeling the I(V) curve of a real CIGS device can be written as Eq. 1.4:

$$J_{light}(V) = -J_{SC} \cdot f_c(V) + J_0 \cdot \left[\exp\left(\frac{q\,(V + R_S \cdot J_{light})}{nkT} \right) - 1 \right] + \frac{V + J_{light} \cdot R_S}{R_{SH}} \quad (1.4)$$

where J_0 is the saturation current corresponding to the recombination current of all the recombination mechanisms.

1.2.3.5. Current-voltage characteristics and quantum efficiency analysis

It is important to know how to analyze the I(V) curves and the external quantum efficiency (EQE) of the solar device.

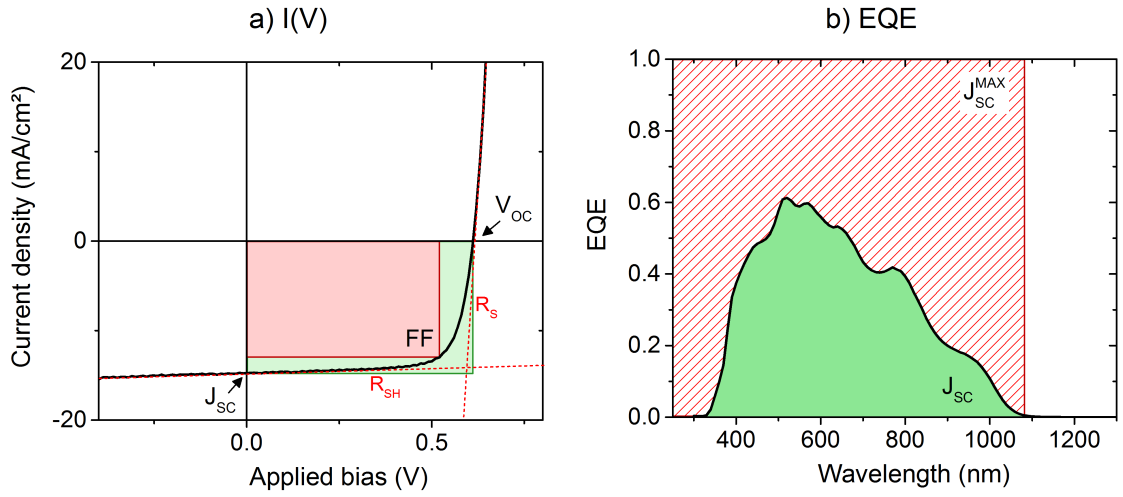

Figure 1.15.: Schematics of a) current-voltage curve of a solar device and b) external quantum efficiency. For the data, we took a 250 nm thick CIGS device.

I(V) curve As an example, the measured I(V) curve under illumination of a 250-nm-thick CIGS solar device is presented in Fig. 1.15a. This curve is usually characterized with three particular values:

- **The current for short circuit condition, J_{SC}.** It corresponds to the photocurrent $J_{SC} \cdot f_c(V)$ at $V = 0$ in Eq. 1.4. This is all the charges that are generated in the CIGS layer and collected by the contact of the cell. The maximum J_{SC} for a semiconductor with a band-gap of 1.2 eV under AM1.5G

illumination is approximately 40 mA/cm² [34]. This current is reduced by the parasitic light absorption of the other layer than the CIGS and by the light reflection at the front-window. Recombination of the generated charges before being collected also limits the J_{SC}.

- **The voltage at open circuit condition, V_{OC}.** At open circuit condition, the total current is equal to 0 and therefore all the charges recombine. In the ideal case, the charges only recombine according to a radiative recombination corresponding to the emission of a black-body at the cell temperature. The obtained V_{OC} described by Shockley and Queisser [69] is approximately $E_g/q-$ 250 mV for a semi-conductor with a band-gap of 1.2 eV. However, according to 1.4 the V_{OC} is also reduced by (1) additional recombination (that increases J_0 and the ideality factor), (2) a voltage-dependent J_{ph} or (3) a too low shunt resistance. The analysis of the V_{OC} variation in the case of a 2-diode model is detailed in Appendix A.
- **The Fill Factor, FF.** This is the ratio between ($J_{SC}\cdot V_{OC}$) and the maximum generated power. The maximum FF of a CIGS device is approximately 83% (band-gap of 1.2 eV, ideality factor of 1 and V_{OC} according to the Shockley-Queisser limit). However, the FF is limited by (1) SRH recombination, that decreases the V_{OC} and increases the ideality factor, (2) high series resistances (3) the low shunt resistances.

EQE curve As an example, the measured EQE of a 250-nm-thick CIGS solar device is presented in Fig. 1.15b. The $EQE/(1-R)$, with R the cell reflectance, is the probability to collect an electron generated in the CIGS. The relation between the EQE and the J_{SC} is given by Eq 1.5:

$$J_{SC} = \frac{q}{hc} \cdot \int_0^\infty EQE \cdot \Phi_{sun} \cdot \lambda \cdot d\lambda \tag{1.5}$$

The maximum J_{SC}, indicated in red in Fig. 1.15b, is calculated with $EQE = 1$ for $E > E_G(\text{eV})$ and $EQE = 0$ elsewhere.

The J_{SC} calculated from the EQE should be identical to the J_{SC} measured on the I(V) curve. However, a difference is sometimes observed. It should be noticed that the I(V) curve is performed under high current injection with a polychromatic light, whereas the EQE is performed under a low current injection with a monochromatic light. A high J_{SC} and a low EQE can be due to a barrier which is large under low light intensity or monochromatic illumination but becomes lowered under AM1.5 illumination.

1.2.4. Conclusion

The standard CIGS based solar cell have the following structure : Glass / Mo (500-1000 nm) / CIGS (1.5-3 µm) / CdS (30-50 nm) / ZnO (40-60nm) / ZnO:Al (150-500 nm). A current and a voltage are generated in the cell. The absorption of the sun photons in the CIGS layer generates electron-hole pairs followed by the collection of holes at the Mo/CIGS contact and electrons at the CdS/ZnO/ZnO:Al contact.

In this work, we study how the reduction of the CIGS thickness affects the collection and collect processes.

1.3. Toward ultra-thin CIGS solar cells

1.3.1. Interest of making thinner CIGS layer

Two arguments are suggested to explain why reducing the CIGS layer thickness has an interest for CIGS industries: (1) it would reduce its dependence to the metal market, and (2) it would reduce the manufacturing cost of a module. Those two arguments are analyzed in the following.

The Tab. 1.2 gives an overview of the Cu, In, Ga and Se resources (estimation of the quantity that can be mined), reserves (quantity easily available), production and price [70][71]. In and Ga are costly materials. Even if the price has recently greatly decreased, a large price fluctuation was observed over the past years. Moreover the reserve of In is low and depends on various geopolitical aspect.

Table 1.2.: Overview of the metal market. From [70] and [71].

	Resources (t)	Reserves (t)	Mine production 2015 (t)	Price ($/kg) 2014	2015	Price fluctuation 2010-2015 ($/kg)	Other major use
Cu	2M identified	720 000	18 700	7	6	5 - 10	Conductor
In	95 000	50 000	755	705	540	200 - 800	ITO
Ga	>1M	?	435	365	295	150 - 1000	GaN
Se	?	120 000	?	50	50	11 - 165	Impurities

According to the European Commission Report in 2014 [5], Indium and gallium have been identified as critical raw materials, chosen for their supply risk and economic importance. The forecast demand growth to 2020 is expected to be 'very strong' for Ga (>8%) and 'strong' for In (from 4.5 to 8%). The forecast market balance to 2020 places In and Ga in the category of materials having a risk of deficit.

To highlight the need of the CIGS industry in In, we have calculated some key figures:

- If we consider a CIGS module of 14% efficiency with a 2 µm thick CIGS, a GGI = 0.3 and a material yield of 0.9 for its fabrication: the CIGS consumes **3.5 g(In)/m²** (or 2.5g(In)/W) and **2.1 g(Ga)/m²** (or 1.5 g(Ga)/W).
- A power plant of 100MW/year would demand **2.5 tonnes of In** and **1.5 tonnes of Ga** every year.

A constant and predictable supply in In and Ga is therefore crucial for a manufacture.

The reduction of the CIGS thickness can also leads to a cost reduction. In a manufacture, the cost of the CIGS layer can be divided in 2 categories: OPEX (including the material cost) and CAPEX (including the equipment and building depreciation).

A simulation of the CIGS layer cost for a 100MW manufacture in the USA has been performed by Horowitz *et al.* [4]. The detail of the cost is presented in Fig. 1.16. The

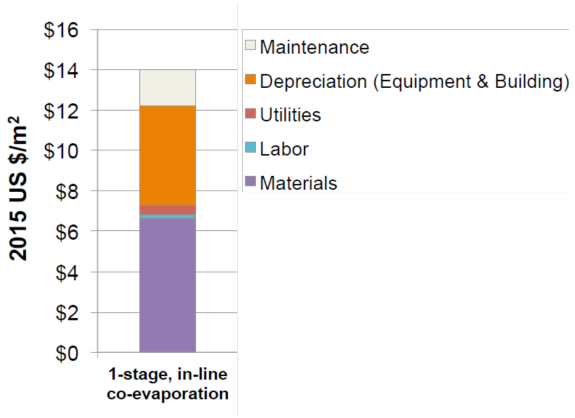

Figure 1.16.: Cost of the CIGS coevaporation step in the production line. The total module cost is 76 $/m². From [4].

materials price represents approximately **6.5 €/m²** and the depreciation represents approximately **4.5 €/m²** for a total CIGS module price at **70 €/m²** (or 500 €/kW).

In the following, we detail the cost reduction due to In and Ga. We assume that the efficiency of the module is the same when thinning down the CIGS thickness and that no additional costs are expected.

- We consider the In price of 550 €/kg and the Ga price of 300 €/kg. In the manufacture described above, the cost of In would be: 1.9 €/m² (or 13.8 €/kW) and the cost for Ga would be 0.6 €/m² (or 4.6 €/kW). This leads to a **total cost for In and Ga of 2.6 €/m²** (or 18.3 €/kW) cost. The price of Cu, In, Ga and Se of 6.5 €/m² calculated by Horowitz *et al.* [4] in Fig. 1.16 is much larger. The assumption of higher materials price and the Se consumption can explain the difference.
- If we reduce the CIGS layer from 2 µm to 400 nm (factor 5) the cost of In and Ga is reduced to **0.6 €/m²** (or 3.7 €/kW). The reduction cost due to the Se consumption is difficult to estimate and is not taken into consideration.
- If we suppose than reducing the CIGS thickness would double the throughput of the manufacture, the equipment and the building depreciation would decrease of **2.2 €/m²** (15.7 €/kW).

Finally, a gain of **4.2 €/m²** (30 €/kW). However, the efficiency of the final module would also impact the total manufacturing price of the module:

- For a module at 70 €/m² (or 500 €/kW at 14% efficiency), a change in 1% efficiency leads to an opposite change in the cost of around **35 €/kW**. As a consequence, keeping module efficiency at the same level while reducing the CIGS thickness is crucial [72]. According to simulations performed in sec. 2.3.1 and from B. Vermang *et al.* [73], a possible increase of efficiency compared to the thick CIGS devices for thickness of around 600 nm.

Finally, according to our rapid cost estimation, a reduction of several €/m² can be

expected over the total cost of the CIGS solar device when thinning down the CIGS thickness.

1.3.2. State of the art on the ultra-thin CIGS cells issues

The CIGS solar cells with a reduced absorber thickness have been first studied by Shafarman *et al.* in 1997 [74], and Negami *et al.* in 1998 [75]. The CIGS was deposited by a fast 3-stage process and they observed a decrease of the cell efficiency due to a decrease in all the cell parameter.

Up to now, several studies aimed to understand the physical reasons explaining the impact of the CIGS thickness on the cell performance. All these results are:

- **a lack of absorption** due to the penetration depth of visible light that reduces the J_{SC} [76, 77]. The reduced EQE has been studied in detailed by optical simulation by Dahan *et al.* [78] highlighting the large absorption in the Mo layer for thin CIGS layer. The impact of the back-contact reflectance was studied by Orgassa et al. [28] and Jehl *et al.* [79] for different materials. However, the Mo back contact remains the best metal layer for a direct deposition of the CIGS [28]. A highy reflective back-contact would improve the J_{SC} [73].
- **higher risk of shunts** was observed by Shafarman *et al.* [74]. The shunts reduce the FF.
- **an increased impact of the back-contact recombination** that reduces the J_{SC} and V_{OC}. This effect was highlighted by O. Lundberg *et al.* [80] using a back-surface field in $CuGaSe_2$ and by J. Pettersson *et al.* [81]. M. Gloeckler *et al.* [82] have simulated the effect of a band-gap grading at the back-contact to reduced the recombination: a perfect electron back-reflector inserted in a 500 nm thick CIGS cell would lead an increase of the V_{OC} of 100 mV and the J_{SC} of 5 mA/cm². B. Vermang *et al.* [73] has simulated on SCAPS a V_{OC} increase of 10 mV for a CIGS thickness of 1500 nm if the electron velocity at the back-contact is reduced from 10^6 to 10^3 cm/s [73]. Interestingly, E. Jarzembowski *et al.* [77], deduced from the optical modelisation of their sample that the back-contact recombination has a minor impact compared to the light non-absorption.
- **difficulties to implement the 3-stage process.** If the CIGS thickness is proportional to the deposition duration, ultra-thin CIGS can be deposited in a too short duration to create the required composition gradient [83]. Moreover, E. Leonard [84] has observed that the recrystallization phase forms a region with a high sodium concentration close to the CIGS/CdS interface. This region has a higher valence-band position that enhances the tunneling recombination and reduces the cell performances;

- **a reduction of the total recombination** due to the thinner CIGS layer [34, 85] that increases the V_{OC}.

It is therefore necessary to work on the CIGS deposition (no pin-hole, a Ga gradient, a suitable coevaporation process) and on the cell structure (limitation of the back-contact recombination, improvement of the absorption in the CIGS layer) to reach high efficiencies with an ultra-thin CIGS solar cell.

1.3.3. State of the art on the ultra-thin CIGS cells performances

An overview of the studies performed on the CIGS cells with various CIGS thickness is given in Fig. 1.17, Fig. 1.18, Fig. 1.19 and Fig. 1.20.

The cell parameters are presented for the cells with the standard configuration Mo / CIGS / CdS / ZnO / ZnO:Al as a function of the CIGS thickness (empty symbol) and for the cells with an improved configuration indicated in the legend (full symbol). For the cell with standard configuration, we observe in Fig. 1.17 a clear negative trend of the cell efficiency when the CIGS thickness decreases. This effect is mainly correlated to the similar trend of the J_{SC}. The V_{OC} slightly decrease when the CIGS thickness decrease. The large variations of J_{SC} and V_{OC} between the different studies are mainly related to the band-gap of the CIGS. However, the FF is poorly correlated to the CIGS thickness for thickness above 300 nm. The large variations between the different studies can be related to the cell quality that is achieved.

The following list corresponds to the number indicated in the legend of the figures Fig. 1.17, Fig. 1.18, Fig. 1.19 and Fig. 1.20:

1. K. Ramanathan *et al.* [86]. CIGS layers with different thicknesses were deposited by a 3-stage coevaporation process on Mo back contact.
2. Z. Jehl *et al.* [6]. Thick CIGS layers was deposited on Mo back by coevaporation at *Würth Solar*. The absorber was then etched in a solution of HBr/Br_2 to reach to different thicknesses. This method allow an accurate study of the evolution of the CIGS solar cell performance without change in the CIGS quality. The study clearly pointed out the light non-absorption as the main responsible for the reduced cell performance. It also suggest that the CIGS thickness becomes thinner than the SCR which limits the V_{OC}.
3. Z. Jehl *et al.* [79]. Equivalent samples as (2) were prepared. To improve of cell performance, the CIGS/CdS/ZnO/ZnO:Al was peeled-off from the Mo substrate then a gold back contact was evaporated onto the CIGS back-surface. A large increase in the J_{SC} is observed compared to the reference on Mo (+ 4 mA/cm^2 for a 400-nm-thick-CIGS cell).
4. E. Leonard [84]. CIGS layers with different thicknesses were deposited by coevaporation using a 3-stage process on Mo back contact. To improve the cell efficiency, a reflective back-contact was fabricated using a 100 nm thick ZnO:Al

layer coated on Mo. In this case, a 500-nm-thick CIGS was deposited using a 2-stage coevaporation process. Openings were created though the ZnO:Al layer to improve the electrical contact at the Mo/ZnO:Al/CIGS interface. They observed an increase of the J_{SC} compared to the reference on Mo related to the back interface reflectivity.

5. O. Lundberg *et al.* [80]. CIGS of different thicknesses were deposited by coevaporation using a 1-stage in-line process on Mo back-contact. To improve the cell efficiency, The create a composition gradient that achieves a back-surface field effect. The higher conduction-band close the back-contact repels the electrons and minimizes the recombination. For this purpose, a thin (10-100 nm) layer of pure CGS was evaporated on the Mo back-contact. They observed an increase in the V_{OC} of approximately 30 mV and in the FF of 5%abs. for CIGS thickness below 1000 nm compared to the reference on Mo.

6. J. Petterson *et al.* [85]. CIGS of different thicknesses were deposited by coevaporation using a 1-stage in-line process on Mo back-contact. This study aimed to understand the variation of the cell performance when thinning down the CIGS thickness with both SCAPS simulation and experiments. To improve the photocurrent in the cell, the CdS-buffer layer was replaced by an ALD-Zn(O,S) layer.

7. B. Vermang *et al.* [87]. A 400-nm-thick CIGS was deposited by 1-stage co-evaporation process. To improve the cell performance, a combination of a 5 nm thick ALD-Al_2O_3 layer and a 60 nm thick MgF_2 layer was inserted between the Mo and the CIGS layer. The Al_2O_3 layer passivates the CIGS surface. The MgF_2, which has a low refractive index, increases the reflection coefficient the interface. A NaF precursor was evaporated on the back-contact prior to the CIGS deposition. The electrical contact between the CIGS and the Mo layer was permitted by openings on the MgF_2/Al_2O_3 layers. This configuration leads to a large increase in J_{SC} (+7.9 mA/cm^2) and V_{OC} (+57 mV) compared to the reference on Mo for the 400-nm-thick CIGS.

8. B. Vermang *et al.* [88]. The same CIGS fabrication procedure than in (7) was used with a 240-nm-thick CIGS. The passivation was achieved by a 10 nm thick Al_2O_3 layer perforated by e-beam lithography. They observed a large increase in J_{SC} (+3.7 mA/cm^2) and V_{OC} (+58 mV) compared to the reference on Mo.

9. J. Larsen et al. [89]. 100- to 1000-nm-thick CIGS layers were deposited by a single stage coevaporation process. To improve the cell performance, a roof-top configuration was studied: Glass / ITO(300nm) / MoO_{3-x}(10nm) / CIGS(100-1000nm) / CdS / ZnO / ZnO:Al / Ag(500nm). In this configuration, the light comes from the rear-side of the glass substrate. A previous study has demonstrated an ohmic behavior of the ITO/MoO_{3-x}/CIGS contact [90]. A large increase in the J_{SC} of approximately 5 mA/cm^2 is observed for CIGS thickness below 500 nm compared to the reference on Mo. For CIGS thickness

above 500 nm, the charge carrier are generated too far from the SCR, leading to a poor charge-carrier collection.

10. G. Yin *et al.* [83]. A 460-nm-thick CIGS was deposited by 3-stage coevaporation process using different substrate temperatures. The substrate temperature modifies the composition gradient along the CIGS layer. A low substrate temperature reduces In-Ga inter-diffusion and creates a larger back-contact Ga grading. This gradient improves the cell efficiency due to a broader absorption spectrum and due to a back-surface field that improves the charge collection at the back-contact.

11. E. Jarzembowski *et al.* [77]. This article studies the impact of the CIGS thickness on the cell performance for a CIGS deposited with a 3-stage process. Unlike the other laboratories, they find a very low impact of the back-contact recombination on the EQE curves. The reduction of the cell efficiency for reduced thickness is therefore mainly attributed to the incomplete absorption of light.

12. E. Jarzembowski *et al.* [91]. A back-contact reflector was prepared with a periodic nano-structured SiO_2 array coated on the Mo layer to increase the back-contact reflection and scattering. They boost the cell efficiency to 5.9% for a 190-nm-thick CIGS on Mo back-contact to a record efficiency of a 9% with the nano-structured SiO_2 array.

13. C. van Lare *et al.* [92]. A 460-nm-thick CIGS was deposited by a 3-stage coevaporation process. A back-contact reflector was prepared with arrays of SiO_2 nanoparticules at the Mo/CIGS interface. After optimization of the reflector, they achieved a light trapping effect in the CIGS layer and increased the J_{SC} of 2.0 mA/cm^2 compared to the reference on Mo.

14. W. Ohm *et al.* [93]. A 620-nm-thick CIGS was deposited on a SnO_2:F transparent substrate. They used a multi-stage coevapoation process followed by a NaF post-deposition treatment. They also introduced a porous Al_2O_3 layer between the SnO_2:F and the CIGS. This layer passivate the SnO_2:F/CIGS interface. Compared to the reference on Mo, the SnO_2:F/porous-Al_2O_3 back-contact leads to an increase in the J_{SC} (+1.5 mA/cm^2) and the V_{OC} (+37 mV) of the cells.

15. J. Posada *et al.* [94]. The 460-nm-thick CIGS was deposited with a method alternative to the coevaporation process: an hybrid process combining a co-sputtering of Cu, In and Ga and an evaporation of Se.

The most noticeable cell efficiencies are: 9% for a 190 nm thick CIGS (E. Jarembowski *et al.* not published), 11.8 % for a 240 nm thick CIGS [88], 13.5% for a 400 nm thick CIGS [87] and 12.3% for a 460 nm thick CIGS [83].

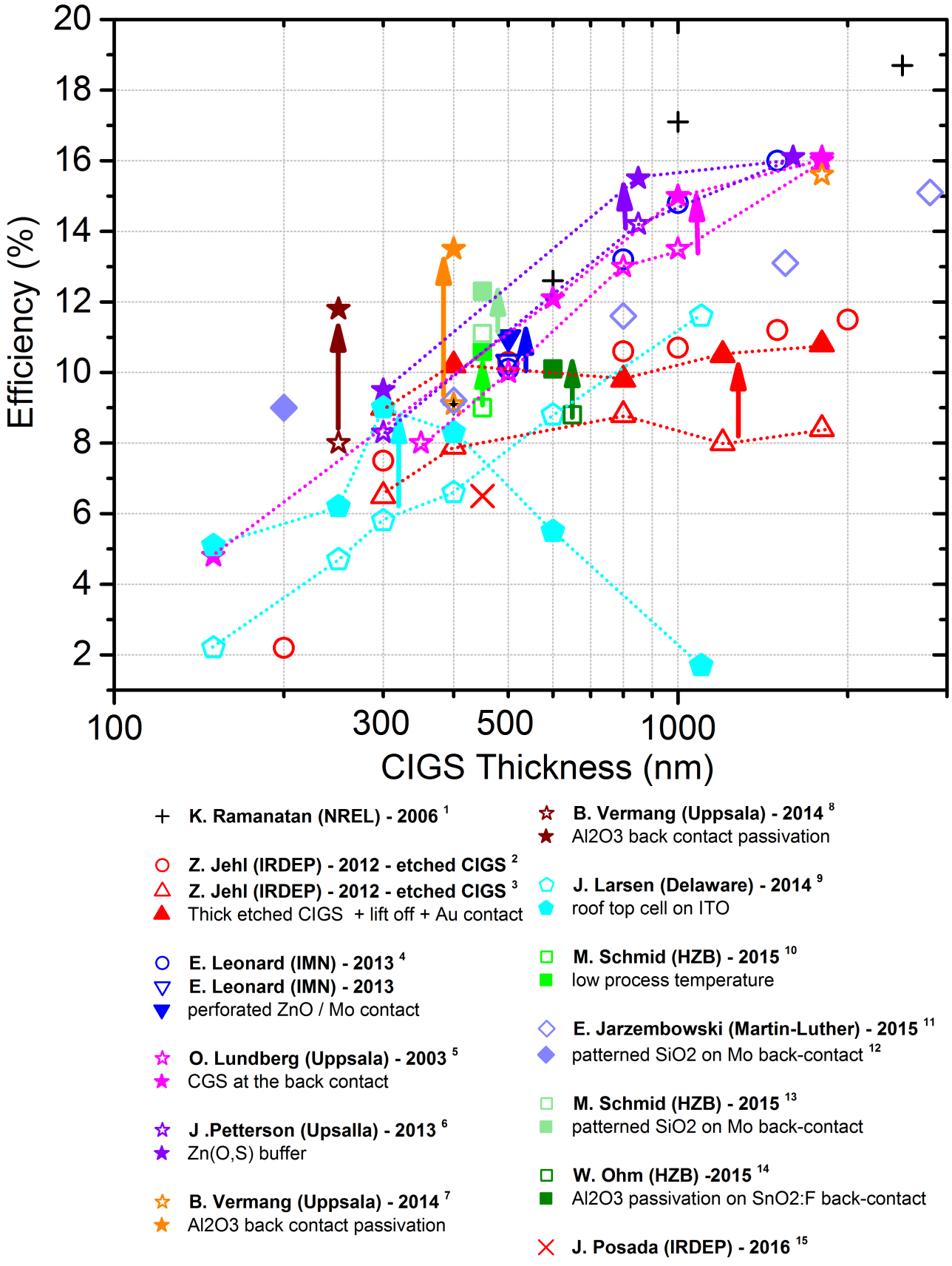

Figure 1.17.: Overview of the cell efficiency for various CIGS thicknesses.

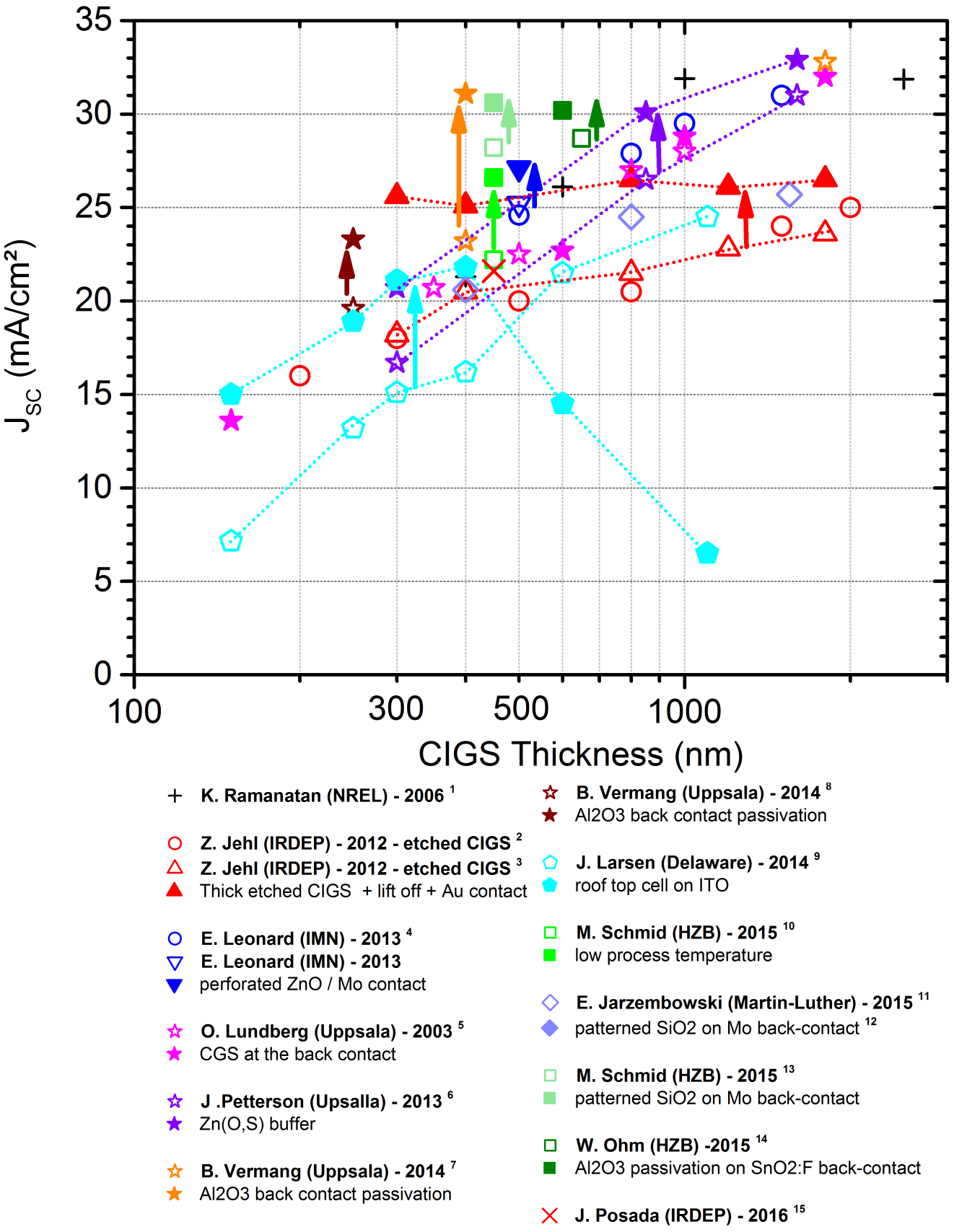

Figure 1.18.: Overview of the cell J_{SC} for various CIGS thicknesses.

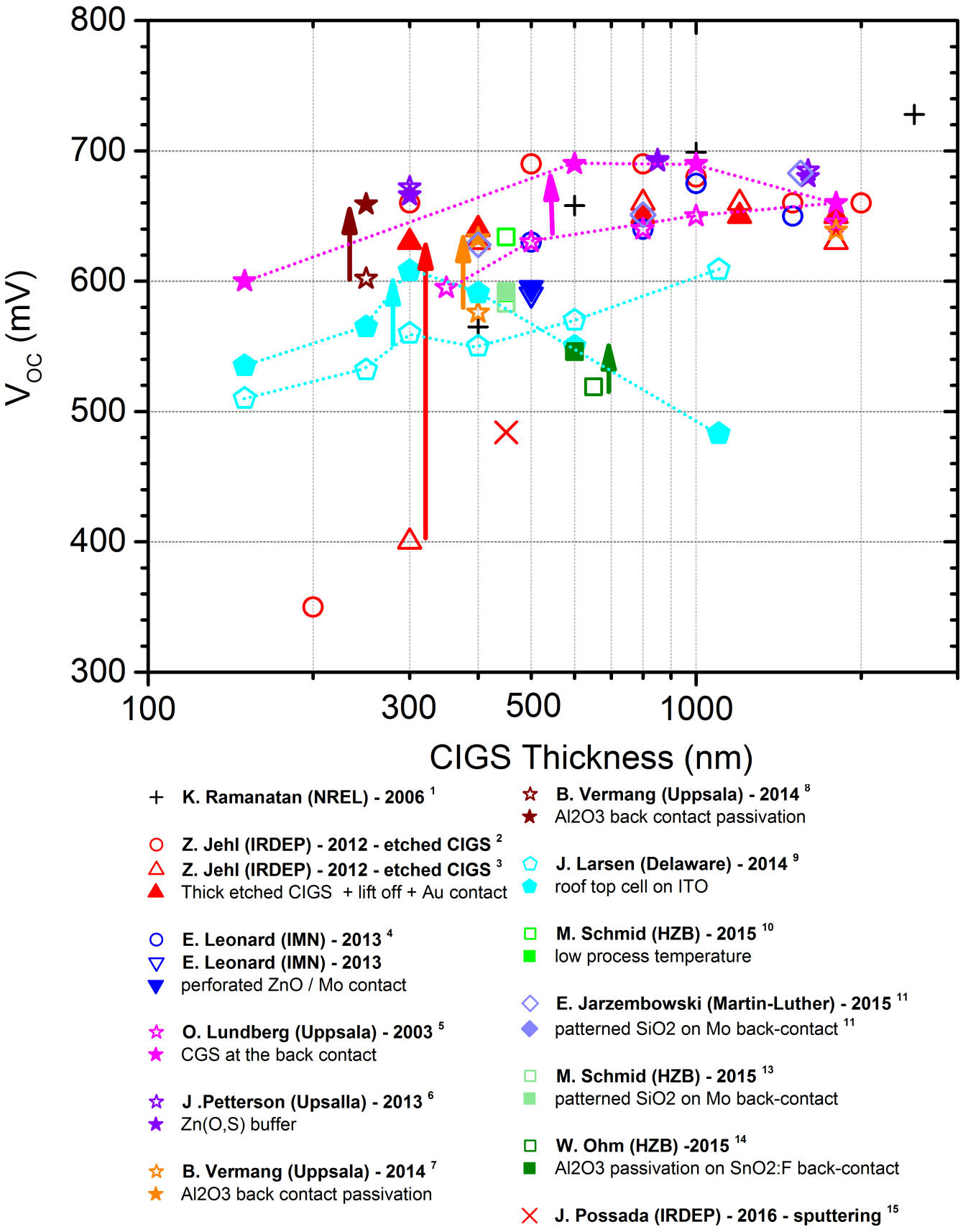

Figure 1.19.: Overview of the cell V_{OC} for various CIGS thicknesses.

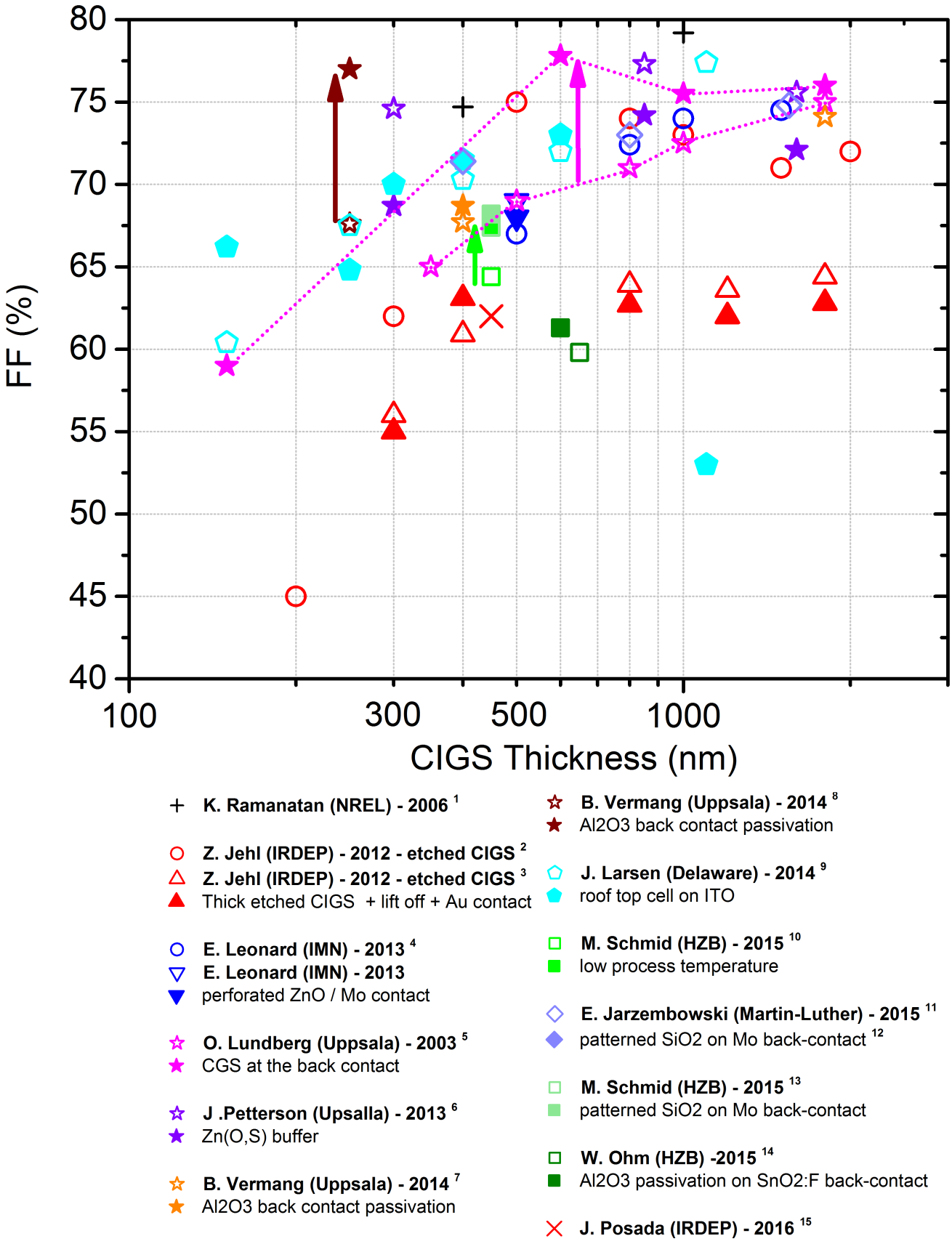

Figure 1.20.: Overview of the cell FF for various CIGS thicknesses.

1.4. Conclusion of the chapter

In the past three years, record efficiencies of $Cu(In,Ga)Se_2$ (CIGS) based solar cells have improved from 20% up to 22.6%. These results show clearly that CIGS is an ideal absorber material for thin-film solar cells. Moreover, the Levelized Cost Of Electricity (LCOE) can still be reduced to boost the CIGS market. One way to reduced the LCOE is to reduce the module fabrication cost. For this purpose, we decided study to the impact of a thinner CIGS layer.

The development of ultra-thin CIGS solar cells (*i.e.* with a CIGS thickness below 500 nm) presents several industrial advantages compared to standard CIGS solar cells (*i.e.* with a CIGS thickness between 2.0 to 2.5 µm). It limits the dependence of the industries on international metal market. It could also slightly reduce the cost of the module by decreasing the material consumption and by increasing the throughput of the factory. In return, the efficiency of the ultra-thin cells has to, at least, match that of standard cells.

However, it has been observed in previous studies that thinning the CIGS layer reduces of the cell efficiency, especially for CIGS thicknesses below 1 µm. This effect is mainly attributed to an increased impact of recombination at the back contact and the reduced light absorption in the CIGS absorber. Recent studies have shown that these losses can be mitigated by the introduction of a back-surface passivation layer in combination with a highly reflective or scattering/reflective back- contact.

2. Ultra-thin CIGS on Mo back-contact

2.1. Introduction

CIGS based solar cells with a CIGS layer deposited by the coevaporation technique leads to the state of the art cell efficiency (22.6%, [95]). Record efficiencies are reached after optimization of both CIGS layers (composition gradient, low defect density, suitable interfaces, alkali doping) and front contacts (transparency, conductivity and quality of the buffer layer).

The CIGS solar cells with only 200- to 500-nm-thick CIGS can be deposited with an equivalent procedure. However, we have seen in the previous chapter that ultra-thin CIGS solar cells typically exhibit lower cell efficiencies than thick CIGS solar cells.

It is therefore necessary to understand the impact of the CIGS thickness on the CIGS quality and on the cells performances. This study was performed first by using electrical simulation of CIGS devices and an optical simulation of the light absorption. Then, samples were fabricated with different CIGS thicknesses.

The samples were first fabricated without any Ga gradient for easier characterization of the materials and electrical properties. Then, we optimized the CIGS deposition process: Ga gradient or multi-step processes.

However, when the CIGS is replaced by an alternative back-contact, the CIGS deposition condition may change. It would require for example a lower substrate temperature or an external supply of alkali. This is why, we have studied the 4 different parameters (substrate temperature, Na diffusion, KF treatment and $MoSe_2$ layer) for ultra-thin CIGS solar cells grown on Mo substrate. The impact of these parameters on the solar cell performances are discussed.

2.2. Materials and methods

2.2.1. CIGS deposition by coevaporation

2.2.1.1. The coevaporation reactor

The CIGS absorber is grown by coevaporation in a commercial reactor developed by *MBE – Komponenten* [96]. The Cu, In, Ga and Se elements are evaporated on the substrate in a high-vacuum chamber (10^{-7} mbar) schematized in Fig. 2.1. The substrate is placed facing-down in a rotating substrate holder. The substrate temperature is regulated by a heater and a thermocouple placed behind the substrate. Each pure element (Cu, In, Ga, Se, NaF and KF) is placed in a crucible inside an evaporation source. The elements are evaporated at their saturation vapor pressure. The evaporation rate of each element is controlled by the power of the sources heater and is measured by a quartz crystal microbalance prior to each deposition. Precise and automatized recipes are followed: the substrate shutter and the evaporation source shutters can be closed or opened, the substrate temperature and the materials flux can be rapidly changed.

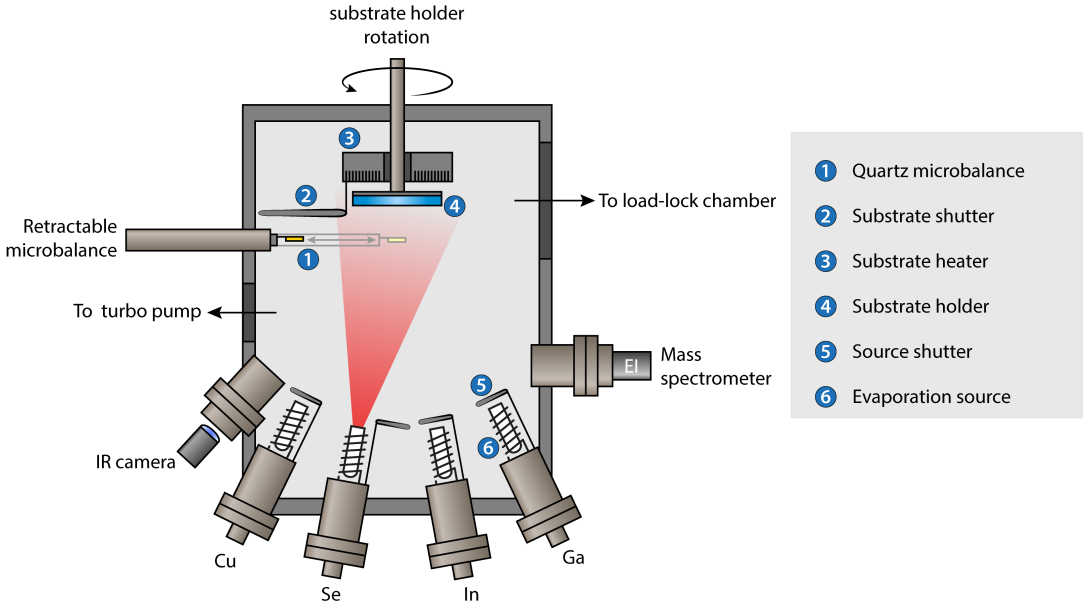

Figure 2.1.: Schematics of the coevaporation reactor used for the deposition of the CIGS layer.

2.2.1.2. One-stage process

The CIGS absorbers were deposited in a one stage process described in Fig. 2.2.

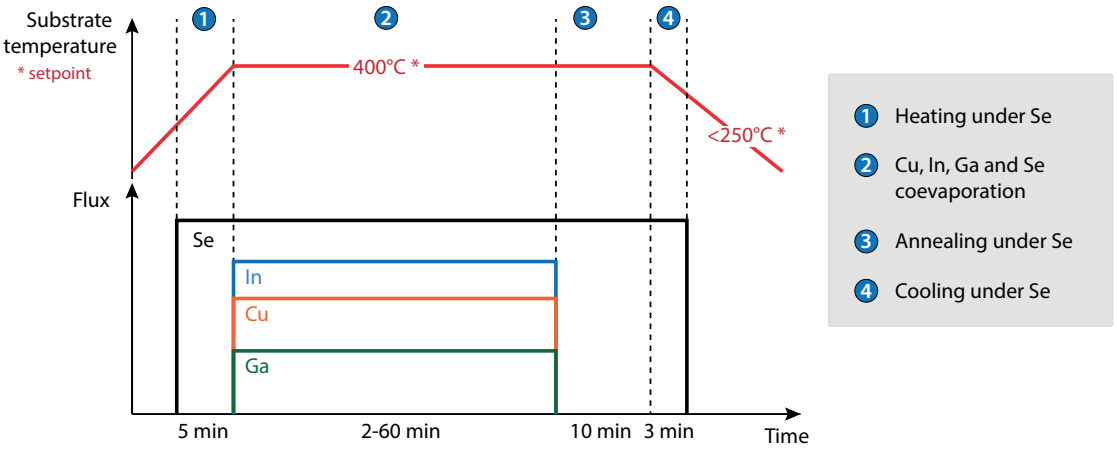

Figure 2.2.: Sketch of the 1 stage process.

The substrate is heated to approximately 500°C, then Cu, In, Ga, and Se are evaporated all together. At the end of the CIGS deposition the substrate is annealed 10 min at 500°C under Se atmosphere and is cooled down to below 250°C under Se evaporation in few minutes. In the 1-stage process, the CIGS thickness and the [Cu]/([In]+[Ga]) and [Ga]/([In]+[Ga]) atomic ratio (CGI and GGI)) are fully determined by the evaporation rates and deposition time.

2.2.1.3. Evaluation of the uncertainties

The system allows a good control of the process parameters (substrate temperature and sources temperature). However, developing a recipe requires a good knowledge of the sources of uncertainties.

Composition and thickness uncertainty. The element fluxes are calculated in nm/min by averaging the flux for around 1 min after the stabilization of the effusion cell temperature. The fluxes evolution, the microbalance sensibility and the background re-evaporation lead to an uncertainty of ±0.1 nm/min. Thus, a process with the standard flux such as 4 ± 0.1 nm/min for Cu, 6.8 ± 0.1 nm/min for In and 2.7 ± 0.1 nm/min for Ga during 15 min deposit a CIGS of 500 ± 10 nm with a composition of $CGI = 0.85 \pm 0.04$ and $GGI = 0.35 \pm 0.02$ (assuming a direct conversion between the flux and the composition). This uncertainty has an impact on the reproducibility of the experiments.

Substrate temperature error. The substrate temperature is measured using a thermocouple placed between the substrate and the heater. This distance leads to a shift between the measured temperature and the real temperature of the growing layer. An accurate measurement of the substrate temperature was performed by using an infrared (IR) camera during the Ph.D. thesis of T. Klinkert [97] and pointed out that for a temperature setpoint at 400°C, the real substrate temperature is measured at 500°C ± 20°C. As a consequence, a

substrate temperature uncertainty remains during the deposition.

2.2.2. Deposition method for the contacts and the buffer layer

The standard structure of a CIGS based solar cell has been presented in sec. 1.2.2. In addition of the CIGS layer, a standardized process for the Mo back contact and the CdS/ZnO/ZnO:Al front windows are used for the fabrication of solar cells. Their deposition methods and characteristics are detailed in the following.

Molybdenum back-contact

The 3-mm-thick soda-lime glass is first cleaned by a detergent and by plasma argon etching. The 800-nm-thick molybdenum layer is a bilayer deposited on the glass by DC magnetron sputtering: an adhesion layer deposited at high Ar pressure and the main layer, with a better conductivity, deposited at lower Ar pressure and at higher power.

The Mo layer layer has a conductivity of 0.20 Ωsquare.

CdS buffer layer

The CIGS surface is treated in an aqueous solution of KCN to remove binary copper phases (Cu_xSe), the excess of alkali and the remaining elemental selenium. The CdS layer is deposited by chemical bath deposition (CBD) [53] at 60°C in a solution containing cadmium acetate $Cd(CH_3CO_2)_2$ as cadmium donor, ammonium as complexing agent and thiourea $SC(NH_2)_2$ as sulfur precursor. The required CdS thickness of 40 nm is reached in approximately 6-8 min depending on the characteristics and composition of the CIGS surface.

ZnO/ZnO:Al front contact

A 60-nm-thick intrinsic ZnO layer is deposited by RF magnetron sputtering using a ZnO ceramic target in an Ar/O_2 plasma.

Subsequently, a 350- to 400-nm-thick Al-doped ZnO (ZnO:Al) layer is deposited by RF magnetron sputtering using a ZnO with 2%wt Al_2O_3 ceramic target in an Ar/O_2 plasma. Typically, the ZnO:Al has a donor concentration of 10^{20}-10^{21} cm^{-3}, a mobility of 10 cm^2/V and a resistivity of 25 Ω_{square}. A light absorption between 4 to 10% was measured between wavelengths of 500 and 800 nm by optical spectroscopy.

2.2.3. Characterization techniques

Materials characterization

The morphology of the samples was characterized by taking images of the CIGS surface and cross-section using a Scanning Electron Microscope (SEM) *Zeiss Merlin VP*. The acquisition of the cross-section images requires a thin evaporated conductive carbon layer. The Cu, In, Ga and Se content were measured by Energy Dispersion Spectroscopy (EDS) installed in the SEM at the acceleration voltage of 15 kV and working current of 1.6 nA. The signal calibration on standard metallic samples allows for the quantification of the layer composition.

The CIGS thickness was measured with a *Veeco* profilometer on a step created by a scratch of a blade or on the cross sectional SEM images. An accurate optical thickness can also be determined by fitting the interference shapes of the EQE measurements with the optical simulation tool described in the following section (assuming that the other layer thicknesses and their optical indexes are well known).

The composition profiles of the Cu, In, Ga, Se, Na and K element were measured by Glow Discharge Optical Emission Spectroscopy (GD-OES) on a *Horiba Jobin-Yvon* instrument with an argon pressure of 350 Pa and a source power of 15 W. The Cu, In, Ga and Se atomic ratios in the GD-OES were estimated based on the calibration of the GD-OES signal intensities with the EDS results of the same samples.

To determine the CIGS crystallization, X-Ray diffraction measurements (XRD) were carried out using a *PANalytical Empyrean* with a Cu Kα_1 radiation in the $\theta - 2\theta$ Bragg-Brentano geometry.

The Raman spectroscopy analysis were carried out with a *Horiba Jobin-Yvon LabRam* instrument with a 532 nm excitation laser. The laser is focalized at the surface of the CIGS and covered a surface of around 10x10 µm^2.

Electrical characterization

Completed solar cells of 0.1 cm^2 were mechanically separated by an automatic scribing tool that removes all layers except the back-contact. The current-voltage I(V) characteristics were measured by a 4 points probe connected to an Agilent voltage source and on a surface thermostated at 25°C. The front contact is assured by 2 gold pins mechanically placed on the surface of the sample (ZnO:Al layer) and the rear contact is solded to the back-contact with pure indium. The measurements can be performed in the dark and under light illumination (AM1.5 global spectrum, 1000 W/m^2, Newport class AAA instrument).

The External Quantum Efficiency (EQE) is measured with a IQE200 from Newport instrument. The Internal Quantum Efficiency (IQE) is calculated according to Eq.

2.1:

$$IQE(\lambda) = \frac{EQE(\lambda)}{1 - R(\lambda)} \tag{2.1}$$

where R is the total reflectance at the surface of the sample measured at each wavelength (λ) with an integration sphere on the same instrument.

2.2.4. Introduction to the CIGS modeling

2.2.4.1. Modeling a standard CIGS solar cell

The simulation were carried out with a simulation tool developed for thin film solar cells: SCAPS 3.2.01 software created by Prof. Burgelman *et al.* from university of Gent [59, 60]. This 1-dimension program simulates the electrical characteristics of thin film heterojunction solar cells, such as (list not exhaustive) current-voltage curves, capacitance-voltage curves, recombination calculations, band-diagrams simulations. Each layer is simulated by physical parameters that need to be measured, calculated or only estimated. They can be found in an abundant literature. The values may vary as regard to the quality or the deposition technique of the materials, especially for the CIGS.

On the basis of previous studies [6, 41, 98, 99, 100], we keep the CIGS solar cell model as simple as possible. The parameters of the ZnO:Al, ZnO, CdS and Mo layer are detailed in Appendix D. The guideline for the CIGS model are:

- The CIGS valence band was fixed at 5.6 eV and is independent of the CIGS band-gap;
- No interface state was used;
- A single neutral defect was localized mid-gap;
- The back interface was taken flat-band;
- Orders of magnitude of the effective density of states, carrier thermal velocity and carrier mobility were used. A careful analysis of each parameters influence on the global performance of the cells shows that a rough estimation of those values is sufficient;
- The acceptor density, the defect concentration and the absorption coefficient, which were identified as the most critical parameters, were chosen to fit the global cell performance with experimental samples.

The parameters used in SCAPS for the CIGS model is detailed in Tab. 2.1.

Note that the calculation of light absorption in SCAPS is based on an exponential intensity decay with the thickness. For layers thinner than 1 µm, multiple reflections and the interferences has to be taken into account. Therefore the J_{SC} calculated by SCAPS for ultra-thin CIGS solar cell may not be accurate enough.

Table 2.1.: Details of the parameters used in SCAPS for the CIGS layer baseline model.

CIGS parameters	Symbol	Value used
Band-gap	E_g	1.2 eV
Electron affinity	χ	4.4 eV
Dielectric permittivity	ε_r	13.6
CB / VB effective density of states	N_C / N_V	10^{18} / 10^{19} cm^{-3}
Electron mobility	μ_e /μ_h	100 / 25 cm^2.(V.s)$^{-1}$
Acceptor density	N_A	5.10^{15} cm^{-3}
Defect density (neutral; mid-gap)	N_D	8.10^{13} cm^{-3}
Defect capture cross section electron / hole	σ_e / σ_h	10^{-13} / 10^{-15} cm^2
Electron / hole diffusion length	L_n / L_h	1.8 / 9 µm
Absorption coefficient	α	$4.10^4.\sqrt{E-E_g}$ cm^{-1}.eV$^{\frac{1}{2}}$

2.2.4.2. Optical modeling of the CIGS solar cells

To improve the optical models, the light absorption in each layer of the cell structure was simulated with a realistic model taking into account the multiple reflections and the interferences. The model is based on the Ray Transfer Matrix (RTM) method [101, 102] developed on MATLAB at *Institut d'Optique Graduate school* by J-J. Greffet *et al.*, in the frame of the ANR UltraCIS^M. This method describes the propagation of an electromagnetic wave across a stack of materials (see details in Appendix C).

In this method, each materials is modeled by its real and imaginary optical indexes (n, k). k refers to the extinction coefficient and is related to the absorption coefficient at a wavelength λ ($\alpha(\lambda)$) of a material by the relation: $\alpha(\lambda) = 4\Pi.k/\lambda$. The optical indexes of the materials used were obtained from various source and are reported in Tab. 2.2 and in Appendix F. They were chosen as close as possible to the materials deposited in the laboratory. In particular, the constants of the CIGS at different band-gap was carefully determined by ellipsometry spectroscopy (see Appendix B).

At each interface, the incident wave is separated in 2 components directed upward and downward (reflection and transition) different in module and phase. It is convenient to analyses separately the energy flux (F) propagating upwards (F^+) and downwards (F^-). The net flux at an interface i is given by $F_i = F_i^+ - F_i^-$. At the end, for the incident flux (F_{inc}) propagating downwards in stack of n layers, the reflectance (R) and transmittance (T) and the absorption of a layer between the

Table 2.2.: Source of the (n, k) indexes used in the optical simulations. [1]Good correlation with the measured R and T values obtained on the in-house ZnO:Al layers. [2]See Appendix B for the experimental and calculation detail. [3]Fit of R and T with an extended Drude-Lorentz model. ILV: *Institut Lavoisier of Versailles*. LPN: *Laboratoire de Photoniques et Nanostructures*.

Layer	Material source	(n, k) calculation	Source
ZnO:Al	DC-magnetron sputtering	Ellipsometry [1]	[103]
ZnO	DC-magnetron sputtering	Ellipsometry	LPN
CdS	-	Ellipsometry	[104]
$CuIn_{1-x}Ga_xSe_2$	In-house CIGS for various x	Ellipsometry [2]	ILV / Horiba
Mo	In-house Mo	Ellipsometry	ILV / Horiba
SnO_2:F	Commercial	Spectrometry [3]	IRDEP
Cu, Au, Ag	Evaporated thin films	Ellipsometry	[105]

interface i, $i+1$ ($A_{i,i+1}$) correspond to:

$$R = \frac{F_0^+}{F_{inc}} \qquad T = \frac{F_n^+}{F_{inc}} \qquad A_{i,i+1} = \frac{F_i - F_{i+1}}{F_{inc}} \tag{2.2}$$

In addition, N. Dahan *et al.* [106] have extended the model to take into account the light scattering. The light scattering can be generated by rough interfaces, scattering reflectors or by particles in a different media. In this case, the light propagation is divided in a specular component and a diffuse component. The specular component is treated using the RTM method and the diffuse part is treated using the radiative transfer equations which are a transport equations for diffuse intensity in scattering and absorbing media.

The simulations of the cell performances highlight the opportunities and the drawback of making ultra-thin CIGS solar cells and identify the key issues of the project.

2.3. Impact of the CIGS thickness on the materials and solar cells properties

In this section, we focus on the impact of thinning down the CIGS on the opto-electrical properties of a standard solar cell on molybdenum substrate. We have proceeded in 3 steps: simulations of the system, then material analysis, and finally cell performance analysis.

2.3.1. Simulated impact of the CIGS thickness on the cell performances

The simulation of the optical and electrical properties of ultra-thin CIGS have been studied previously in the project. Jehl *et al.* [6] have demonstrated that from 2500 nm down to 500 nm, the J_{SC} is the only parameter that is affected by the thickness reduction. From 500 nm down to 100 nm, the absorber is thinner than the Space Charge Region leading to an incomplete separation of the quasi-Fermi level and a reduction of the V_{OC}. Dahan *et al.* [106] have quantified the optical impact of replacing the Mo back-contact by a reflecting and scattering contact.

In this study, the solar cells properties were first simulated on SCAPS for CIGS thicknesses between 2000 to 100 nm. The CIGS parameters used were described in Tab. 2.1. We assume that these parameters are independent to the CIGS thickness. With this hypothesis, we model the cell performances with an ultra-thin CIGS quality similar to the thick CIGS.

In order to understand the impact of the back-contact we used for 3 different settings to simulate the Mo/CIGS interface:

1. a reflection at the back-contact of 20% and an electron back-contact recombination velocity of 10^7 cm/s [107].
2. with a passivated back-contact: the electron recombination velocity is set at a negligible value: 10 cm/s.
3. with a passivated and perfectly reflective back-contact: the electron recombination velocity is set at 10 cm/s and the reflection at 100%.

The important material parameters are summarized in Tab. 2.3.

The result of the simulation is shown in Fig. 2.3. As observed in Fig. 2.3, the simulated cell efficiency with a standard Mo back-contact (black line) decreases when the thickness of CIGS decreases. This effect is mainly due to a dramatic decrease in J_{SC} (approximately -6 mA/cm^2 between 2000-nm- and 500-nm-thick CIGS), and also a decrease in the V_{OC} (-50 mV between the 2000-nm- and 500-nm-thick CIGS). This decrease is even more pronounced for CIGS thinner than 500 nm.

With the passivated back-contact the simulated cell efficiency is improved compared to the standard back-contact. This is mainly due to the V_{OC} which turns out to

CIGS layer	Thickness	100-2000 nm		
	Band-gap	1.2 eV		
		1.	2.	3.
	Reflection	0.2	0.2	1
	Electron surface recombination velocity ($cm.s^{-1}$)	10^7	10	10

Table 2.3.: Main CIGS parameters used in SCAPS simulation for the 3 different settings.

increase when the thickness decreases. The change in V_{OC} trend highlights 2 phenomena. On one hand, charges generated in a thinner CIGS layer are less exposed to recombination in the quasi neutral region. The total recombination is then reduced leading to an increase in the V_{OC}. On the other hand, when the CIGS thickness is short compared to the electron diffusion length (1.8 µm in this model) and when the back-contact is not passivated, the recombination at the back-contact becomes dominant and leads to a decrease of the V_{OC}.

Moreover, as observed in Fig. 2.3 in blue, the use of a perfectly reflective back contact in addition to the back-contact passivation greatly improves the J_{SC} of the cells. It is important to note that the efficiency of a 700-nm-thick CIGS cell with a passivated and reflective back-contact has even a better efficiency than 2000-nm-thick one (+2.9% absolute). If the light absorption in the CIGS is enhanced by a light trapping mechanism, we can assume that the maximum efficiency would be reached at an even lower CIGS thickness.

The cell absorption was also simulated by RTM for a more accurate optical calculations. The photocurrent generated by the cell, J_{ph}, and the contribution of each layer can be calculated to identify the optical effect of thinning down the CIGS layer.

The absorption of a layer i (A_i) in the cell is first calculated by RTM. The equivalent in current density (J_i) can then be calculated according to Eq. 2.3.

$$J_i = \frac{1}{S} \cdot \frac{q}{hc} \cdot \int_{370\,\mathrm{nm}}^{1070\,\mathrm{nm}} \lambda.\Phi(\lambda).A_i(\lambda).d\lambda \tag{2.3}$$

with λ the wavelength, Φ the spectral irradiance, q the electron charge, h the planck constant, c the light velocity and S the cell surface. The 370 - 1070 nm spectral range corresponds to the wavelength between the absorption edge of the ZnO and the bang-gap of the CIGS ($E_g = 1.18$ eV).

Concerning the CIGS, assuming no wavelength- or voltage-dependent collection loss, A_{CIGS} is equivalent to the definition of EQE and $J_{CIGS} = J_{ph} = J_{SC}$. The absorption of the other layers on the same spectral range reduces the J_{SC}.

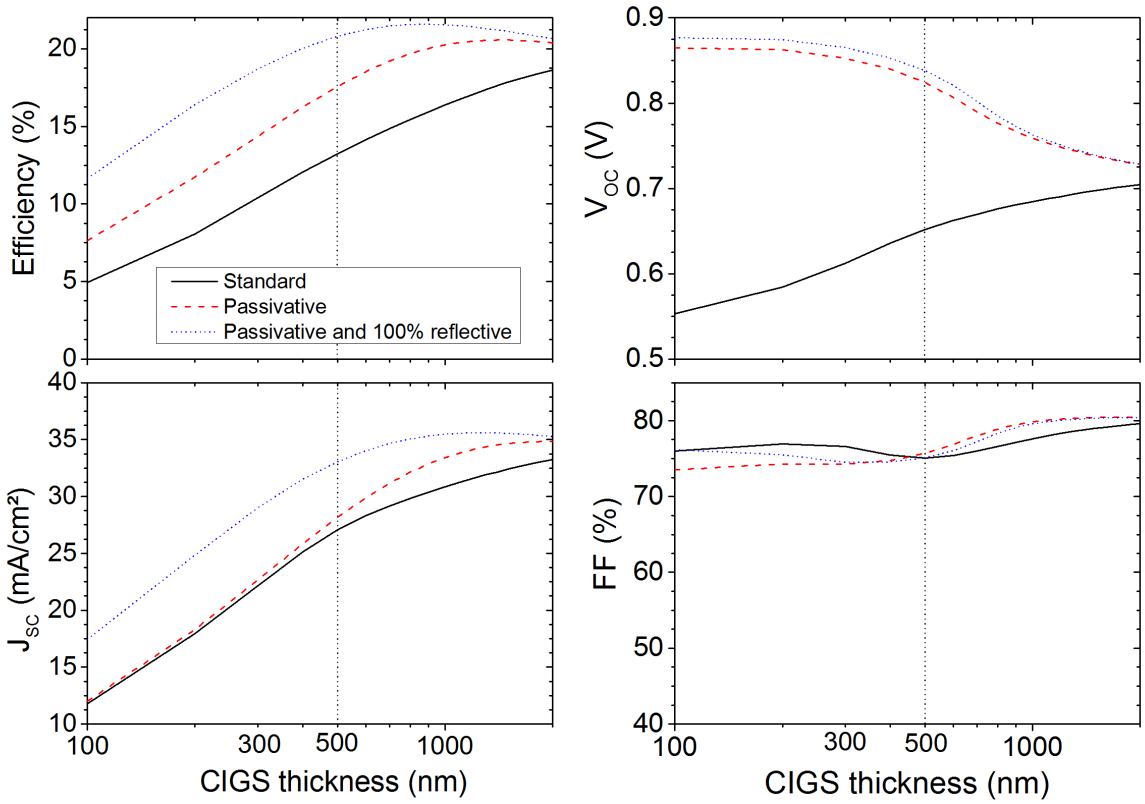

Figure 2.3.: Simulated I(V) parameters of a standard CIGS cell on Mo back-contact as a function of the CIGS thickness. The CIGS material parameters are independent to the CIGS thickness but different back-contact properties were used (detailed in Tab. 2.3).

The simulated J_i of each layer as a function of the CIGS thickness is presented in Fig. 2.4a. The $A_i(\lambda)$ for a 450 nm and 2000 nm thick CIGS is detailed in Fig. 2.4b and Fig. 2.4c.

The maximum current achievable by a CIGS layer with a band-gap of 1.2 eV is 41 mA/cm². For a 2000-nm-thick-CIGS cells, the J_{SC} is lower than the maximum of current (32.6 mA/cm²) mainly because of the absorption of the front windows (-1.7 mA/cm² by CdS; -2.4 mA/cm² by the ZnO/ZnO:Al). The detailed absorption spectra for 2000-nm-thick CIGS (Fig. 2.4c) shows that the CdS impacts the short wavelength (370 and 550 nm) whereas the ZnO:Al impacts the red to IR wavelengths (800 and 1070 nm).

As observed in Fig. 2.4a, the J_{SC} decreases when the CIGS thickness decreases. Apart from the CIGS absorber, only the absorption of the Mo layer significantly varies. For a 450-nm-thick CIGS, the J_{SC} is reduced to 26.0 mA/cm² which is 6.6 mA/cm² lower than the 2000-nm-thick one. The detailed absorption spectrum for 450-nm-thick CIGS (Fig. 2.4b) shows that: on one hand, the reduced J_{SC} is caused by a downshift of the CIGS absorption close to the band-gap edge whereas the Mo absorption increases (-6.6 mA/cm²); and on the other hand, the reflected

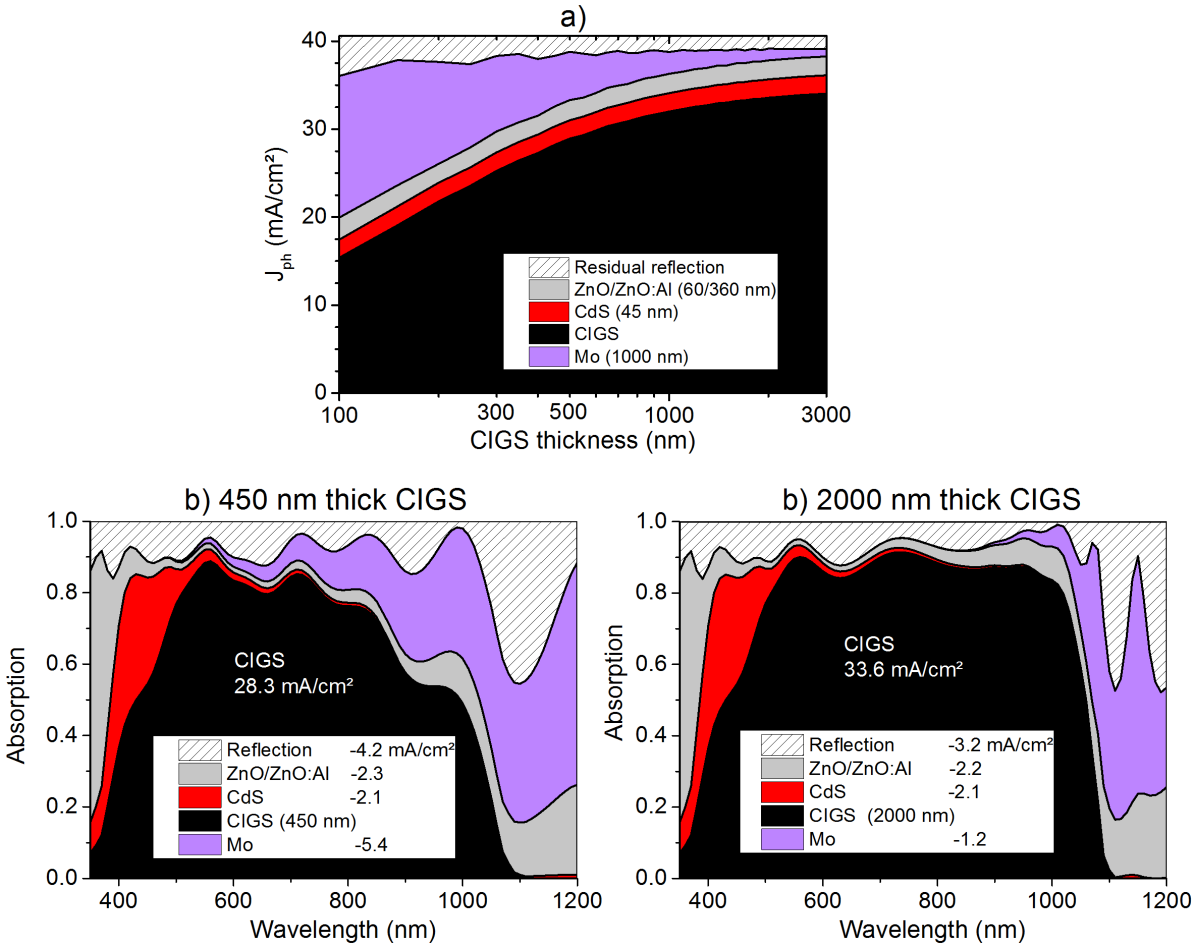

Figure 2.4.: Simulation of the absorption in a standard CIGS cell. Fig. 2.4a: Calculated J_i of each layers. Fig. 2.4b and Fig. 2.4c details the absorption spectra for cells with a 450 nm thick and 2000 nm thick CIGS and the corresponding J_i.

light remains constant. This observation highlights that the absorption coefficient of the CIGS is too low to ensure a complete light absorption in only 450 nm of CIGS and that the Mo/CIGS interface is weakly reflective. As a consequence, the photon absorption at high wavelength shifts from the CIGS to the Mo and lowers the available photons that could generate charges. The use of a reflective back-contact could save up to 6.6 mA/cm².

To conclude, thinning down the CIGS thickness of a standard cell on Mo back-contact below 1000 nm has a negative impact on the cell performance (on both the J_{SC} and V_{OC}). The J_{SC} is reduced because a larger part of photons are absorbed in the Mo layer instead of the CIGS layer. The V_{OC} is reduced because the charges are generated closer to the CIGS/Mo interface which increases the recombination in the cell. As a consequence, the reduction of J_{SC} can be limited and the V_{OC} can be increased by using a reflective and passivative back-contact. In this condition, ultra-thin CIGS solar cells would be competitive against thick CIGS cells.

However, experimental samples may differ from the model because the CIGS properties may vary with its thickness. The following sections are dedicated to the understanding of the materials and electrical change between thin and thick CIGS solar cells.

2.3.2. Experimental results

2.3.2.1. Material analysis

In order to change the CIGS thickness, the deposition time was varied between 2 min and 60 min while keeping the same targeted composition. The final composition and thickness of the CIGS layers are summarized in Tab. 2.4. Samples with CIGS thicknesses between 2100 nm and 80 nm were then fabricated. Only little variations of composition were observed between the samples.

Table 2.4.: Final composition and thickness of the samples with various CIGS thickness.

Deposition time	60 min	30 min	15 min	7.5 min	2 min
Thickness (nm)	2100 ± 100	1100 ± 50	530 ± 20	260 ± 10	80 ± 10
Cu/(In+Ga)	0.70	0.70	0.71	0.74	0.86
Ga/(In+Ga)	0.36	0.37	0.36	0.36	0.46

Fig. 2.5a shows the SEM images of the samples for each deposition time. As observed for all samples, the grains are columnar. We also notice a decrease of the surface roughness with a decreasing CIGS thickness. At the surface, the lateral grain size is small (<1 µm) and not uniform. From these SEM images, we have measured the lateral size of all grains visible at the surface of the CIGS and the distribution of the diameters is reported in Fig. 2.5b. When the thickness of the CIGS decreases, the maximum size decreases (from 900 nm for the 2100-nm-thick CIGS to 150 nm for the 80-nm-thick CIGS) and the size distribution also decreases. The size distribution for each CIGS thickness can be fitted with a log-normal model. This log-normal behaviors is probably related to a Volmer-Weber crystal growth mode [108, 109] indicating a three dimensional growth in island where atoms are more strongly bonded to each other than to the substrate and where the atoms diffusion is not dominant.

This mechanism is different than the CIGS growth by a 3-stage process where the CIGS lateral grain size are much larger [110, 111, 112]. Various models explain the enhancement of the CIGS lateral grain size: a topotactic reaction during the Cu-rich step [113] or a grain boundary migration by recrystallization [114].

Consequently to the 1-stage process, thinner CIGS leads to smaller grains and therefore to a higher grain boundary density compared to the 3-stage process. The effect of grain boundaries in CIGS on the cell performance is still extensively analyzed and depends on the defects concentration, Na content or potential barrier at the

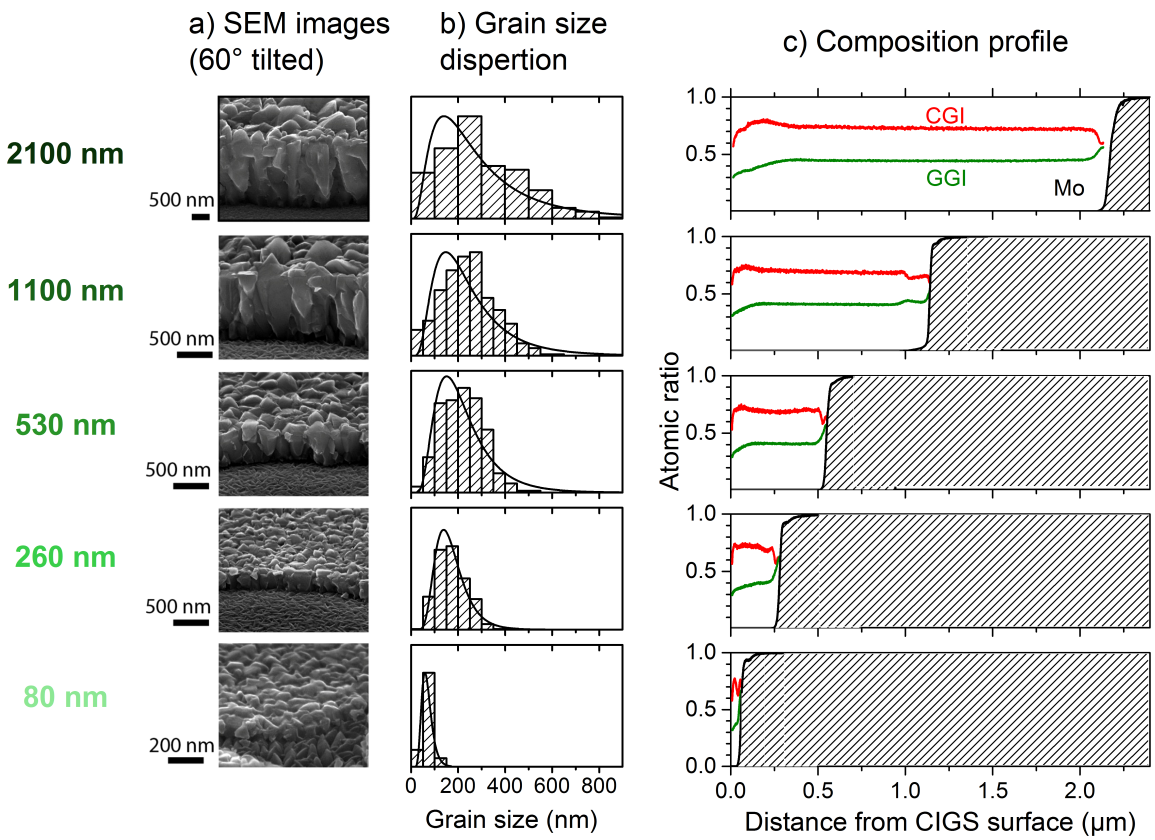

Figure 2.5.: Morphology and composition profile of the samples with various CIGS thicknesses: a) 60° tilted SEM images, b) grain diameter measured at the CIGS surface and fitted with a log-normal model and c) GD-OES analysis. CGI and GGI refers to the Cu/(In+Ga) and Ga/(In+Ga) atomic ratio.

grain boundary [115, 42] in the CIGS. Only well documented on the standard 3-stage process, the studies principally show only minor loss mechanisms at the grain boundaries [116, 117, 118].

Fig. 2.5c displays the composition profile measured by GD-OES along the thickness for samples with different CIGS thicknesses. As observed, whatever the thickness, the CGI and GGI ratio are uniform in the CIGS bulk. The composition variation observed at the CIGS/Mo interface are due to a GD-OES measurement artifact. Indeed XPS analysis at the back contact (no shown here) showed no GGI variation at back interface. Thus, the 1 step process allows for a uniform composition along the CIGS thickness.

We also analyzed the crystal orientation and crystallinity by XRD in the Bragg-Brentano geometry at the surface of the CIGS layer. The diffractograms of the samples with different CIGS thicknesses are shown in Fig. 2.6a. According to the CIGS definition file 00-035-1102, all diffractograms exhibit peaks corresponding to

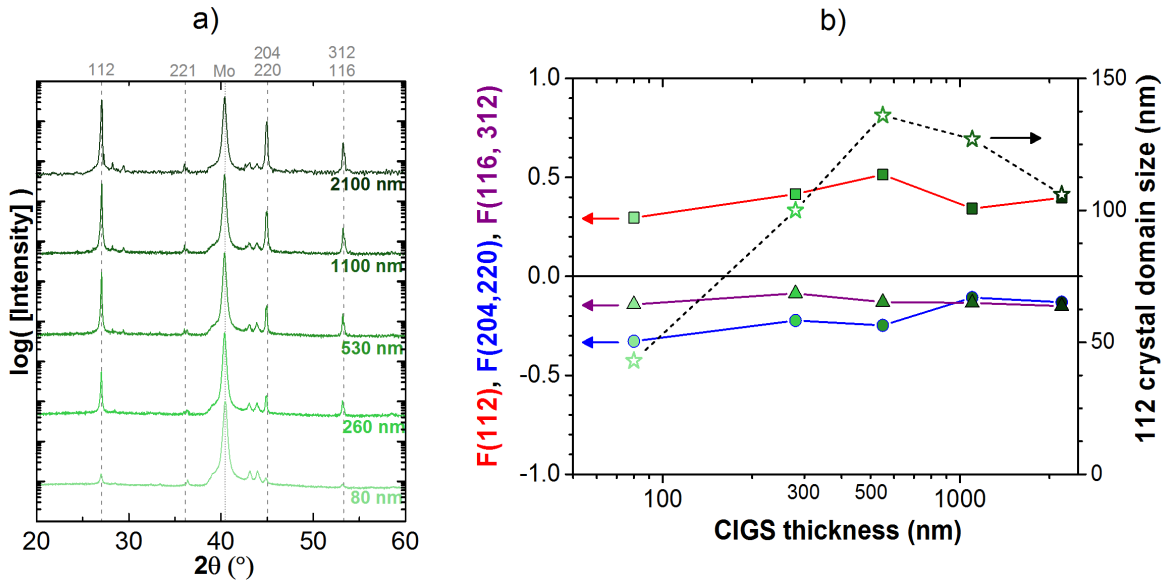

Figure 2.6.: XRD analysis of the samples with various CIGS thicknesses: a) patterns and b) peak area ratio of the main orientations (left axis) and cristallite size of the 112 lattice plane calculated according Scherrer formula (right axis). The point in blue are related to the 3-stage process according to [30].

the CIGS phases, in particular at $2\theta = 27.070°$(112) which is most intense, at 2θ =44.88° and 44.99° (204,220), and at 55.22° and 53.41° (312,116). We analyzed the preferential orientation by calculating the Lotgering factor. The Lotgering factor for an orientation (hkl) ($F_{(hkl)}$) is defined by Eq. 2.4:

$$F_{(hkl)} = \frac{I_{(hkl)} - I^0_{(hkl)}}{1 - I^0_{(hkl)}} \tag{2.4}$$

where $I_{(hkl)}$ is the integrated intensity of the (hkl) reflection normalized as regards to the total CIGS integrated reflection. $I^0_{(hkl)}$is the equivalent value for randomly oriented CIGS obtained on powder [119]. The Lotgering factor varies from 0 (non oriented along the corresponding plane) to 1 (completely oriented along the corresponding plane).

The Lotgering factor for 112, (204 ,220) and (312,116) lattice planes ($F_{(112)}$, $F_{(204,220)}$, $F_{(321,116,)}$) are presented Fig. 2.6b on the left. The calculation gives $F_{(112)} > 0$ whereas $F_{(204,220)}$ and $F_{(321,116,)} < 0$ for all samples meaning that the CIGS is slightly (112)-preferred oriented. A similar preferred orientation were obtained for a 3-stage process CIGS on the same coevaporation machine [30]. For comparison, it has been reported a much more <112>-preferred orientation for a thick CIGS grown by 1-stage deposition [110] and a study of the cell performance has highlighted that the best results are fund for a $F_{(112)} = -0.5$ [120] that is to say non (112)-preferred orientation.

We also analyzed the 112 peak, which is the preferred orientation, to calculated the size of the coherent crystal domains. The crystal domain size (c) is defined by the Scherrer equation (Eq. 2.5):

$$c = \frac{0.9.\lambda_{k\alpha-Cu}}{FWHM_{(112)}.\cos(\theta_{(112)})} \tag{2.5}$$

where $\lambda_{k\alpha-Cu}$ is the wavelength of the incident X-ray (0.154 nm), $FWHM$ the Full Width at Half Maximum of the 112 peak and $\theta_{(112)}$ the position of the peak on the 2θ axis. The crystallite size are reported for each sample on Fig. 2.6b on the right. As observed, the 112 crystal domain size is similar for CIGS thicknesses from 260 to 2000 nm and ranges between 100 to 150 nm. However for the 80-nm-thick CIGS, the crystal domain size is only 40 nm. For very short deposition time, the crystal domain size grow with the CIGS thickness whereas after few minutes they reach their maximum size.

Raman spectra are presented in Fig. 2.7 and shows the typical CIGS vibration mode (A_1 at 178 cm^{-1}, B_2 at 220 cm^{-1} and E at 255 cm^{-1}) [121, 122]. No binary phase is visible (such as $Cu_{2-x}Se$ [123, 124]or $(In,Ga)_2Se_3$ [125, 126]) even for short deposition time. The peak observed at 155 cm^{-1} is generally associated with a Cu-poor phase ($Cu(In,Ga)_3Se_5$ or $Cu(In,Ga)_5Se_8$) at the surface of the CIGS called Ordered Vacancy Compounds (OVC) [127, 128] and plays an important role in the cell by favorably adjusting the band misalignment at the CIGS/CdS interface [52]. The intensity of this OVC phase compared to the CIGS phases seems to decrease when the CIGS thickness decreases. A shorter OVC could be detrimental for ultra-thin CIGS cells performances. We can also observe that the Raman spectra of the 80-nm-thick CIGS exhibits an additional peak at 240 cm^{-1} corresponding to a $MoSe_2$ layer [129]. The laser is indeed weakly absorbed by 80 nm of CIGS which, in turn, allows the observation of the Mo/CIGS interface. Thus, even with very short deposition time, the $MoSe_2$ layer is formed.

To conclude, the growth of ultra-thin (200 to 500 nm) CIGS layer with a 1-stage short deposition process leads to some similar materials properties compared to thick CIGS layer: the same CIGS composition reached for the same fluxes, the same chalcogenide phases with a (112)-preferred orientation, the same crystallite size of 100-150 nm and a $MoSe_2$ formation at the back-contact. However some changes are also observed: higher grain boundaries density due to smaller grains, lower surface roughness, shorter OVC. However, the sample with only 80-nm-thick CIGS deposited in 2 min exhibits major change in morphology and crystallinity. These changes can have an impact on the solar cells performances and have to be taken into consideration during the electrical characterization.

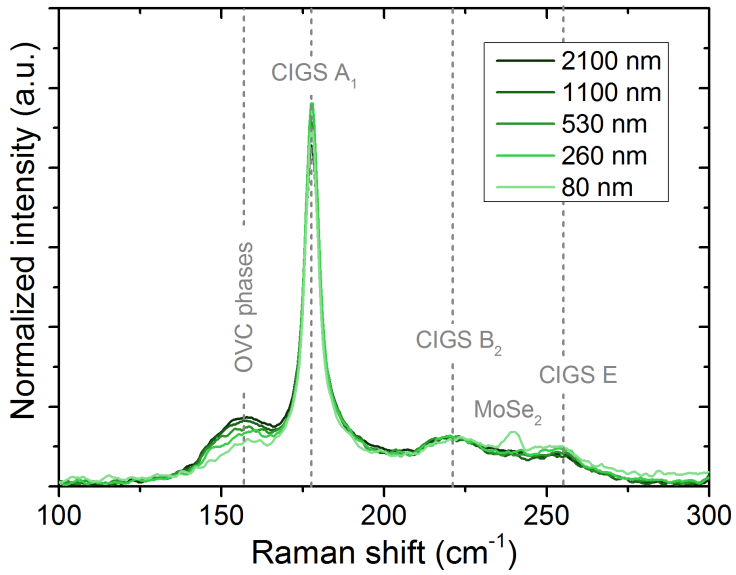

Figure 2.7.: Raman spectra of samples with various CIGS thickness normalized to their integrated signal.

2.3.2.2. Impact on the cell performances.

The 5 CIGS samples previously described were completed with the standard CdS/ZnO-ZnO:Al front window. For an easier comparison of the cell performances, the samples were processed in the same batch.

The I(V) curve and the I(V) parameters as a function of the CIGS thickness are displayed in Fig. 2.8a and Fig. 2.8b. From 2100 nm to 260 nm thick CIGS the cell efficiency decreases from 14.6% to 6.8% mainly due to the decrease in the J_{SC} from 28.9 mA/cm² to 14.8 mA/cm² and slightly due to the decrease in the V_{OC} from 655 mV to 611 mV. The cell with only 80 nm CIGS successfully exhibits a diode behavior but a low efficiency (0.7%).

One should noticed that a cell efficiency of 5.7% was achieved with a 180-nm-thick CIGS cell.

The following sections are dedicated to the understanding of the J_{SC} and V_{OC} decrease. In order to explain the origin of the losses, the results will be confronted to different model and to the simulation performed in sec. 2.3.1 where we assumed that all materials parameters remain constant while decreasing the thickness

2.3.2.3. Impact on the J_{SC}

According to sec. 2.3.1, the J_{SC} dramatically depends on the CIGS thickness below 1000 nm (Fig. 2.4). In our experiments, the J_{SC} decreases from 28.9 mA/cm² for

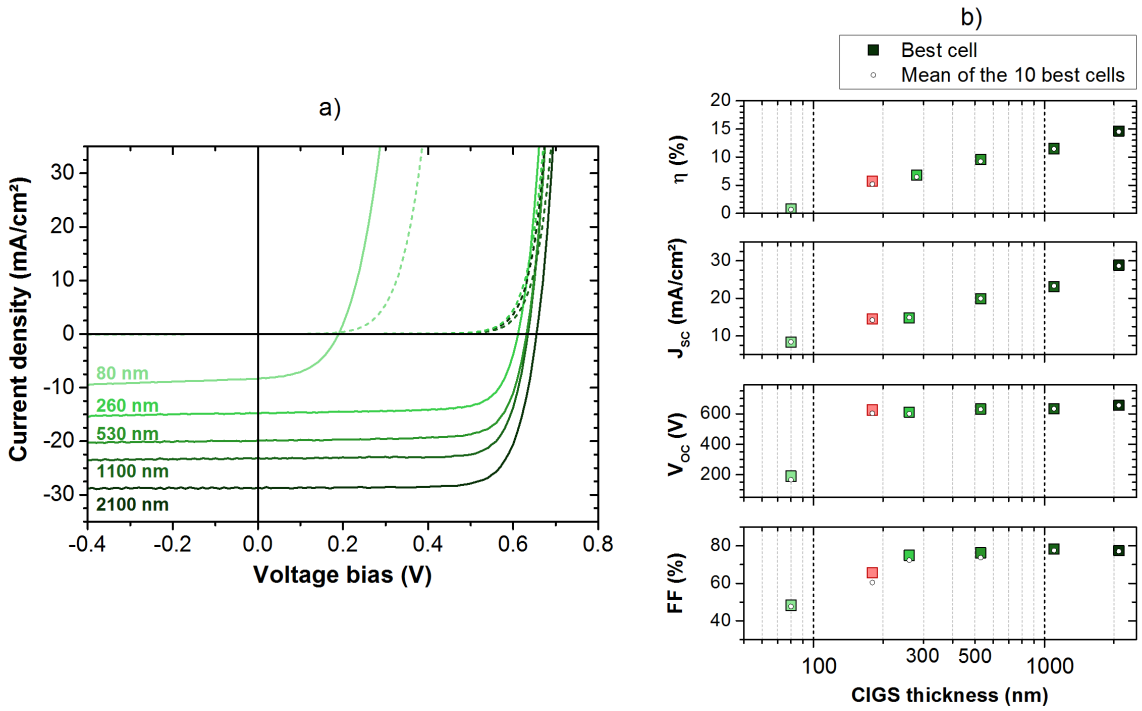

Figure 2.8.: Performance of the cells with various CIGS thicknesses: a) I(V) curves and b) I(V) parameters of cells with various CIGS thicknesses. The red point is a cell with 180-nm-thick CIGS processed in another CIGS batch.

2100 nm thick CIGS to 8.3 mA/cm² for 80 nm thick CIGS. The respective EQE were measured and are presented Fig. 2.9a. A downshift of the EQE curves, principally for the red and IR wavelength, is observed when the thickness decrease from 1100 nm to 2100 nm. However, for thicknesses below 1100 nm, the EQE decreases on the whole spectra. The IQE curves were also calculated according to Eq. 2.1 and are presented in Fig. 2.9b. The IQE, instead of the EQE, reduces the influence of the surface roughness of the samples. We observe the same tendency than the EQE, meaning that the lower J_{SC} is due to a weaker photon conversion in the CIGS layer.

Two main reasons can cause a decrease in J_{SC}: a lower charge carrier generation (less photons are absorbed into the CIGS layer) or a lower charge carrier collection (charge-carriers loosed by recombination). In order to separate these 2 influences, we calculate the charge-carrier generation without taking into account the charge-carrier collection by RTM. This way, the theoretical IQE and J_{SC} were modeled on a system equivalent to the samples (same layer thicknesses, same CIGS band-gap and CIGS model described in Tab. 2.1).

The modeled IQE for each CIGS thickness are displayed in dotted line in Fig. 2.9 and are compared to the experimental IQE. The simulated IQE show the same downshift tendency when the thickness decreases than the experimental EQE. However in the simulation, this downshift is less pronounced than the experiments which leads to a significant difference between both curves. As a consequence, the lower charge

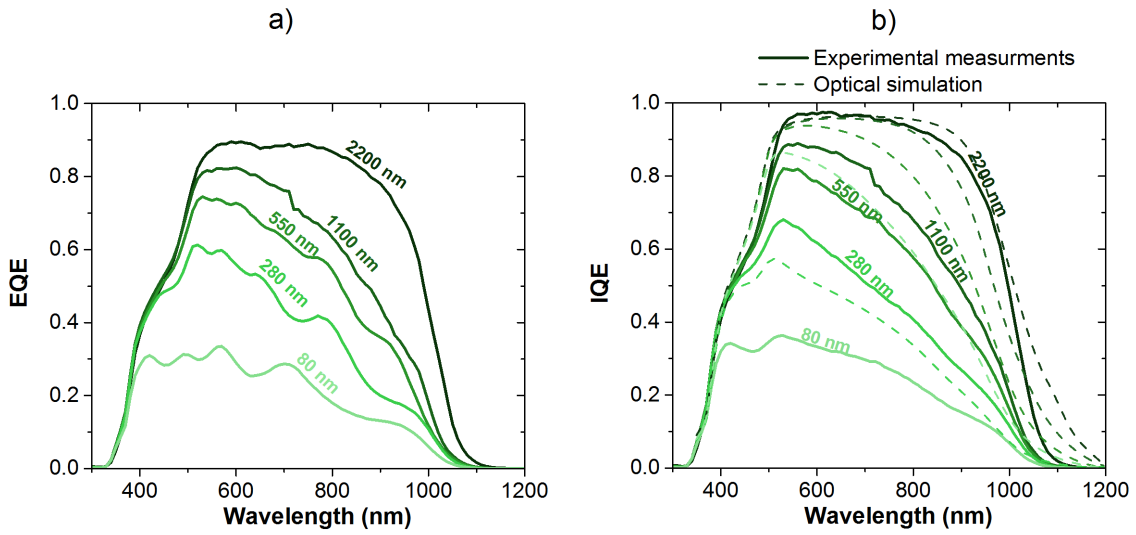

Figure 2.9.: a) Experimental EQE and b) Experimental and simulated IQE of the cells with various thicknesses.

carrier generation cannot fully explain the decrease of IQE: each generated charge carrier is not actually collected. A lower charge carrier collection has to be also implemented by using a collection function.

The collection effect is modeled by a collection function $f_c(z)$ which is the probability to collect a charge generated at a distance z of the CdS/CIGS interface. The IQE taking into account the charge carrier collection is then calculated according to Eq. 2.6:

$$IQE(\lambda) = \frac{1}{1 - R(\lambda)} \int_{z=0}^{d} A(z, \lambda).f_c(z).dz \tag{2.6}$$

where $A(z, \lambda)$ is the absorption in a thin slab of CIGS at a distance z from the CdS/CIGS interface and at a wavelength λ, $f_c(z)$ is the collection function at this distance and d is the whole CIGS thickness.

- $A(z, \lambda)$ is calculated by the RTM model (see Appendix C) using the refraction indices of the CIGS calculated in Appendix B.
- $f_c(z)$ is calculated by using the the equation F.1 in sec. 1.2.3.3 written as:

$$\begin{cases} f_c^{SCR}(z) = h \\ f_c^{QNR}(z) = f(c, w, d, S_{n,BC}, L_n, D_n) < h \end{cases} \tag{2.7}$$

where h is a constant between 0 and 1 that model the SCR losses, w and d are respectively the thickness of the SCR and the CIGS, $S_{n,BC}$ is the

electron recombination velocity at the back contact, L_n is the electron diffusion length in the CIGS (>1 µm) and D_n is the electron diffusion coefficient (2 cm²/s).

The collection function were then fitted the experimental IQE (Fig. 2.9b) as close as possible by adjusting $S_{n,BC}$, w and h. The model allows to separate the influence of the front-contact / drift collection loss (*via* the factor h) and of the back contact recombination (*via* the factor $S_{n,BC}$). The use of $S_{n,BC} = 10^7$ cm/s was necessary to reduce the IQE values at wavelength above 600 nm. However, the SCR width w is a critical parameter and we were not able to performed an accurate estimation of its value by impedance spectroscopy due to parasitic capacitances (not shown here). The value is usually around 200-300 nm for standard CIGS cells at open circuit condition [81]. Unfortunately, decent fit of the IQE was possible for various h and w couples. Consequently, the minimum (maximum) back-contact recombination loss was estimated for the maximum (minimum) h and the minimum (maximum) w. The remaining EQE loss is then attributed to the drift loss and front contact recombination. A summary of the parameters used are displayed in Tab. 2.5.

All previous calculations are summarized in Fig. 2.10. The figure shows the theoretical and the experimental J_{SC} for each cell with different CIGS thicknesses. The back-bar plot is the J_{SC} deduced from from the experimental EQE measurements. The maximum J_{SC} achievable for the band-gap of each sample is represented by the maximum bar height. In-between, the theoretical J_{SC} is the sum of several contributions: the contributions that lower the charge generation (in purple and already discussed in Fig. 2.4) and the contributions that lower the charge collection (in red).

For the optical contributions, in purple in Fig. 2.10, the photocurrent of the different layers was calculated by RTM (as explained in sec. 2.3.1). The same tendency than Fig. 2.4a is observed: an equivalent contribution of the Reflection/ZnO:Al/ZnO/CdS front window whatever the thickness (7 to 9.5 mA/cm²) and a dramatic absorption in the Mo layer (from 2.9 mA/cm² for the 2100 nm thick CIGS sample to 11.7 mA/cm² for the 260 nm thick CIGS sample).

Table 2.5.: Parameters of the collection function to fit the optical absorption of the CIGS layer with the experimental EQE.

	D_n	L_n	$S_{n,BC}$	w	h
2200 nm	2 cm²/s	2 µm	10^7cm/s	300	1
1100 nm	2 cm²/s	2 µm	10^7cm/s	150⟷300	1⟷0.95
550 nm	2 cm²/s	2 µm	10^7cm/s	100⟷200	1⟷0.93
280 nm	2 cm²/s	2 µm	10^7cm/s	100⟷150	1⟷0.93
80 nm	2 cm²/s	2 µm	10^7cm/s	20⟷40	1⟷0.90

For the electrical contribution, the J_{SC} loss that is attributed without ambiguity to the back-contact recombination and the J_{SC} that can be due to both drift or back-contact recombination are presented in red in Fig. 2.10. We observe that a

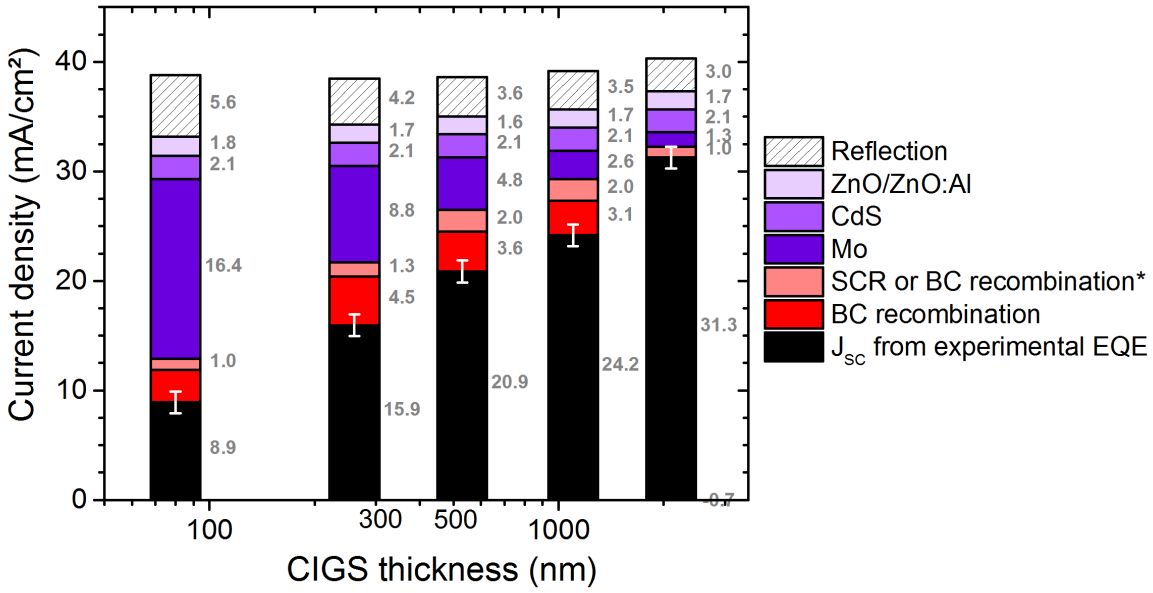

Figure 2.10.: Details of the J_{SC} contributions that explains the difference between the experimental J_{SC} (calculated from the EQE measurements) and the maximum J_{SC} expected for a CIGS cell with the corresponding band-gap. Error-bar indicates the missfit between simulation and experiment. In purple: losses explained by a lower charge carrier generation. In red: losses explained by a lower charge collection. The value of each contribution is written in gray in mA/cm². BC: Back-Contact recombination. SCR: Space Charge Region. ⋆: separation of the BC and SCR recombination influence cannot be made.

large part of the J_{SC} loss in ultra-thin CIGS is attributed to the recombination at the Mo back-contact (0 mA/cm² at 2100 nm but from 3.5 to 4.8 mA/cm² for the 260-nm-thick CIGS sample). For each CIGS thickness between 1100 nm and 260 nm, we have calculated a similar J_{SC} loss amplitude attributed to the recombination at the back-contact.

We can compare this result with the SCAPS simulation in Fig. 2.3 where the back-contact passivation had almost no impact on the J_{SC}. We suppose that for the experimental CIGS cells, the SCR width is always thinner than the CIGS thickness, whereas for ultra-thin CIGS the SCAPS model neglects the electron diffusion toward the back-contact. Large defect density close to the back-contact may explain that the CIGS layer cannot be fully depleted.

Finally, the low photocurrent in ultra-thin CIGS compared to thick CIGS solar cells is both due to a weak charge-carrier generation in the CIGS layer and a weak collection of charge-carriers generated close to the back contact.

2.3.2.4. Impact on the V_{OC}

According to Fig. 2.8, the V_{OC} of the cell decreases from 655 mV for 2100-nm-thick CIGS to 190 mV for 80-nm-thick CIGS. The value of V_{OC} is a combination of different factors (recombinations, charge injection, band-gap). The purpose of this section is to separate their influences and to highlight the role of the recombination for each thickness of CIGS.

In order compare the V_{OC} between the 5 samples, it is convenient to use the V_{OC} deficit (written V_{OC}^{def}) which is independent of the band-gap E_g:

$$V_{OC}^{def} = V_{OC} - V_{SQL}(E_g) \tag{2.8}$$

where $V_{SQL}(E_g)$ is the theoretical maximum V_{OC} according to the Shockley-Queisser Limit [69] (Black-body radiation at room temperature emitted by radiative recombination, $V_{OC}^{def} \approx E_g/q - 250$ mV for the CIGS band-gap). E_g is calculated from the extrapolation of the $IQE^2 = f(h\nu)$ curve.

Considering a negligible series resistance ($R_S = 0$), infinite shunt resistance ($V/R_{Sh} = 0$) and a voltage bias dependent photocurrent, the V_{OC} can be written as Eq. F.2:

$$V_{OC} = \frac{nkT}{q} \ln\left(\frac{f_c(V_{OC}).J_{SC}}{J_0}\right) \tag{2.9}$$

with n the ideality factor, k the Boltzmann constant, q the charge of the electron, $T = 300$ K, J_0 the saturation current and J_{SC} the current density at V=0 and $f_c(V_{OC})$ the collection function for a voltage bias equal to the V_{OC}. $f_c(V)$ were estimated by comparison of the light and dark I(V) curve and normalized at V=0. (Eq. 2.10):

$$f_c(V) = \frac{J^{Light}(V) - J^{Dark}(V)}{J_{SC}} \tag{2.10}$$

The ideality factor (n) and the saturation current (J_0) are obtained by fitting the $J^{light}(V) - f_c(V).J_{SC}$ or the $J^{dark}(V)$ equation.

At present, to explain the V_{OC} variations and to really separate the influence of the J_{SC}, the f_c and the J_0, we calculate the difference of V_{OC}^{def} between the 2100-nm-thick CIGS cell and the samples with other CIGS thickness (Eq. 2.11) and then we linearise Eq. F.2 leading to Eq. 2.12. For this purpose, we consider that the ideality factor is equal to 1.35 and independent to the CIGS thickness.

$$\Delta V_{OC} = V_{OC}^{def,2100\text{ nm}} - V_{OC}^{def} \tag{2.11}$$

$$\Delta V_{OC} = \underbrace{\frac{1.35.k.T}{q} \cdot \ln\left(\frac{J_{SC}^{2100\,\mathrm{nm}}}{J_{SC}}\right)}_{\Delta V_{OC}^{J_{SC}}} + \underbrace{\frac{1.35.k.T}{q} \cdot \ln\left(\frac{f_C^{2100\,\mathrm{nm}}(V_{OC}^{2100\,\mathrm{nm}})}{f_C(V_{OC})}\right)}_{\Delta V_{OC}^{f_c}} + \underbrace{\frac{1.35.k.T}{q} \cdot \ln\left(\frac{J_0}{J_0^{2100\,\mathrm{nm}}}\right)}_{\Delta V_{OC}^{J_0}} \tag{2.12}$$

where $\Delta V_{OC}^{J_{SC}}$, $\Delta V_{OC}^{f_c}$ and $\Delta V_{OC}^{J_0}$ are respectively the V_{OC} variation due to the photocurrent variation, the collection function variation and saturation current variation.

	$J^{dark}(V)$					$J^{light}(V) - f_C(V).J_{SC}$ with $n = 1.35$		
CIGS thickness	J_{01}	J_{02} (mA/cm²)	R_S (Ω.cm²)	R_{SH} (Ω.cm²)	Misfit	J_0 (mA/cm²)	Misfit	$f_C(V_{OC})$
2100 nm	$1.7 \cdot 10^{-11}$	$1.1 \cdot 10^{-6}$	0.2	5.10^4	4.10^{-4}	$1.3 \cdot 10^{-7}$	1.10^{-3}	0.69
1100 nm	$1.1 \cdot 10^{-11}$	$2.8 \cdot 10^{-6}$	< 0.1	2.10^4	2.10^{-3}	$8.8 \cdot 10^{-8}$	2.10^{-3}	0.32
530 nm	$1.1 \cdot 10^{-11}$	$7.3 \cdot 10^{-7}$	0.2	6.10^4	1.10^{-3}	$1.6 \cdot 10^{-7}$	1.10^{-3}	0.60
260 nm	$1.8 \cdot 10^{-11}$	$1.5 \cdot 10^{-6}$	0.2	1.10^4	1.10^{-3}	$1.4 \cdot 10^{-7}$	1.10^{-3}	0.44
80 nm	$2.6 \cdot 10^{-6}$	$6.2 \cdot 10^{-4}$	0.6	$< 1.10^5$	1.10^{-3}	$1.0 \cdot 10^{-3}$	1.10^{-3}	0.03

Table 2.6.: 2-diode fit parameter of $J^{dark}(V)$, measured in the dark and 1-diode fit parameter of $[J^{light}(V) - f_C(V).J_{SC}]$, measured in the light. The ideality factor n is fixed at 1.35 to linearise 2.12. This approximation only leads to a slight increase of the missfit.

The value of J_{01} and J_{02} calculated from the dark I(V) curves of the CIGS with various thicknesses are summarized in Tab. 2.6. The J_{01} and J_{02} only slightly vary between the 2100 nm and 260 nm thick CIGS cell indicating an absence of major change in the recombination process. On the opposite, the 80 nm thick CIGS cell has a much higher J_{01} and J_{02} that indicated the increased contribution of both the interfaces and the SCR.

The light I(V) curves were also analyzed. The collection function $f_c(V)$ for each curve was calculated according to 2.10 and the $J^{light}(V) - f_c(V).J_{SC}$ were fitted by setting the ideality factor at $n = 1.35$. The value of 1.35 was empirically determined to minimize the misfit. The obtained misfit (reported in Tab. 2.6) is reasonable compared to the fit of the dark I(V) curves. The obtained $f_c(V_{OC})$ and J_0 are also reported in Tab. 2.6. Concerning the collection function, the value is clearly below 1: 0.3 to 0.7 for CIGS thicknesses between 2100 and 260 nm and is even close to 0 for the 80-nm-thick CIGS. This result means that the cells suffer of a strong voltage-dependent photocurrent due to either a cross-over effect or from a violation of the superposition principle [34]. The cross-over effect is commonly observed in CIGS

solar cells. One explanation is the presence of an electron barrier at the CdS/CIGS interface which is reduced under illumination [68]. The violation of the superposition principle can be due to the large electron recombination velocity at the back contact that limits the collection in the QNR (sec. 2.3.2.3) coupled with the thinner SCR under applied forward voltage [34]. Therefore an increasing forward bias can lead to a decrease in photocurrent. However, at this stage it is difficult to comment the variation $f_c(V_{OC})$ observed between the different samples without in-depth electrical characterization.

Finally, the results of the calculations for each sample with different CIGS thicknesses are summarized in Fig. 2.11. The V_{OC}^{def} (star symbol) were calculated according to the experimental V_{OC} and the experimental E_g. The E_g error bar corresponds to the uncertainty in the determination of E_g. Then, $\Delta V_{OC}^{J_{SC}}$, $\Delta V_{OC}^{f_c}$ and $\Delta V_{OC}^{J_0}$ were calculated from the value summarized in Tab. 2.6. In this figure, $V_{OC}^{def,\ 2100\ nm}$ is taken as reference.

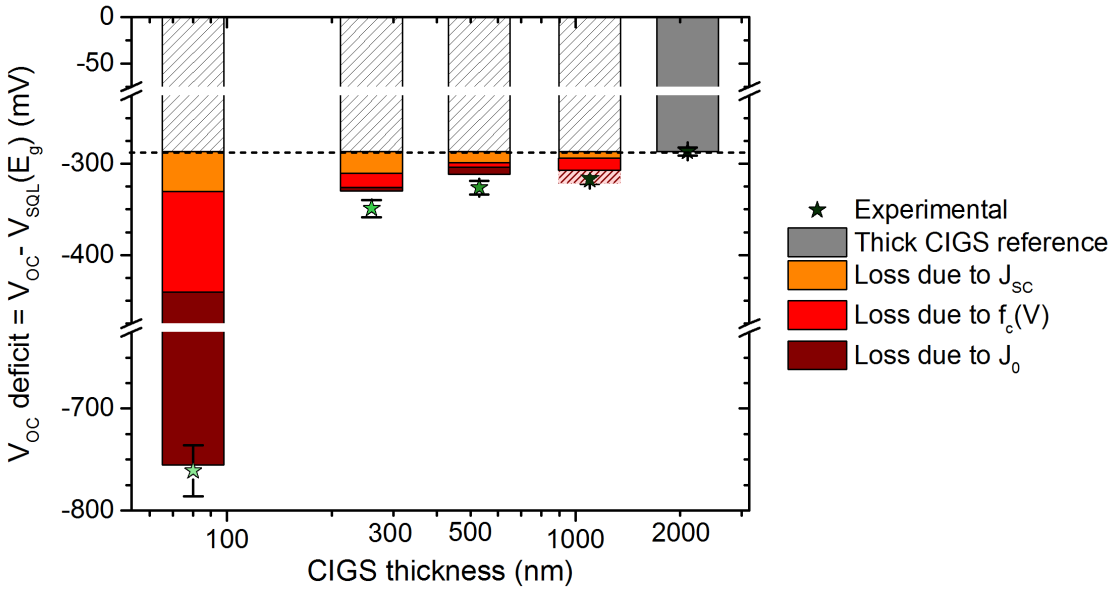

Figure 2.11.: V_{OC} deficiency (V_{OC}^{def}) of the samples with various CIGS thicknesses. Star symbol : V_{OC}^{def} from the experimental V_{OC} taken on the I(V) curve and from the optical band-gap E_g obtained by extrapolation of the $IQE^2 = f(h\nu)$. Bars: V_{OC}^{def} compared to $V_{OC}^{def,\ 2500\ nm}$ according to Eq. 2.12 with the collection function $f_c(V_{OC})$ obtained according to Eq. 2.10 and J_0 the saturation current obtained by a 1-diode fit of $J^{light}(V) - f_C(V).J_{SC} = f(V)$ function with an ideality factor of 1.35 detailed in Tab. 2.6.

As observed in Fig. 2.11, when the CIGS thickness decreases from 2100 nm to 260 nm, the V_{OC}^{def} decreases of roughly 50 mV. However between CIGS thicknesses of 260 to 80 nm, we observe an important drop in V_{OC} of around 410 mV.

Moreover, the V_{OC} loss between cells with 220-nm- and 260-nm-thick CIGS is mainly due to the decrease in J_{SC} (which is explained in previous section sec. 2.3.2.3). The lower $f_c(V_{OC})$ leads to additional V_{OC} loss. On the contrary, the saturation current does not significantly affect the V_{OC}. For cells with a CIGS thicknesses between 260 nm and 80 nm, the loss in V_{OC} is mainly due to the larger J_0. The particularly low $f_c(V_{OC})$ also leads to a large decrease in V_{OC}.

For CIGS thicknesses larger than 250 nm, the decrease in V_{OC} is comparable to the results obtained by the SCAPS simulation in Fig. 2.3 for high back-contact recombination.

2.3.3. Conclusion

Ultra-thin CIGS layers (250-500 nm) deposited by a fast 1-stage process have similar physical properties than the thick CIGS layers.

The best cell efficiency achieved with a 1-stage CIGS coevaporation process are: **5.7% for a 180-nm-thick CIGS**, **8.0% for a 275-nm-thick CIGS**, **9.6% for a 450-nm-thick CIGS**.

The analysis on the cells validates the hypothesis of the simulation sec. 2.3.1: the CIGS physical parameters remain constant between 2100-nm- and 260-nm-thick CIGS. Ultra-thin solar cells suffer of one main drawback: the CIGS/Mo interface which is both **weakly reflective** and generates **high surface recombination**. The low reflection reduces the charge-carrier generation in the CIGS layer leading to a decrease in J_{SC}. The high surface recombination rate reduces the charge-carrier collection in the QNR which leads to a decrease in J_{SC} and which cancels the increase in V_{OC} normally expected for thinner CIGS.

Ultimately, with a reflective and passivative back-contact, we can expect **an even higher efficiency for ultra-thin CIGS solar cell** than the standard µm thick cells. Interface properties can be changed by varying the CIGS band gap or by implementing a band-gap gradient. In the following section the effect the Ga content on the band-gap and on the solar cells performance is studied.

2.4. Impact of the CIGS band-gap on the materials and solar cells properties

2.4.1. Materials analysis

To analyze the impact of the CIGS band-gap on ultra-thin CIGS solar cells properties the CIGS composition GGI were varied. For this study, we prepared samples with 2 different CIGS thicknesses (500-nm and-2000 nm), with 5 different GGI (from 0.18 to 0.64) and with a fixed CGI composition of 0.75-0.80. The CIGS layer were deposited by a one stage process. Tab. 2.7 presents the final composition and thickness of each sample measured using an EDS and a profilometer respectively. The CIGS band-gap was determined from the IQE measurements detailed in section

Table 2.7.: Final composition, thickness and band-gap calculated from the IQE of the samples with various compositions.

	A	B	C	D	E
Thickness (nm)	460 ± 10	470 ± 10	450 ± 10	430 ± 10	500 ± 10
Cu/(In+Ga)	0.81	0.81	0.77	0.83	0.73
Ga/(In+Ga)	0.18	0.29	0.42	0.50	0.64
Band-gap (eV)	1.09 ± 0.01	1.15 ± 0.01	1.24 ± 0.01	1.29 ± 0.01	1.40 ± 0.01
	F	G	H	I	J
Thickness (nm)	2000 ± 50	2000 ± 50	2000 ± 50	2000 ± 50	2000 ± 50
Cu/(In+Ga)	0.78	0.74	0.74	0.69	0.72
Ga/(In+Ga)	0.18	0.29	0.43	0.54	0.63
Band-gap (eV)	1.08 ± 0.01	1.16 ± 0.01	1.24 ± 0.01	1.32 ± 0.01	1.37 ± 0.01

Fig. 2.12 displays the SEM images of the samples with different GGI and for the 500-nm-thick CIGS (A-E). As observed, the GGI of the sample has no real impact on the morphology of the CIGS.

XRD patterns of the layers are displayed in Fig. 2.13a. All diffractograms exhibits the 112 and (220,204) CIGS peaks already reported in the diffractograms sec. 2.3.2 independent of the CIGS composition. The peaks shift to higher 2θ for higher GGI. In Fig. 2.13b, the 112 position is plotted as a function of the GGI measured by EDS. For comparison, 112 the position expected according to the calculated with the CIGS lattice constant is displayed in black (data from CIGS on the same device [30] and from crystals [130]).

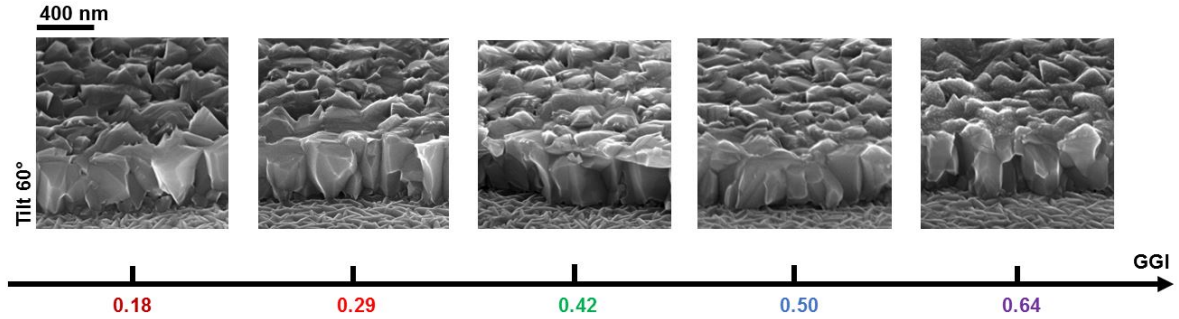

Figure 2.12.: SEM images of the samples with various CIGS composition (A-E). Samples are tilted by 60°.

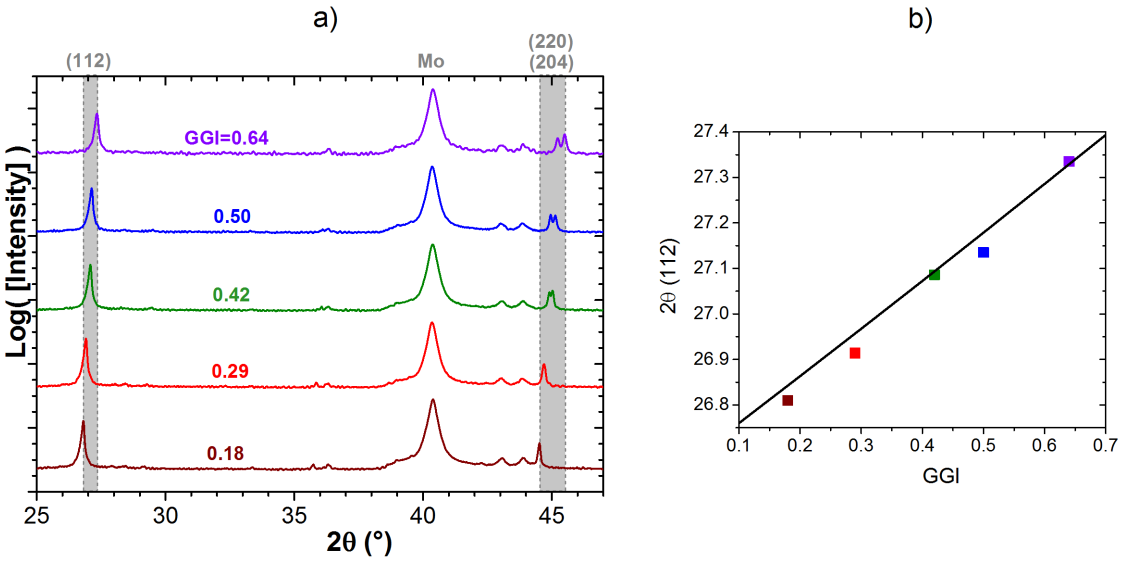

Figure 2.13.: a) XRD patterns of the samples with different CIGS composition (A-E). b) corresponding (112) position. The black line is the relation calculated from the CIGS lattice constante obtained by [130, 30].

From the experimental value of Fig. 2.13b, we can estimate the Ga composition of the CIGS (GGI) from the 112 peak position ($2\theta_{(112)}$ in degrees) following the relation:

$$2\theta_{(112)}(GGI) = 1.13GGI + 26.59 \pm s(GGI) \tag{2.13}$$

where $s(GGI)$ denotes the confidence envelope (a risk of 10% of error were used for calculations): $s(0.2) = 0.04$, $s(0.4) = 0.02$ and $s(0.65) = 0.04$.

A linear relation is observed and is related to the linear rise in the Cu(In,Ga)Se_2 primitive cell parameters (the $CuGaSe_2$ primitive cell is larger than the one of $CuInSe_2$). The peak positions obtained are close to the expected peak positions, meaning a good estimation of the GGI value by EDS.

2.4.2. Electrical analysis

The impact of the variation of the GGI composition on cell performances were studied. For this purpose, the samples previously described were completed with the standard CdS/ZnO/ZnO:Al front window. For an easier comparison of the cell performances, the samples were processed in the same batch.

2.4.2.1. Band-gap calculation

In order to calculate the electrical band-gap, the IQE were measured for each sample. In Fig. 2.15, the $IQE^2 = f(E)$ curve are plotted and centered on the CIGS absorption edge. The band-gap is calculated by a linear fit of the curve closed to the absorption edge.

According to the Tab. 2.7 an empirical relation can be found between GGI (x) and the band-gap (E_g in eV):

$$E_g = 0.956 + 0.683 \cdot x \qquad r^2{=}0.996 \tag{2.14}$$

$$E_g = 0.956 \cdot x + 1.638 \cdot (1 - x)$$

This relation is close to the relations observed in the literature [31, 32, 131]. Note that the uncertainty on the composition and the band-gap makes it difficult to estimate the bowing factor.

2.4.2.2. Impact of the Ga content on the CIGS cell performances

The I(V) curves of the best 500- nm-thick CIGS cells for different GGI composition are displayed in Fig. 2.14a. The evolution of the I(V) parameters of the 10 bests cells with 2000- and 500-nm-thick CIGS as a function of the GGI is reported in Fig. 2.14b. The corresponding band-gap in abscissa were calculated according to formula 2.14.

As observed in Fig. 2.14b, when the GGI composition increases, the cell efficiency increases to a maximum at GGI = 0.4 (9.1 ∓ 0.3 % for 500-nm-thick CIGS and 13.9 ∓ 0.5 % for 2000-nm-thick CIGS) then decreases for both cells with 2000 nm and 500 nm. Therefore, the optimal composition for a cell without composition gradient seems to be obtained for $GGI = 0.40 \mp 0.05$ (E_g = 1.27 to 1.33 eV) whatever the thickness of the CIGS. If we look into details, when the GGI increases, the V_{OC} of the cells increases, the J_{SC} decreases. For the 2000-nm-thick CIGS, the FF is independent of the GGI, whereas for the 500-nm-thick CIGS the FF is lower for low and high GGI.

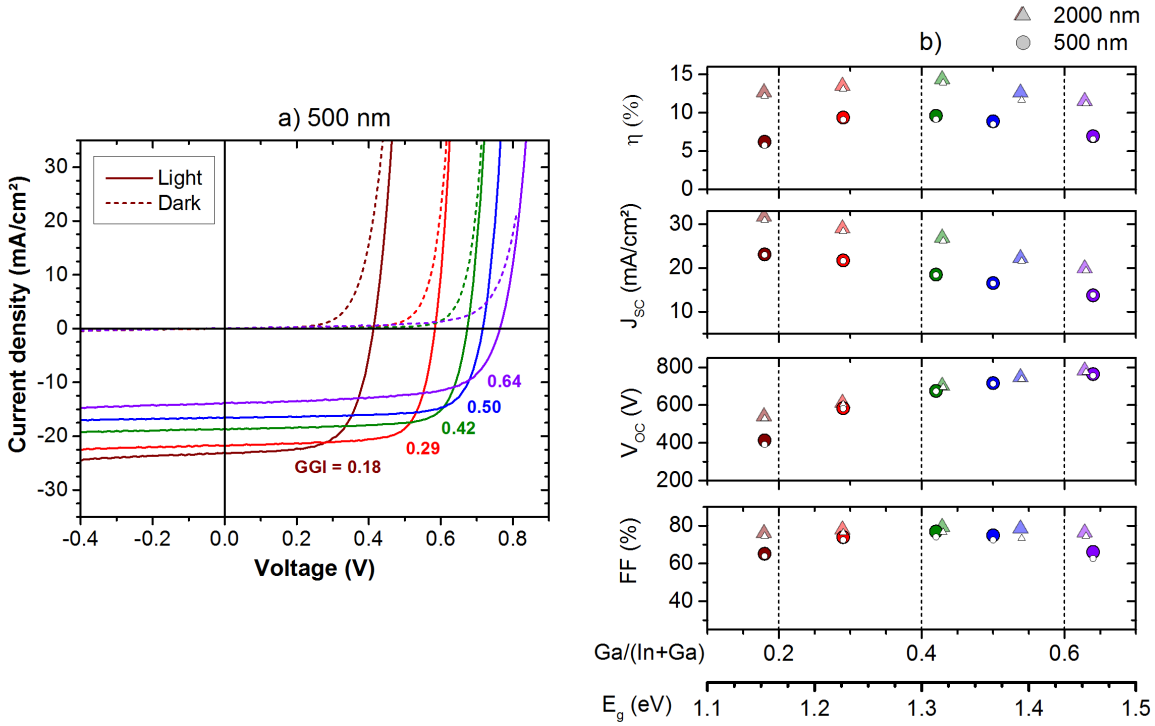

Figure 2.14.: Cells performance with various CIGS composition: a) I(V) curve for the 500-nm-thick CIGS cells and b) I(V) parameters of the 10 best cells cells for the 500 nm and 2000 nm thick CIGS cells.

This V_{OC} and J_{SC} tendency is expected according to the Shockley-Queisser calculation. The band-gap fixes the build-in potential in the junction (V_{OC} is proportional to E_g) but limits the spectral absorption of the CIGS (J_{SC} is inversely proportional to E_g). As a consequence, the maximum efficiency is then obtained for a semi-conductor band-gap of 1.2 to 1.4 eV [69], which correspond to the maximum efficiency obtained in our samples.

Fig. 2.15 also shows the evolution of the IQE for the cells with different GGI compositions. We clearly see the shift of the absorption edge toward the lower wavelength when the GGI increases due to the increasing band-gap. This shift is correlated to the decreases the J_{SC}. However, we also observe a downshift of maximum IQE when GGI increases.

In order to illustrate and to understand the V_{OC} and J_{SC} evolution with the CIGS composition, it is convenient to evaluate the V_{OC} and the J_{SC} as independent values on the band-gap. For this purpose, we calculate the V_{OC} deficit ($V_{OC} - E_g/q$) and the normalized current $J_{SC}/J_{ph}^{max}(E_g)$ for each sample. J_{ph}^{max} is the maximum photocurrent by taking the EQE equal to 1 for wavelength between 0 and the CIGS band-gap.

The normalized J_{SC} and the V_{OC} deficit as a function of the GGI are displayed in Fig. 2.16a and Fig. 2.16b. As observed, the normalized current slightly decreases

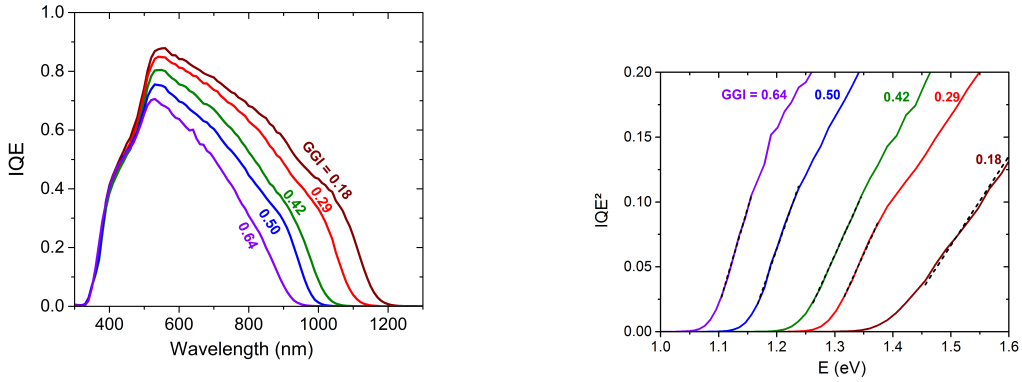

Figure 2.15.: IQE measurements of the cells with different CIGS compositions for the 500-nm-thick CIGS. On the right: the same curves plotted as IQE^2 as a function of energy. The dotted black line denotes the fit used for the band-gap calculation.

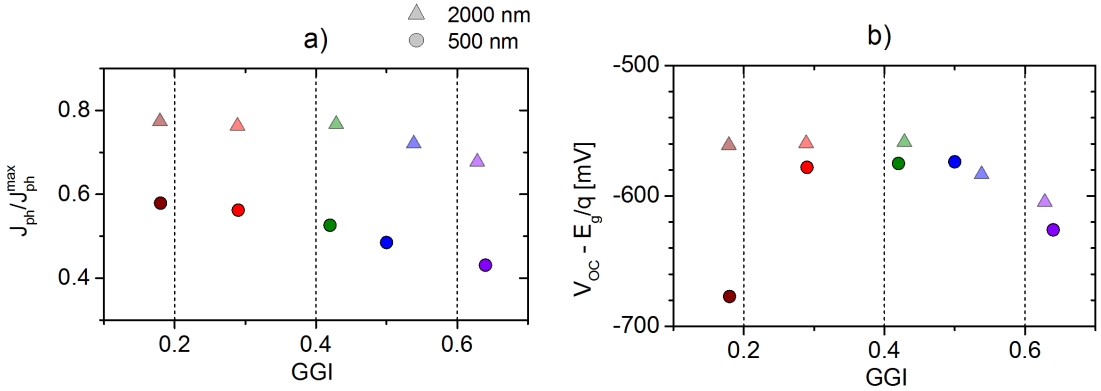

Figure 2.16.: Normalized current $J_{ph}/J_{SC}^{max}(E_g)$ and V_{OC} deficiency ($V_{OC} - E_g/q$) for the cells with various CIGS compositon and for CIGS thicknesses of 2000 and 500 nm. J_{ph} is calculated by integrating the EQE.

when the GGI increases, in particular for the cell with 500 nm thick CIGS. This effect is related to the downshift in the maximum IQE already observed in Fig. 2.15. This effect can be related to a better CIGS absorption or collection in the space charge region at low GGI.

According to Fig. 2.16b, the lower V_{OC} deficit is reached for a GGI = 0.29 - 0.50 for cells with 500 nm thick CIGS and for a GGI < 0.43 for cells with 2000 nm thick CIGS. For the cell with 500 nm thick CIGS, the V_{OC} for GGI = 0.18 is around 100 mV lower than expected. For the cell with 500 nm and 2000 nm, the V_{OC} for GGI = 0.64 is around 25 mV lower than expected.

Previous works showed that a low CIGS band-gap in contact with the CdS lower the V_{OC} due to a band misalignment between the CIGS and the CdS [132, 133, 134] (the electron affinity of the the $CuIn_{1-x}Ga_xSe_2$ and CdS are respectively $4.0 + E_g(CuIn_{1-x}Ga_xSe_2) - E_g(CuInSe_2)$ eV and 4.2 eV). The formation of the OVC phase

at the surface of the CIGS is generally sufficient to form the required band-alignment for low band-gap CIGS.

Previous works also commonly observed a V_{OC} saturation phenomenon effect for GGI > 0.55 [135, 136, 137, 33]. The origin of this phenomenon is still under debate but it seems clear that it is related to an increased density of deep defects, supposedly the antisite defects M_{Cu} [138, 139].

To conclude, for CIGS absorber deposited in 1 stage, the optimum composition to reach the maximum cell performance is GGI $= 0.40 \mp 0.5$ for both 500 and 2000 nm thick CIGS. Comparison between Fig. 2.16 and the literature showed that low GGI allows a better collection but may not lead to the required band-alignment with the CdS, whereas high GGI creates detrimental defects in the CIGS bulk.

2.4.3. Cells with a Ga gradient

2.4.3.1. Implementation of a Ga gradient with different process

The variation of the CIGS band-gap impacts the energy of the CIGS conduction-band. The valence-band can be considered as fixed independently from the composition [41]. Therefore a CIGS composition gradient would implement a conducting band gradient. An increasing gradient of GGI toward the back-contact leads to a gradient of chemical potential which reduces minority carrier recombination at the back-contact and increases the current collection.

This effect, that approaches a back surface field effect, leads to a passivation of the CIGS/Mo interface. M. Gloeckler and R. Sites [82] have shown by AMPS-1D simulation that for a band-gap increase higher than 0.2 eV toward the back contact as sharp as possible the electron recombination velocity are reduced by a factor of 3. This leads to an increase in ultra-thin CIGS (<500 nm) cell efficiency is increased. Experimental results performed by Lundberg *et al.* [80] showed an increase in cell efficiency of 2% absolute by depositing a pure $CuGaSe_2$ layer at the beginning of the CIGS growth process.

In this section we analyze the effect of a Ga grading in the CIGS layer on ultra-thin CIGS cell performances. We also compared 3 different processes, so called 1-stage, 2-stage and 3-stage. The description of the non-graded and graded process are detailed below and in Fig. 2.17a.:

1-stage (Fig. 2.17a-i) A Cu-poor CIGS (CGI = 0.85) is deposited at 350°C during the whole process. The GGI is fixed at approximatly 0.35.

1-stage graded (Fig. 2.17a-ii) The same process as 1-stage but the process starts with a short Ga-rich CIGS (GGI = 0.60) and finishes Ga-poor (GGI = 0.20). The integrated composition is approximatly 0.35.

2-stage (Fig. 2.17a-iii) This process, also called Boeing process, includes a Cu-rich stage. This stage increases the In and Ga migration and improves the CIGS

crystallization. A Cu–rich CIGS (CGI = 1.10) is first deposited, then the Cu evaporation is shuttered until a Cu-poor composition is reached (CGI = 0.85). The temperature is fixed at 350°C. The GGI is fixed at approximatly 0.35.

2-stage graded (Fig. 2.17a-iv) The same process as the 2-stage GGI ratio but the process starts with a short Ga-rich CIGS (GGI = 0.60) and finishes Ga poor (GGI = 0.20). The integrated composition is approximately 0.35.

3-stage graded (Fig. 2.17a-v) This process is usually used for the high performance thick CIGS cells. It includes the Cu-rich step as the 2-stage process and allows the formation of a double Ga gradient to the front and to the back-contact. During the first stage, only the III elements are deposited (GGI = 0.40) at a medium temperature (350°C). In the 2^{nd} stage, the temperature is raised to 420°C and only Cu is deposited until a Cu-rich composition is reached (CGI = 1.10). In the 3^{rd} stage, only the III elements are evaporated (GGI = 0.25) at high temperature (420°C) until a Cu-poor composition is reached (CGI = 0.85). No variation of the CIGS emissivity is observed in such short processes. The duration of the 2^{nd} and the 3^{rd} are calculated before the process.

The thickness, measured from the cross-sectional SEM images, and the integrated composition, measured by X-Ray Fluorescence (XRF), are summerized for CIGS grown with each process in Tab. 2.8. Note that the thickness and the integrated composition varies with the process making the analysis more challenging.

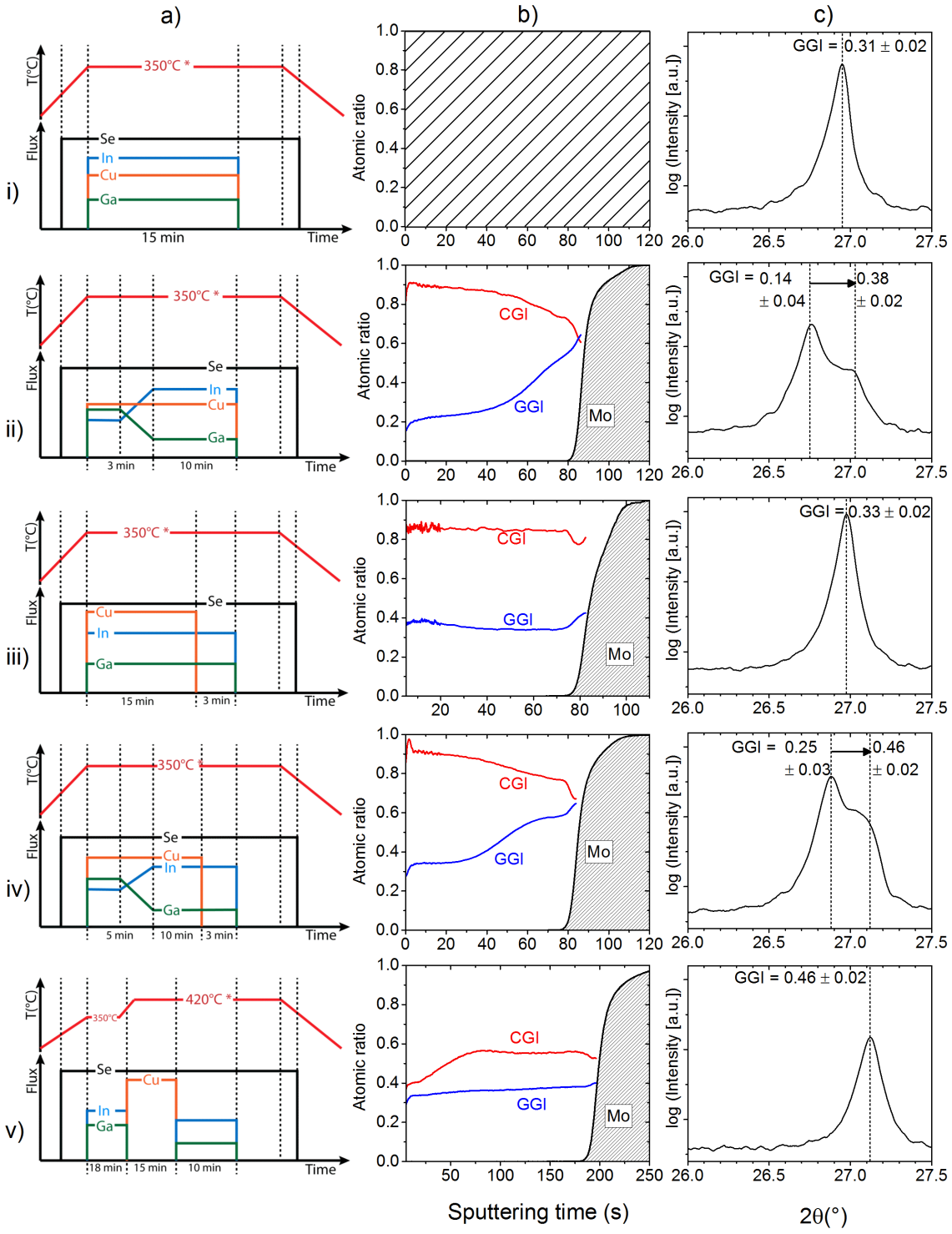

Figure 2.17.: Process description for ultra-thin CIGS solar cells and materials analysis: a) scheme of the process, b) composition profile by GD-OES, c) details of the (112) phase by XRD. i) 1-stage , ii) 1-stage graded, iii) 2-stage, iv) 2-stage graded, v) 3-stage. .

The composition profile of each sample were measured by GD-OES and are pre-

sented in Fig. 2.17b. The GD-OES signal were converted in atomic ratio by using the integrated composition measured by XRF. As observed, the GGI profiles of the 1-stage and 2-stage samples are uniform. On the opposite, the 1-stage graded sample shows a GGI increase from the front toward the back contact, from 0.20 to 0.55 ($\Delta GGI = 0.35$) . The 2-stage graded sample shows a GGI increase from the front to the back-contact as well, from 0.35 to 0.57 ($\Delta GGI = 0.22$). The higher GGI at the front contact may be due to a higher Ga mobility during the 2-stage process. For both processes with gradient, a decrease in the CGI toward the back-contact is observed, meaning that Cu diffused toward the front-contact. The sample prepared by 3-stage process shows hardly any GGI gradient and the CGI is low. The deposition temperature were maybe too high, leading to an excessive Ga diffusion [83] and the 3^{rd} stage was too long, leading to a low CGI.

The estimation of the composition gradient is also permitted by the analysis of the (112) peak measured in XRD according to the relation 2.13. As observed in the diffractograms of the 1-stage (Fig. 2.13c-i), 2-stage (Fig. 2.13c-iii) and 3-stage process (Fig. 2.13c-v), only a single (112) peak is measured, signifying the absence of composition gradient in the CIGS layer. Some differences between the estimated GGI value from XRD and the measured GGI by XRF are observed and can be due to some calibration error in XRF. On the opposite, an enlargement of the (112) peak observed for the 1-stage graded and 2-stage graded samples signifies that a composition gradient were well implemented in the layer. We can identify 2 extreme peaks meaning that gradient is not uniform and that the two evaporated compositions are kept in the final composition. Therefore the Ga and In migration is low. The gradient amplitude is estimated with the extreme position of the peak: from 0.14 to 0.38 ($\Delta GGI = 0.24$) for the 1-stage graded sample and from 0.25 to 0.46 ($\Delta GGI = 0.21$) for the 2-stage graded sample. For the 1-stage graded sample, the ΔGGI were maybe over-estimated by GD-OES.

The electron barrier, or conductive band offset (ΔE_{CB}), implemented by the composition gradient from the front to the back contact can be calculated according to the relation between the GGI value and the CIGS band-gap Eq. 2.14. Finally, the 1-stage and 2-stage process with gradient leads respectively to $\Delta E_{CB} = 0.16$ to 0.22 eV and $\Delta E_{CB} = 0.15$ to 0.14 eV.

2.4.3.2. Impact of the Ga gradient on the cell performances

The impact of the CIGS deposition process and the Ga gradient composition on cell performances were studied. The samples were completed with a standard CdS/ZnO/ZnO:Al front window. Note that the different samples were not processed on the same CdS and ZnO/ZnO:Al batches.

The I(V) and EQE curves of the best cells of each sample are displayed in Fig. 2.18. The I(V) parameters averaged over the best 10 cells are reported in Tab. 2.8. In

Table 2.8.: Cell performance of the samples with the CIGS layer deposited by various process. The integrated composition is measured by X-Ray Fluorescence. The J(V) parameters are means ± standard variation of the 10 best cells. The J(V) dark of the best cells are fitted with a 2-diode model (n = 1 and n = 2). The decomposed influence of the two diodes on the V_{OC} are analyzed with the formulas given in Appendix A.

	1-stage	**1-stage graded**	**2-stage**	**2-stage graded**	**3-stage**
Thickness (nm)	380 ± 20	430 ± 20	400 ± 20	410 ± 20	650 ± 20
Cu/(In+Ga)	0.95	0.89	0.85	0.90	0.55
Ga/(In+Ga)	0.36	0.22	0.32	0.34	0.37
Efficiency (%)	9.5 ± 0.2	7.5 ± 0.2	7.5 ± 0.3	10.4 ± 0.1	7.6 ± 0.2
V_{OC}**(mV)**	614 ± 11	520 ± 3	586 ± 8	607 ± 2	515 ± 24
J_{SC}**(mA/cm²)**	21.0 ± 0.2	24.3 ± 0.2	19.8 ± 0.1	23.7 ± 0.1	21.8 ± 0.3
FF (%)	71 ± 2	59 ± 1	65 ± 2	72 ± 1	68 ± 3
J_{01}**(mA/cm²)**	$7.1.10^{-11}$	$4.1.10^{-9}$	$4.3.10^{-10}$	$3.2.10^{-10}$	$2.7.10^{-9}$
J_{02}**(mA/cm²)**	$2.5.10^{-5}$	$3.4.10^{-5}$	$7.6.10^{-5}$	$6.9.10^{-5}$	$4.6.10^{-5}$
R_{Sh}**(Ω.cm)**	$> 5.10^5$	1.10^2	1.10^3	1.10^3	2.10^5
R_S**(Ω.cm)**	0.2	0.4	<0.1	<0.1	<0.1
$J_{SC}/J_{SC}^{MAX}(E_g)$	0.53	0.56	0.48	0.59	0.60
	’1 stage-graded - 1 stage’		’2 stage-graded - 2 stage’		’3 stage - 1 stage’
$\Delta V_{OC}(exp)$ **(mV)**		-94		21	-99
$\Delta V_{OC}(\triangle J_{01,}J_{02})$ **(mV)**		-84		13	-79
$\Delta V_{OC}(\triangle J_{001})$ **(mV)**		-1		2	-125
$\Delta V_{OC}(\triangle J_{002})$ **(mV)**		16		3	-20
$\Delta V_{OC}(\triangle E_g)$ **(mV)**		-95		14	75

addition the dark I(V) curves of the best cells were fitted with a 2-diode model and the parameters are reported in Tab. 2.8. Surprisingly, the 1-stage process leads to higher cell efficiency than the 2-stage process (9.5% compared to 7.5%). The cell with a 1-stage graded process (430-nm-thick CIGS) has a lower efficiency than the cell with 1-stage process (380-nm-thick CIGS): 7.5% compared to 9.5%. On the opposite, the cell with a 2-stage graded process (410-nm-thick CIGS) has a higher efficiency than the cell with a 2-stage process (400-nm-thick CIGS): 10.4% compared to 7.5%. At the end, the 3-stage cell (650-nm-thick CIGS) has a low efficiency: 7.6%.

To quantify the impact to the Ga gradient on the cell performances we need to analyses the J_{SC}, V_{OC} and FF variations. However, the J_{SC} and V_{OC} of each cell are difficult to compare due to the variation of CIGS thicknesses and compositions.

For a better understanding, the J_{SC} was normalized by the maximum J_{SC} possible for a CIGS band-gap ($J_{SC}/J_{SC}^{MAX}(E_g)$) and the variation of V_{OC} is decomposed in the relative influence of the band-gap (E_g), $J_{001}(J_{01} = J_{001}\exp(-E_g/kT))$ and $J_{002}(J_{02} = J_{002}\exp(-E_g/2kT))$. Note that we suppose that the activation energy of the dark current is the band-gap. We also approach the band-gap of the graded

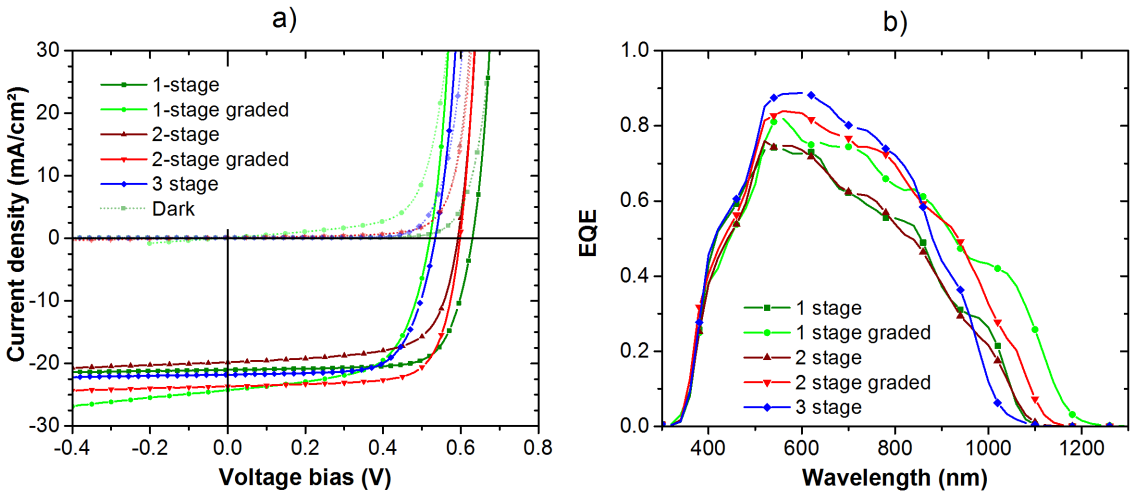

Figure 2.18.: a) I(V) and b) EQE measurements for the best cell of each sample with a CIGS layer deposited with different processes.

cell form the integrated composition over the thickness measured by XRF with the formula Eq. 2.14. The interest of this calculation is that J_{001} refers to the recombination at the interface and in the QNR, whereas J_{002} refers to the recombination in the SCR. Details of the calculation are given in Appendix A. The results are displayed in Tab. 2.8.

According to the EQE measurements Fig. 2.18b, the higher J_{SC} of the 1-stage graded cell compared to the 1-stage non-graded cell is partly due to the lower GGI that moves the absorption edge to higher wavelength but is also due a curve up-shift in the 550 - 900 nm spectral range. The 1-stage graded process has a slight higher $J_{SC}/J_{SC}^{MAX}(E_g)$ ratio than the with the 1-stage process. This effect should be mainly due to the larger CIGS thickness. However, the V_{OC} is lower for the cell with the 1-stage graded process compared to the cell with the 1-stage graded process (-95 mV). According to the relative variation of the V_{OC} due to E_g, J_{001} and J_{002}, the decrease of V_{OC} is mainly due to the difference in E_g (Tab. 2.8). The lower FF for the sample with gradient is mainly due to the low shunt resistance, probably related to a scribing procedure issue. Finally, the Ga gradient has hardly any impact on the passivation of the back-contact.

Concerning the 2-stage process, a much higher J_{SC} is observed in the case with gradient compared to the case without gradient (+3.9 mA/cm²). According to the EQE measurements Fig. 2.18b, this J_{SC} increase is due to a curve up-shift on the whole spectral range. A large increase of the $J_{SC}/J_{SC}^{MAX}(E_g)$ ratio is also calculated (Tab. 2.8) meaning that a passivation effect may happen in addition of the difference of thickness. Moreover, a higher V_{OC} is observed (+20 mV). According to calculation of the relative influence of the J_{001}, J_{002} and E_g on the V_{OC}, this increase in V_{OC} is mainly due to the small difference of band-gap (Tab. 2.8). As a consequence, no improvement of the cell interface can be noticed. Therefore, the impact of the Ga

gradient has only a poor impact on the passivation of the back-contact.

Concerning the 3-stage process, the low performance is mainly due to a low V_{OC}, 515 mV, much lower than 680 mV expected for a CIGS with a band-gap of 1.27 eV (according to Fig. 2.16b with GGI=0.46 taken from the XRD measurements Fig. 2.17c-v and the band-gap calculated from Eq. 2.14). According to calculation of the relative influence of the J_{001}, J_{002} and E_g on the V_{OC}, high recombination happens in the QNR and at the interfaces. A too long third-stage was already demonstrated to leads to low cell efficiency [112].

To conclude, no clear interface passivation was observed when using a Ga gradient. It should nevertheless be noted that the cell efficiency of 10.4% was obtained for a 410-nm-thick CIGS deposited using a 2-stage graded process.

2.4.4. Conclusion

The Ga content and a Ga gradient in the CIGS absorber are the key parameters to optimize both standard and ultra-thin CIGS solar cells. Without any composition gradient, an optimum efficiency for GGI $= 0.40 \mp 0.5$ ($E_g = 1.27$ to 1.33 eV) was observed for 2000-nm-thick CIGS and for 500-nm-thick CIGS. In ultra-thin CIGS cells, a too low GGI may lead to an unsuited band alignment whereas a too high GGI may increase the defect density.

A GGI gradient was also implemented in 500-nm-thick CIGS cells. If this gradient does not exceed the range of GGI leading to the best cell efficiency (0.3-0.5), the efficiency of the graded cells is slightly improved compared to the ungraded cell but a back-contact passivation effect of the Ga-gradient is not clear. This gradient were achieved with a 2-stage process, starting with the evaporation of a Cu-rich CIGS, with a Ga and In flux variation. This sample reaches 10.4 % for a 400-nm-thick CIGS.

However, for a question of reproducibility of the process, only an ungraded 1-step process was used for a majority of experiments. In the following section, the optimization of the CIGS absorber deposition under imposed constrained will be discussed.

2.5. Impact of the deposition parameters on ultra-thin CIGS properties

High performance CIGS solar cells require optimal Na and K contents [38, 140, 18] either provided by diffusion from the glass substrate (concerning Na) or by a post-deposited treatment (PDT) (concerning Na or K). The CIGS growth temperature should be sufficient [141, 142, 17]. Moreover, a suitable MoSe2 film formed at the Mo/CIGS back-interface is required to facilitates the achievement of a ohmic back-contact [143, 26]. For ultra-thin CIGS solar cells, the Mo back-contact is not suitable and some alternative back-contact should be find.

The purpose of this section is to determine the behavior of ultra-thin CIGS solar cells for other growth condition: low substrate temperature and no diffusion of Na from the glass.

However, the Na diffusion, $MoSe_2$ formation, substrate temperature and alkali incorporation are highly interconnected. For example, the CIGS growth temperature affects the diffusion of Na from the glass to the absorber [142], the CIGS growth temperature and the Na diffusion affect the $MoSe_2$ interfacial layer formation [26, 144, 27], and the KF PDT affects the Na concentration in CIGS [19].

In the literature, the impact of each of these parameters has been extensively studied on thick (2-3µm) CIGS absorbers. However, a cross experiment taking into account the impacts of the deposition temperature, the Na diffusion, the KF PDT and of the formation of $MoSe_2$ layer at the same time on ultra-thin CIGS solar cells down to 350 nm has not been performed.

2.5.1. Description of the design of experiment

The CIGS layers were deposited by a classical one stage co-evaporation process. Its final composition measured by EDS over the all set of samples is CGI = 0.90±0.02 and GGI = 0.35±0.01 as atomic ratios. Its thickness measured by profilometry over the all set of samples, is 350±10 nm.

A KCN treatment of the absorbers was carried out prior to further depositions and characterizations. The cells were completed a standard CdS/ZnO/ZnO:Al front contact. The impact of four different parameters were studied:

- **Impact of Na diffusion from glass substrate:** comparison between samples with and without a 300-nm-thick Al_2O_3 barrier layer deposited by atomic layer deposition (ALD) between the glass and Mo. The 300-nm-thick Al_2O_3 layer hinders Na diffusion through the Mo layer [145];
- **Impact of K incorporation:** comparison between samples with and without a post-treatment deposition of KF (KF PDT). The KF PDT was carried out at 300°C under Se flux for 10 min at around 1 nm/min;

- **Impact of substrate temperature:** comparison between samples grown at the estimated substrate temperature of 390°C, 450°C and 500°C;
- **Impact of the $MoSe_2$ layer:** comparison between samples with and without a pre-grown $MoSe_2$ layer on the glass/Mo substrate. The pre-grown $MoSe_2$ indicates a Glass/Mo/$MoSe_2$ substrate of a standard CIGS processed at 500°C where the CIGS layer has been removed by lift-off. A detailed description of the lift-off process can be found in [146].

Overall, this 4-level full factorial design leads to a total of 24 samples. The CIGS layers were deposited in 6 batches, for each temperature and with and without KF PDT. In each batch 4 substrates were processed: substrates with/without Al_2O_3 barrier layer and with/without pre-grown $MoSe_2$. For all samples, the same batch of Mo, CdS, i-ZnO, ZnO:Al layers were used. For convenience, samples are named according to the following nomenclature : (Na or Ø, K or Ø, Mo-MoSe2 or Mo, 390°C or 450°C or 500°C), for the following conditions respectively: (without or with Al_2O_3 barrier layer, with or without KF PDT, with or without pre-grown $MoSe_2$ layer, CIGS deposition temperature). For example, the standard sample grown at 500°C on Mo substrate without KF PDT is named (Na, Ø, Mo, 500°C).

2.5.2. Material analysis

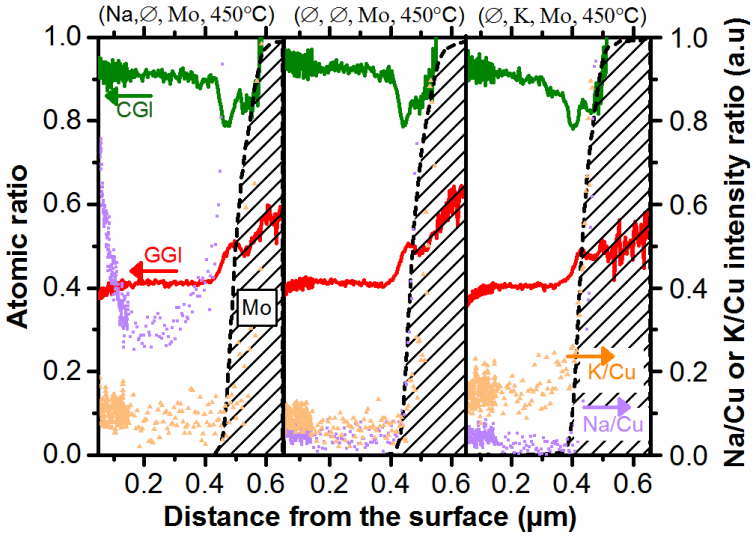

Figure 2.19.: GD-OES depth profile of samples after the CIGS process. CGI (green) and GGI (red) deduced from signal quantification are on the left axis. Na/Cu (violet) and K/Cu (orange) signal intensity ratios are on the right axis.

For a better understanding of the alkali incorporation, GD-OES measurements were first performed on all samples. To compare the Na and K concentration between the different samples, the Na/Cu and K/Cu ratio were reported. Fig. 2.19 shows

the atomic ratio GGI and CGI and the Na/Cu and K/Cu signal intensity ratio of the CIGS layer grown at 450°C, without Al_2O_3 barrier (Na, Ø, Mo, 450°C), with Al_2O_3 barrier (Ø, Ø, Mo, 450°C) and with KF PDT (Ø, K, Mo, 450°C). As observed, for samples with Al_2O_3 barrier (Fig. 2.19b) the signal of Na/Cu is close to the background noise, indicating no diffusion of Na in the absorber. The KF PDT treatment (Fig. 2.19c) leads to a K signal higher than the background noise, indicating a K incorporation in the CIGS layer.

The Fig. 2.21 summarizes the estimated K and Na concentrations in the absorbers measured by GD-OES for all samples. The Na (and K) concentration was estimated with the average ratio Na/Cu (and K/Cu) over the CIGS thickness normalized with respect of the standard samples (Na, Ø, Mo, 500°C) for Na/Cu and (Ø, K, Mo, 500°C) for K/Cu.

As expected, the Al_2O_3 barrier hinders the Na diffusion from the glass whatever the process. For samples without Al_2O_3 barrier, the Na content increases with lower substrate temperature whatever the process used. This effect can be explained by an enhanced diffusion of Na toward the surface at high substrate temperature [39] leading to an accumulation of Na on the top of the CIGS layer which is therefore removed during the KCN treatment.

Concerning the KF PDT, as observed in Tab. 2.9, when K is supplied, the Na content in the absorber is reduced whatever the growth temperature. Similar effect was observed on thick CIGS layer with both NaF and KF PDT [19] and was attributed to a partial ion exchange between K and Na in the CIGS layer. However no correlation is observed between the K concentration and the deposition temperature.

Raman measurements were also performed on all CIGS absorbers. Fig. 2.20a displays the Raman spectrum of a CIGS layer (Na, Ø, Mo, 450°C) showing typical vibrations of a chalcopyrite CIGS structure (A_1 at 178 cm^{-1}, B_2 at 220 cm^{-1} and E at 255 cm^{-1}) [127]. Identical spectra were obtained for all different CIGS samples and were therefore not shown here.

In addition, the formation of $MoSe_2$ was also analyzed by Raman measurements after peeling off the CIGS layer from the glass/Mo/$MoSe_2$ substrate: as a function of the deposition temperature (Fig. 2.20b), the alkali content or the pre-grown $MoSe_2$ for CIGS grown at 450°C (Fig. 2.20c).

For all peeled-off substrates, peaks at 170 and 240 cm^{-1} are observed on Raman spectra and identified as the E_{1g} and A_{1g} vibration of the $MoSe_2$ structure [147]. The A_{1g} peak intensities of all samples normalized with respect of the standard sample (Na, Ø, Mo, 500°C) are reported in Fig. 2.21. Fig. 2.20b, it is observed that the A_{1g} peak intensity increases with the increase in the temperature from 390°C to 500°C, revealing a larger $MoSe_2$ formation at high temperature. The effect of the temperature on $MoSe_2$ is the same whether alkali are present or not in the samples (Fig. 2.21). The diffusion of Na and the KF PDT seem to have no influence on the A_{1g} peak intensity and position (Fig. 2.20c and Fig. 2.21). They have a poor influence on the $MoSe_2$ formation.

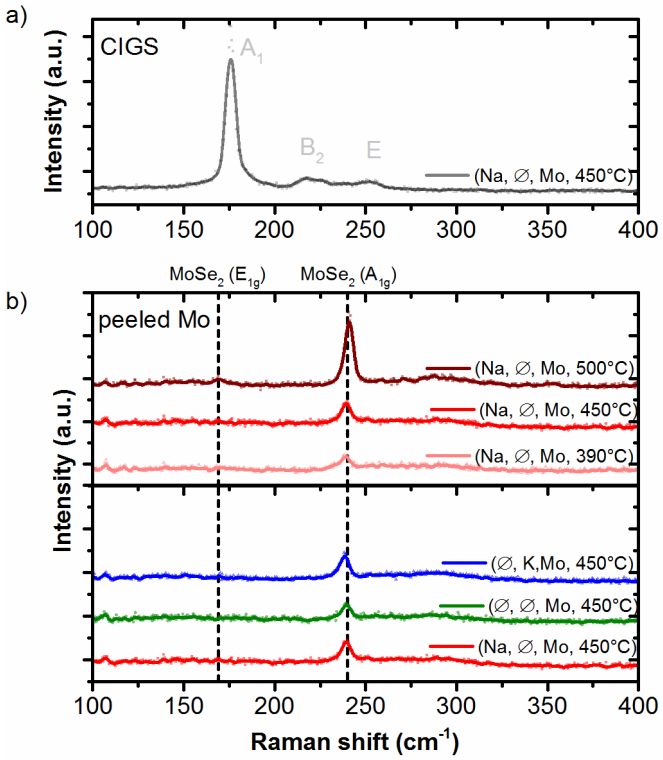

Figure 2.20.: Raman spectra of a) the CIGS layer after the CIGS process for the sample grown (Na, Ø, Mo, 450°C), b) the Mo substrate after peeling of the CIGS layer.

The use of a pre-grown $MoSe_2$ substrate allow for a similar $MoSe_2$ thickness whatever the process, and in a larger amount compared to the directly-used Mo substrate.

2.5.3. Cell performances

2.5.3.1. Global cell analysis

For more reliability in the statistical analysis, the I(V) parameters was averaged over the 5 best cells of each sample and the results are displayed in Fig. 2.22. Note that the 5 best cells mainly differ by their FF (Correlation coefficient between the efficiency and FF of 0.90), especially because of the shunt resistance variation.

The Fig. 2.22 clearly shows that the cells without both K and Na exhibits degraded performances due to low V_{OC} and FF whereas the presence of Na and/or K leads to an important improvement of the cell efficiencies. This improvement is mainly due to the increase of the V_{OC} and FF while the J_{SC} decreases. Moreover, for cells with alkali supply, cell performance are improved for high deposition temperature. The presence of only Na seems to have a similar effect on the cell performances than the presence of only K. The presence of both Na and K increases the cell efficiencies.

		(Ø, Ø, Mo)	(Ø, Ø, $MoSe_2$)	(Na, Ø, Mo)	(Na, Ø, $MoSe_2$)	(Ø, K, Mo)	(Ø, K, $MoSe_2$)	(Na, K, Mo)	(Na, K, $MoSe_2$)
KF PDT		**no**	**no**	**no**	**no**	**yes**	**yes**	**yes**	**yes**
Al_2O_3 barrier		**yes**	**yes**	**no**	**no**	**yes**	**yes**	**no**	**no**
Substrate		**standard**	**reused**	**standard**	**reused**	**standard**	**reused**	**standard**	**reused**
$MoSe_2$ Normalized by the sample (Na, Ø, Mo, 500°C).	**500°C**	1.2	2.1	**1.0**	1.8	--	2.4	0.7	1.7
	450°C	0.2	1.5	0.3	1.8	0.4	1.9	0.4	1.2
	390°C	0.1	1.8	0.2	1.8	0.1	1.8	0.2	1.4
Na concentration Normalized by the sample (Na, Ø, Mo, 500°C).	**500°C**	0.0	0.1	**1.0**	1.2	0.0	--	0.3	0.2
	450°C	0.0	0.0	1.9	1.7	0.0	--	1.3	0.4
	390°C	0.0	0.0	2.6	2.8	0.0	--	1.4	2.1
K concentration Normalized by the sample (Ø, K, Mo, 500°C).	**500°C**	0.1	0.0	0.0	0.2	**1.0**	--	0.8	1.3
	450°C	0.0	0.0	0.1	0.0	1.5	--	1.1	2.2
	390°C	0.0	0.0	0.2	0.1	1.0	--	0.7	1.7

Figure 2.21.: Material characterization of the 24 samples fabricated according to the design of experiment. The Na and K concentration are estimated by the corresponding GD-OES signal intensity ratio with copper after removing of background signal. The $MoSe_2$ layer is characterized by the 240 cm^{-1}. Raman peak intensity after removing the background signal.

We also observe that the cells with a pre-growth $MoSe_2$ seem to reach higher performances compared to directly-used Mo substrate.

Finally, the highest efficiency of 7.8% is obtained for sample deposited at 500°C, with Mo-pre-growth $MoSe_2$ back contact and with both Na & K supply (Na, K, Mo-$MoSe_2$, 500°C).

However at this stage, it is quite difficult to clearly separate the impact of the different parameters independently from each other. A statistical analysis of the effect of different parameters on the solar cell performances will now be detailed.

2.5.3.2. Impact of pre-grown $MoSe_2$ samples on cell performance

The cell parameters of all samples with and without the pre-grown $MoSe_2$ are compared in Fig. 2.23. The mean comparison significance and interval of confidence are given in this figure by a pairwise student test with a risk of 10% [148].

Regardless of the other deposition conditions, the efficiency of cells significantly increases by $1.0\% \pm 0.4\%$ with the pre-grown-$MoSe_2$ layer, mainly due to the increase of V_{OC} and FF.

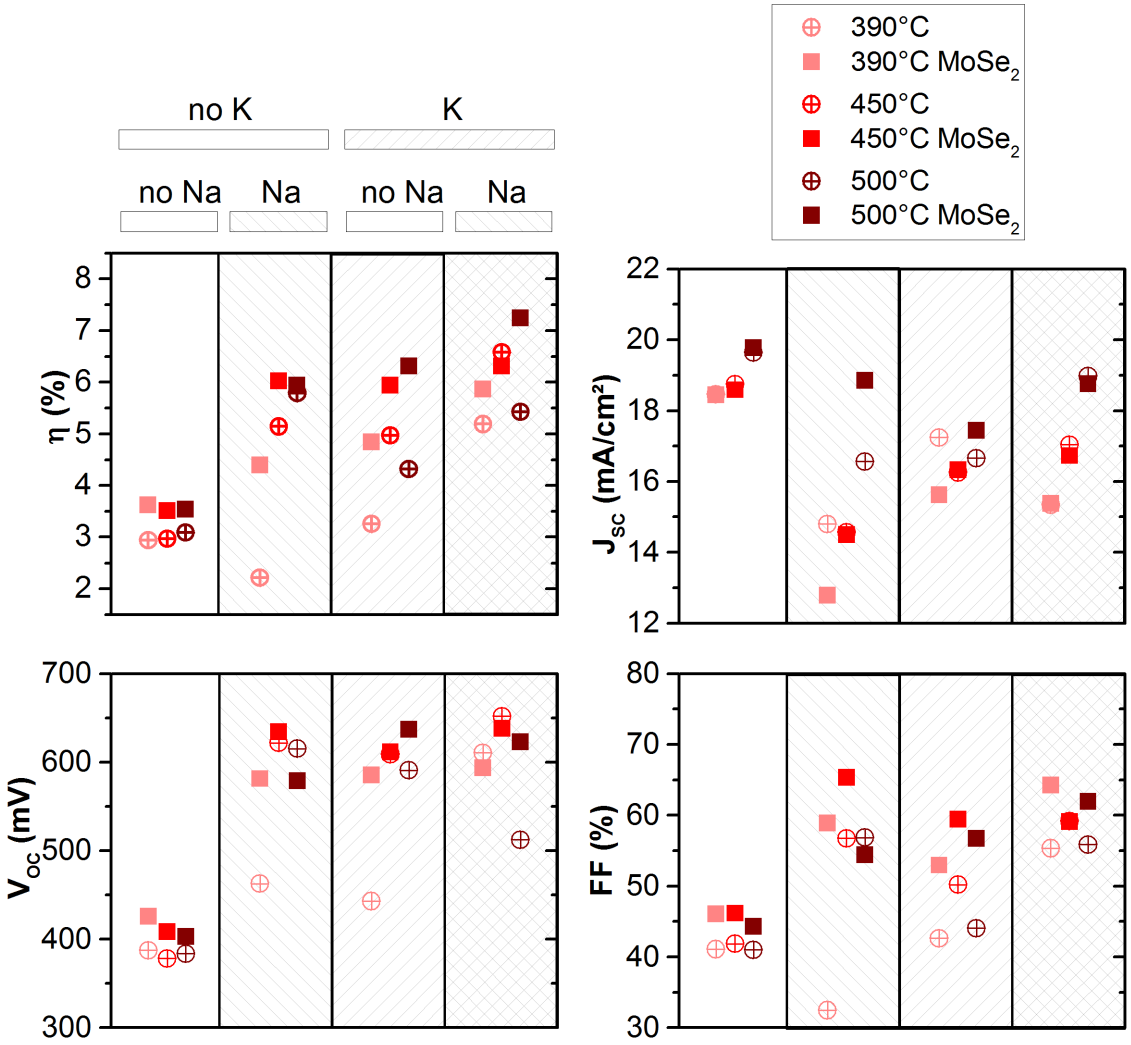

Figure 2.22.: Mean efficiency, V_{OC}, J_{SC} and FF of the 5 best cells taken from each of the 24 different samples.

According to Fig. 2.22, this increase is stronger at 390°C. We observed for those samples a very low $MoSe_2$ formation from Raman analysis (Fig. 2.21). It has been shown that the interfacial $MoSe_2$ layer facilitates a quasi-ohmic contact between the CIGS and Mo layers by achieving a better energy-band alignment at the contact [149]. Therefore, the $MoSe_2$ formation seems to be insufficient for sample grown at 350°C. To overpass this difficulty, it is possible to recycle the Mo-$MoSe_2$ substrate already formed during the fabrication of a standard CIGS layer at high temperature.

For the analysis of the temperature influence only samples with the pre-grown $MoSe_2$ will be taken into consideration.

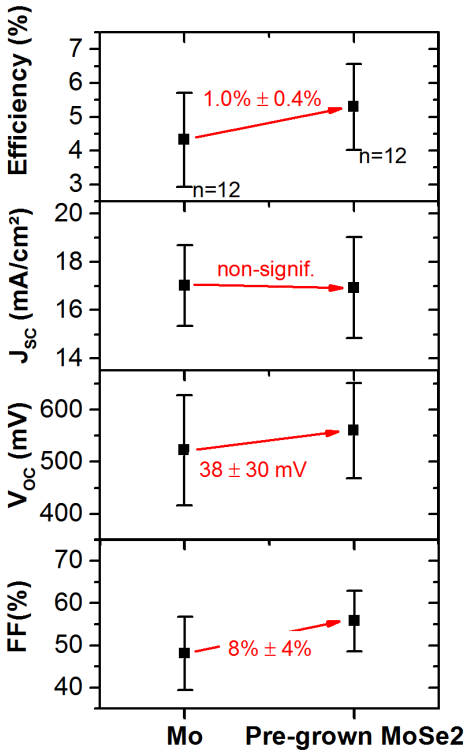

Figure 2.23.: Comparison of the cell parameters between the standard Mo substrate and the substrate with a pre-grown $MoSe_2$. Data as mean ± standard deviation (n samples) are in black. Mean variation ± interval of confidence are in red and are the result of a pairwise Student test with a risk of 10%. "non-signif" is indicated when the mean variation is not significant (p-value>0.1).

2.5.3.3. Impact of alkalis on cell performance

In order to have a better understanding of the effect of Na and K supplies on cells parameters we first focused, on a single substrate temperature (500°C): without alkali (Ø, Ø, Mo-$MoSe_2$, 500°C), with the diffusing Na (Na, Ø, Mo-$MoSe_2$, 500°C), with a KF PDT (Ø, K, Mo-MoSe2, 500°C) and with both diffusing Na and KF PDT (Na, K, Mo-$MoSe_2$, 500°C). Fig. 2.24a and Fig. 2.24b present the I(V) curves and the EQE curves of these cells. The I(V) curves fitting parameters according to a 2-diode model are reported on Tab. 2.9.

For alkali free samples, the efficiency is only of 3.6% (Ø, Ø, Mo-$MoSe_2$, 500°C), due to a low V_{OC} and FF. The V_{OC} is affected by the high saturation currents (J_{02}), calculated with the dark I(V) parameters, which are generally attributed to a low p-doping and a high defects density in the CIGS absorber [40]. Alkali-free samples also show higher J_{SC} compared to samples with Na or K with an upshift of the EQE for wavelength around 500 nm.

For samples with only Na or only K, the cell efficiency increases up to 6.7% for sample with only K (Ø, K, Mo-$MoSe_2$, 500°C) and 6.1% for sample with only Na

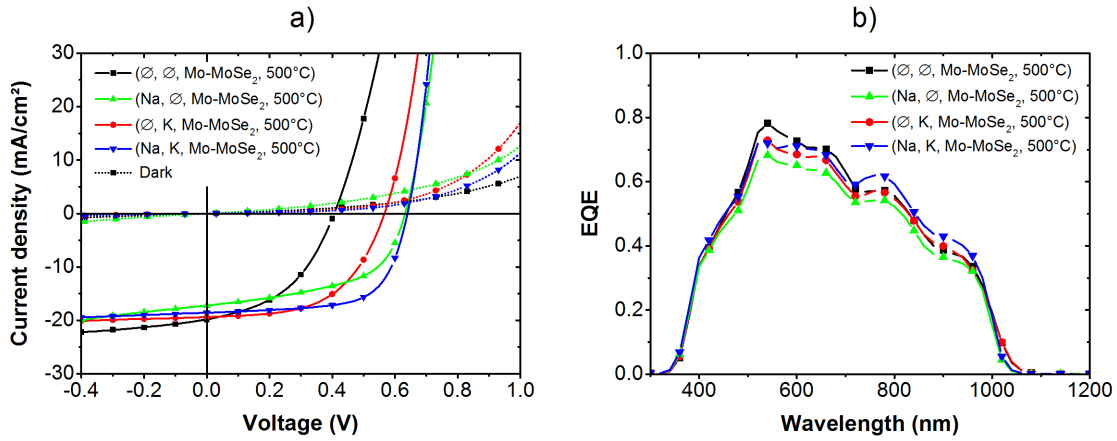

Figure 2.24.: Cell characterization of the samples grown at 500°C with a pre-grown $MoSe_2$ back-contact. a) Current voltage current, b) External quantum efficiency.

	J_{02} (mA/cm²)	R_{SH} (Ω.cm²)	R_S (Ω.cm²)
(Ø, Ø, Mo-$MoSe_2$, 500°C)	$5 \cdot 10^{-2}$	40	3
(Na, Ø, Mo-$MoSe_2$, 500°C)	$1 \cdot 10^{-4}$	140	1.2
(Ø, K, Mo-$MoSe_2$, 500°C)	$9 \cdot 10^{-5}$	150	1.2
(Na, K, Mo-$MoSe_2$, 500°C)	$9 \cdot 10^{-5}$	450	0.7

Table 2.9.: I(V) curve fitting parameters with a 2-diode model (J_{01} and J_{02} are respectively the saturation current of diode with ideality factor of 1 and 2, R_{SH} the shunt resistance and R_S the series resistance). J_{01} was found negligible compared to J_{02}.

(Na, Ø, Mo-$MoSe_2$, 500°C) with a much better V_{OC} and FF. These results show that it is possible to compensate the absence of Na by K incorporation for 350-nm-thick CIGS absorber grown at 500 °C.

The best efficiency (7.8%) is obtained when both Na and K are incorporated (Na, K, Mo-$MoSe_2$, 500°C).

In order to confirm these trends regardless of the other deposition conditions, the cell parameters of all samples without alkali are compared with all samples with Na and/or K (Fig. 2.25). The mean comparison significance and interval of confidence are given in this figure by a Student test with a risk of 10% [148]. The efficiency increases by 2.0% ± 0.9% from the case without alkali to the case with at least one alkali, due to an increase in the V_{OC} (+190 ± 40 mV), an increase in the FF (+11 ± 6%) and a decrease in the J_{SC} (-2.6 ± 1.2 mA/cm²).

Large variation of J_{SC} are observed in Fig. 2.25 over the all set of samples and can be related to the alkali concentration in the CIGS absorbers. An empirical alkali quantity estimation was calculated using the sum of the normalized values Na/Cu and K/Cu obtained by GD-OES (as reported in Fig. 2.21). The Fig. 2.26 shows the

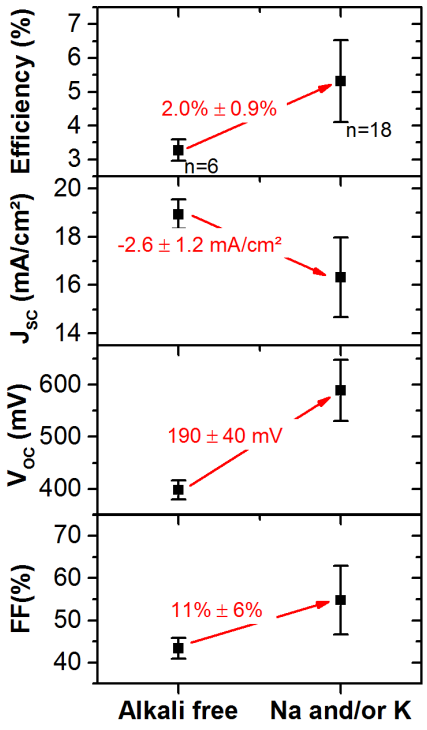

Figure 2.25.: Comparison of the cell parameters between alkali-free samples and Na and/or K containing samples. Data as mean ± standard deviation (n samples) are in black. Mean variation ± interval of confidence are in red and are the result of a Student test with a risk of 10%. "non-signif" is indicated when the mean variation is not significant (p-value>0.1).

plot of the J_{SC} as function of the empirical alkali quantity. We observe a significant inverse relation between the J_{SC} and the alkali content from 18.9 ± 0.5 mA/cm² for alkali free samples to 14.7 ± 1.2 mA/cm² for high alkali concentration. This effect was already reported on 3-stage process CIGS for high N_a content [145, 150].

The variation of J_{SC} can be related to the variation of the doping content (N_a) that leads to variation of the space charge region width (w) ($w \propto \sqrt{N_a}$). For high N_a content, the shorter the space charge region is narrowed and the charge collection is reduced. This effect is amplified if the carrier diffusion length is short due to interface recombination or defects in the QNR. Measurements by impedance spectroscopy showed hardly any information on the doping content and the space charge region width due to the presence of parasitic capacitance making the analysis difficult (not shown here). Moreover it is also expected that the V_{OC} varies with the doping content ($V_{OC} \propto \ln(1/N_a)$) leading to a V_{OC} and J_{SC} variation in an opposite direction, as observed between the sample with and without alkali.

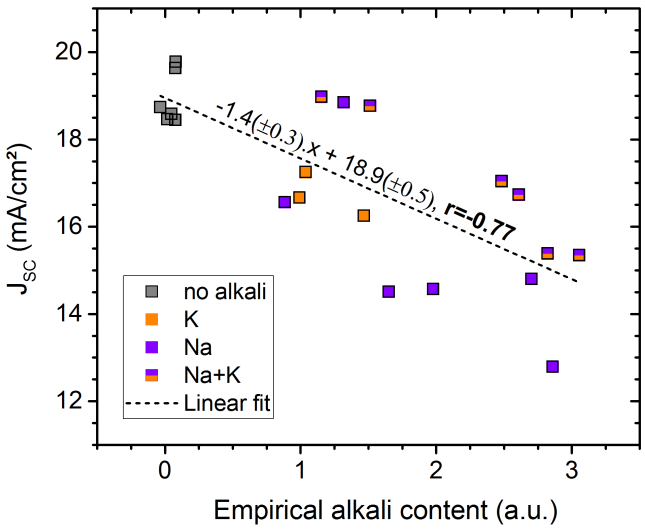

Figure 2.26.: Variation of the J_{SC} of the different cells as a function of an empirical value of the alkali content corresponding to the addition of the Na/Cu + K/Cu normalized ratio reported in Table 1. Parameters of the linear fit is presented with the standard deviation and with the Pearson coefficient (r).

2.5.3.4. Cross effect of the alkalis and the substrate temperature

The effect of alkalis and the CIGS growth temperature on cell performances is highlighted in Fig. 2.27a and Fig. 2.27a. In this analysis, only alkali-containing samples with a pre-grown $MoSe_2$ where used to get rid of the effect of temperature dependent $MoSe_2$ formation. The pairwise mean comparison and the interval of confidence were performed by a two-way ANOVA analysis coupled with a Fisher test [148]. Overall, the cell parameters of 9 samples were analyzed. No statistically relevant cross-effect were found between the CIGS growth temperature and the presence of Na and/or K.

As observed in Fig. 2.27a, the cells with only K (Ø, K, Mo-$MoSe_2$, all) have a statistically similar efficiency than cells with only Na (Na, Ø, Mo-$MoSe_2$, all). This results confirms that the KF PDT compensates the absence of diffusion of Na for ultra-thin CIGS absorbers without any loss.

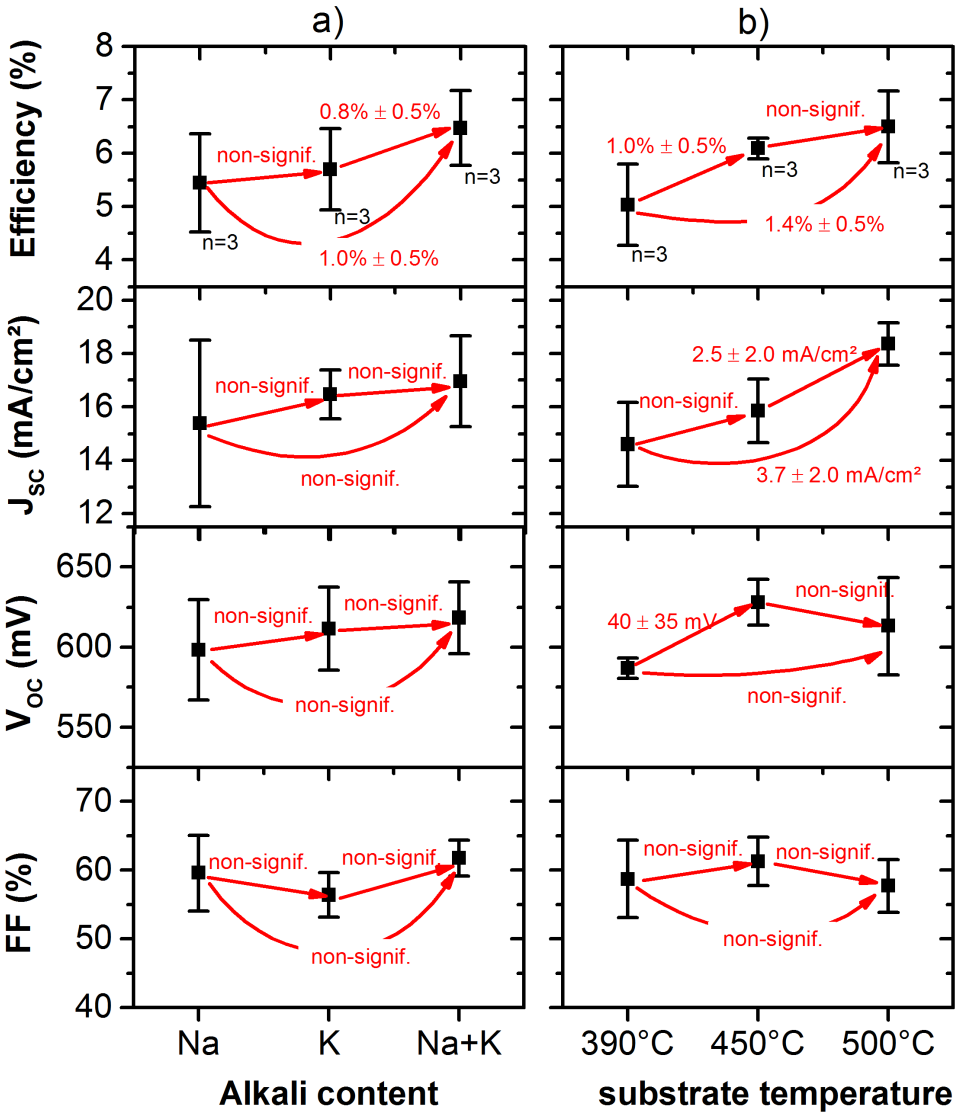

Figure 2.27.: Comparison of the cell parameters a) for samples Na diffusing from the glass, K from a KF PDT or both Na and K, and b) for samples grown at different substrate temperatures. Data as mean ± standard deviation (n samples) are in black. Mean variation ± interval of confidence are in red and result from the two-way ANOVA test with pairwise Fisher test for mean comparison with a risk of 10%. %. "non-signif" is indicated when the mean variation is not significant (p-value>0.1).

As observed inFig. 2.27b, CIGS cells grown at 500°C and 450°C have a statistically similar efficiency. Between 500°C and 390°C the efficiency decreases by 1.4% ± 0.5% mainly due to a decrease of the J_{SC} (-3.7 ± 2.0 mA/cm²) and a slight decrease of V_{OC} (only significant between 390°C and 450°C: -40 ±35 mV). Finally, the efficiency of the population with both Na and K (Na, K, Mo-MoSe2, all) is even better than with only the diffusing Na (+0.8 ± 0.5%).

Looking more into the detail in Fig. 2.22, the J_{SC} of the cell with Na at low tempera-

ture (Na, Ø, Mo-MoSe2, 390°C) is very low (12.6 mA/cm²) and is greatly increased with the KF PDT (Na, Ø, Mo-$MoSe_2$, 390°C). On the contrary, the J_{SC} of the cell with Na at high temperature (Na, Ø, Mo-$MoSe_2$, 500°C) is close to the J_{SC} of the alkali-free cells (18.9 mA/cm²) and is reduced with the KF PDT (Ø, K, Mo-$MoSe_2$, 500°C). This effect can be explained by the variation of Na content which is strongly related to the substrate temperature whereas the incorporation of K by PDT is poorly related to the substrate temperature. As a consequence, the substrate temperature affects much more the samples when Na diffuses than samples with PDT.

However, if a larger p-doping is obtained for substrate temperature of 350°C, it would theoretically lead to a larger V_{OC} , whereas a V_{OC} loss is observed. Therefore these results highlight that the low substrate temperature limits the V_{OC} , due to probably a higher density of defects.

2.5.4. Conclusion

This work analyses the joint influence of the CIGS growth temperature, the Na diffusion into the CIGS layer, the K incorporation by a PDT and the $MoSe_2$ layer on the performances of 350-nm-thick CIGS based solar cells.

A cross analysis of the results shows clearly that:

- Recycled Mo substrates (having a pre-grown $MoSe_2$) increases the cell efficiency by 1%abs.
- A KF PDT can compensate the absence of Na, if Na diffusion is hindered;
- Best efficiencies are obtained for CIGS growth temperature higher than 450°C. At 390°C, formation of defect, independently to the Mo/$MoSe_2$ back-contact, probably limits the performances.
- Best efficiencies are obtained for a KF PDT performed in addition to the Na diffusion from the glass.

The best cell for a 350-nm-thick CIGS is 7.8% for a sample with both KF PDT and Na diffusion, with a pre-grown $MoSe_2$ and at 500°C.

2.6. Conclusion of the chapter

In this chapter, we have simulated and analyzed samples with different CIGS thicknesses without composition gradient. The following conclusion can be drawn:

> **Making high performance ultra-thin CIGS solar cells poses a problem due to the back-interface: the Mo/CIGS interface is weakly reflective and exhibits too high recombination velocity.**

Ultimately, with a reflective and passivative back-contact, we can expect an even higher efficiency for ultra-thin CIGS solar cell than the standard µm thick cells.

We have not discover other major source of losses compared to thick CIGS deposited with the same 1 stage process. Our tries to improve the efficiency of ultra-thin CIGS cell by using advanced coevaporation deposition of the CIGS layer (composition gradient or multi-stage process) was not successful.

Therefore, high performance ultra-thin CIGS solar cells requires the development of a **(1) reflective** and **(2) passivated back-contact**. Those 2 points will guide our work for the following chapters. This assertion supposes to replace the Mo back contact.

However, the deposition of the CIGS layer on alternative substrates may require a lower substrate temperature and may hinder the Na diffusion from the glass substrate. Experiments on Mo at various temperature show that the substrate temperature should not decrease below 450°C and that the diffusion of Na can be replaced by an alkali fluoride post deposition treatment.

3. Photocurrent enhancement in ultra-thin CIGS solar cells

3.1. Introduction

We have seen in the previous chapter that the Mo back-contact is not satisfying for a back-contact in ultra-thin CIGS solar cells. The light reflection at the interface with the CIGS layer is too low and the collection of the charge carriers close to the contact is reduced by the high surface recombination velocity.

However, the molybdemum is almost exclusively used as back-contact in the CIGS solar cells. The reasons why are:

- the high electron affinity (~4.5 eV) permitting an ohmic contact with the CIGS, supported by the formation of a thin beneficial $MoSe_2$ interfacial layer;
- the adhesion of the CIGS layer on Mo;
- the stability at high temperature under selenium atmosphere permitting the formation of a thin $MoSe_2$ layer without excess;
- the permeability for alkali elements migrating from the soda lime glass substrate;

An alternative back-contact is investigated in this chapter using a transparent conducting oxide (TCO). Based on previous studies, and based on optical and electrical models, the potential of such back-contact for ultra-thin CIGS cells is analyzed. Two different TCOs were selected: aluminum doped zinc oxide (ZnO:Al) and fluorine doped tin oxide (SnO_2:F). The TCOs were characterized before and after the CIGS deposition. The CIGS was deposited by coevaporation with an external supply of Na and was compared to the deposition onto a standard Mo substrate.

Finally, the impact of the TCO back-contact on the contact resistance and on the cell performances is investigated. The semi-transparent cells on TCO back-contact were first characterized without light reflection at the rear side of the glass for a clear comparison with the Mo back-contact. Then, different reflectors were placed at the rear-side to enhance light absorption in the CIGS absorber.

3.2. Replacing the Mo back-contact by a transparent conducting oxide

3.2.1. Choice of the back-contact

To select an alternative back-contact it is important to determine what are the requirements for back-contact in ultra-thin CIGS cells. We will only focus our study on the substrate configuration, where the CIGS is deposited on the rear-contact (the hole collector). Standard cells on Mo back-contact have the same configuration.

The requirements for a satisfying back-contact in the case of substrate configuration ultra-thin CIGS solar cells are:

1. A sufficient conductivity,
2. A sufficient reflectivity,
3. An adhesion with the CIGS,
4. The non-degradation of the optical and electrical performances at high temperature under Se atmosphere,
5. Providing an ohmic contact and a hole collection,
6. Providing an electron barrier to reduce electron surface recombination,

In this study, the TCO materials were selected as back-contact in ultra-thin CIGS solar cells. A scheme of the investigated configuration is displayed in Fig. 3.1.

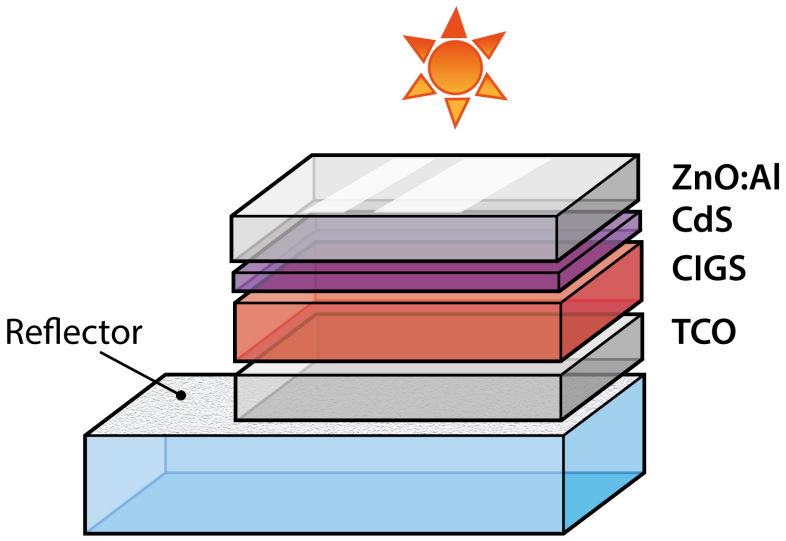

Figure 3.1.: Scheme on the CIGS on TCO based back-contact reflector configuration.

A TCO is a degenerated semi-conductor materials which has a high p- or n- doping and high band-gap. The doping content ensures the conductivity (**requirement no.**

1) and the large band-gap ensures a good transparency in the visible range. The **requirement no. 2** would be permitted by adding a reflective material behind the TCO: a metallic mirror (specular reflection) or a white-paint (Lambertien reflection, *i.e.* isotope scattering without loss). The requirements no. 1 and 2 will be discussed in section 2.2.3 and 2.2.4 with the support of optical and electrical simulations.

The **requirements no. 3 to 6** will be discussed at the light of the previous studies in the literature and experimentally in the following sections.

3.2.2. State of the art

The deposition of a CIGS absorber on a TCO has been extensively studied for diverse applications such as tandem solar cell as a top cell [151, 152, 153], bifacial devices [93] or solar windows [154, 155].

Some well known TCOs are already commonly used in industry, such as tin doped indium oxide (In_2O_3:Sn or ITO), fluorine doped tin oxide (SnO_2:F) or aluminium doped zinc oxide (ZnO:Al). Those n-type TCOs have a decent transparency in the visible and near infra-red range and have a low resistivity. The optical and electrical properties depend on the fabrication process of the TCOs.

Tab. 3.1 presents some general statements and the usual deposition technique of ITO, SnO_2:F and ZnO:Al. ITO generally shows the best performances in terms of transparency and conductivity but is both costly and indium consuming. SnO_2:F and ZnO:Al can be suitable alternatives. SnO_2:F is also known for its durability (temperature and chemical stability).

In our case, a reflector has to be inserted in the structure, ideally between the glass and the TCO back-contact. Both ITO and SnO_2:F require to be deposited at high deposition temperature or to be annealed to reach decent optical and electrical properties. Too high temperature may impact the stability of the reflector if this one is was deposited in a previous step. On the opposite, ZnO:Al can be deposited by magnetron sputtering at room temperature.

Table 3.1.: Selection of transparent conducting oxides.

	General remarks [156]	Deposition technique	Temperature of deposition / annealing
In_2O_3:Sn (ITO)	High cost high conductivity In consumption	Spay pyrolysis Sputtering	>300 [157]
SnO_2:F	Low cost Chemical stability	Spay pyrolysis Sputtering	>300 [157]
ZnO:Al	Low cost Low durability	Sputtering	room temperature but annealing improves properties [158]

When the CIGS is grown on a TCO, different configurations can be studied:

- Substrate configuration: the CIGS is deposited on the semi-transparent Glass/TCO substrate. The TCO/CIGS interface is the p-contact of the cell and has to be ohmic. The cell is completed by a standard CdS / ZnO / ZnO:Al front-window and can be illuminated from the front or from the rear side. A reflector can be added at front or at the rear side to increase the light absorption in the CIGS layer.
- Superstrate configuration: the CIGS is deposited on the semi-transparent Glass/TCO/buffer substrate. The TCO/buffer/CIGS interface is the n-contact and has to be rectifying. As the CdS or Zn(O,S) cannot be used due to their undesirable diffusion into the CIGS at high temperature [159], the buffer is usually an intrinsic ZnO layer. The TCO is usually ZnO:Al. The cell is completed by a hole-collector back-contact that can be transparent or reflective [160].

An overview of the major results in the literature related to the CIGS deposition on ITO, SnO_2:F and ZnO:Al is summarized in Tab. 3.2. This list is not exhaustive, in particular for the cells in superstate configuration. For each study, are mentioned the CIGS deposition process (CIGS thickness, 1- or 3-stage process, maximum substrate temperature), the main highlights (compounds formation, TCO degradation or process optimization), and the best cell efficiency achieved. Overall, it is important to note that, with a suitable process, the efficiency of the cells on ITO, SnO_2:F and ZnO:Al back-contact matches that of standard cells.

In the following, we examine our requirement list for a satisfying back-contact.

Requirement no. 3 About the adhesion of the CIGS on the TCO:

No delamination were reported on ITO, SnO_2:F and ZnO:Al.

Requirement no. 4 About non-degradation of the performances at high temperature under Se atmosphere:

During the CIGS deposition, the SnO_2:F temperature has to remain below 500°C: luorine is likely to diffuse into the CIGS above 500°C leading to an increase of the SnO_2:F resistivity [55]. For ITO, the maximum substrate temperature is 520°C [55]. For ZnO:Al, if the layer is not placed in an oxidizing environment, temperature up to 600°C can by applied [158]. However, due to the unstability of the ZnO:Al/CIGS interface, substrate temperature should not exceed 500°C [55].

Requirement no. 5 About the formation of an ohmic contact:

It has been shown that when the CIGS is grown directly on SnO_2:F, an ohmic contact is achieved [55, 93, 153]. However, the series resistances of the cells are slightly higher than the reference cells on Mo substrate.

On the contrary, cell performances in the substrate configuration are degraded when the CIGS is grown directly on ITO [55, 151, 24, 90, 152] or ZnO:Al [55, 161, 162]. On one hand, a rectifying behavior is observed due to the formation of a

pn-junction between the n-type TCO and the p-type CIGS. This behavior is required for the superstrate cell on ZnO:Al-contact/ZnO-buffer [55, 163, 164]. On the other hand, a high contact resistance is observed due to the formation of a thin resistive GaO_x layer (possibly Ga_2O_3, thinner than 50 nm) at the CIGS/ITO interface [55, 90, 152] and at the CIGS/ZnO interface [55, 162, 164]. The GaO_x phase is generally n-doped, acts as a blocking layer and therefore degrades the performance of the cell. It was observed that the GaO_x formation can be inhibited and an ohmic contact behavior can be achieved if a thin interfacial layer is deposited at the surface of the TCO: 5-15 nm of Mo on ITO [24]or on ZnO:Al [55, 161, 165] that reacts in $MoSe_2$ during the process, or 10 nm of MoO_3 on ITO [90]. Some authors have also shown that the GaO_x formation can also be inhibited if the process starts without introduction of Ga, but in return, this leads to the formation of an InO_x phase [162].

Requirement no. 5 About the recombination at the back-contact:

The TCO/CIGS interface was demonstrated to exhibit a high surface recombination velocity: at the SnO_2:F/CIGS interface [93] or the ZnO:Al/$MoSe_2$/CIGS interface [166]. W. Ohm *et al.* [93] developed a passivation of the SnO_2:F/CIGS back-interface using of a porous Al_2O_3 layer. In this case, a cell efficiency higher than the reference cell on Mo back-contact was achieved for a cell with 700-nm-thick CIGS (10.1% instead of 8.8%).

Na incorporation in the CIGS layer.

It has been reported that the ITO, SnO_2:F and ZnO:Al hinder the Na diffusion from the soda-lime glass [167, 55]. As the absence of Na is detrimental for the CIGS cell (low doping concentration or high defect density), the Na has to be supplied by an external source. Na can be added as NaF precursor on the TCO layer or during a NaF post-deposition treatment to improve the cell efficiency (for ITO: [153, 93], for ZnO:Al: [55, 161, 165]).

According to the literature, it is possible to fabricate CIGS solar cells on TCO back-contact. The potential of such back-contact is now investigated.

	References	CIGS process	Highlight	Best cell efficiency
In_2O_3:Sn (ITO)	**Nakada *et al.* [55, 168]**	2 µm, 3-stage, 450-550°C	>520°C: high resistance contact Interfacial $MoSe_2$ layer: low resistance ohmic contact	15.2%
	Nishiwaki *et al.* (2003) [151]	$CGSe^b$ Baseline Shell Solar	High resistance (poor contact or ITO degradation)	4.3%
	Abou-Ras *et al.* (2005) [24]	thick, 3-stage, 450°C	High resistance contact Interfacial $MoSe_2$ layer: low resistance ohmic contact	11.8%
	Simshi *et al*, Larsen *et al.* (2014) [89, 90]	2 µm, 1-stage, 550°C	High resistance contact Evidence of a of Ga_2O_3 phase formation Interfacial MoO_3 layer: low resistance ohmic contact	11.9%
	Choi *et al.* (2015) [152]	CGS^b, 3 stage, 550°C	High resistance contact Evidence of a of Ga_2O_3 phase formation	5%
SnO_2:F	**Young *et al.* (2002) [169]**	2 µm, 3-stage, 600°C	Rectifying behavior	2.5%
	Haug *et al.* (2002) [167]	thick, 550°C	Inhibition of diffusion of Na	
	Nakada *et al.* (2004) [55, 168]	2 µm, 3-stage, 450-550°C	< 500°C low resistance ohmic contact >500°C removal of fluorine: high resistance contact	13.7%
	Caballero *et al.* (2016) [153]	CGS^b, 3 stage, 500-520°C NaF precursor	>510°C: increase of the SnO_2:F resistivity 500°C: slightly higher series resistance than Mo substrate	4.2%
	Ohm *et al.* (2015) [93]	0.6-0.7 µm, 3 stage, 425°C NaF PDT^a	Ohmic contact Interfacial porous Al_2O_3 layer passivates Interfacial $MoSe_2$ layer slightly passivates	10.1%
ZnO:Al	**Terheggen *et al.* (2002) [162]**	3 µm, 550°C	Rectifying contact Evidence of a of Ga_2O_3 phase formation : electron barrier Ga-free initial process leads to In oxidation	FF∼60%
	Haug *et al.* (2002) [167, 163]	Thick, 550°C **Superstrate config. (ZnO buffer)**	Inhibition of diffusion of Na Addition of Na by evaporation	11.2 %
	Nakada *et al.* (2004) [55]	2 µm 3-stage 450-550°C	Resistive contact Evidence of a of Ga_2O_3 phase formation	0.04%
		2 µm, 3-stage, 550°C **Superstrate config. (ZnO buffer)**	Rectifying behavior Na_2S evaporation: optimum quantity of Na	12.8%
	Rostan *et al.* (2005) [161] **Mattheis *et al.* (2007) [166]**	1.8 µm, 3-stage, T_{SUB} not given 5-15 nm NaF precursor	Rectifying contact Interfacial $MoSe_2$ layer: low resistance ohmic contact Role of Na in p-doping and $MoSe_2$ formation High recombination velocity at the back contact	13.4%
	Seyrling *et al.* (2009) [165]	1.8 µm, 3-stage, 450°C NaF precursor	Use of an interfacial $MoSe_2$ layer	13.5%
	Heinemann et al. (2015) [164]	2 µm, 3-stage, 550°C, NaF PDT^a **Superstrate config. (ZnO buffer)**	Rectifying behavior NaF PDT enhances GaO_x formation NaF PDT increases acceptor states in GaO_x	11.4%

Table 3.2.: State of the art on CIGS deposited in ITO, SnO_2:F and ZnO:Al. ^{a}: PDT = Post-Deposition Treatment. ^{b}: CGS=$CuGaSe_2$.

3.2.3. Photocurrent calculation

In this section, we have simulated the impact of a structure TCO/reflector on the device photocurrent.

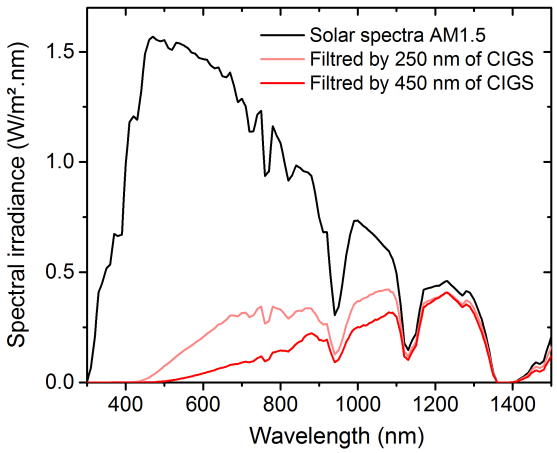

(a) Simulated irradiance transmitted after a ZnO:Al(360nm) / ZnO(60nm) / CdS(45nm) / CIGS stack.

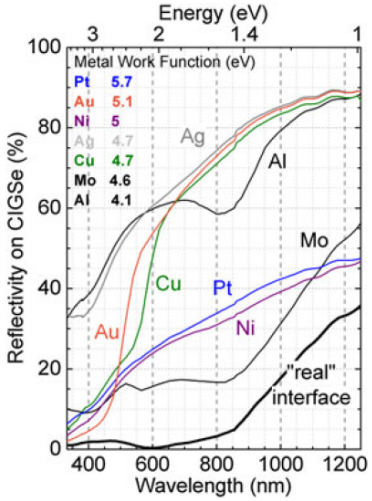

(b) Reflectivity of different metals at the CIGS/metal calculated with Fresnel's equation. The corresponding electron work functions are indicated on the top of the figure. From Z. Jehl *et al.* [79].

Figure 3.2.: Determination of the back-contact reflector: a) Spectral range transmitted through the CIGS cell and b) spectral range reflected by different metals.

The light that reach the back-contact is first filtered by the front-contact and by by the CIGS layer. For an clear comprehension, the spectral irradiance transmitted trough a ZnO:Al(360nm) / ZnO(60nm) / CdS(45nm) / CIGS stack was calculated by RTM for CIGS thicknesses of 250 nm and 450 nm. According to the result of the simulation shown in 3.2a, wavelengths above 600 nm are mainly transmitted. Therefore, to be efficient, the back-contact has to reflect light above 600 nm. The reflectance calculated for various metallic films at the CIGS/metal interface is shown in 3.2b (from [79]). The most suitable reflectors are Ag, Cu and Au. Some oxide/metal combination can lead to higher reflectance such as MoO_{3-x}/Ag [160]. But the CIGS cannot be grown directly of such materials. This is why, a TCO layer is used.

To evaluate the impact of the reflectivity of the TCO back-contact on the J_{SC}, we have calculated the cell photocurrent by RTM. Cells on Mo back-contact are compared to 3 alternative back-contacts:

- a TCO (ZnO:Al, 500 nm) coupled with a planar reflector (Au, 500 nm);

- a TCO (ZnO:Al, 500 nm) coupled with a Lambertien reflector;
- a Lambertien reflector directly in contact with the CIGS. This system is not realistic because it does not permit the charge collection. However some solutions could be implemented, like for example, a metallic grid between the white paint and the CIGS.

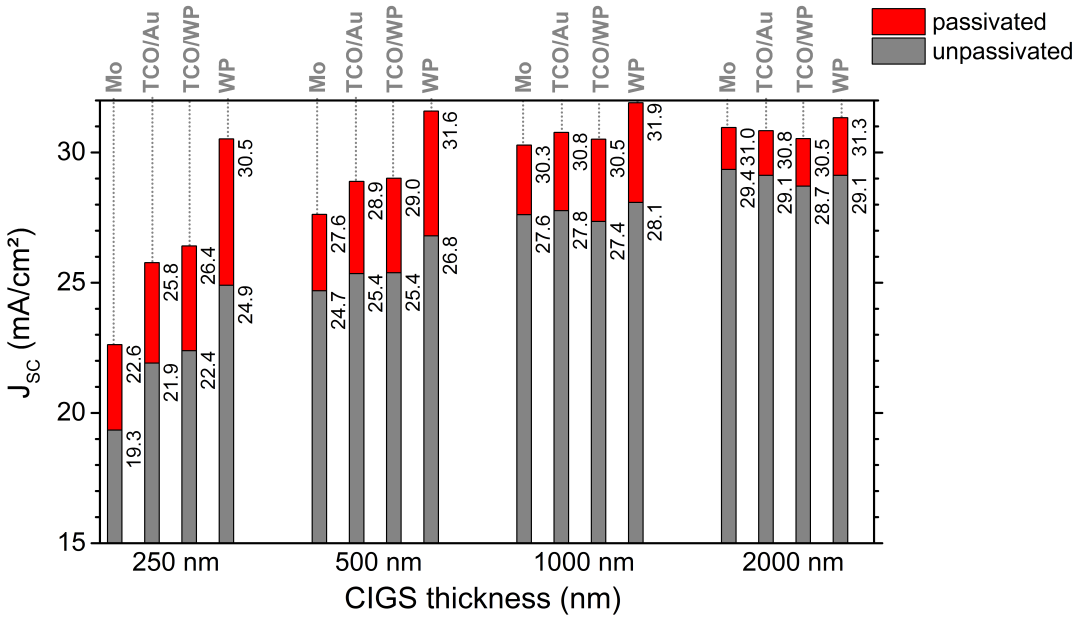

Figure 3.3.: Simulated J_{SC} for CIGS at various thicknesses and for 4 different back-contacts: Mo, 500-nm-ZnO:Al/Au (TCO/Au), 500-nm-ZnO:Al/white-paint (TCO/WP) and CIGS directly in contact with the white-paint (WP).

These simulations were made for a CIGS thickness varying between 250 and 2000 nm.

In addition, the back-contact recombination was taken into account by correcting the simulated EQE with a collection function (see Eq. F.1 and 3.7). The parameters used for the simulation are:

- electron diffusion length: $L_n = 2$ µm,
- electron diffusion coefficient: $D_n = 10^2$ m^2/s,
- back-contact electron recombination velocity: $S_{n,BC} = 10^7$ cm/s (case without passivation) and 10^1 cm/s (case with passivation),
- space charge region width: $w = 300$ nm (for 1000 and 2000-nm-thick CIGS), $w = 250$ nm (for 500-nm-thick CIGS) and $w = 150$ nm (for 250-nm-thick CIGS),
- correction factor for non-ideal SCR collection: $h = 0.95$.

The result of the simulations is presented in Fig. 3.3. The J_{SC} plot bars are gray for non-passivated back-interface and are red for passivated back-interface.

We observe in Fig. 3.3 that the Lambertien reflector on the CIGS layer theoretically leads to the best light trapping effect with hardly any optical loss for ultra-thin CIGS.

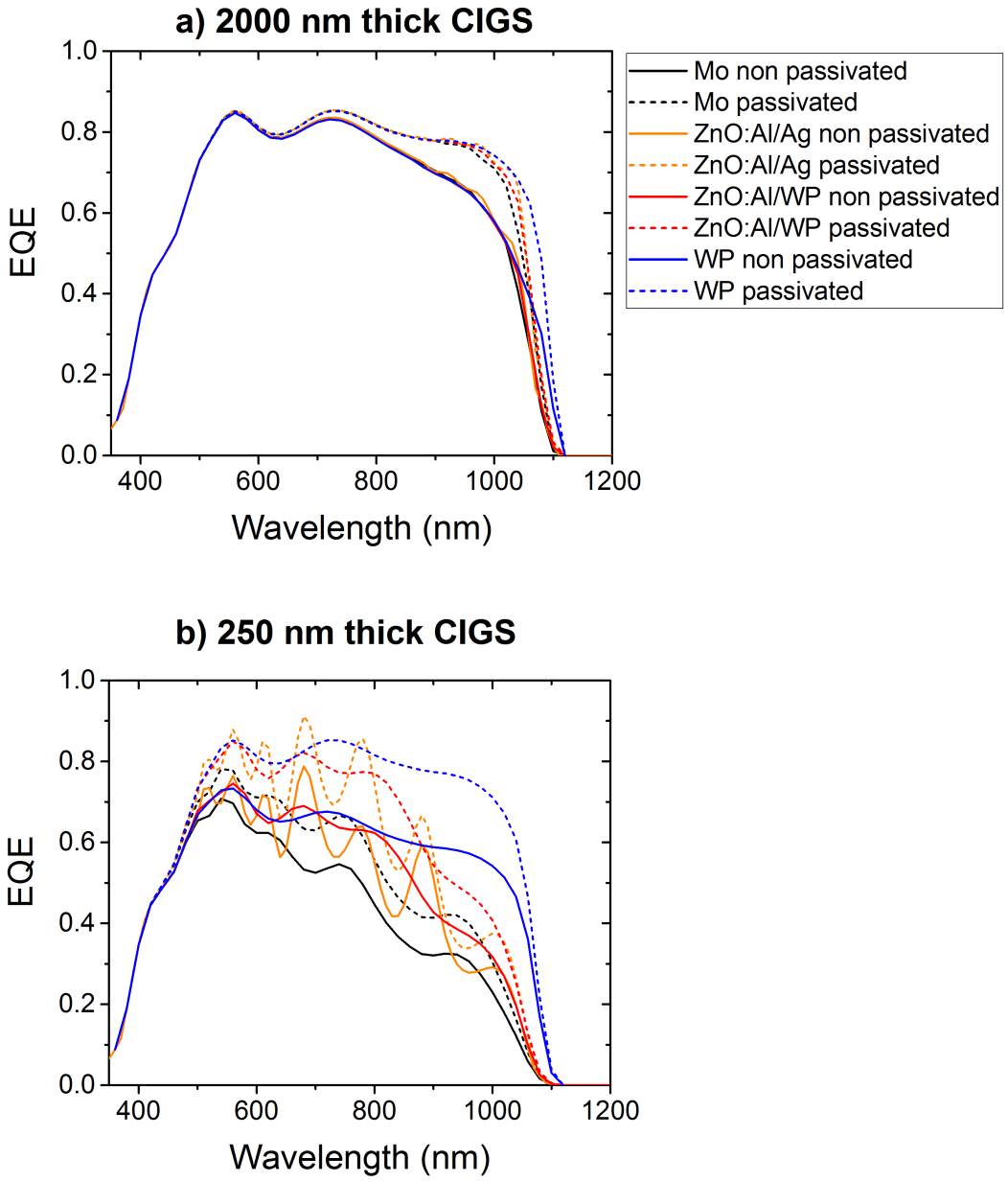

Figure 3.4.: Simulation of the EQE for a) 2000-nm-thick CIGS and b) 250-nm-thick CIGS on different back-contacts. The charge collection was calculated according to Eq. F.1 with $L_n = 2$ µm, $D_n = 10^2$ m²/s, $w = 300$ nm and 150 nm for respectively 2000 nm and 250-nm-thick CIGS, $h = 0.95$ and $S_{n,BC} = 10^7$ cm/s (non passivated, solid line) and 10^1 cm/s (passivated, dotted line).

This configuration approaches the Yablonovitch limit where the optical path length is increased by a factor of $4n^2$ compared to the flat surface [170] (n is the refractive index of the CIGS, in the limit of weak absorption). With $n = 3$ for the CIGS, the optical path length of wavelength close to the band-gap is increased by a factor of 36, leading to a perfect light absorption even for CIGS thicknesses down to 100 nm. However, as this absorption is enhanced close to the back-contact, the photocurrent is dramatically reduced if the interface is not passivated: for a 250-nm-thick CIGS the J_{SC} is reduced from 30.5 mA/cm² with passivation to 24.9 mA/cm² unpassivated. The comparison between EQE of the passivated and non-passivated Lambertien reflector (Fig. 3.4) shows that all wavelengths are impacted.

As observed in Fig. 3.3, for the non-passivated cells, the TCO/Au back-contact increases the J_{SC} compared to the Mo back-contact only for CIGS thicknesses below 500 nm (+2.6 mA/cm² for 250-nm-thick CIGS, +0.7 mA/cm² for 500-nm-thick CIGS). The impact of the reflector is more pronounced for thinner CIGS. The J_{SC} increase is only slightly higher if a white-paint is used (+3.1 mA/cm² for 250-nm-thick CIGS). The refractive index of the TCO ($n = 1.9$) is actually lower than the refractive index of the CIGS ($n = 3$). The TCO/CIGS interface narrows the acceptance angle for a light-trapping effect and weakens the benefits of the Lambertien reflector.

The passivation of the TCO/Au back-contact increases the beneficial effect of the reflective back-contact compared to the non-passivated Mo (+6.5 mA/cm² for 250-nm-thick CIGS).

The EQE curves for the 250- and 2000-nm-thick CIGS are shown in Fig. 3.4. For the 2000-nm-thick CIGS, the back-contact reflectivity has hardly any impact on the EQE curves. On the opposite, the beneficial impact of the different TCO/reflectors is correlated to the increase in J_{SC}. The CIGS interference shapes in EQE for TCO/Au back-contact are due to the flat interfaces in the model.

3.2.4. Impact of the TCO resistivity on the cell performance

When a reflector is placed behind the TCO, the choice of the TCO thickness is a balance between its transparency and its conductivity. The transparency of the TCO impacts the J_{SC} of the cell. The calculations of the J_{SC} as a function of the TCO thickness can be carried out by RTM. The resistivity of the TCO impacts the series resistance of the cell and therefore impacts the FF. The resistivity ρ of a layer is calculated according to Eq. 3.1:

$$\rho = R_{sheet} \cdot t \tag{3.1}$$

where R_{sheet} is the sheet resistance measured by 4-point probe, and t the thickness of the layer.

The resistance of a material with a section S and a length L is given by Eq. 3.2:

$$R = \rho \cdot \frac{L}{S} \tag{3.2}$$

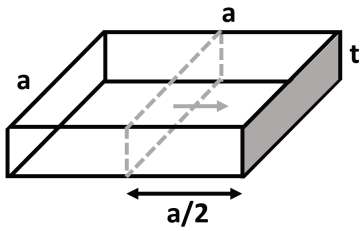

Figure 3.5.: Schematics of the current flux in the TCO layer of a thickness t in a cell of square length a .

Considering a square cell of length a, with a thickness t of TCO (see schematics in Fig. 3.5) and where charges are collected across one edge of the cell, we have: $L = a/2$ and $S = a \cdot t$. Eq. 3.2 leads to Eq. 3.3:

$$R(t) = \rho \cdot \frac{1}{2 \cdot t} \tag{3.3}$$

FF was calculated by varying the $R(t)$ as series resistance in SCAPS simulation using the model described in sec. 2.2.4.1.

Finally, assuming a V_{OC} of 600 mV on Mo substrate, the cell efficiency can be estimated from the J_{SC} and FF calculated for each TCO thickness. This efficiency was compared to the efficiency of a cell with the same CIGS thickness on Mo back-contact:

$$\Delta\text{Efficiency} = J_{SC}^{TCO}(t) \cdot FF^{TCO}(t) \cdot \left[V_{OC}^{Mo} + 1.5 \cdot \frac{kT}{q} \cdot \ln\left(\frac{J_{SC}^{TCO}(t)}{J_{SC}^{Mo}} \right) \right] - J_{SC}^{Mo} \cdot FF^{Mo} \cdot V_{OC}^{Mo} \tag{3.4}$$

The J_{SC} and the FF were calculated for TCO/Ag back-contact with TCO thicknesses between 50 nm and 2000 nm and for CIGS thicknesses of 500 nm and 250 nm. We used a resistivity of 1.10^{-3} Ω.cm, 1.10^{-4} Ω.cm and 0 Ω.cm. The TCO is assumed to have unvariant absorption coefficient to simulate different TCO qualities. It was modeled with the optical parameter of the ZnO:Al. The case 0 Ω.cm refers to the case where the Ag reflector is able to collect charges.

For each configuration, the efficiency variation as a function of the TCO thickness is displayed in Fig. 3.6. The interference shapes are due to the flat interfaces in the RTM simulation.

As observed in Fig. 3.6a, for a **500-nm-thick CIGS**, without TCO resistance, the cell efficiency of the cell on TCO/Ag is inversely proportional to the TCO thickness: from +1.25% abs. (+2.6 mA/cm²) compared to the cell on Mo for a 50-nm-thick TCO to +0.35% abs. (+0.8 mA/cm²) for a 2000-nm-thick TCO. This effect is due to the absorption of the TCO in the near-IR spectral range. For higher TCO resistivity, the cell efficiency decreases, in particular for thin TCO, due to the increase in series resistance. As a consequence, for a TCO resistivity of 10^{-4} Ω.cm, an optimum cell efficiency is found for a 400-nm-thick TCO back-contact that increases the cell efficiency by 0.7% abs. compared to the one on Mo. For a TCO resistivity of 10^{-3} Ω.cm, the configuration leads to hardly any benefit compared to the cell on Mo.

As observed in Fig. 3.6b, the **250-nm-thick CIGS** has the same tendency than the 500-nm-thick CIGS but with a better cell improvement. Without TCO resistance, the gain in efficiency is +2.3% abs. (+4.4 mA/cm²) for a 50-nm-thick TCO compared to the cell on Mo. It decreases to +1.1% abs. (+2.2 mA/cm²) for a 2000-nm-thick TCO. For higher TCO resistivity, the best efficiency is found for an optimum TCO thickness. For a TCO resistivity 10^{-4} Ω.cm, the optimum TCO thicknesses are 200 or 400 nm (+1.6% abs. of efficiency compared to the cell on Mo). For a TCO resistivity 10^{-3} Ω.cm, the optimum TCO thickness is 800 nm (+1.1% abs. of efficiency compared to the cell on Mo).

To conclude, in comparison to Mo, the benefit of a TCO/reflector back contact depends on its configuration:

1. **If the reflector is electrically separated from the TCO back-contact**: an increase in the cell efficiency of 1.6% abs. is expected for a 250-nm-thick CIGS with a TCO thicknesses of 200 or 400 nm (high quality TCO with a resistivity of 10^{-4}Ω.cm). A sufficient TCO back-contact thickness is required to allow a suitable lateral charge conduction.
2. **If the reflector participates to the lateral conduction**: an increase in the cell efficiency of 2.3% abs. is expected for a 250-nm-thick CIGS with a TCO thickness of 50 nm. The reflector needs to be chemically and mechanically stable at high temperature.

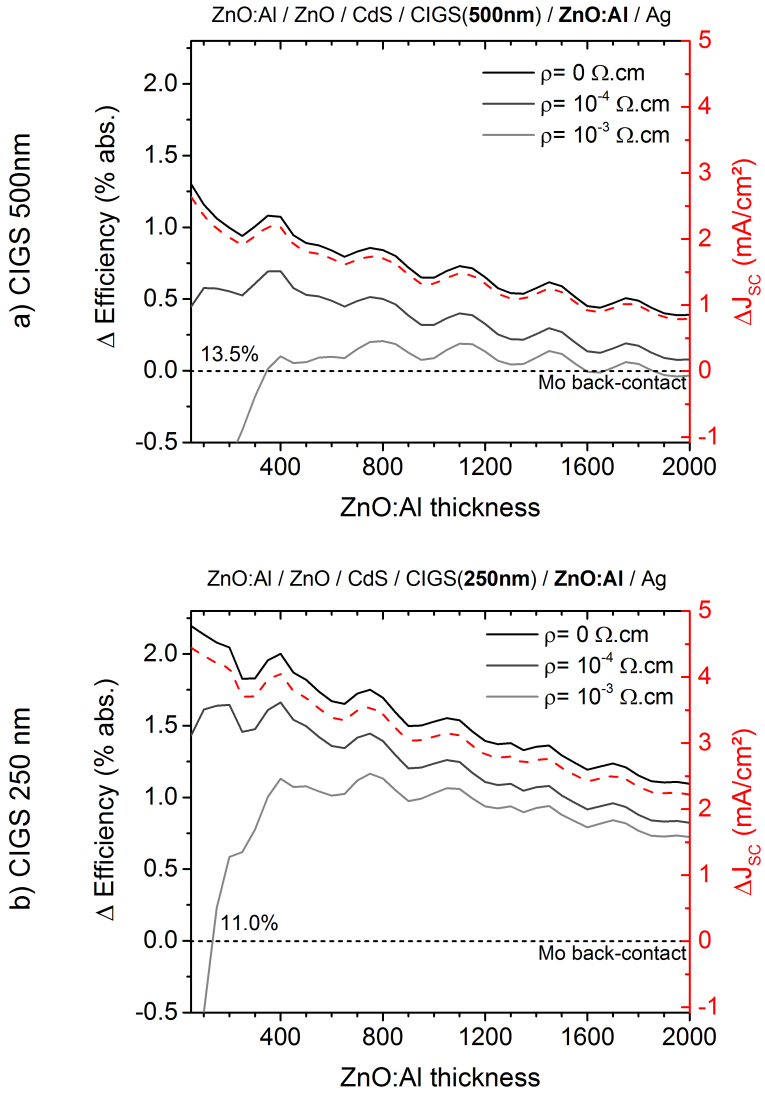

Figure 3.6.: Cell efficiency of a a) 500-nm-thick CIGS and b) 250-nm-thick CIGS on TCO/Ag back-contact as a function of the thickness and the resistivity ρ of the TCO layer compared to a cell on Mo with the same CIGS thickness.

3.2.5. TCO/CIGS band-alignment

In the substrate configuration, the back-contact must be ohmic with a low resistance.

However, a contact between the p-type CIGS and the n-type TCOs can possibly create a pn-junction. For example, a rectifying contact between CIGS and ZnO:Al has been observed when the ZnO:Al is deposited on the CIGS [171] or when the CIGS is deposited on the ZnO/ZnO:Al in the superstrate configuration [55, 163, 164].

Two cases can lead to the ohmicity of the contact:

Ohmic contact by band alignment: if the electron affinity of the TCO is higher than the electron affinity of CIGS. Fig. 3.7 displays the band-diagrams between CIGS and SnO_2:F or ZnO:Al. The electron affinity of SnO_2:F is 5.0 eV which could be sufficiently high to create an ohmic contact with CIGS. On the contrary, the electron affinity of ZnO:Al (4.5 eV) is close to the electron affinity of CIGS and could lead to a rectifying contact. However, experimental, the interfaces does not necessarily follow this rule and mainly depends on the chemical surface reconstruction of the TCO and the CIGS layers.

Ohmic contact by high doping: by a tunneling conduction. A tunneling effect is theoretically possible if a thin p^+-type materials is inserted between the TCO and the CIGS. CuO_x or $CuGaO_x$ can be some potential materials to achieved such contact [6].

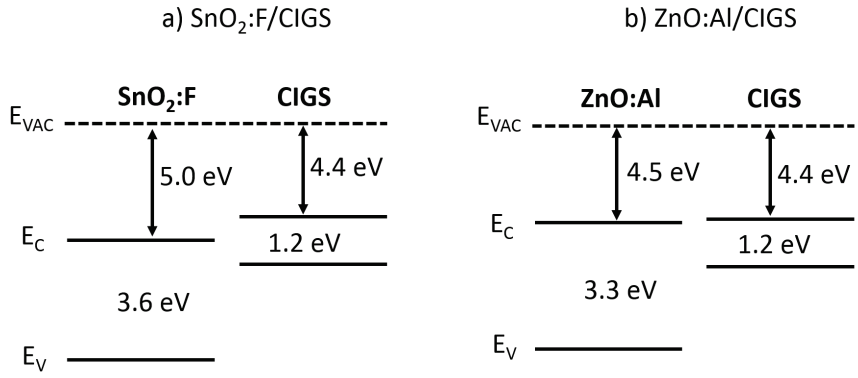

Figure 3.7.: Energy level in the TCO/CIGS contacts before equilibrium.

3.2.6. Conclusion

To improve the photocurrent of ultra-thin CIGS solar cells, we decided to evaluate a TCO back-contact coupled with a reflector as back-contact. Based on simulations, in the best case, an improvement of 1.6 to 2.0% abs. in the cell efficiency is expected with a 250-nm-thick CIGS compared to the cell on Mo. To achieve this result, the TCO is should be conductive enough ($\rho < 10^{-4}$ Ω.cm) and with a neglectible

TCO/CIGS contact resistance. Even if this increase seems low, this configuration is simple to fabricate. Moreover, there are still room for improvements.

Two different TCOs were chosen: SnO_2:F and ZnO:Al. They are both low cost and, unlike ITO, they do not consume indium. Moreover, based on literature it is possible to achieve a low resistance ohmic contact when the CIGS is directly grown on SnO_2:F. Concerning ZnO:Al, it was observed that the interface is not chemically stable and generally requires an interfacial layer to create an ohmic contact with CIGS. In the following section, we will detail the characteristics of the SnO_2:F and ZnO:Al back-contact used.

3.3. Characterization of the TCOs as back-contact

The CIGS absorbers were deposited on two different TCOs: SnO_2:F and ZnO:Al. The high temperature of the CIGS process may change the properties of the TCO. This is why, we first studied the chemical, electrical and optical behaviors of the SnO_2:F and ZnO:Al layers on glass.

3.3.1. Experimental details

The ZnO:Al as back contact was grown on a 3-mm-thick soda-lime glass following the same procedure than the ZnO:Al used for the front contact. The layer was deposited by radio-frequency (RF) sputtering using a ZnO with 2%wt Al_2O_3 ceramic target under argon plasma and O_2 flux and at a RF power density of $3W/cm^2$. We compared two thicknesses of ZnO:Al: 350 and 1200 nm.

The SnO_2:F substrate is a commercially available product from *Solems*. The SnO_2:F layer was deposited by spay pyrolysis on a 2-mm-thick soda-lime glass. Its thickness is 600-700 nm with a roughness of ± 40 nm.

3.3.2. Electrical characterization

The sheet resistance of the samples was measured by 4-point probe. We measured 17 Ω_{square} for 1200-nm-thick ZnO:Al (resistivity of $6.0 \cdot 10^{-4}$ Ω.cm), 4.5 Ω_{square} for 350-nm-thick ZnO:Al ($5.4 \cdot 10^{-4}$ Ω.cm) and 7 Ω_{square} for 650-nm-thick SnO_2:F ($4.0 \cdot 10^{-4}$ Ω.cm).

3.3.3. Optical characterization

The absorption spectra of the 650-nm-thick SnO_2:F, the 350-nm-thick ZnO:Al and the 1200-nm-thick ZnO:Al were first analyzed.

The total transmission (T) and reflection (R) were measured by optical spectroscopy using an integration sphere to take into account the diffuse light. In order to compare the optical properties of the layers with different thicknesses, the comparison of the absorption coefficient was preferred. The absorption coefficient α can be approached with the Eq. 3.5:

$$\alpha = -\frac{1}{d} \cdot \ln\left(\frac{T}{1-R}\right) \tag{3.5}$$

where d is the thickness of the TCO.

The absorption coefficient of the ZnO:Al and SnO_2:F is displayed Fig. 3.8. The absorption coefficient can be decomposed in 3 parts that are clearly observed Fig. 3.8:

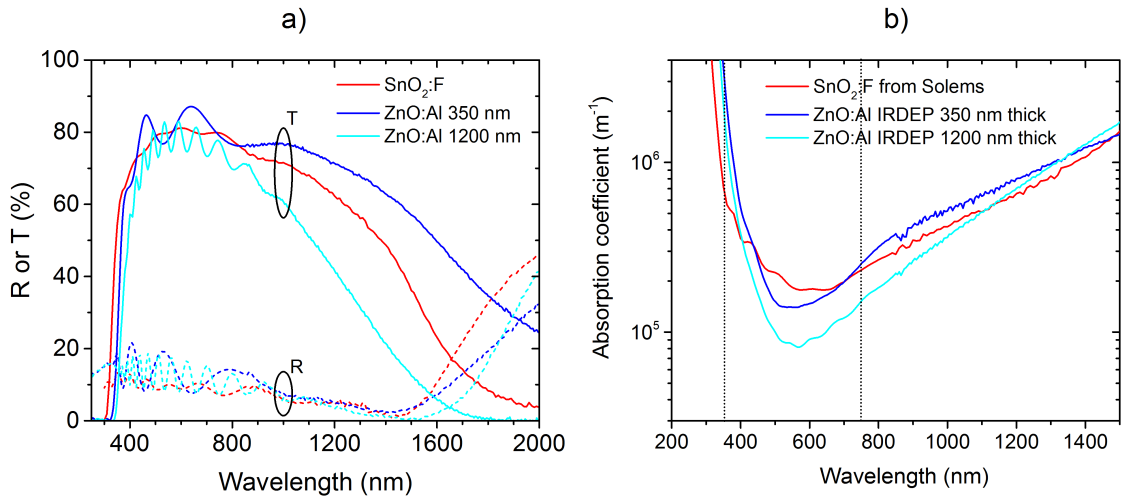

Figure 3.8.: Optical characterization of the TCOs: a) reflectance and transmittance and b) Absorption coefficient calculated according to Eq. 3.5.

$\lambda < 350$ nm High absorption coefficient: corresponding to the absorption edge of the band-gap of the TCO (approximately 3.4 eV for ZnO:Al and 3.6 eV for SnO_2:F);

$350 < \lambda < 750$ nm Low absorption coefficient in the visible range;

$\lambda > 750$ nm Increase in the absorption coefficient due to the free-carrier absorption. The free-carriers are responsible for the conductivity of the TCO and their influence on the optical properties can be simply described by the Drude model. Assuming that the valence electrons are independent to their ions and neglecting the eletron-electron interaction (ideal electron gas) the dielectric function of the material can be expressed as :

$$\varepsilon(\omega) = 1 - \frac{n \cdot e^2}{\epsilon_0 \cdot m \cdot \omega^2}$$

where ϵ is the dielectric function ($\sqrt{\varepsilon} = n + i \cdot k$ with (n,k) the optical indexes), n the electron density, ω the frequency ($\omega = 2\pi/\lambda$), e the electron charge, m the electron mass and ϵ_0 the electric constant. For frequency above a resonance frequency ω_p, called plasma frequency $\omega_p = \sqrt{(n \cdot e^2)/(\epsilon_0 \cdot m)}$, $\varepsilon(\omega)$ becomes negative leading to a strictly positive index k. Therefore the absorption coefficient ($\alpha = 4\pi/k$) increases for high wavelength. A plasma frequency of 1100 nm was calculated for SnO_2:F.

As observed in Fig. 3.8, at 550 nm, an absorption coefficient of 9.10^4 - 1.10^5 m^{-1} was measured for a 1200-nm-thick ZnO:Al and an absorption coefficient of 1.4 $.10^5$ m^{-1} was measured for 350-nm-thick ZnO:Al. This difference can be due to various reasons such as an evolution of the ZnO:Al properties with the deposition time due

to a slight temperature annealing. The SnO_2:F layer is more absorbent in the visible range ($\alpha = 2.10^5$ m^{-1}) than the ZnO:Al.

According to the solar spectrum filtered by a 250 nm of CIGS (see 3.2a for a CIGS band-gap of 1.2 eV) and the EQE of a solar cell (see Fig. 3.4), the back-contact absorption has to be minimized in the spectral range from 600 nm to 1030 nm while keeping a sufficient conductivity. To quantitatively evaluate the TCO performance, the electrical conductivity ($1/\rho$) is divided by the absorption coefficient at 900 nm (α(900 nm)). This value is also called Figure of Merit of the TCO [156]. The higher the figure of merit, the best performance the TCO.

$$\text{Figure of Merit} = \frac{1}{\alpha \cdot \rho}$$

Table 3.3.: Figure of merit of the different back-contacts.

	α(900 nm) cm^{-1}	ρ Ω.cm	Figure of merit Ω^{-1}
350-nm-thick ZnO:Al	$4.2 \cdot 10^3$	$6.0 \cdot 10^{-4}$	0.4
1200-nm-thick ZnO:Al	$2.6 \cdot 10^3$	$5.4 \cdot 10^{-4}$	0.7
650-nm-thick SnO_2:F	$3.5 \cdot 10^3$	$4.0 \cdot 10^{-4}$	0.7

In Tab. 3.3 we have reported the Figure of Merit of the samples. We can see that 650-nm-thick SnO_2:F and 1200-nm-thick ZnO:Al substrates have both the best figure of merit and are therefore selected for cell fabrication.

3.3.4. Chemical stability of the TCO at high temperature under selenium flux

The chemical, electrical and optical properties of the ZnO:Al and SnO_2:F layers can change during the CIGS process. Indeed, the CIGS is deposited at high temperature (500 to 550°C) under Se atmosphere.

In order to evaluated the evolution of the TCO parameters under similar conditions, the ZnO:Al and SnO_2:F layers were annealed at 500°C and 600°C under Se atmosphere in a graphite box. The Glass/1200-nm-thick ZnO:Al, Glass/1200-nm-thick and the Glass/650-nm-thick SnO_2:F substrate were placed with 50 mg of Se pellets in a 20 cm^3 graphite box inserted in a tubular furnace under atmospheric pressure of Ar. The box was heated at 500°C or 600°C with a linear heating ramp of 15 min, and the temperature was maintained for 20 min. Finally the box was naturally cooled down to reach 200°C in 1h.

Before and after annealing each sample was analyzed by XRD, its reflectance and transmittance was measured by optical spectroscopy and its resistivity by 4-point probe.

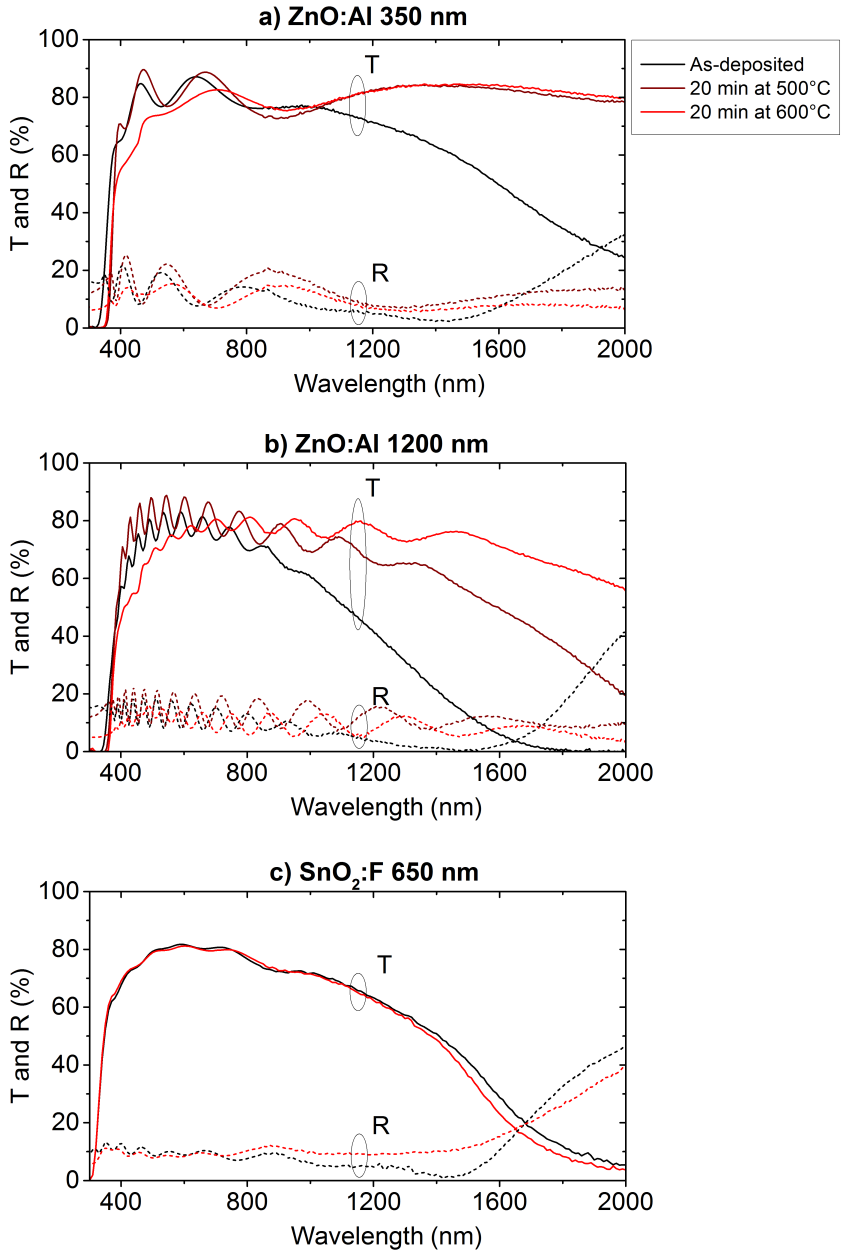

Figure 3.9.: Transmittance (solid line) and reflectance (dotted line) of the TCO substrates without annealing and annealed at 500°C and 600°C: a) 350-nm-thick ZnO:Al on glass, b) 1200-nm-thick ZnO:Al on glass and c) 650-nm-thick SnO_2:F on glass.

The reflectance and transmittance measured for each TCO substrate without annealing and annealed at 500 and 600°C are presented Fig. 3.9. The sheet resistance measurements are presented Fig. 3.10. According to Fig. 3.9a and Fig. 3.10, annealing of the 350-nm-thick ZnO:Al at both 500 and 600°C under Se atmosphere largely increases the transmittance in the near infra-red region and dramatically increases the sheet resistance. According to Fig. 3.9b and Fig. 3.10, annealing of the 1200-

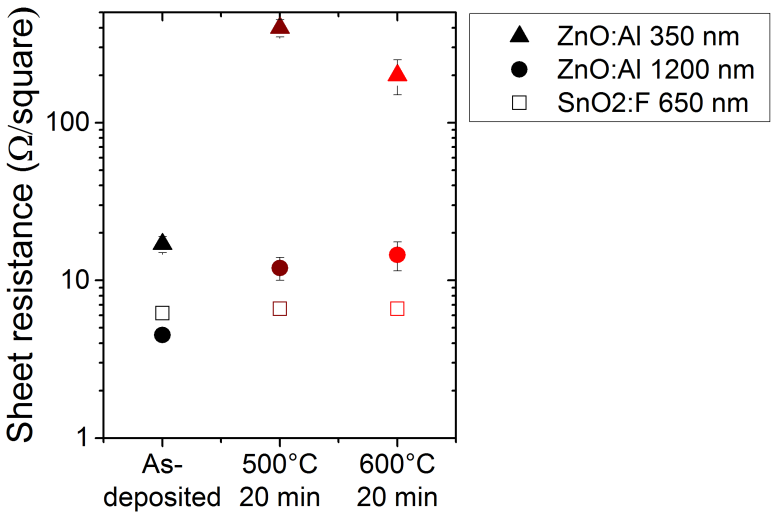

Figure 3.10.: Sheet resistance of the different TCO substrates without annealing and with an annealing at 500°C and 600°C.

nm-thick ZnO:Al at 600°C is also detrimental whereas annealing at 500°C only moderately increases the sheet resistance and transmittance. The opposite trends between the transmittance in near infra-red region and the sheet resistance is symptomatic of a loss of the doping concentration, according to the Drude model. It has been shown that annealing in air removes the oxygen vacancies in the ZnO:Al. Se element, in the same column than O in the periodic table, could have the same effect. The deterioration of the ZnO:Al is probably only a surface effect explaining why the 1200-nm-thick ZnO:Al is less affected by annealing.

Concerning the SnO_2:F substrate, annealing has no effect on the transmittance (Fig. 3.9c) and the resistivity (Fig. 3.10). Therefore the SnO_2:F layer is perfectly stable at high temperature.

During the deposition of the CIGS layer, the TCO can be not only in contact with Se but also with Cu(In,Ga)Se_2 phase and the associated ternaries and binaries. We should note that no evidence of ternaries and binaries formation was reported for short 1-stage process (see Fig. 2.6). The reactivity of the binaries and ternaries with the TCO is estimated by the calculation of the standard Gibbs free energy of the reaction (ΔG_f). If ΔG_f<0, the reaction is thermodynamically favored.

Tab. 3.4 summarizes the ΔG_f of different reactions potentially occurring at the interface between the TCO and the CIGS absorber. The thermodynamical stability of CIS and CGS were estimated by [172] and their stabilization energy ΔG_f are positive (approximately 50 and 25 kJ/mol, reaction A and B). Consequently, the CIGS decomposition is not allowed if any reaction with the constituent binaries (Cu_2Se, In_2Se_3, Ga_2Se_3) is thermodynamically not allowed.

For the ZnO:Al back-contact, the ΔG_f calculated for the reactions between ZnO and

	Reaction equation	Gibbs free energy at 500°C per mol of Mo, ZnO or SnO_2 ΔG_f (kJ/mol)
A	$CuInSe_2 = 0.5(Cu_2Se + In_2Se_3)$	*∼50* [1]
B	$CuGaSe_2 = 0.5(Cu_2Se + Ga_2Se_3)$	*∼25* [1]
C	$Mo+Se_2 = MoSe_2$	-153 [2]
D	$2ZnO+1.5Se_2(g) = 2\ ZnSe + SeO_2\ (g)$	-30 [2]
E	$In_2Se_3 + 3ZnO = In_2O_3 + 3ZnSe$	-21 [2]
F	$Ga_2Se_3 + 3ZnO = Ga_2O_3 + 3ZnSe$	-53 [2]
G	$Cu_2Se + ZnO = Cu_2O + ZnSe$	87 [2]
H	$CuSe + ZnO = CuO + ZnSe$	*63* [2]
I	$SnO_2 + 1.5Se_2(g) = SnSe_2 + SeO_2(g)$	176 [2]
J	$SnO_2 + Se_2(g) = SnSe(g) + SeO_2(g)$	286 [2]
K	$In_2Se_3 + 1.5SnO_2 = In_2O_3 + 1.5SnSe_2$	71 [2]
L	$Ga_2Se_3 + 1.5SnO_2 = Ga_2O_3 + 1.5SnSe_2$	7 [2]
M	$2Cu_2Se + SnO_2 = 2Cu_2O + SnSe_2$	287 [2]
N	$2CuSe + SnO_2 = 2CuO + SnSe_2$	241 [2]
	Decomposition reaction	
O	$2CuInSe_2 + 3ZnO = Cu_2Se + In_2O_3 + ZnSe$	12
P	$2CuGaSe_2 + 3ZnO = Cu_2Se + Ga_2O_3 + ZnSe$	-36

Table 3.4.: Gibbs free energy of the potential reactions at the CIGS/back-contact. Favored reaction are highlighted in green. [1]: from [172]. [2]: from HSC Chemistry 7.

Se (reaction D), In_2Se_3 (reaction E) and Ga_2Se_3 (reaction F) are negative. Therefore, ZnSe, In_2O_3 and Ga_2O_3 layers can be formed if In_2Se_3 and Ga_2Se_3 is formed at the beginning of the process. Moreover, the instability of the ZnO:Al/CIGS interface is increased by the favored decomposition reaction (reaction P) of the CGS phase to Ga_2O_3, ZnSe and Cu_2Se.

On the opposite, for the SnO_2:F back-contact, the ΔG_f calculated for the reactions between SnO_2 and Se, Cu_2Se, In_2Se_3 and Ga_2Se_3 (reaction I-N) are positive. The SnO_2:F would not react during the CIGS depostion.

In conclusion, the CIGS process is likely to impact the ZnO:Al layer performance leading not only to a reduction of the doping concentration but also to some thermodynamically favored reactions between CIGS and ZnO:Al. On the opposite, the SnO_2:F layer is perfectly stable up to 600°C. However, it is important to note that the kinetic of the reaction may be too long and that the coevaporation process is

not at thermodynamical equilibrium. Therefore, the experimental results can differ from the conclusions based on these calculations.

3.3.5. Impact of the TCO on the Na diffusion from glass substrate

To highlight the impact of the ZnO:Al and SnO_2 on the Na diffusion, the Na concentration in the CIGS layer was estimated by GD-OES.

500-nm-thick CIGS was coevaporated by a 1-stage process at 450°C on the following substrates:

- a commercial SnO_2:F substrate,
- a 1200-nm-thick ZnO:Al substrate,
- a standard Mo substrate,
- a Mo back-contact on a Al_2O_3-coated glass.

The standard Mo substrate allows the Na diffusion from the soda-lime glass to the CIGS through the Mo layer, while the Al_2O_3-coated glass hinders the Na diffusion. The CIGS surface was treated with a KCN solution before the GD-OES measurements. A qualitative amount of Na was estimated from the GD-OES profile. To compare the Na concentration in the different samples, the Na signal was divided by a reference element such as Cu.

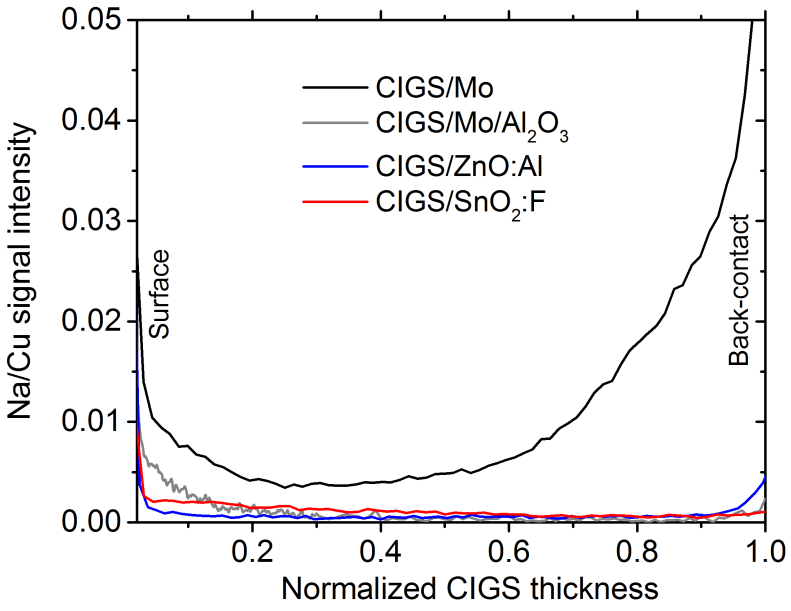

Figure 3.11.: Na/Cu signal intensity ratio from the GD-OES profile for CIGS grown on different back-contacts.

The Na/Cu signal intensity ratios measured in the CIGS layers for the 4 different back-contacts are reported in Fig. 3.11. We observe that the Na/Cu ratios for CIGS on SnO_2:F and ZnO:Al back-contact are closed to 0 and are comparable to the one for Mo/Al_2O_3 back-contact. Therefore, both SnO_2:F and ZnO:Al back-contact hinder the diffusion of Na.

3.3.6. Conclusion

A commercial 650-nm-thick SnO_2:F layer on glass, a sputtered 350-nm and 1200-nm-thick ZnO:Al layer were characterized before and after annealing. The following conclusions were deduced:

- The resistivity of the SnO_2:F and ZnO:Al substrates ranges between 4-6.10^{-4} Ω.cm. According to Fig. 3.6, the TCO thickness should be above 400 nm to avoid a detrimental series resistance. The 350-nm-thick ZnO:Al back-contact is therefore not suitable.
- The SnO_2:F and the 1200-nm-ZnO:Al substrates have the best Figure of Merit.
- The temperature has no impact on the SnO_2:F substrate up to 600°C, whereas the temperature should remain below 500°C for the 1200-nm-thick ZnO:Al.
- During the CIGS deposition, SnO_2:F substrate is the most stable: no reaction are thermodynamically favored between the CIGS phases and SnO_2. However, CIGS decomposition reaction is thermodynamically possible at the ZnO interface with the formation of a Ga_2O_3 phase.
- Both SnO_2:F and ZnO:Al layer hinder the Na diffusion from the glass to the CIGS leading to a lack of Na compared to the standard Mo substrate.

Based on these results, for the following experiments, the 1200-nm-thick ZnO:Al and the SnO_2:F commercial substrates were chosen. Even if the 1200-nm-thick ZnO:Al is not optimal from an optical point of view, its stability makes it easier for cell fabrication. In the following, the deposition of CIGS on SnO_2:F and on 1200-nm-thick ZnO:Al is optimized.

3.4. Optimization of the CIGS deposition on transparent conductive oxides

To avoid a degradation of the ZnO:Al back-contact, the substrate temperature was chosen below 550°C. As Na cannot diffuse from the glass through the TCO to the CIGS, an external supply of Na has to be provided to ensure high cell performances. In this study Na were provided by NaF evaporation subsequently to the CIGS deposition without removing the sample from the reactor. This treatment is called NaF post-deposition treatment (NaF PDT). Na incorporation by NaF PDT can be different depending on the substrates. Therefore, the NaF PDT was optimized on each back-contact.

3.4.1. Experimental details

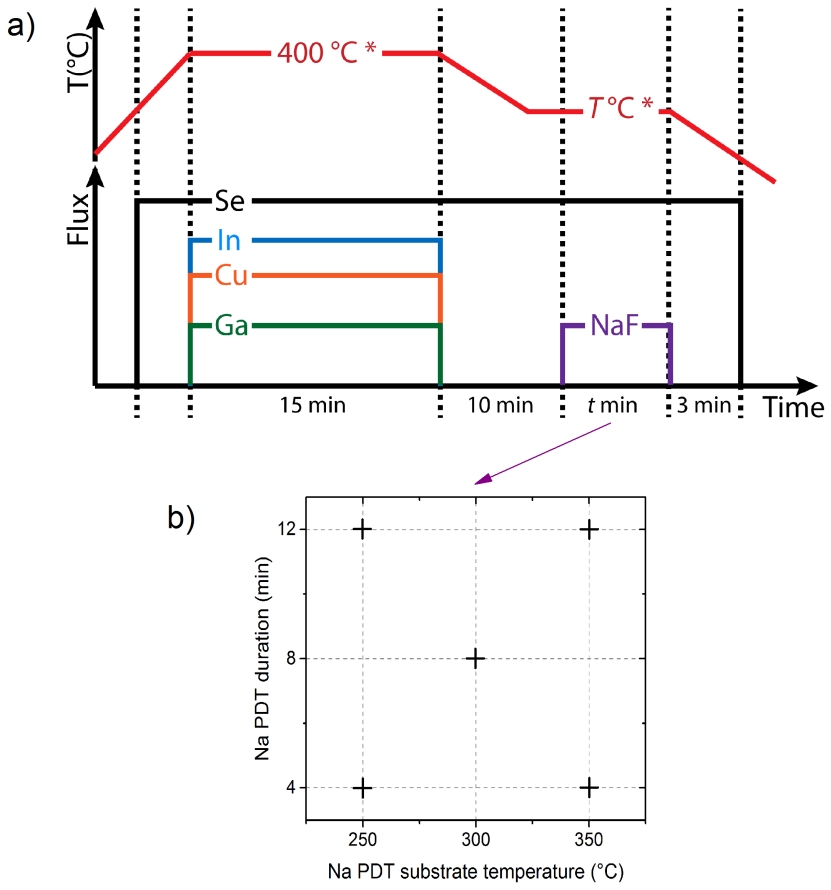

Figure 3.12.: Details of the coevaporation CIGS recipe used for the optimization of the NaF PDT on different substrates. *set point temperature (real temperature: 500-550°C).

First, to understand the impact of the Na PDT on the CIGS properties and cell

performances, different NaF PDT process were performed on 250-nm- and 450-nm-thick CIGS absorbers.

The whole CIGS deposition is presented Fig. 3.12a and the NaF PDT process variation is summarized in Fig. 3.12b. In each experiment, the CIGS is deposited in 1-stage. The substrate temperature ranged from 500 to 550°C. The evaporation rates were kept constant during the CIGS deposition. Subsequently to the CIGS deposition, NaF is evaporated at around 1 nm/min under a Se flux. The NaF PDT duration (t) were varied between 4 and 12 min and the substrate temperature (T) during the NaF PDT were varied between 250 and 350°C (set point temperature)..

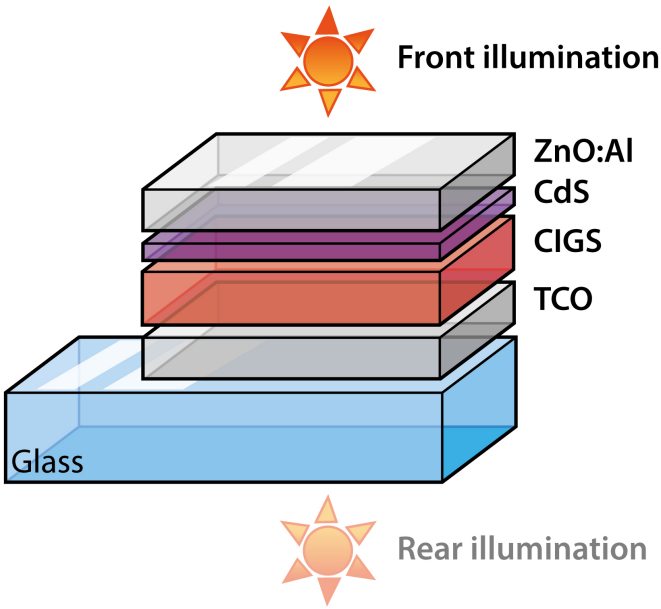

Figure 3.13.: Structure of the cell fabricated with a TCO back-contact. Cells can be characterized with illumination from the front contact (front illumination) or from the rear contact (rear illumination).

In addition, to understand the impact of the alternative back-contacts on the CIGS properties and the cell performances, 4 different substrates on soda-lime glass were used:

- a sputtered 800-nm-thick Mo layer as reference sample where Na is diffusing from the glass;
- a sputtered 800-nm-thick Mo layer deposited on a glass substrate coated with a 300-nm-thick Al_2O_3 layer. The Al_2O_3 layer, deposited by atomic layer deposition, hinders the Na diffusion from the glass during the CIGS deposition;
- a commercial SnO_2:F layer (650-nm-thick, R_{sheet}=7 Ω/square). The samples were washed with 5% RBS, ethanol, acetone and concentrated nitric acid prior to the CIGS deposition;
- a sputtered 1100-nm-thick ZnO:Al layer (R_{sheet}=8 Ω/square);

In total, 10 batches were prepared: for 2 CIGS thicknesses (250 nm and 450 nm) and the 5 NaF PDT condition variations (see Fig. 3.12b). In each batch, the 4 different substrates were processed together. A KCN treatment was carried out prior to the characterizations and the cell fabrication. The solar cells were completed with the standard chemical bath deposited CdS (50 nm) / rf-sputtered ZnO (60nm) / rf-sputtered ZnO:Al (350 nm) stack detailed in sec. 2.2.2. The final cell fabricated on TCO is schematized Fig. 3.13.

3.4.2. Materials analysis

3.4.2.1. Bulk CIGS analysis

The final composition measured by EDS and thickness measured by profilometry of each samples with 450-nm-thick CIGS and 250-nm-thick CIGS are summarized in Tab. 3.5. The CIGS deposited on the different substrates and with the different NaF PDT conditions have similar thicknesses, CGI and GGI. They are indicated as standard variation in Tab. 3.5.

Table 3.5.: Composition and thickness of the samples.

Name	450-nm-thick CIGS	300-nm-thick CIGS
CIGS thickness	450 ± 20 nm	270 ± 20 nm
CGI	0.86 ∓ 0.02	0.91 ∓ 0.02
GGI	0.36 ∓ 0.01	0.40 ∓ 0.02

The morphology of the CIGS on Mo, SnO_2:F and ZnO:Al was investigated using SEM cross-sectional images presented on Fig. 3.14. For all samples, we observe small size grains as already observed in sec. 2.3.2 for the CIGS with a reduced thickness. The SnO_2:F/CIGS interface is rough due to the initial roughness of SnO_2:F, whereas the ZnO:Al/CIGS interface is very flat.

The CIGS orientation was analyzed by XRD in the Bragg-Brentano configuration. The diffractogram of each sample with the NaF PDT performed at 300°C for 8 min is presented in Fig. 3.15. As observed, the CIGS deposited on Mo, Al_2O_3/Mo and SnO_2:F show the (112) and [(220), (204)] peaks already observed in sec. 2.3.2. For the CIGS deposited on ZnO:Al only the (112) peak is observed.

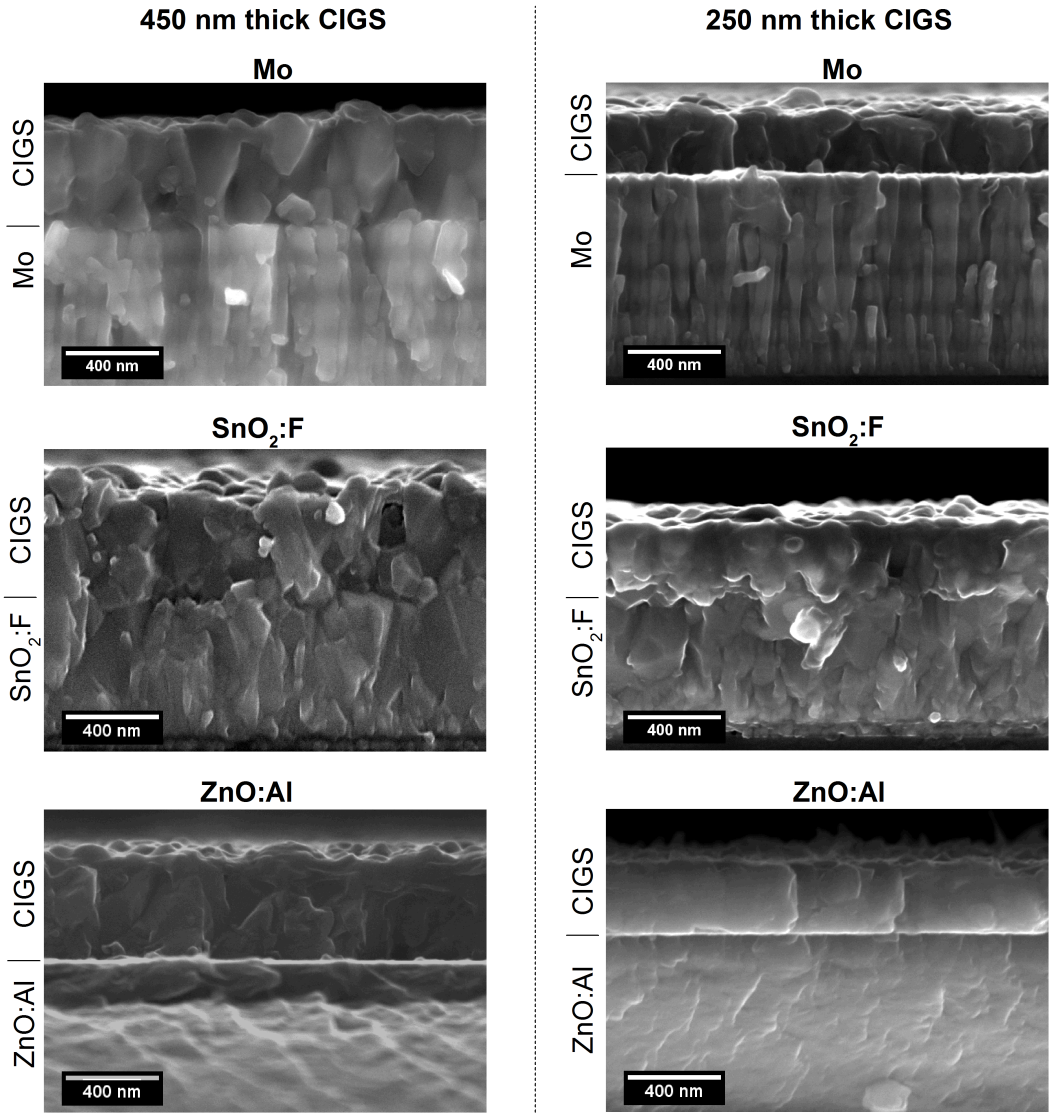

Figure 3.14.: Cross sectional SEM images of the 450 nm and 300-nm-thick CIGS on different back-contacts.

Moreover, depending on the substrate used, the relative intensity of the 112 peak compared to the (220, 204) peak varies. To estimate the orientation of the CIGS, the Logtering factors of the 112 and (220,204) peaks, $F_{(112)}$ and $F_{(220,204)}$, were calculated according to Eq. 2.4 for all the samples. The results are summarized in Fig. 3.15. The more $F_{(hkl)}$ is closed to 1, the more the layer is preferentially oriented along the (hkl) plane. As observed, the NaF PDT condition has only few influence on the preferred orientation of the CIGS. The CIGS on Al_2O_3/Mo substrate is slightly less <112>-preferred oriented than the CIGS on Mo probably the CIGS growth in Na free condition [173, 145]. The CIGS on SnO_2:F has almost no preferred orientation, whereas the CIGS on ZnO:Al is completely <112> oriented.

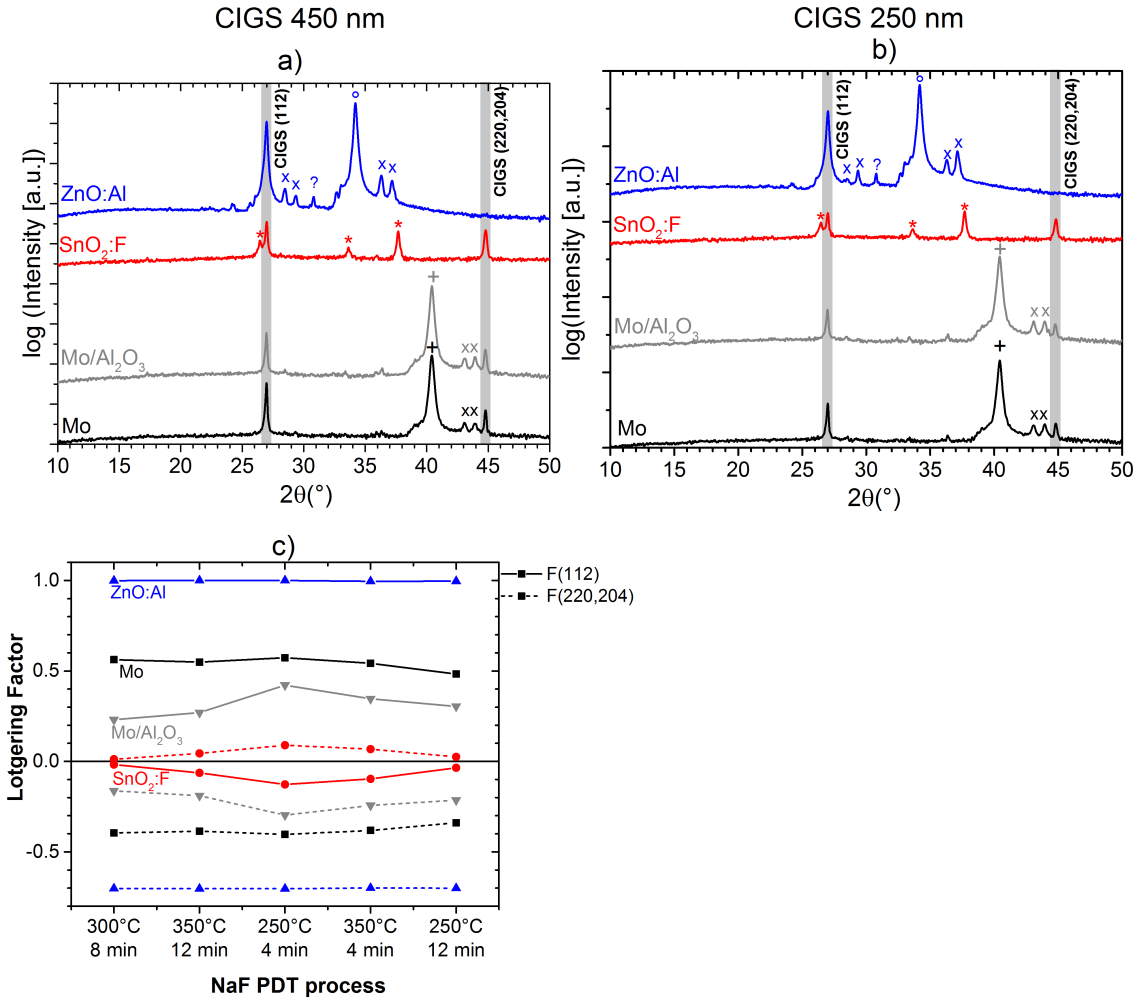

Figure 3.15.: a-b) XRD patterns of the CIGS samples on different back-contacts. c) Logtering factor of the 450-nm-thick CIGS for the different process conditions. °: ZnO, *: SnO_2, +: Mo. ×: additional peaks due to cathode impurities.

The substrate seems to have a major impact on the CIGS growth and can be due to the surface properties of the TCO. In the case of the SnO_2:F, the surface roughness can reduce the orientation along the normal axis. In the case of the ZnO:Al, the <0001>-preferred orientation of the ZnO hexagonal structure can favor the CIGS <112> orientation by minimizing the interface energy.

The Na content profile in the CIGS layer was analyzed by GD-OES for all samples. The KCN treatment had removed the accumulated Na at the surface. For an easier analyses of the Na profile, the Na signal was divided by the total intensity received by the spectrometer (Fi) and the etching time was normalized as regard to the back interface position. The beginning of the interface is estimated by the signal appearance of Mo, Zn or Sn and the end of the interface is estimated by the Se signal disappearance. The Na profiles of all the samples with 450-nm-thick CIGS

are shown in Fig. 3.16 and are compared with a sample without NaF PDT performed on the same substrate.

For the Mo substrate, the NaF PDT performed at 250°C has no effect on the Na concentration in the CIGS compared to the sample without NaF PDT. At 300°C or 350°C, the Na signal increases, meaning that further Na was incorporated in the CIGS by the NaF PDT in addition to the Na diffusion. The Na signal at the interface is difficult to analyses and can be due to an artifact in the measurement.

For the Mo/Al_2O_3 substrates, all the NaF PDT conditions lead to a large increase in the Na signal compared to the case without NaF PDT meaning that Na was incorporated in both the CIGS and Mo. The highest Na/Fi signal was obtained for the NaF PDT at 350°C for 12 min and at 300°C for 8 min. Globally, for each NaF PDT condition, the ratio Na/Fi ratio in the CIGS bulk is similar to CIGS on Mo. The variation of Na concentration in the Mo layer indicates that Na diffuses from the CIGS to the Mo. Mo could therefore regulates Na quantity by absorbing the excess of Na.

For the SnO_2:F substrates, all the NaF PDT conditions also lead to a large increase of the Na signal in the CIGS layer compared to the case without NaF PDT. This means that Na was incorporated only in the CIGS layer but not in the SnO_2:F layer. The NaF PDT at 350°C for 12 min leads to the highest Na/Fi ratio, which is even higher than that on Mo. For the other conditions, the Na/Fi ratios in the CIGS bulk are similar to CIGS on Mo. The Na signal proportionally increase with the NaF PDT substrate temperature and duration increases. Moreover, the Na/Fi ratio is greatly increased at the SnO_2:F/CIGS back-interface. Even if an artifact of measurement cannot be avoided, the large magnitude of this increase can be interpreted as an Na accumulates at the SnO_2:F/CIGS interface.

For the ZnO:Al substrates, the same tendency than for SnO_2:F is observed with an accumulation of Na at the back interface. However the Na/Fi ratio is surprisingly much higher than the ratio obtained on the other substrates, especially for the NaF PDT at 350°C for 12 min.Note that the Na signal also increases inside the ZnO:Al layer meaning that a Na diffusion into the ZnO:Al is possible and should be avoided to maintain the ZnO:Al performance. Therefore, the PDT at 350°C for 12 min is maybe not suitable to avoid degradation of the ZnO:Al.

Finally, the **Na concentration in the CIGS bulk** for CIGS deposited on SnO_2:F and Al_2O_3/Mo is **comparable to the CIGS deposited on Mo**. Curiously, much **more Na was incorporated in the CIGS on ZnO:Al**. The Na concentration is mainly driven by the temperature during the NaF PDT. Moreover, the observed **Na accumulation at the TCO/CIGS interface** can impact the parameters of the solar cells: it can lead to some metal-sodium compounds [40], increase the p-doping of the CIGS [40], passivate the CIGS [174], enhance the oxidation reaction at the interface or increase the acceptor defects in the interfacial oxide layer [175]. To have a better understanding of this interface, an accurate composition analysis is required.

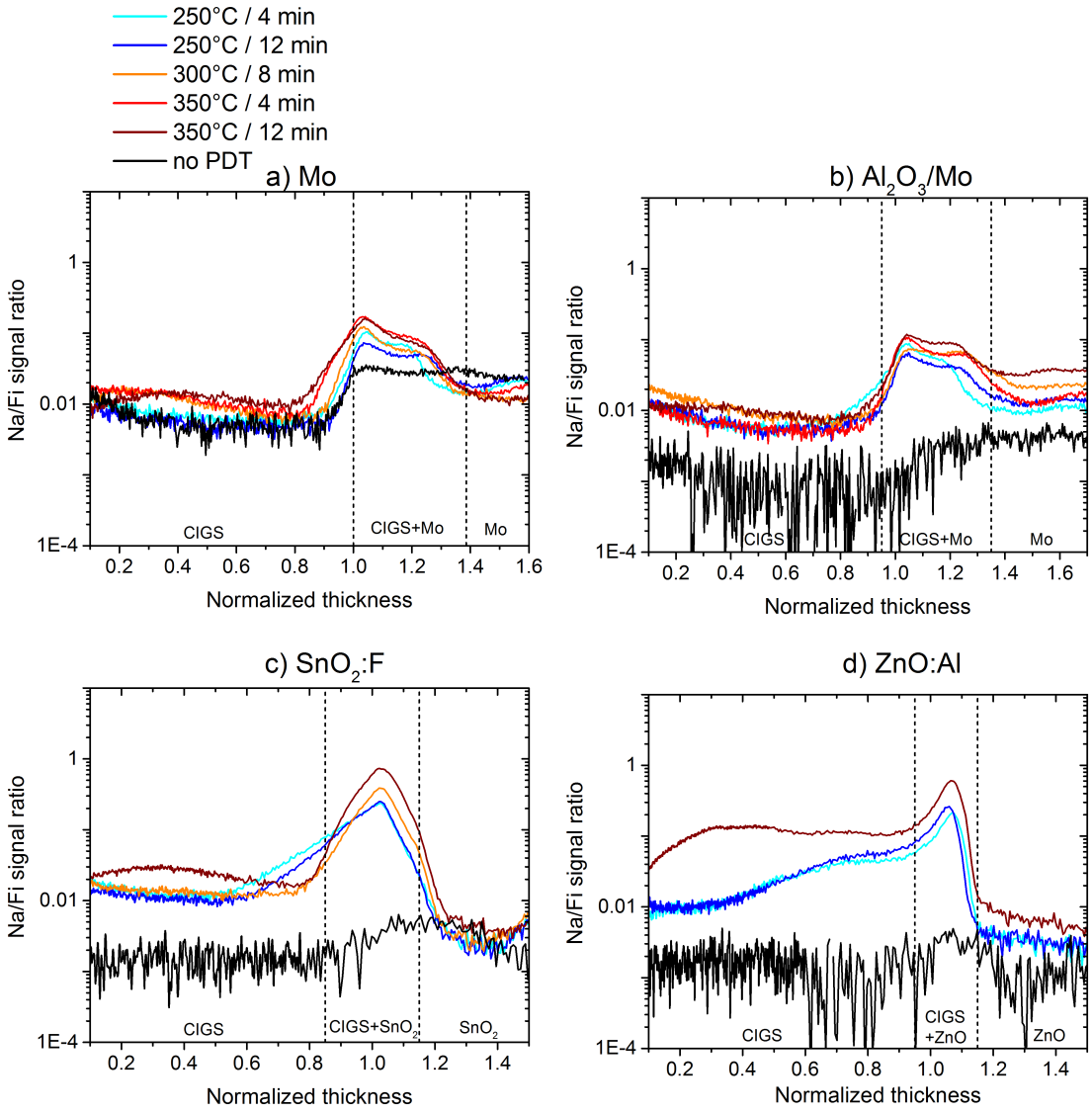

Figure 3.16.: Na profile measured by GD-OES in the samples on different back-contacts and after different Na PDT. Na signal was divided by the total light intensity (Fi) to make the easier comparison.

3.4.2.2. Rear interface analysis

In-depth chemical characterizations of the TCO/CIGS interface were carried out at *Institut Lavoisier de Versailles* (ILV) by X-ray Photoelectron Spectroscopy (XPS) and by nano-Auger Electron Spectroscopy (nano-AES).

Ar^+ sputtering was employed to determine the elements distribution from part-to-part to the interface. The measurements were performed on the ZnO:Al/CIGS and SnO_2:F/ CIGS samples with the NaF PDT at 300°C for 8 min. Indeed, XPS analyses are performed with a spot size of 400 μm spot size. Consequently, the measurements on rough surfaces bring an averaged collection of photoelectrons emitted from the crests and valleys, and modify the dimensions of the interaction volume and of the developed surface. The accuracy of the measurements is reduced and the mixed CIGS /TCO surface is probed with unknown proportions.

In order to start with more favorable conditions for XPS and AES experiments, the CIGS surface was flattened and CIGS thickness was reduced using a bromine solution etching previously developed at ILV and described in reference [176].

The ZnO:Al/CIGS back-interface XPS chemical surface analyses were carried out using Thermo Electron K - Alpha spectrometer with a monochromatic Al-K_α X - Ray source (1486.6 eV). The Thermo Electron K - Alpha spectrometer procedure was used for calibration and verified using Cu and Au samples following the ASTM-E-902-94 standard procedure. Acquisition parameters of high energy resolution photopeaks are: 400 μm spot size, 12 kV primary energy, 6.0 mA emission intensity, CAE 10 eV and 0.05 eV energy step size. Profiling within the XPS was done using Ar^+ ion source operating with 2 keV, 10 mA beam energy. Avantage© software was used for the data treatment.

The quantification was obtained considering O 1s (531.34 ±0.05 eV), Cu $2p_{3/2}$ (bending energy of 932.68±0.05 eV) , In $4d_{5/2}$ (18.23±0.05 eV), Ga $3d_{5/2}$ (20.24±0.05 eV) and Se $3d_{5/2}$ (52.20±0.05 eV) peaks [177]. The ZnO:Al/CIGS interface depth profile is showed in Fig. 3.19. We observe in Fig. 3.19a, that the interface was reached after about 1500 s. The measurement at 2500 s is representative of the interface composition. Then, a plateau of Zn and O with a Zn/O 50:50 ratio is reached evidencing that the interface is crossed.

CGI and GGI quantification. The CGI and GGI were calculated in Fig. 3.19b from the atomic percentages.

It should be noticed that over-estimated CGI values are obtained . This is explained by the fact that Cu $2p_{3/2}$ photopeak is detected at higher binding energy than the In $4d_{5/2}$ and Ga $3d_{5/2}$ ones. Consequently, the Cu photoelectrons escape depth (and so the analyses depth) is a bit smaller than the In and Ga photoelectron ones leading to a small discrepancy with the targeted CGI value (10 nm depth probed in XPS). This is not the case for the GGI determined from the In4d-Ga3d overlapped region.

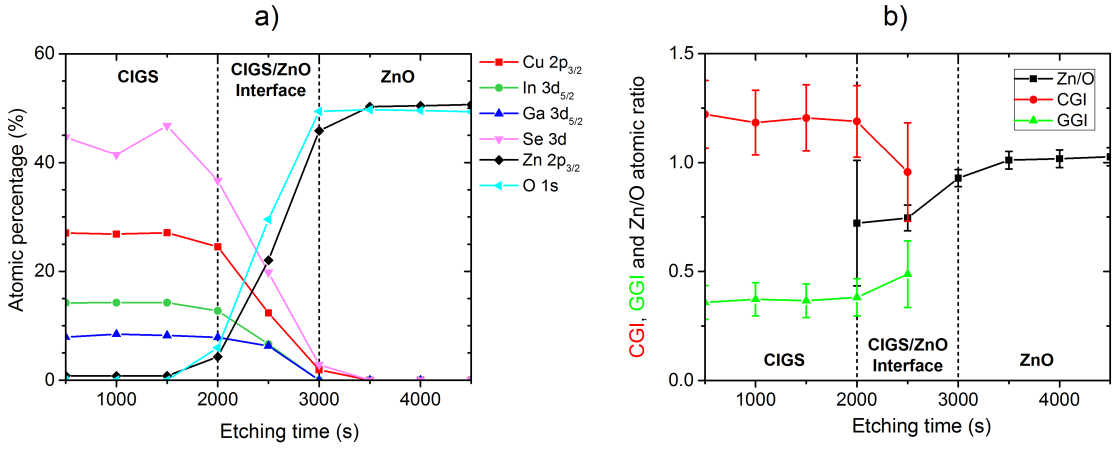

Figure 3.17.: X-ray Photoelectron Spectroscopy (XPS) depth profile of the ZnO:Al/CIGS interface. a) Atomic percentage of the main elements. b) CGI, GGI and Zn/O atomic ratio calculated the atomic ratio. The error bars were calculated with an uncertainty of ±1% on the atomic percentages. The interface is commonly delimited by 16% and 84% of the total concentration change and is approximately represented in dotted lines.

We observe in Fig. 3.19b that no significant composition variation are observed at the interface. The apparent increases in GGI and decreases in CGI are probably correlated to both a slight preferential abrasion and a slight formation of metallic species during the Ar etching.

Oxide identification. We also observe in Fig. 3.19a that O and Zn content evolution are correlated. This means that O is mainly bounded to Zn and that only a small O contents can be attributed to the presence of Cu, Ga, In or Se oxides at the interface. In the literature [**164**, **162**], the presence of GaO_x oxides was commonly reported at the ZnO:Al/CIGS back-interface.

We focused on the Ga 2p 3/2 photopeak (more surface sensitive than the Ga 3d one) measured after 2500 s erosion in middle of the interface, shown in Fig. 3.18. The fitting procedure evidences a main Ga in a CIGS matrix environment (1118.44 ± 0.05 eV binding energy, 1.77 ± 0.05 eV FWHM and Gaussian/Lorentzian = 30%) with a slight contribution of Ga in the metallic state (reduced Ga^0 during the Ar^+ etching). However, the important information is that no contribution of Ga in an oxide phase can be detected but neither excluded. Nevertheless, a maximum concentration of 1% can be deduced from both peak fitting and residual O available (*i.e.* not bounded to Zn). Similar results were obtained with Cu and In.

Finally, hardly any composition variation was observed at the ZnO:Al/CIGS interface. If a GaO_x phase is formed during the CIGS deposition process on ZnO:Al, the content is very low. This result obtained by XPS depth profiling evidences a major difference with observations made by other groups. The latters have clearly demonstrated the presence of a GaO_x phase at the back-interface from the EDS,

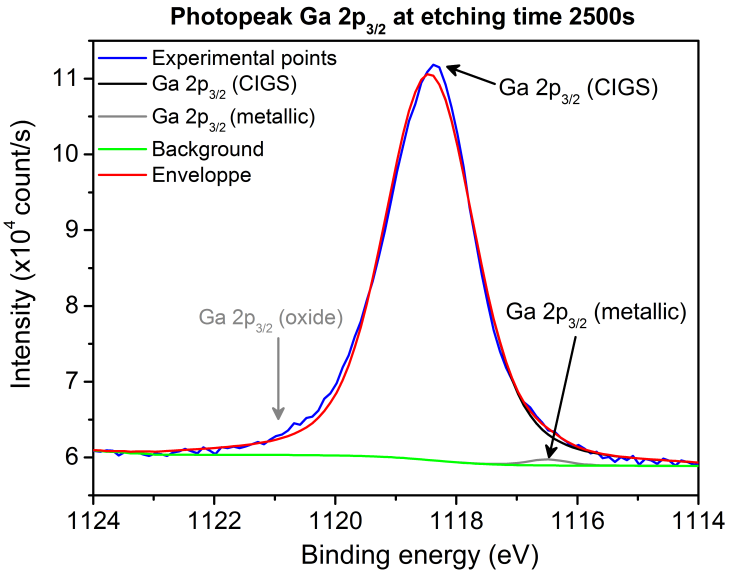

Figure 3.18.: Photopeak of the Ga $2p_{3/2}$ measured by X-ray Photoelectron Spectroscopy (XPS). The contribution of the Ga in the CIGS phase and in the metallic phase are fitted. The position of the Ga in an oxide phase is indicated in grey.

AES or XPS analysis of cleaved samples [178, 179, 164].

The SnO_2:F/CIGS back-interface As shown in Fig. 3.14, the surface of the SnO_2:F sample is much rougher ($\mp$40 nm) than the ZnO:Al one. During the XPS profile, the roughness of SnO_2:F makes difficult an accurate analysis of the interface. In the introduction part of this section, the detrimental effect of roughness on XPS measurements was discussed and the advantages of nano-Auger exposed.

The AES measurement was performed using a JEOL JAMP 9500F device at an accelerating voltage of 20 kV, a beam intensity of 6 nA and an energy resolution of $dE/E = 0.5\%$. Under those conditions, the spot size was approximately 12 nm and the analysis depth was less than 5 nm. The equivalent sputtering rate with respect to SiO_2 was 24 nm/min. Depth profile was performed using Ar^+ sputtering at 2 kV, 2 μA and a 30° tilt angle configuration (Ar pressure of 8.10^{-2} Pa).

The analysis position was controlled between each sputtering sequence and during the acquisition of the spectra using a probe tracking tool enabling to correct from drift (such as beam drift or charging effect). Therefore, a precise control of the analysis location all along the profile could be ensured (static sputtering mode and step by step non automatized profiling) and an accurate profile of the CIGS/SnO_2:F interface obtained.

Composition profile. The SnO_2:F/CIGS interface depth profile is showed in Fig. 3.19. We observe that the interface is well defined. O is used as tracking element to evidence the appearance of the SnO_2 layer signals, Sn-MNN transition

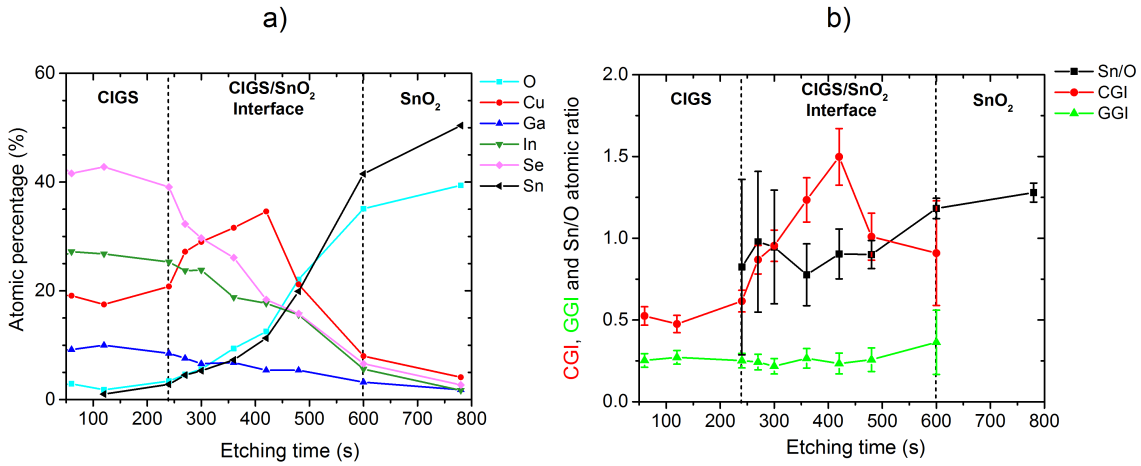

Figure 3.19.: Nano-Auger Emission Spectroscopy (nano-AES) depth profile of the SnO_2:F/CIGS interface. a) Atomic percentages of the main elements. b) CGI, GGI and Sn/O ratio calculated from the atomic ratio. The error bars were calculated with an uncertainty of ±1% on the atomic percentages. The interface is commonly delimited by 16% and 84% of the total concentration change and is approximately represented in dotted lines.

emerging in the low energy scale of the In-MNN one. A progressive decrease of the In, Ga and Se contents is shown when approaching the interface zone, but this is not the case for Cu showing a slight increase. No specific experimental reasons can explain this different evolution and hence, a Cu enrichment at the SnO_2:F/CIGS interface is possible. However, note that, as mentioned previously, Ar^+ sputtering generates some artifacts such as a preferential sputtering effect and a slight reduction of elements.

The GGI, calculated in Fig. 3.19b, remains constant along the interface profile. CGI ratio follows the Cu content trend and highlights a Cu-rich phase. The Sn/O stoichiometry of 1:2 is not reached but the profile was stopped before the interface was totally crossed and the stationary state of Sn-MNN and O-KLL signal in the $SnO_2$was not reached.

Oxides identification. The O and Sn signals are strongly correlated meaning that O is preferentially bounded to Sn. The presence of InO_x, GaO_x, and CuO_x is studied considering the peaks shapes and the energy positions. The Ga LMM peaks (1066 eV and 1093 eV) and the Cu LMM peak (914 eV) are displayed in Fig. 3.20 to illustrate this point. We can notice a conservation of the maximum energy peaks position of all the CIGS elements all along the interface profiling indicating a constant chemical environment. Only the peaks corresponding to the two first levels (without etching - 0s - and 60s) are slightly shifted and exhibit little oxide features due to a slight oxidation of the CIGS surface prior to analysis (native oxide layer). The signal to noise ratio is decreased when approaching the interface and an accurate diagnostic becomes tough. In addition, the metallic trend of the

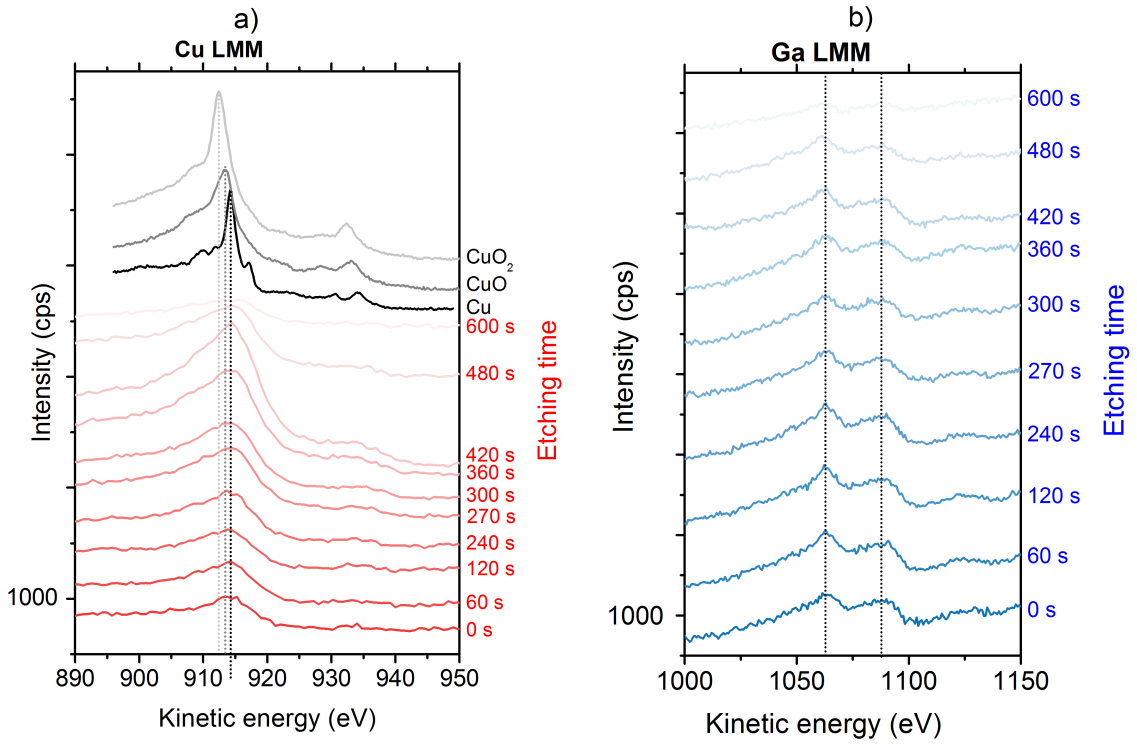

Figure 3.20.: Nano-Auger Emission Spectroscopy (nano-AES) energy peaks at the different etching time for a) Cu LMM and b) Ga LMM transitions. In the case of Cu-LMM, the standard spectra of metallic Cu (in black) and Cu oxides (in grey) provided from JEOL database are displayed (note that the energy resolution of the standards spectra differs: dE/E=0.35%).

peaks shapes may also arise partly from sputtering induced reduction, the inherent depth probes in AES being even lesser than the XPS one (<5nm). But the high surface sensitivity of AES technique enables, on the other hand, to demonstrate that only very low oxide contributions could be present at the interface, the diagnostic reaching the detection limit of AES. Therefore, the presence of a GaO_x phase is unlikely. The same observations can be made on the Ga energy peaks (in Fig. 3.20b) and In-MNN signal (not shown here).

Finally, if an InO_x, GaO_x, or CuO_x oxide phase is formed at the interface, its content should be very low. However, it seems that a Cu-rich phase is formed at the interface.

3.4.3. Opto-electrical analysis

3.4.3.1. Ohmic contact formation

To characterize the electrical behavior of the different TCO/CIGS back contacts, devices with a 150-nm-evaporated gold on top of the CIGS absorber were fabricated. As CIGS/Au contact has a low resistance, the I(V) characteristics of this

structure only depends on the resistance of the back contact. The device structure is schematized in Fig. 3.21.

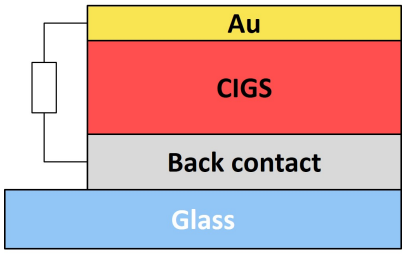

Figure 3.21.: Scheme of the device the analysis the analyses the contact resistance at the back contact.

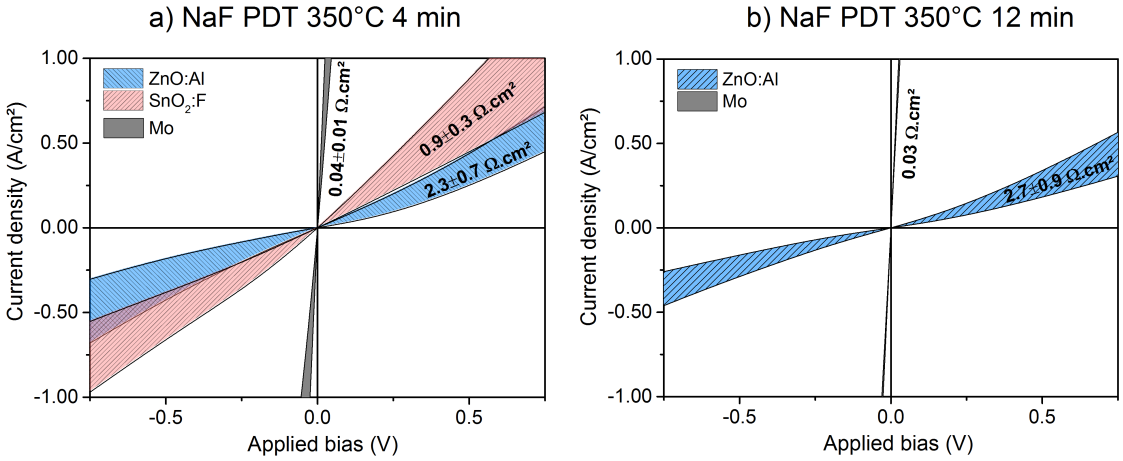

Figure 3.22.: Current-voltage I(V) characteristics of the back-contact/CIGS/Au structure for the NaF PDT at a) 350°C for 4 min and b) 350°C for 12 min. Due to large data variations over the different cells of the samples, extreme curves are displayed. The contact resistance at 0V is indicated as mean ± standard deviation.

Six cells of the Mo/CIGS/Au, SnO_2:F/CIGS/Au and ZnO:Al/CIGS/Au devices with 450-nm-thick CIGS were measured. The I(V) characteristic curves for the highest and the lowest contact resistance was displayed in Fig. 3.22, then the mean resistance and standard variation was calculated. The reason for the resistance inhomogeneity is unclear but can be due to shunt paths in the cells.

As observed in Fig. 3.22, the Mo/CIGS/Au contact exhibits a very low contact resistance ($0.04 \pm 0.01\ \Omega.cm^2$). This value corresponds to the sum of the interfaces and layers contributions.

For the NaF PDT at 350°C for 4 min, the SnO_2:F/CIGS back-contact exhibits an ohmic behavior with a contact resistance of $0.9 \pm 0.3\ \Omega.cm^2$, which is much higher than on Mo substrate. Concerning ZnO:Al/CIGS back-contact, the contact is almost

ohmic with a contact resistance of 2.3 ± 0.7 Ω.cm² at 0V for the NaF PDT at 350°C for 4 min (Fig. 3.22a), and 2.7 ± 0.9 Ω.cm² at 0V for the NaF PDT at 350°C for 12 min (Fig. 3.22b). The NaF PDT duration slightly increases the resistance of the ZnO:Al/CIGS contact.

The observation of a ohmic contact is the case of ZnO:Al back-contact was unexpected: an rectifying behavior associated to the formation of a GaO_x blocking layer has been commonly observed in the literature [55, 161, 162]. For our samples, the XPS photopeak of the CIGS/ZnO:Al back-interface (Fig. 3.18) does not evidence any GaO_x phase. Two hypothesis are suggested to explain the ohmic behavior:

1. The high concentration of Na at the ZnO:Al/CIGS interface leads to a high p-doping layer. The depletion though the CIGS is reduced and the contact becomes ohmic.
2. If the GaO_x phase does exists, it must be very thin. The GaO_x has a large band-gap ($\backsim$4.5 eV), is n-doped and would create a large spike in the valence band and would block the hole collection. A thin enough GaO_x layer would enable a tunneling hole transport, possibly assisted by the high defect concentration leading to an ohmic behavior.

Based on these results, both **ZnO:Al and SnO_2:F back-contact seems to be suitabe suitable for cell fabrication** in the substrate configuration.

3.4.3.2. Cell performances without reflector

The impact of the alternative substrates on the cell performances were studied as a function of the NaF PDT conditions. The 40 CIGS samples previously described with the standard CdS/ZnO/ZnO:Al front-window were characterized. Each sample contains 20 pixel cells. The I(V) characteristics were measured under light illumination with AM1.5G spectrum. As cells on SnO_2:F and ZnO:Al back-contact are semi-transparent, **the samples were first characterized with a black-paper on the rear side of the glass substrate** to avoid light reflection on the substrate holder. The I(V) characteristics were also measured in the dark and fitted according to the 2-diode model to calculate the saturation current for ideality factor of 1 and 2 (J_{01} and J_{02}), the shunt resistance (R_{SH}) and the series resistance (R_S).

For more clarity, only the best NaF PDT conditions are analyzed in this section. The cell characterization of the samples processed at each NaF PDT condition is detailed in Appendix E. We summarize here the conclusions of this study:

- On Mo substrate, the Na can migrate from the glass. Further incorporation of Na by NaF PDT seems detrimental for the performance of the cells. For the 250-nm-thick CIGS, a NaF PDT of 8 min at 300°C seems to be nevertheless beneficial. This effect could be explained by too low Na diffusion for a short deposition time.

- On Al_2O_3/Mo, SnO_2:F and ZnO:Al substrates, Na is only provided from the NaF PDT. A NaF PDT at least at 300°C and for at least 8 min is required for decent V_{OC} and J_{SC}. However, the NaF PDT at 350°C for 12 min seems to incorporate a too high concentration of Na, which is detrimental for the performance and the mechanical stability of the cell. As a consequence, an optimum of Na incorporation has to be found.
- For the 450-nm-thick CIGS, the best efficiency is obtained for the NaF PDT at 300°C for 8 min on Al_2O_3/Mo and for the NaF PDT at 350°C for 4 min on SnO_2:F. However, on ZnO:Al, the best efficiency is obtained for the NaF PDT at 350°C for 4 min.
- For the 250-nm-thick CIGS, the best efficiency on Al_2O_3/Mo, SnO_2:F was obtained for the NaF PDT at 350°C for 4 min. On ZnO:Al, the sample with the latter conditions was the only working sample.

Finally, the ideal NaF PDT performed on ultra-thin CIGS on TCO is a balance between the incorporation of Na (that requires temperature higher than 300°C and a sufficient deposition time) and the degradation of the materials properties (too high Na incorporation and formation of a high resistance back-contact).

To focus on the role of the TCO, only the optimum NaF PDT for each substrate were analysed. The I(V) parameters under illumination are summarized in Fig. 3.23. The data are the mean and the standard deviation of the 10 best cells (one sample contains 20 cells). The dark I(V) parameters obtained from the 2-diode model fit of one of the best cell of each sample are displayed Tab. 3.6. The measured V_{OC} under illumination (V_{OC} (exp)) is compared to the V_{OC} calculated from J_{01} and $J_{02}(V_{OC}(J_{01}, J_{02}))$. The difference between V_{OC} (exp) and $V_{OC}(J_{01}, J_{02})$ is due to the impact of the resistance and the violation of the superposition principle between the dark and light measurements. The V_{OC} variations related the influence of the diode 1, diode 2 and the band-gap ($\triangle V_{OC}(J_{001})$, $\triangle V_{OC}(J_{002})$, $\triangle V_{OC}(E_g)$) were calculated according to the equations in Appendix A. In addition, the I(V) curves and EQE curves are shown in Fig. 3.24.

High performance cells on SnO_2:F. We compare in Fig. 3.23 the cells on SnO_2:F back-contact to the cells on Mo to highlight the impact of the substitution of the Mo back-contact by SnO_2:F. For the 450-nm-thick CIGS, the cells on SnO_2:F back-contact have an **efficiency of 9.2%** ± 0.2% (V_{OC} = 611 ± 3 mV, J_{SC} = 25.5 ± 0.6 mA/cm² and FF = 68 ± 1 %) which is similar to the **reference cell on Mo of 9.3%** ± 0.3% (V_{OC} = 648 ± 3 mV, J_{SC} = 21.4 ± 0.2 mA/cm² and FF = 71 ± 2 %). A higher J_{SC} is observed. It is correlated to the higher EQE curve in Fig. 3.24b and is theoretically expected by a better interface reflection at the SnO_2:F/CIGS interface compared to CIGS/Mo. A slightly lower V_{OC} is observed and can be explained according to the calculated relative influence of the two diodes in Tab. 3.6. Both J_{01} and J_{02} are responsible for the decrease of V_{OC} meaning that the recombination in the CIGS on SnO_2:F was increased in the SCR and QNR. A series resistance of 0.7

Table 3.6.: I(V) dark parameters for one of the best cell on the samples on the different substrates with the best NaF PDT condition. The curves are fitted with a two-diode model (J_{01} and J_{02}: saturation current for ideality factor of 1 and 2, R_{SH}: shunt resistance, R_S: series resistance). The measured V_{OC} under illumination (V_{OC} (exp)) is compared the V_{OC} calculated from J_{01} and J_{02}($V_{OC}(J_{01}, J_{02})$). The V_{OC} variations related to J_{01} and J_{02} were calculated according to the equations in Appendix A. * The J_{01} is negligible and is therefore not fitted accurately: a range of $10^{-13} - 10^{-18}$ mA/cm² was considered for calculations. ⊗ measured with a 2-points probe leading to high series resistance.

Experiments			Dark I(V) parameters				V_{OC} comparison		V_{OC} variation compared to Mo		
CIGS thickness	Substrate	NaF PDT	J_{01} (mA/cm²)	J_{02} (mA/cm²)	R_S (Ω.cm²)	R_{SH} (Ω.cm²)	V_{OC}(exp) (mV)	$V_{OC}(J_{01}, J_{02})$ (mV)	$\triangle V_{OC}(J_{001})$ (mV)	$\triangle V_{OC}(J_{002})$ (mV)	$\triangle V_{OC}(E_g)$ (mV)
450 nm	Mo	4 min / 250°C	6.10^{-11}	1.10^{-5}	0.6	2.10^{3}	651	658			
	Mo/Al_2O_3	8 min / 300°C	1.10^{-15}*	3.10^{-5}	0.3	1.10^{3}	641	676 - 677	54	-38 to -50	-9
	SnO_2:F	12 min / 350°C	2.10^{-10}	4.10^{-5}	0.7	2.10^{4}	613	624	-20	-11	-1
	ZnO:Al	4 min / 350°C	1.10^{-18}*	3.10^{-5}	3.0	2.10^{3}	633	668-669	54	-37 to -48	-15
250 nm	Mo	8 min / 300°C	1.10^{-13}	3.10^{-5}	6.7 ⊗	4.10^{4}	612	686			
	Mo/Al_2O_3	4 min / 350°C	5.10^{-14}	5.10^{-5}	5.6 ⊗	4.10^{4}	609	649	-4	-26	-10
	SnO_2:F	4 min / 350°C	4.10^{-10}	2.10^{-5}	3.6 ⊗	$>1.10^{6}$	615	633	-60	26	-10
	ZnO:Al	4 min / 350°C	3.10^{-12}	5.10^{-5}	5.8 ⊘	2.10^{3}	610	677	8	-10	-10

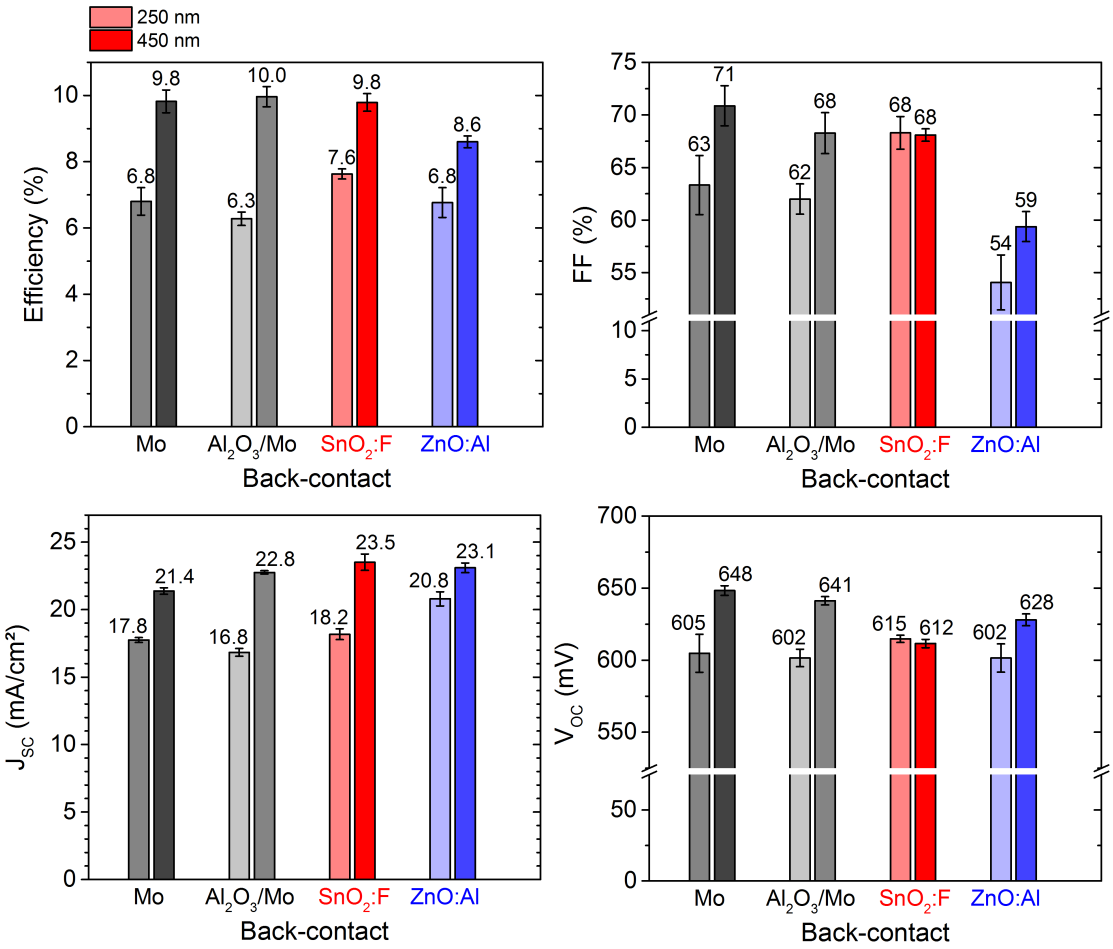

Figure 3.23.: I(V) light parameters for the samples on the different substrates with the best NaF PDT condition. Light I(V) parameters are given as mean ± standard deviation of the 10 best cells (one sample contains 20 cells). A black-paper was inserted at the rear-side of the glass substrate to avoid light reflection.

$\Omega.cm^2$ was measured which is in the range of the SnO_2:F/CIGS contact resistance calculated in Fig. 3.22. This value is low enough to have no impact on the FF.

For the 250-nm-thick CIGS, as observed in Fig. 3.23, the cell on SnO_2:F back-contact has an **efficiency of 7.3%** ± 0.1% (V_{OC} = 615 ± 3 mV, J_{SC} = 18.2 ± 0.4 mA/cm² and FF = 68 ± 1 %) which is even higher than the **reference cell on Mo with 6.8%** ± 0.2% (V_{OC} = 604 ± 13 mV, J_{SC} = 17.7 ± 0.2 mA/cm² and FF = 63 ± 3 %). This interesting result is permitted by an increase in all the parameters. The increase in J_{SC}, correlated the higher EQE curves Fig. 3.24d), is related to the interface reflection. According to the relative influence of the two diodes in Tab. 3.6 the variation of the V_{OC} is due to a slight positive effect of the J_{02} (lower recombination in the SCR) and a negative effect of J_{01}(higher recombination in the QNR and interface). Therefore, high recombination at the SnO_2:F/CIGS back interface is possible.

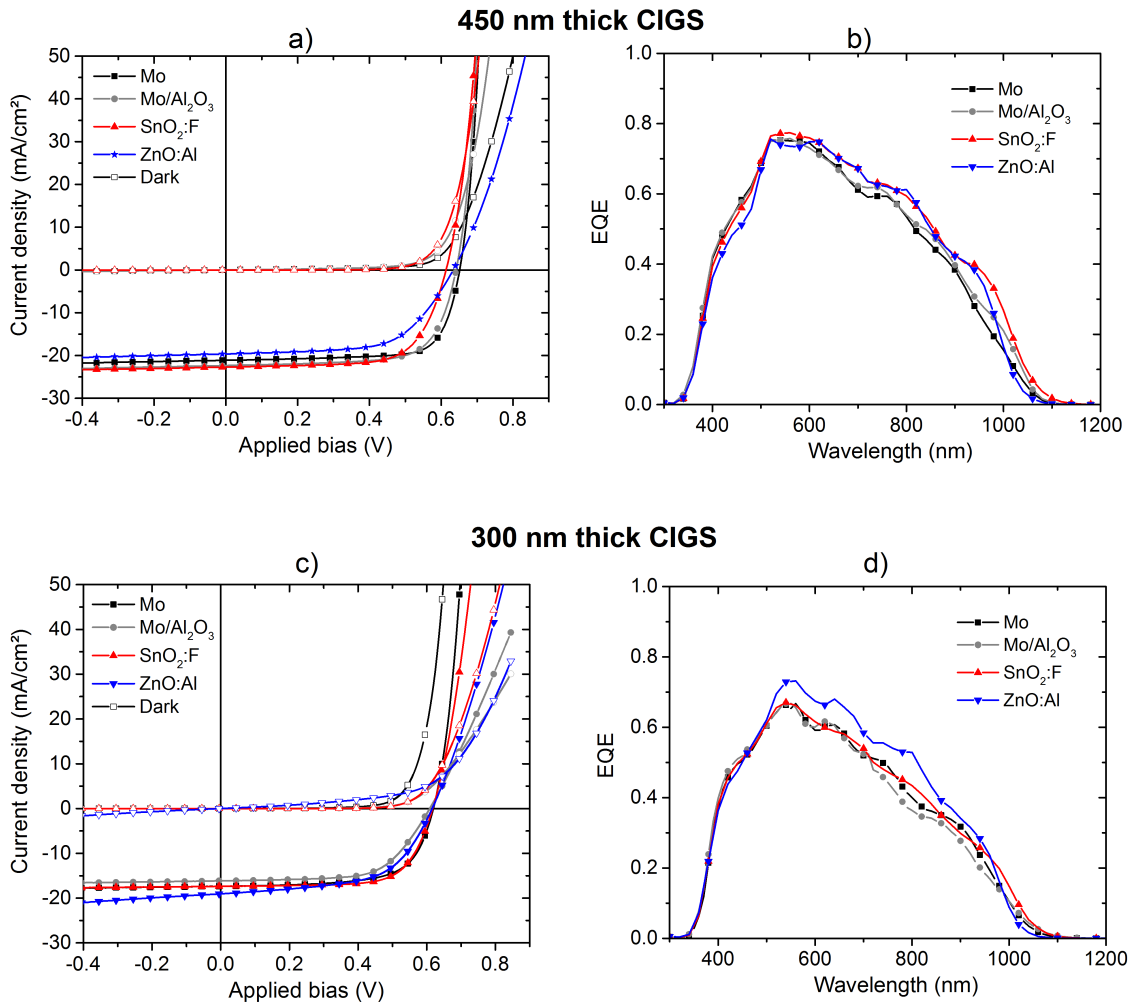

Figure 3.24.: I(V) and EQE of the best cells with the optimized Na PDT and for CIGS thicknesses of 450 nm (a and b) and 300 nm (c and d). A black-paper was inserted at the rear-side of the samples.

High performance ZnO:Al for low CIGS thickness. For the 450-nm-thick CIGS, as observed in Fig. 3.23, the cells on ZnO:Al back-contact have **an efficiency of 8.6%** ± 0.2% (V_{OC} = 628 ± 4 mV, J_{SC} = 23.1 ± 0.4 mA/cm² and FF = 59 ± 1 %) which is lower than the **reference cell on Mo with 9.3%** ± 0.3% (V_{OC} = 648 ± 3 mV, J_{SC} = 21.4 ± 0.2 mA/cm² and FF = 71 ± 2 %). This lower performance is due to a lower FF related to a high series resistance (3.0 Ω.cm²). This value is consistent with the ZnO:Al/CIGS contact resistance calculated in Fig. 3.22. The higher J_{SC}, correlated with the higher EQE curve in Fig. 3.24b is mainly related to the interface reflection. According to the relative influence of the two diodes in Tab. 3.6 the lower V_{OC} is due to the higher J_{02} (higher recombination in the SCR). However, we also observe a lower J_{01} that is related to lower recombination in the QNR and interface.

For the 250-nm-thick CIGS, as observed in Fig. 3.23, the cells on ZnO:Al back-contact have **an efficiency of 6.8%** ± 0.4% (V_{OC} = 601 ± 4 mV, J_{SC} = 20.8 ± 0.5 mA/cm² and FF = 54 ± 3 %) which is similar to the **reference cells on Mo with 6.8%** ± 0.2% (V_{OC} = 604 ± 13 mV, J_{SC} = 17.7 ± 0.2 mA/cm² and FF = 63 ± 3 %). The FF is lower than the FF of the other substrates. A much higher J_{SC} is observed compared to the cells on other substrates, clearly correlated to the EQE measurements Tab. 3.6d. According to the relative influence of the two diodes in Tab. 3.6 a lower J_{01} is observed which as a slight positive effect on the V_{OC}. Therefore, a possible passivation effect at the interface can explain the better charge collection.

To conclude, the cell efficiency obtained on SnO_2:F and ZnO:Al back-contact is almost similar to the reference cells on Mo back-contact. However, the variation of the J_{01} parameter has highlighted a possible variation in the recombination process at the interface. The study of the recombination velocity at the back contact is developed in the following section.

3.4.3.3. Recombination analysis

To understand the impact of the recombination at the TCO/CIGS interface, we analyzed the EQE curves when the cells are illuminated from the rear-side.

The EQE measurement denotes both charge generation and collection. Unlike the front illumination, with a rear illumination most of the charge carriers are generated close to the TCO/CIGS back interface. As a consequence, the interface recombination at the back-contact has a major impact on the EQE curves. The best cells on ZnO:Al and SnO_2:F back-contact were therefore measured with a rear illumination. The I(V) parameters are shown in Tab. 3.7 and the EQE are shown in Fig. 3.25.

Table 3.7.: I(V) parameters of the cells measured for rear illumination.

CIGS thickness	Substrate	Efficiency (%)	J_{SC} (mA/cm²)	V_{OC} (mV)	FF (%)
450 nm	SnO_2:F	6.6	15.3	660	72
	ZnO:Al	7.7	20.2	612	62
250 nm	SnO_2:F	5.5	15.1	615	59
	ZnO:Al	6.0	18.8	537	59

The simulation of the EQE can bring quantitative information on the back-contact recombination. The method was explained in sec. 2.3.2.3 and is briefly remind. The generation function $G(z, \lambda)$ inside the CIGS is modeled from the the absorption

profile with the RTM method along the thickness (z) for each wavelength. The collection function is calculated in the SCR and the QNR according to Eq. 3.6:

$$\begin{cases} f_c^{SCR}(z) = h \\ f_c^{QNR}(z) = f(c, w, d, S_{n,BC}, L_n, D_n) < h \end{cases} \tag{3.6}$$

where h is a constant between 0 and 1 that model the SCR losses, w and d are respectively the thickness of the SCR and the CIGS, $S_{n,BC}$ is the electron recombination velocity at the back contact, L_n is the electron diffusion length in the CIGS (>1 µm) and D_n is the electron diffusion coefficient (2 cm²/s).

The simulated EQE is written as Eq. 3.7:

$$EQE(\lambda) = \int_{z=0}^{d} G(z, \lambda).f_c(z).dz \tag{3.7}$$

The EQE for rear illumination of a ZnO:Al(380nm) / ZnO(60nm) / CdS(45nm) / CIGS(450nm) / ZnO:Al(1000nm) / Glass and ZnO:Al (380nm) /ZnO(60nm) / CdS(45nm) / CIGS(450nm) / SnO_2:F(670nm) / Glass stack were simulated with h=0.95, w=250 nm and $S_{n,BC}$ varying from 10^3 to 10^7 cm/s. The same stacks with 250-nm-thick CIGS were simulated with h=0.95, w =150 nm and $S_{n,BC}$ varying from 10^3 to 10^7 cm/s. The values for w were taken from the w obtained in the simulation performed in sec. 2.3.2.3 for ultra-thin CIGS cells in Mo back-contact.

The results of the simulation are displayed in Fig. 3.25. A downshift of the EQE is observed when the $S_{n,BC}$ increases especially between 10^4 to 10^6 cm/s. For $S_{n,BC} > 10^6$ cm/s, hardly any charges generated closed to the TCO contact are collected, whereas for $S_{n,BC} < 10^4$ cm/s most of the generated charges are collected.

This result is compared to the experimental EQE.

SnO_2:F/ CIGS interface is strongly recombining. The experimental EQE of cells on SnO_2:F back-contact (Fig. 3.25b and d) shows a low collection over the whole spectra especially for wavelengths below 500 nm. This effect can be explained by a high recombination velocity at the TCO/CIGS interface. From the qualitative comparison between the experiments and the simulations, we can approximate $S_{n,BC}$ at 10^7 cm/s for the cell on SnO_2:F back-contact with 450-nm- and 250-nm-thick CIGS. Similar result were obtained for the Mo/CIGS interface in sec. 2.3.2.3. As a consequence, no passivation effect of the Na accumulation at the interface expected according to reference [174] was noticed.

ZnO:Al / CIGS interface is slightly passivated. The experimental EQE of cells on ZnO:Al back-contact (Fig. 3.25a and c) also shows a low collection over the

whole spectra but the curves are higher than the EQE on SnO_2:F. From the qualitative comparison between the experiments and the simulations, $S_{n,BC}$ approximately ranges from 10^5 to 10^6cm/s for the cell with 450-nm-thick CIGS and 10^5 for the cells with 250-nm-thick CIGS. For comparison, Mattheis *et al.* [180] has calculated $S_{n,BC} > 10^6$ cm/s for cells on $MoSe_2$/ZnO:Al back-contact. The lower recombination velocity observed in our samples is still under discussion. If a very thin GaO_x layer is formed with a high acceptor state density as observed by Heineman *et al.* [164]it would creates a conduction-band spike at the back-contact, blocking the electron transport and reducing the recombination [164]. However, the presence of such oxide layer was not identified in our samples (see sec. 3.4.2.2)

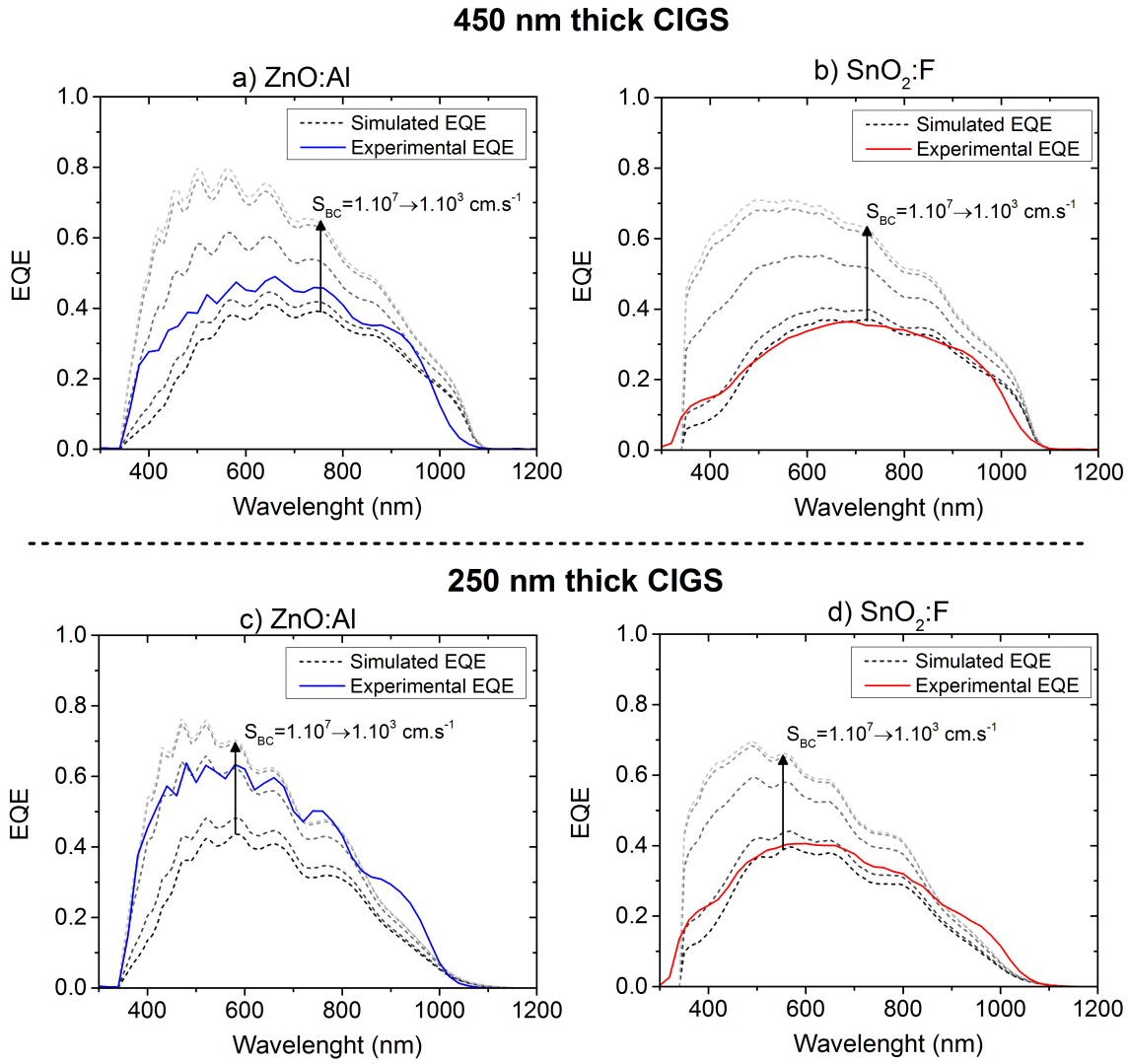

Figure 3.25.: Rear illuminated experimental EQE (solid line) and simulated EQE (dotted line) for a CIGS thcickness of a) 450 nm on ZnO:Al, b) 450 nm on SnO_2:F, c) 250 nm on ZnO:Al and d) 250 nm on SnO_2:F back-contact. The collection model was set with a back-contact recombination velocity $S_{n,BC}$ varying between 10^3 to 10^7 cm/s, w=250 nm (150 nm) for the 450 nm (250 nm) thick CIGS and h=0.95.

3.4.4. Conclusion

In this section, the deposition of CIGS on SnO_2:F and ZnO:Al back-contact were studied and optimized. The following conclusion were drawn:

- **The CIGS grows differently on SnO_2:F and ZnO:Al compared to Mo.** The CIGS on SnO_2:F is less (112)-preferred oriented and is more rough than the CIGS on Mo. The CIGS on ZnO:Al has a different morphology and is completely [(220),(204)]-preferred orientated.
- **The NaF PDT condition needs to be optimized on each substrate.** The NaF PDT were optimized on Mo (Na migrates from the glass substrate), Al_2O_3/Mo (no Na migration), SnO_2:F (no Na migration) and ZnO:Al (no Na migration). The NaF PDT duration and substrate temperature is a balance between the incorporation of Na (that requires temperature higher than 300°C and a sufficient deposition time) and the degradation of the materials properties (formation of unstable phases and formation of a high resistance back-contact).
- **At the TCO/CIGS interface:** Na seems to accumulates close to the back-contact. In-depth material analysis of the interface indicated no *in-situ* interfacial layer formation at the ZnO:Al/CIGS back-interface. On the contrary, other groups have commonly observed a GaO_x layer at the CIGS/ZnO interface [55, 178, 164, 162]. Concerning the SnO_2:F, a Cu-rich phase seem to be formed at the SnO_2:F/CIGS back-interface. We were not able to determine this phase.
- **High performance cells on SnO_2:F and ZnO:Al back-contact.** A low resistance back-contact was achieved for the cells on SnO_2:F. A slightly higher resistance is observed for the cells on ZnO:Al back-contact that sightly reduced the FF of the final cells compared to the cell on SnO_2:F back-contact. Cells were measured with a black-paper at the rear side of the glass to suppress light reflection. With a 450-nm-thick CIGS, an efficiency of 9.2% is achieved on SnO_2:F and 8.6% on ZnO:Al which are close to the efficiency on Mo (9.3%). With a 250-nm-thick CIGS, an efficiency of 7.6% is achieved on SnO_2:F and 6.8% on ZnO:Al which are higher than the efficiency on Mo (6.8%).
- **A small passivation of the CIGS/ZnO:Al interface.** The study of the EQE and the J_{01} of the cells highlight high recombination velocity at the SnO_2:F back-contact ($> 10^6$ cm/s). However, for the cells on ZnO:Al, a lower back-contact recombination velocity was calculated: 10^5 - 10^6cm/s for 450-nm-thick CIGS cells and 10^5 for 250-nm-thick CIGS cells.

For the best cells obtained on SnO_2:F and ZnO:Al back-contact, light absorption can be improved by substituting the black-paper placed at the rear-side of the glass substrate by a reflector.

3.5. Addition of a reflector at the rear side of the glass substrate

In this section, a metallic reflector (Au or Cu layer coated on glass) or a white-paint were used to reflect the light. The impact of the reflectors on the cell performances were analyzed from the I(V) and EQE measurements.

3.5.1. Methods and back-contact reflection

We used 2 different back-reflectors:

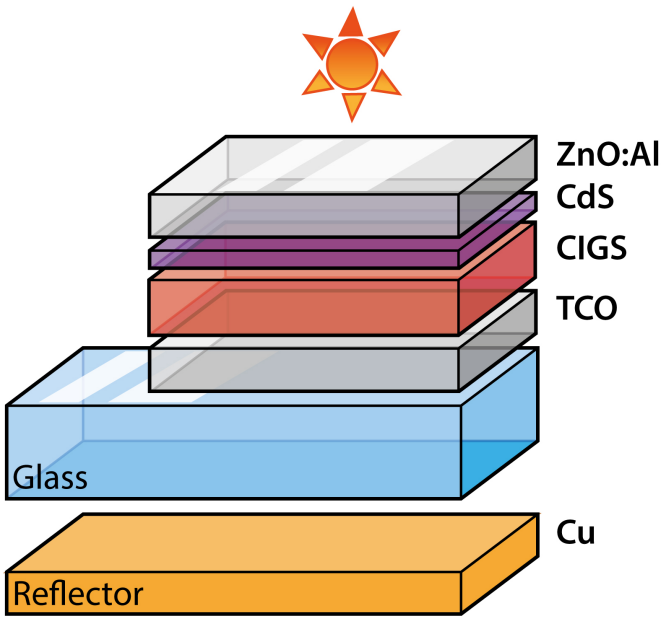

Figure 3.26.: Schematics of the cell on TCO back-contact coupled with a reflector.

- 150-nm-evaporated Au or Cu on a glass substrate. The use of Au or Cu makes almost no difference on the photocurrent according to the modeling of both stack. The reflector is simply placed behind the sample, at the rear-side of the glass substrate. The configuration is schematized in Fig. 3.26.
- A highly reflective and diffusive white paint is coated directly at the rear side of the glass substrate. The white paint used was A*vian B Pre-Mix Reflectance Coating* from *Avian Technologies LLC*. It consists of a pure barium sulfate dispersed in ethanol and distilled water and sprayed on the surface.

The optical potential of the back-contact were analyzed by measuring the total reflectance of the reflector/glass/TCO samples with an integrating sphere. The reflectance of the 650-nm-thick SnO_2:F and the 1200-nm-thick ZnO:Al coupled with a 150-nm-Au coated glass or the white-paint coated on glass is presented in Fig. 3.27.

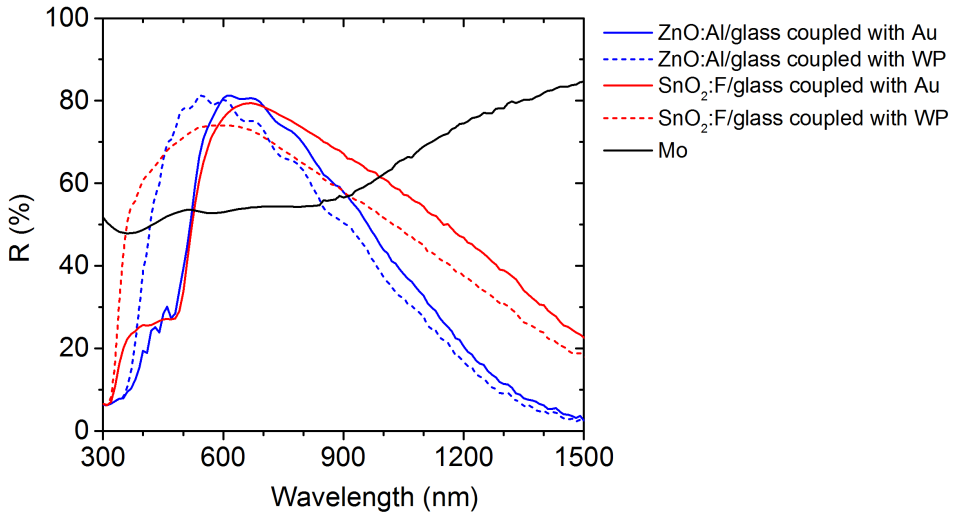

Figure 3.27.: Reflectance of the different transparent back-contacts coupled with a Au coated glass or a white paint (WP).

As observed in Fig. 3.27, the reflectance in air of the 650-nm-thick SnO_2:F coupled with Au is higher than the Mo reflectance between 550 and 1150 nm. The reflectance in air of the 1200-nm-thick ZnO:Al coupled with Au is higher than the Mo reflectance between 550 and 950 nm. This difference is due to the higher free carrier absorption of the ZnO:Al according to Fig. 3.8. Compared to the Au reflector, the white-paint leads to a much better reflection between 400 and 550 nm, but leads to a lower reflection in near infra-red region.

According to the solar irradiance filtred by a 250-nm of a CIGS with a band-gap of 1.2 eV (see 3.2a) and its EQE (see Fig. 3.4b) the back-contact reflection need to be maximized in the spectral range from 600 nm to 1030 nm. This is why, according to Fig. 3.27, the SnO_2:F back-contact coupled with the Au-reflector is possibly the most advantageous back-reflector.

3.5.2. Impact of the reflector on the cell performances

The I(V) characteristics and the EQE of the best samples on ZnO:Al and SnO_2:F described in the previous section were measured with different reflectors. The results are compared to the reference sample, which is the cell on Mo back-contact with the NaF PDT of 4 min at 250°C. The impact of the reflector on the photocurrent is characterized by measuring the difference of J_{SC} between each sample and the reference samples (ΔJ_{SC}). Both J_{SC} measured on the I(V) (high charge injection) curves and the J_{SC} calculated from the EQE curves (low charge injection) were taken into consideration.

The I(V) parameters are summarized in Tab. 3.8. The I(V) and EQE curves are displayed Fig. 3.28 and Fig. 3.29.

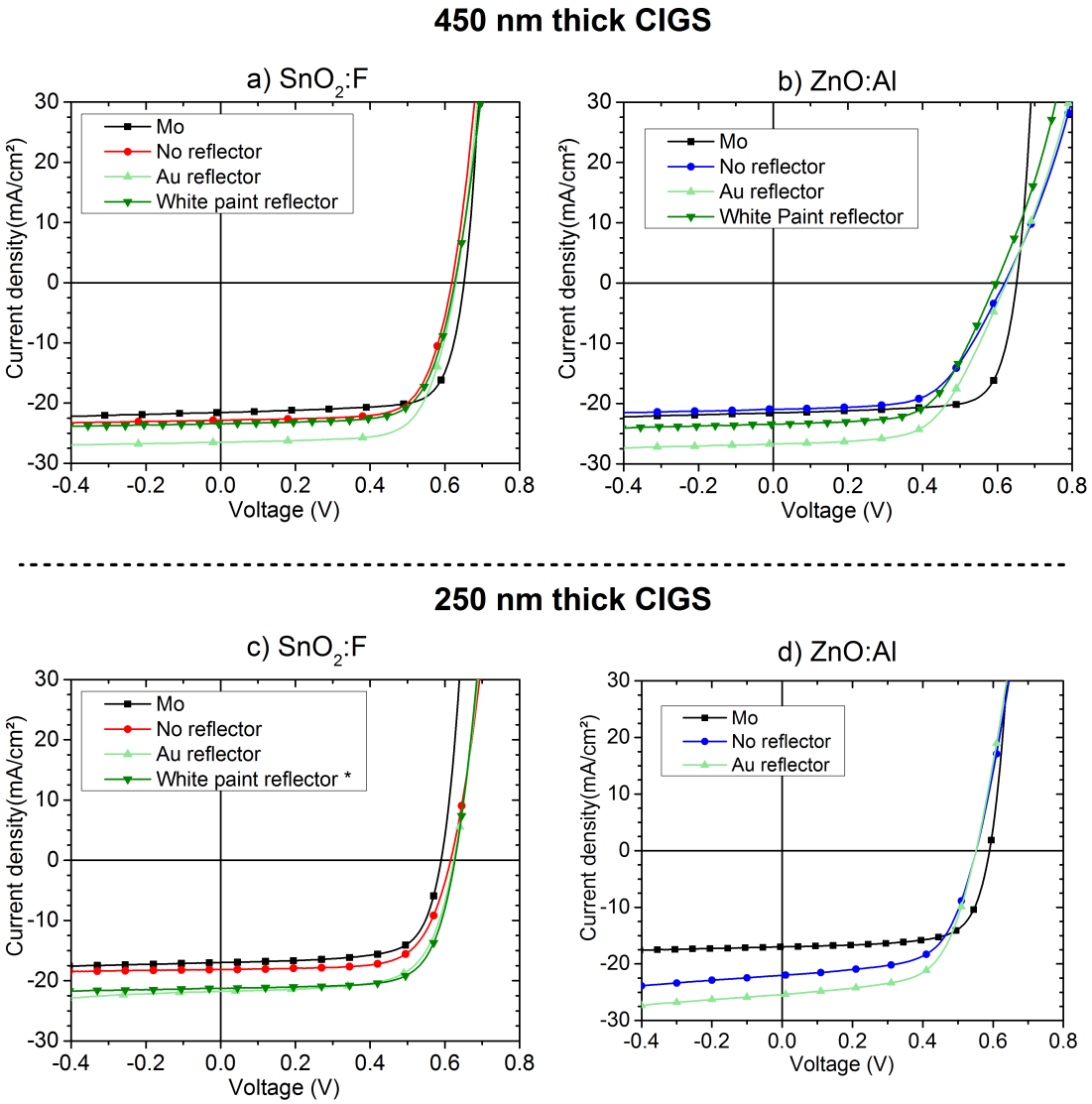

Figure 3.28.: I(V) curves of cells with a) 450-nm-thick CIGS on SnO_2:F, b) 450-nm-thick CIGS on ZnO:Al, c) 250-nm-thick CIGS on SnO_2:F, d) 250-nm-thick CIGS on ZnO:Al, with different reflectors placed at the rear of the glass substrate.

Cells with 450-nm-thick CIGS on SnO_2:F back-contact. As observed in Tab. 3.8, the use of a Cu-reflector behind the cells on SnO_2:F back-contact greatly improves the J_{SC} of +3.4 mA/cm² compared to the measurement on SnO_2:F without reflection and +4.7 mA/cm² compared to the reference sample on Mo. This increase is higher than the increase expected according the simulation performed in Fig. 3.3 (approximately +1 mA/cm² for a 500-nm-thick CIGS cell on 500-nm-thick ZnO:Al back-contact). Finally, the cell on SnO_2:F back-contact coupled with Cu-reflector

has a better efficiency than the cell on Mo (**11.5% compared to 10.4%** in Tab. 3.8). A light-soaking effect was observed and a stabilization of the J_{SC} in 15 min was required to reach the previous value.

The Cu-reflector leads to an upshift of the EQE curve (Fig. 3.29a) in the spectral range of 700 nm to 1000 nm. The increase in J_{SC} deduced from the EQE curves J_{SC} is only about 1 mA/cm² higher than the measurement without reflection.

The increase in V_{OC} expected for the increase in photocurrent can be calculated from a simple one diode model:

$$\Delta V_{OC} = \frac{nkT}{q}(\Delta \ln J_{SC}) \tag{3.8}$$

where n is the ideality factor taken at 1.6 and k the Boltzman constant, q the charge of electron and $T = 300K$.

Between the measurement without reflection and the measurement with the Cu reflector, a V_{OC} increase of 6 mV is expected according to Eq. 3.8. Experimentally, a V_{OC} increase of 11 mV was observed (Tab. 3.8).

From:

1. the difference between the J_{SC} deduced from the EQE curve;
2. the J_{SC} measured from the I(V) curve, the increase in J_{SC} higher than the theory (see sec. 3.2.3);
3. the observation of a light soaking effect
4. the increase in V_{OC} larger than expected

we deduce that the recombination in the cell are probably reduced under high injection (measurement with 1 sun illumination). EQE measurements were also performed with a bias illumination of moderate intensity (rear-side illlumination). A small increase in the EQE curves was noticed. However, a bias illumination at higher irradiance is required to highlight a clear effect of the injection level.

The white-paint improves the J_{SC} of only 0.60 mA/cm² compared to the measurement without reflection. As we have seen in Fig. 3.27, the lower reflectance of the white-paint reflector in the 800 - 1000 nm spectral range compared to the Cu-reflector explains this low improvement in J_{SC}.

Table 3.8.: Cell performance with different reflectors placed at the rear-side of the glass substrate. The difference between the J_{SC} of the cell and the J_{SC} of the Mo reference were calculated for both J_{SC} measured under illumination ($\triangle J_{SC}$ I(V)) and J_{SC} deduced from the EQE curves ($\triangle J_{SC}$ EQE).$*$: performed on another cell of the sample. $\triangleright$ 15 min required to stabilized the J_{SC}. †measurement defers from Fig. 3.23 due to cell aging. $\otimes J_{SC}$ may be overestimated of 0 - 1.5 mA/cm² due to surface overestimation.

Experiments			Light I(V) parameters				J_{SC} analyze	
CIGS thickness	Substrate	Reflector	Efficiency (%)	J_{SC} (mA/cm²)	V_{OC} (mV)	FF (%)	ΔJ_{SC} I(V) (mA/cm²)	ΔJ_{SC} EQE (mA/cm²)
450 nm	Mo	⊘	10.4	21.5	651	74	0	0
	Al_2O_3/Mo	⊘	10.4	22.8	641	71	1.3	-
	SnO_2:F	No reflection	9.9	22.8	619	71	1.3	1.4
		Cu$\triangleright$	11.5	26.2	629	70	4.7	2.4
		White paint$*$	10.0	23.4	626	70	1.9	1.5
	ZnO:Al	No reflection	8.2	22.6	618	59	0.9	1.1
		Cu	9.7	26.7	624	58	5.2	2.3
		White paint$*$	8.1	22.8	596	60	1.3	3.3
260 nm	Mo	⊘	7.0	17.0	590	70	0	0
	Al_2O_3/Mo	⊘	6.6	17.3	604	63	0.3	-
	SnO_2:F	No reflection	7.7	18.2	615	69	1.2	1.4
		Au	9.2	21.8	624	68	4.8	3.3
		White paint$*\otimes$	9.4	21.2	627	71	4.2	2
	ZnO:Al	No reflection †	7.4	21.9	552	62	4.9	3.6
		Au †	8.7	25.4	552	62	8.4	6.2

Cells with 450-nm-thick CIGS on ZnO:Al back-contact. As observed in Tab. 3.8, the use of a Cu-reflector for cells on ZnO:Al back-contact also greatly improves the J_{SC} of 4.1 mA/cm^2 compared to the measurement without reflection and of 5.2 mA/cm^2 compared to the Mo reference. This variation is higher than the variation of J_{SC} deduced from the EQE curves (see Fig. 3.29b). However the cell efficiency is still lower than the cell on Mo (**9.7% compared to 10.4%**). In this case, no light soaking effect was observed but the increase in J_{SC} is still higher than the simulated J_{SC} (see Fig. 3.3). The V_{OC} measured with the Cu-reflector is 6 mV higher than the V_{OC} measured without reflection. This difference can be explained by the increase in J_{SC} according to the Eq. 3.8. Unlike the cell on SnO_2:F, no beneficial effect in high injection is demonstrated.

The cell measured with the white-paint reflector almost not improves the J_{SC} compared to cell measured without reflection (Tab. 3.8). This reflector is therefore less beneficial than the Cu-reflector. The EQE curve is nevertheless not correlated to the J_{SC} measurement.

Cells on 250-nm-thick CIGS on SnO_2:F back-contact. As observed in Tab. 3.8, the use of the Au-reflector for samples on SnO_2:F back-contact improves the J_{SC} of 3.6 mA /cm^2 compared to the measurement without reflection and of 4.8 mA/cm^2 compared to the reference cell on Mo. Finally **a cell efficiency of 9.2% is reached**. This efficiency is much higher than the reference on Mo (7.0%). The increase in J_{SC} is correlated to the EQE curves up-shift in the spectral range between 500 nm and 1000 nm (see Fig. 3.29c) but the improvement of photocurrent deduced from the EQE curves is only 1.9 mA/cm^2 compared to the measurement without reflection.

The V_{OC} increases of 9 mV and is mainly due to the J_{SC} according to Eq. 3.8 with $n = 1.7$. The beneficial effect of the high injection observed for the 450-nm-thick CIGS on SnO_2:F back-contact is not clearly observed for the 250-nm-thick CIGS.

The white paint reflector only largely improves the J_{SC} of 1.5 - 3 mA/cm^2 compared to the measurement without reflector (Tab. 3.8).

Cells on 250-nm-thick CIGS on ZnO:Al back-contact. The use of the Au reflector for samples on ZnO:Al back-contact improves the J_{SC} of 3.5 mA /cm^2 compared to the measurement without reflection and of 8.4 mA/cm^2 compared to the reference cell on Mo. Finally, **an efficiency of 8.7% is achieved**. This efficiency is much higher than the reference cell on Mo (7.0%) but lower than the cell on SnO_2:F back-contact (9.2%). The increase in J_{SC} is correlated to the up-shift of the EQE curve (see Fig. 3.29d). The low back-contact recombination velocity reported for the 250-nm-thick CIGS on ZnO:Al (see Fig. 3.25c) may explain the significantly higher EQE of the cell measured with the Au-reflector compared to the EQE of the other samples. A large part of the light which is reflected at back-contact is actually collected whereas the high back contact recombination of the Mo/CIGS or SnO_2:F/CIGS interface reduces the impact of the reflector. Surprisingly, no change in the V_{OC} was observed.

To conclude, the use of a planar metallic reflector at the rear-side of the transparent

cell leads greatly improves the efficiency. However, the white paint only slightly improves the photocurrent. An increase comparable to the planar reflector was expected according to the simulations with a perfect Lambertian reflector (Fig. 3.3). The experimental white-paint coated on glass differs too much from the perfect Lambertian reflector. Finally, **efficiencies higher than the reference cell on Mo back contact were achieved**, especially for the 250-nm-thick CIGS: 9.2% for the cell on SnO_2:F back-contact with Au reflector and 8.7% for the cell on ZnO:Al back-contact with Au reflector.

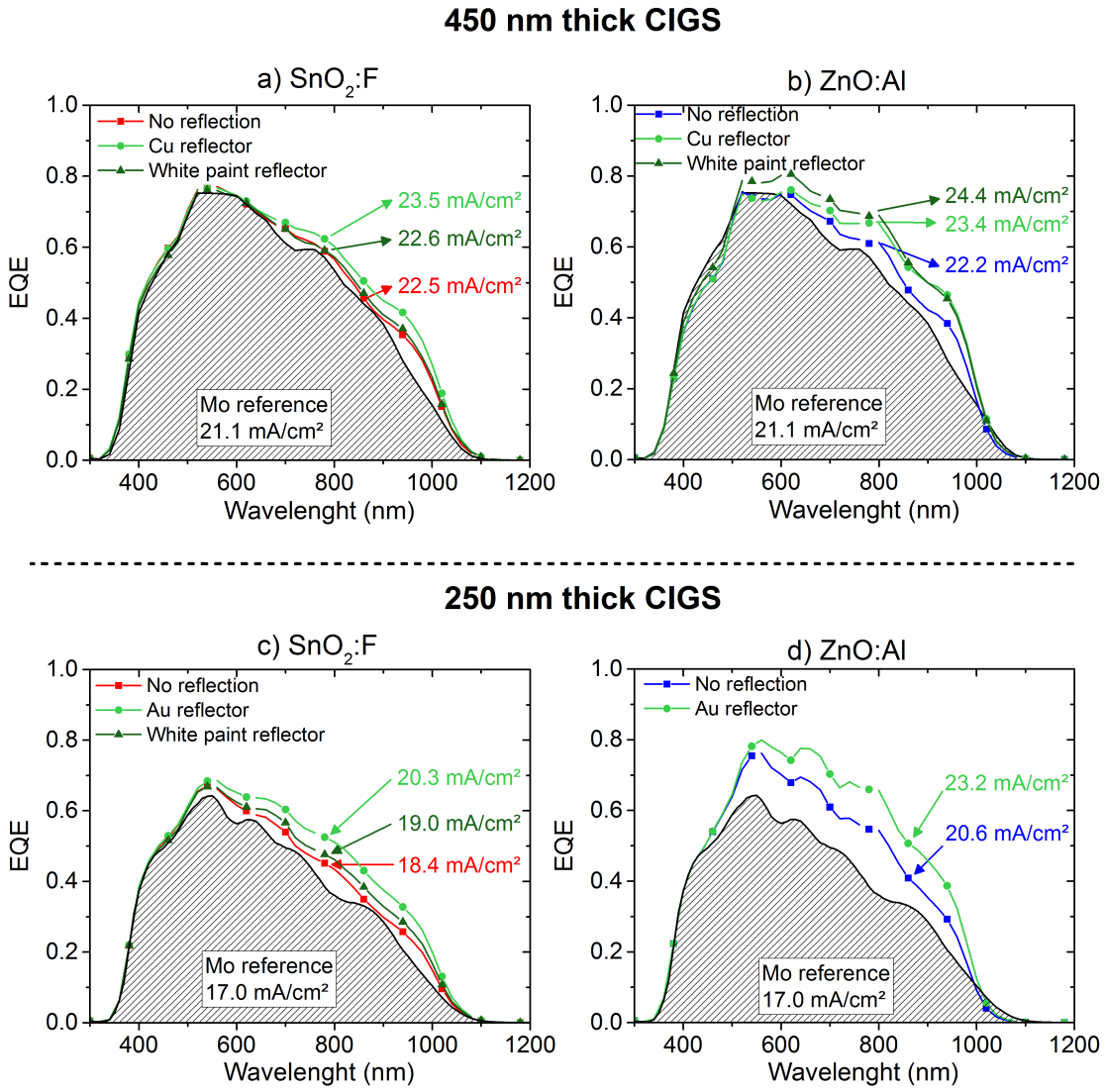

Figure 3.29.: EQE of cells on TCO back-contact with a) 450-nm-thick CIGS on SnO_2:F, b) 450-nm-thick CIGS on ZnO:Al, c) 250-nm-thick CIGS on SnO_2:F, d) 250-nm-thick CIGS on ZnO:Al, with different reflectors placed at the rear-side of the glass substrate.

3.6. Conclusion of the chapter

To enhance the light absorption in the CIGS absorber in ultra-thin CIGS solar cells, the Mo back-contact was replaced by a TCO back-contact coupled with a reflector. After the materials and electrical characterizations of this system, we highlight the following conclusions:

1. Theoretically, the use a TCO back-contact coupled with a metallic Au-reflector instead of the standard Mo back-contact is only beneficial for cells with CIGS thicknesses below 500 nm. The J_{SC} is then improved of **1.3 mA/cm² for a 500-nm-thick CIGS** and **3.2 mA/cm² for a 250-nm-thick CIGS**. The passivation of the back-contact is a key parameter to ensure the J_{SC} enhancement. If the resistivity of the TCO is taken into consideration, an increase of the cell efficiency of **+0.5% abs. for a 450-nm-thick CIGS** and **1.5% abs. for a 250-nm-thick CIGS** can be achieved.
2. The Mo back-contact was replaced by a 1000-nm-thick ZnO:Al and a 650-nm-thick SnO_2:F electrode, selected for their low cost, well known process and high Figure of Merit. However, unlike Mo layer, TCO back-contacts hinder the diffusion of Na from the glass substrate to the CIGS layer during the process. Moreover, ZnO:Al is suspected to easily react with the Se and with the CIGS during the deposition.
3. The CIGS layer was deposited by a 1-stage coevaporation process with **NaF PDT optimized** on the different back-contacts. The temperature and the duration of the NaF PDT is a balance between a sufficient Na incorporation to obtain the electrical benefits (that requires temperature higher than 300°C and a sufficient deposition time) and a too high Na incorporation (that degrades of the materials properties and forms a high back-contact resistance). The CIGS layers were observed **to grow differently** on Mo, SnO_2:F and ZnO:Al. The CIGS grown on SnO_2:F is not preferentially oriented, whereas the CIGS grown on ZnO:Al is perfectly (112)-preferred orientated. The NaF PDT seems to lead to **an accumulation of Na at the TCO/CIGS interface**.
4. **At the ZnO:Al/CIGS interface, no interfacial phase** was observed. On the contrary, **at the SnO_2:F/CIGS interface, a Cu-rich phase** was identified. **An ohmic contact** between the CIGS and SnO_2:F layer and the CIGS and the ZnO:Al layer was achieved leading to a contact resistance of approximately **0.9 Ω.cm²** and **2.3 Ω.cm²** respectively. In the case of ZnO:Al, a non negligible increase of the series resistance is therefore expected. The study of the recombination at the back-contact highlights a **lower surface recombination velocity at the ZnO:Al/ CIGS interface** (10^6- 10^5 cm/s) compared to Mo/CIGS or SnO_2:F/CIGS (10^7 cm/s). In depth comprehension of the ZnO:Al/CIGS interface is required to understand the observed ZnO:Al/CIGS back contact behavior.
5. A cell efficiency of **9.2% on a SnO_2:F back-contact** with Au reflector and

8.7% on a ZnO:Al back-contact with Au reflector was achieved with a **260-nm-thick CIGS** (accurate thickness for this particular simple). For comparison, the reference sample on Mo back-contact reached an efficiency of 7.0%. This increase in efficiency is permitted by light reflection at the back-contact but also by the lower back-contact recombination for ZnO:Al/CIGS and SnO_2:F/CIGS (at high injection) back-contact compared to Mo/CIGS back-contact.

The passivation of the back-contact is a crucial parameter to achieve high efficiency ultra-thin CIGS solar cells. A controlled passivation method is therefore studied in the following chapter.

4. Back-contact passivation in ultra-thin CIGS solar cells

4.1. Introduction

We have demonstrated that the recombination at the back-contact of ultra-thin CIGS solar cells plays a key role. The whole CIGS thickness contributes to light absorption, especially at the back-contact where light is reflected. Thus, high recombination of the charge carriers at the back-contact dramatically contributes to the limitation of the V_{OC} and the J_{SC}.

Experiments in the previous chapter have demonstrated a high back contact recombination velocity on Mo, SnO_2:F (10^7 cm/s) and ZnO:Al (10^{5-6} cm/s). A control of the back-contact passivation is therefore required to achieve high efficiency solar cells with ultra-thin CIGS absorber.

The passivation of the n- or p-type silicon with oxides and nitrides layers is extensively studied in Si PV industry but few works have been done in CIGS thin films. Notably, a positive effect of alumina (Al_2O_3) films has been demonstrated on CIGS [87] and paves the way to further improvements of the CIGS devices.

In this chapter, we analyzed the possibility to passivate the interface between the CIGS and the Mo, ZnO:Al or SnO_2:F layers. For that, we compared the capacity of Al_2O_3 and TiO_2 films to passivate the previous interfaces. Films were fabricated with techniques that can be easily used by industry. Then, ultra-thin CIGS cells were fabricated and measured.

4.2. Recombination management at the back-contact

4.2.1. State of the art on the passivation of the CIGS layer.

The development of cell architecture involving an advanced passivation management at the interface is partly responsible for the recent progress of Si solar devices. The Inter-digitated Back Contact (IBC), Passivated Emitter Rear Locally-Diffuse (PERL) or the Passivated Emitter and Rear Cell (PERC) have reached an efficiency higher than 22% [58]. The passivation of the p-type Si layer is usually achieved by a combination between alumina (Al_2O_3), SiC, SiO_2 or hydrogenated silicon nitride (SiN_x:H). As these layers are insulating, the electrical contact is made through openings in the passivation layer. In general, the micro-size openings are made [181] with a distance of hundreds micrometers .

The quality of the Mo/CIGS contact largely depends on the process condition. The back-contact barrier formation [34], the $MoSe_2$ formation and the presence of species such as Na [26, 27, 112, 174] change the carrier transport and the recombination at this interface. Electron back-contact recombination velocity at the CIGS/$MoSe_2$ interface is generally high ($S_{n,BC} > 10^6$ cm/s) [166, 107, 174] but in some condition, it can be reduced to $S_{n,BC} > 10^2$ cm/s [174]. As calculated before from the EQE measurements sec. 3.4.3.3, the back-contact recombination velocity at the Mo/CIGS interface in our samples was estimated very high: $S_{n,BC} > 10^6$ cm/s.

In CIGS solar cells, diffusion length of the carrier is much lower than in Si materials [182] and a contact-to-contact distance below 50 µm [183] is required. Different methods are available to achieve a contact-to-contact distance around the micrometer magnitude:

- Dispersion of particles onto the surface. E. Leonard *et al.* [84] used an alumina powder dispersed in a solution. The Mo substrate is dipped in the solution and is dried. B. Vermang *et al.* [73, 87] used CdS particles by dipping the substrate in a CdS CBD solution. B. Vermang *et al.* [184] also used Mo nanoparticules fabricated in a highly ionized plasma. The layer that need to be perforated is then deposited and the particles are removed by ultra-sonic agitation, liquid CO_2 or mechanical wiping.
- Self organized spray-pyrolysis: W. Ohm *et al.* [93] fabricated a composited layer based on Al_2O_3 and ZnO particules by spray-pyrolysis. The etching of the ZnO in an acidic solution creates the openings in the layer.
- Lithography process: B. Vermang *et al.* [88] used a electron beam lithography to fabricated a well controlled array of nanosized openings.

Few studies have investigated the use of various oxide films to passivate the CIGS:

Al_2O_3 Atomic Layer Deposited (ALD) Al_2O_3 layer is extensively studied by the Si photovoltaic community for its ability to passivate the n- and p-type Si surface [185]. The passivation is attributed to a field-effect due

to a high density of fixed negative charge in the Al_2O_3 bulk (Q_f = 10^{12}-10^{13} .cm^{-2}) and a chemical passivation at the Si/Al_2O_3 related to a low interface trap charge density (D_{it}= 10^{10}-10^{12} eV^{-1}.cm^{-2}).

The use of Al_2O_3 for CIGS thin film at the Mo/CIGS interface was first studied using photoluminescence (PL) measurements. [107, 186]. The PL yield decreases under the influence of non-radiative recombination. W.-W. Hsu *et al.* [107] have observed an increase of the PL signal for the Mo/Al_2O_3/CIGS samples compared to the Mo/Al_2O_3 samples and have calculated a surface recombination velocity below 100 cm/s. Similar results were obtained by J. Joel *et al.* [186] with a direct analysis of the back interface: the CIGS is excited directly from the rear side using a thin semi-transparent Mo back-contact. Moreover, the fixed charge density and the interface-trap charge density at the ALD-Al_2O_3/CIGS interface have been investigated by R. Kotipalli *et al.* [187] using capacitance-voltage and conductance-frequency. Similarly to the Si/ALD-Al_2O_3/Si case, the CIGS is passivated by: 1/ a high density of fixed negative charges in the Al_2O_3 bulk (Q_f = 10^{13} cm^{-2}) that repels the minority carrier away from the back-contact; 2/ a low interface trap charge density (D_{it}= 10^{12} eV^{-1}.cm^{-2}) underlying a chemical passivation of the CIGS surface.

The first passivated CIGS back-contact device was presented by B. Vermang *et al.* [73] using an ALD-Al_2O_3 layer with randomly located openings of 220 ±25 nm spaced by 1.5 - 3 µm. For a 1.5 µm thick CIGS, an increase of V_{OC} of 14 mV was observed compared to the unpassivated cell and the surface recombination velocity was then estimated at around 10^2 cm/s. The improvement of the method leads to a cell efficiency of 13.5 % for a 400-nm-thick CIGS [87] and 11.8% for a 240-nm-thick CIGS [88]. Compared to the unpassivated 400-nm-thick CIGS cell (respectively the 240-nm-thick CIGS cell), the V_{OC} is 57 mV (57 mV) higher, the J_{SC} is 7.9 mA/cm^2 (3.8 mA/cm^2) higher whereas the FF remains almost constant (9.5%abs. higher).

The passivation effect of Al_2O_3 was also reported on SnO_2:F back-contact by Ohm *et al.* [93]. They observed a large increase of the V_{OC} (+52 mV) compared to the unpassivated SnO_2:F back-contact. Recently, the passivation effect of Al_2O_3 with linear opening spaced by 3 µm, 9 µm or 27 µm was studied by P. Casper *et al.* [188]. Only a poor electrical passivation effect was observed but, surprisingly, no decrease in FF was observed even for contact-to-contact distance of 9 µm. The collection of majority carrier over a long distance paves the way to further improvement.

TiO_2

TiO_2 has not been investigated yet as hole filter at the CIGS back-contact. The doping type of the TiO_2 is an important issue as it can be both n- or p-type, depending on the preparation method. The in-

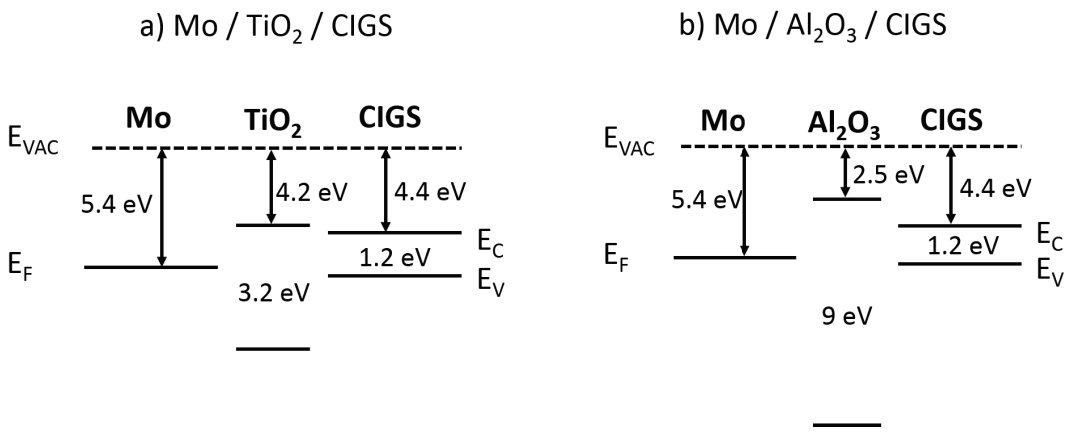

Figure 4.1.: Non equilibrium band-diagram of a) the $Mo/TiO_2/CIGS$ interface and b) the $Mo/Al_2O_3/CIGS$ interface.

trinsic doping is produced by the balance of 3 point defects: the donor oxygen vacancies ($V_O^{\bullet\bullet}$), the donor Ti interstitial (Ti_i^{3+}), and the acceptor Ti vacancies (V_{Ti}^{IIII}) [189, 190]. Anatase TiO_2, which is the most stable phase when annealed at a high temperature, is generally n-type. However, following the annealing condition, the doping can switch from n-type to p-type in a strongly oxidizing condition (temperature >450°C, 1-3h in air) [191, 192, 193]. Oxygen molecules are adsorbed at the TiO_2 surface which changes the ratio between the oxygen and metal vacancies. P-type can also be achieved by a suitable acceptor doping (such as Cr^{3+}, Fe^{3+}, Ni^{2+}, Ci^{2+}).

TiO_2 has an electron affinity of 4-4.2 eV and bandgap of 3-3.2 eV [194]. In contact with a CIGS with an electron affinity of 4.4 eV and band-gap of about 1.2 eV, we find roughly 0.2 eV offset for the conduction band and about 1.4 eV for the valence band (see Fig. 4.1). For an extremely p-doped TiO_2, a hole conduction would be possible and a electron blocking behavior could be possible. For a n-type TiO_2 hole transport. would be blocked point contacts between the CIGS and the Mo layer would be required.

MgF_2 The MgF_2 has a low refractive index permitting to improve the reflection at the back-contact. P. Casper et al. [188] have studied the possibility to also use it as a passivation layer. Compared to the unpassivated cells, the use of the MgF_2 layer increases the J_{SC} due to the higher reflection at the $Mo/MgF_2/CIGS$ interface but does not exhibit an electrical passivation effect. In this study, a poor electrical passivation effect was also observed with Al_2O_3.

SiO_2 C. Lare *et al.* [92] have studied the improvement of the cell performance by using arrays of SiO_2 particles at the Mo/CIGS interface. A light trapping can be achieved leading to an improvement of the J_{SC}. However

the possibility of a passivation effect was suggested but was not studied in details.

4.2.2. Choice of the passivation oxide

In this work, we have selected and compared two oxide films as passivation layer for the Mo/CIGS interface: Al_2O_3 and TiO_2. The reasons for these possibilities are:

Al_2O_3 Atomic Layer Deposited (ALD) Al_2O_3 layer has already been demonstrated to lead to an excellent passivation of the Mo/CIGS interface [87]. As no hole transport can be achieved trough the Al_2O_3 layer, point contacts between the CIGS layer and the Mo layer are required. Nano-imprint lithography was used to create the point contacts at various distance. However this technology involves many steps that are challenging for industrialization (see Fig. 4.4).

TiO_2 Due to the unique and versatile characteristics of the TiO_2, it is difficult to predict the behavior of the TiO_2 at the interface between CIGS and Mo. This is therefore an exploratory study about the impact of the TiO_2 on the cell performance and its passivation at the back interface. We have selected a sol-gel TiO_2 for its simple deposition technique by spin-coating. To prevent from a hole transport blocking behavior, the layer was also nano-structured by nano-imprint lithography.

Patterned and non-patterned Mo/oxide substrates were then prepared and characterized.

4.3. Materials, Methods and materials characterizations

Perforated sol-gel TiO_2 and ALD-Al_2O_3 were selected to achieve a passivation effect of the CIGS/Mo interface. The TiO_2 deposition, the different steps of the nano-structuration of TiO_2 and the different steps of the nano-structuration of the Al_2O_3 were performed in the frame of a collaboration with the *Laboratory of Photonics and Nanostructures* (LPN-C2N, UMR9001, Marcoussis). The Al_2O_3, the CIGS layers and the front-windows were deposited at IRDEP. The procedure is detailed in this section.

4.3.1. Substrate preparation

4.3.1.1. Preparation of the nano-imprint mold

A silicon master with the targeted patterns is first fabricated by electron beam lithography. The patterned used is detailed in Fig. 4.2 and contains 4 regions to develop square openings with a lateral size of 100 or 500 nm and a pitch of 2 µm, 4 µm or 8 µm. A negative mold is then obtained by stamping the silicon master with PDMS.

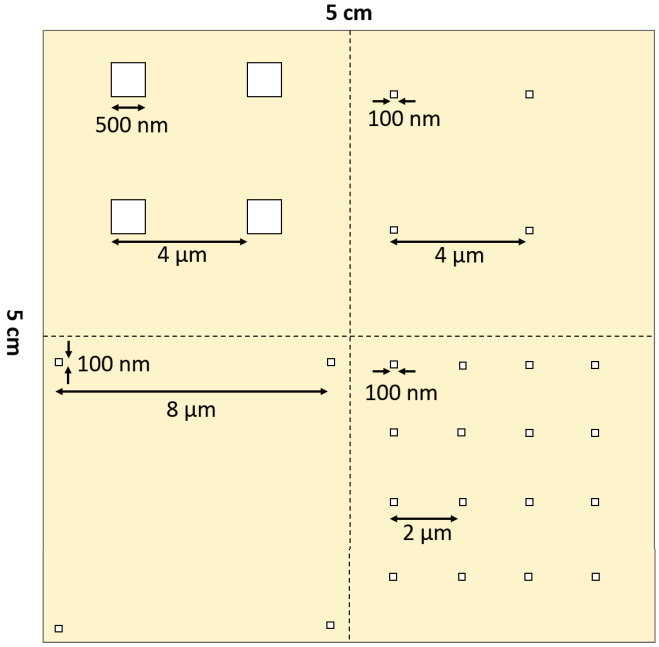

Name	Opening size	Pitch
C0	No patterning	
C100P2	100 nm	2 µm
C100P4	100 nm	4 µm
C500P2	500 nm	4 µm
C100P8	100 nm	8 µm

Figure 4.2.: Schematics of the patterns used for the nano-imprint process. Square size and pitch are displayed with the same scale.

4.3.1.2. Nano-patterned TiO_2 layer on Mo

The procedure for the deposition and nano-structuration of the TiO_2 layer is schematized in Fig. 4.3.

4.3.1.3. Nano-patterned Al_2O_3 layer on Mo

The procedure for the deposition and nano-structuration of the Al_2O_3 layer is schematized in Fig. 4.4.

4.3.1.4. CIGS deposition and device fabrication.

The CIGS was deposited on the patterned and non-patterned TiO_2 and Al_2O_3 layers on Mo using a 1 stage process as explained in Fig. 3.12a. The evaporation rate was kept constant to avoid a composition gradient. To analyze the impact of the oxide layers on the Na diffusion, a NaF post deposition treatment (NaF PDT) was performed on half of the samples. For the NaF PDT, NaF was evaporated for 8 min at 300°C at a rate of 1-2 nm/min under Se. Complete cells were competed using the standard front window detailed in sec. 2.2.2.

For the samples without NaF PDT, 8 cells of 0.5 cm^2 for each pattern were separated by the standard mechanical scribing and a Ni/Al grid was evaporated. For the samples with NaF PDT, 20 cells of 0.1 cm^2 were separated by chemical etching of the front-window/CIGS layers. Results are more reproducible with the chemical etching.

For the photoluminescence characterizations, only a CdS layer was deposited to prevent the degradation of the CIGS surface.

1. Spin-coating of the sol-gel TiO_2 on the Mo substrate. The sol-gel TiO_2 was prepared from a solution containing molar ratios of 1 $TiCl_4$: 40 EtOH: 15 H_2O in presence of a structuring agent. The resulting TiO_2 layer has a thickness of 50-60 nm and well covers the Mo substrate;

2. The PDMS mold is applied on the TiO_2 film;

3. Calcination at 110°C to stabilize the nano-structures. The mold is withdrawn;

4. The remaining TiO_2 inside the opening is removed by Reactive Ion Etching.

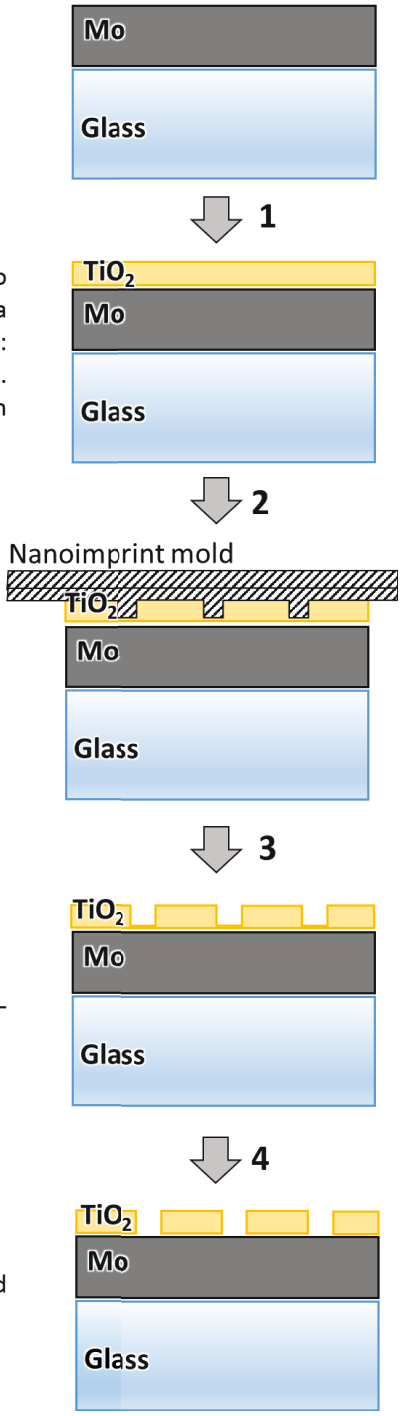

Figure 4.3.: Schematics of the procedure for the deposition and nano-structuration of the TiO_2 layer. More details on the sol-gel preparation in [195].

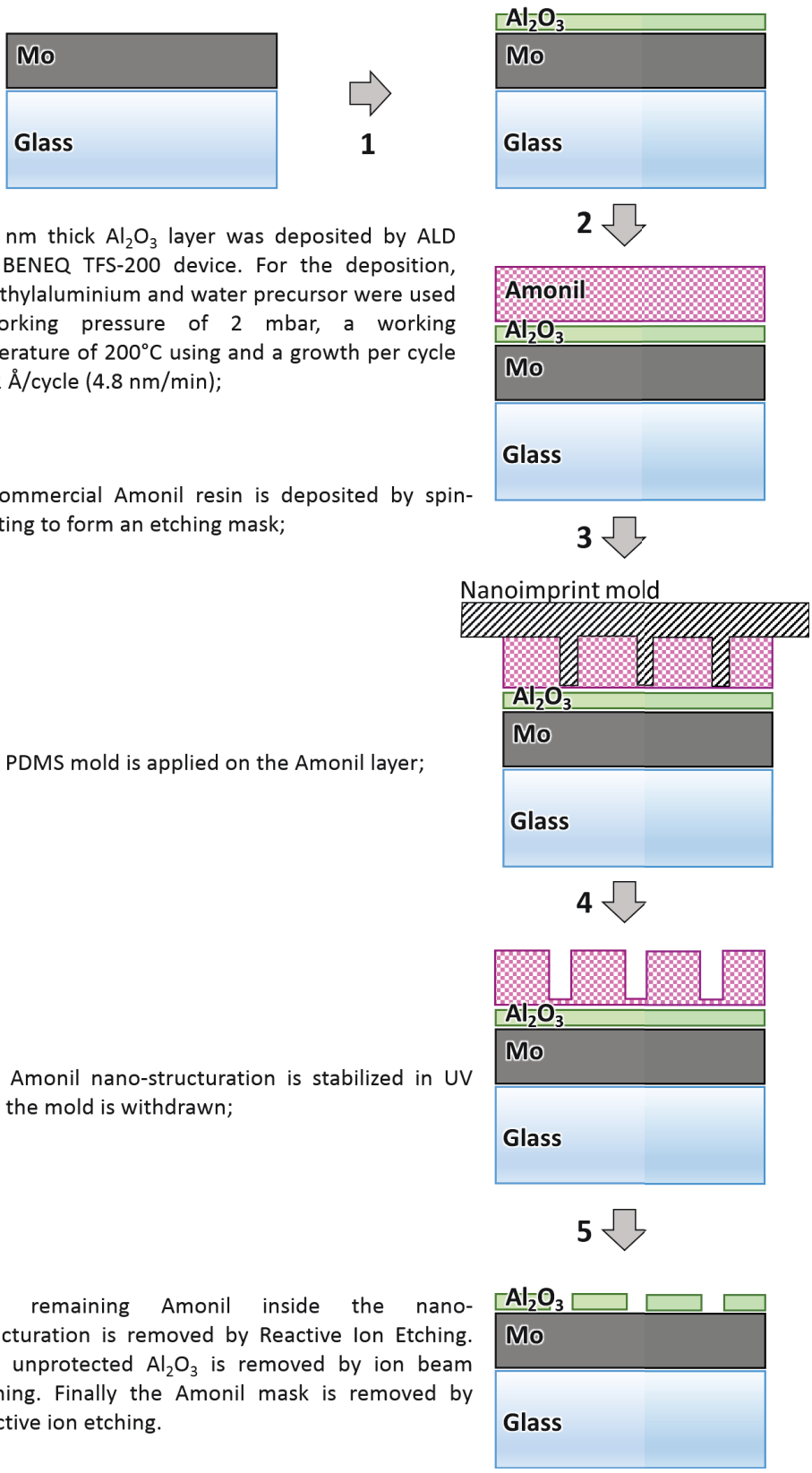

1. A 20 nm thick Al_2O_3 layer was deposited by ALD with BENEQ TFS-200 device. For the deposition, trimethylaluminium and water precursor were used a working pressure of 2 mbar, a working temperature of 200°C using and a growth per cycle of 1.2 Å/cycle (4.8 nm/min);
2. A commercial Amonil resin is deposited by spin-coating to form an etching mask;
3. The PDMS mold is applied on the Amonil layer;
4. The Amonil nano-structuration is stabilized in UV and the mold is withdrawn;
5. The remaining Amonil inside the nano-structuration is removed by Reactive Ion Etching. The unprotected Al_2O_3 is removed by ion beam etching. Finally the Amonil mask is removed by reactive ion etching.

Figure 4.4.: Schematics of the procedure for the deposition and nano-structuration of the Al_2O_3 layer.

4.3.2. Materials characterization

4.3.2.1. Morphology, light reflection and resistivity of the Mo/oxide substrate before CIGS deposition

The Mo/oxide substrates were first analyzed to verify the quality of the samples.

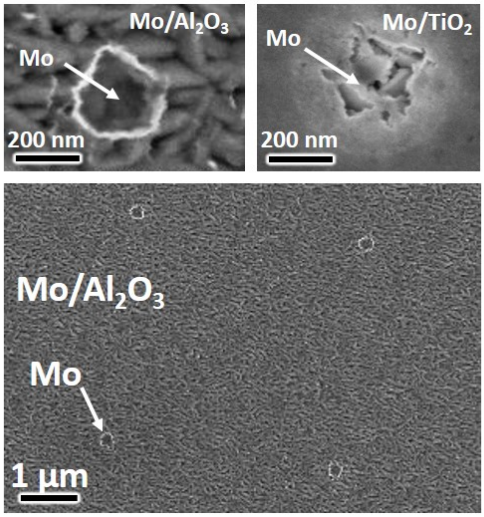

Figure 4.5.: SEM images of the surface of the patterned Al_2O_3 and TiO_2 . Only the pattern with the 100 nm lateral size structures and a pitch of 4 µm are presented.

SEM images of the openings fabricated with the pattern of 100 nm lateral size structures and a pitch of 4 µm are showed in Fig. 4.5. Note that the Al_2O_3 layer is thin enough to be transparent for the SEM electron beam. The Mo morphology is discernible but the edges of the openings are clear. The lateral size of the opening is approximately 200 nm.

Reflection measurements were performed on the Mo, Mo/TiO_2 and Mo/Al_2O_3 substrates without nanostructurations and are shown in Fig. 4.6. The oxide films tends to decrease the reflectance of the Mo layer. However, its impact on the light absorption in the CIGS layer in a compete cell is difficult. Hence, the Mo/oxide stacks were simulated using the optical simulation by RTM (more details in sec. 2.2.4.2). These calculations showed that both Mo/TiO_2 and Mo/Al_2O_3 substrate can enhancement the cell photocurrent of approximately 0.5 mA/cm^2 for a 400-nm-thick CIGS .

We tried to measure the resistivity of the substrate by a 4-point probe. For both Mo/TiO_2 and Mo/Al_2O_3, the sheet resistance was too high for our device ($>10^2$ Ω.cm).

4.3.2.2. Electrical characteristics of the oxide layer substrate after CIGS deposition

Electrical characterization of the Al_2O_3 and TiO_2 layer after the CIGS deposition was not performed in this study. Impedance spectroscopy of transistor like structure

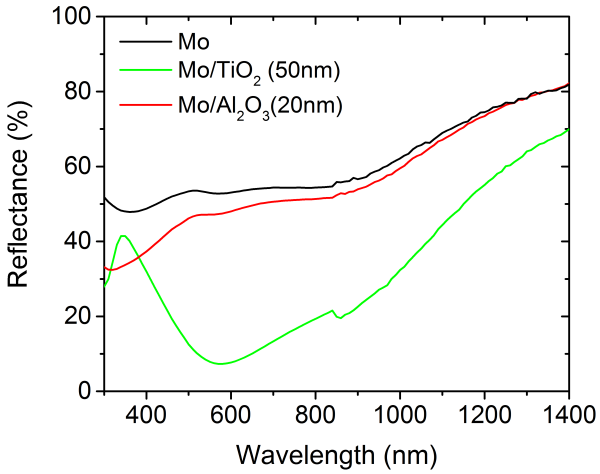

Figure 4.6.: Light reflectance of the non-patterned substrate.

would have given substantial information.

The TiO_2 structure was characterized by Grazing-Incident XRD (GIXRD). An incident angle of 0.7° was chosen to maximize the signal at the Mo/CIGS interface. To increase the signal intensity, CIGS thickness was reduced to below 100 nm using a dibromide solution. The diffractogram of samples with and without TiO_2 layer are presented in Fig. 4.7. We observe a small (101) peak of the TiO_2 anatase at $2\theta = 25.35°$ but no peak of the TiO_2 rutile. Therefore, during the CIGS deposition at 500°C, the TiO_2 slightly crystallizes in the anatase phase.

During the annealing, the TiO_2 retracts and could crack. The presence of cracks in the TiO_2 layer was verified by an EDS cartography. For a better EDS signal, the CIGS thickness was almost completely removed using a dibromide solution. No discontinuity in the Ti signal was observed at the micro- and macro-scaled (not shown here).

4.3.2.3. Characterization of the CIGS layer

The final composition measured by EDS and the CIGS thickness measured on the SEM cross-sectional images of the samples are summarized in Tab. 4.1.

Table 4.1.: Composition and thickness of the samples.

	Without NaF PDT	With NaF PDT
CIGS thickness	380±20	390±20
CGI	0.75	0.87
GGI	0.30	0.33

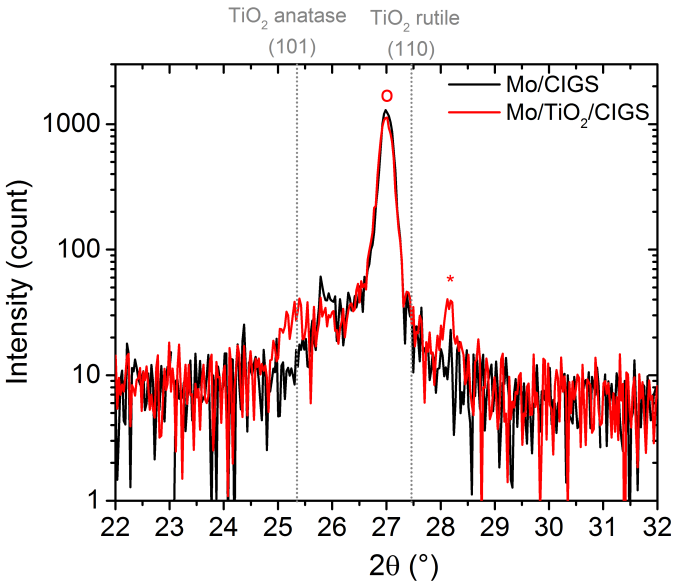

Figure 4.7.: GI-XRD diffractogram of sample with and without the TiO_2 layer. The angle of incidence was 0.7°. The CIGS thickness was reduced by a chemical etching. o: CIGS (112). *: CdS (101). Reference patterns: TiO_2 anatase 00-004-0477, TiO_2 rutile 00-004-0551, CdS 00-041-1049.

The SEM cross-sectional images are shown in Fig. 4.8. No change in morphology was observed when the CIGS is grown on TiO_2 or Al_2O_3 instead of Mo. The 50 nm TiO_2 and 20 nm Al_2O_3 are dense.

Composition profile of the samples was measured by GD-OES. The atomic ratio as a function of the sputtering time is presented in Fig. 4.9. The profiles show no composition gradient. The Cu, In, Ga and Se signals rapidly decrease inside the oxide layer indicating no excessive diffusion elements. The Na signal intensity of the CIGS grown on Mo/oxide is compared to the CIGS grown on Mo. Without NaF PDT, the CIGS on Mo/TiO_2 and on Mo has a similar Na signal intensity. In Fig. 4.9a and Fig. 4.9b, similar trends for Na diffusion is observed when using a Mo or a Mo/TiO_2 back-contact. Therefore, Na easily diffuses from the glass through TiO_2 layer. The Na concentration with and without NaF PDT remains close. On the opposite, without NaF PDT, the Na signal of the CIGS on Mo/Al_2O_3 is close to the background noise. The NaF PDT seems to accumulate Na in the CIGS layer. This indicates that the Al_2O_3 layer acts as a barrier for Na diffusion between the Mo and the CIGS layer. It should be noticed that the Na concentration obtained in the CIGS layer seems very excessive compared to the CIGS on Mo.

The CIGS layers grown on Mo, TiO_2 and Al_2O_3 with and without NaF PDT were characterized by XRD using the standard Bragg-Brentano configuration. The Log-tering factors, calculated as explained in sec. 2.3.2.1 and Eq. 2.4, are presented in Fig. 4.10. We observe that the CIGS is (112)-preferred oriented for each substrate. The CIGS grown on Mo/TiO_2 is only slightly less (112)-preferred oriented compared

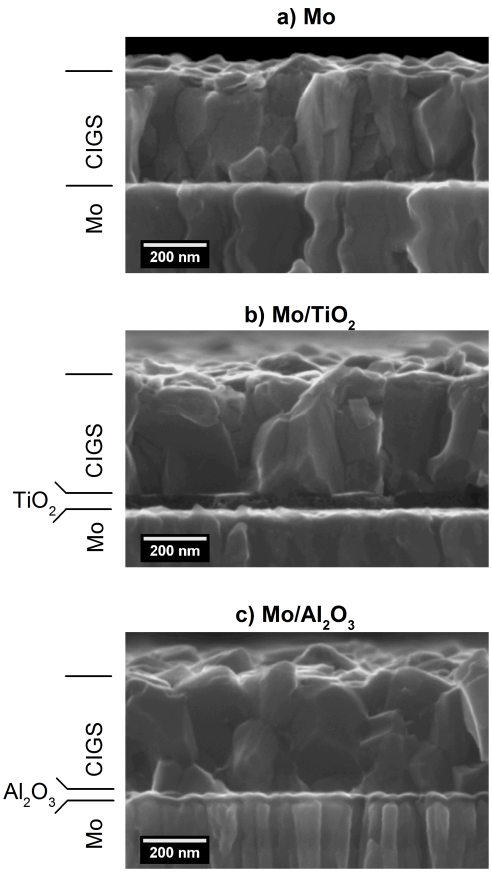

Figure 4.8.: Cross sectional SEM images of the sample with NaF PDT a) without oxide, b) with TiO_2 and c) with Al_2O_3.

to the CIGS on Mo and Mo/Al_2O_3. The NaF PDT has few impact on the CIGS preferred orientation. This comparison indicates similar CIGS growth behavior and therefore the different samples should be comparable.

4.3.3. Conclusions

Sol-gel TiO_2 and ALD-Al_2O_3 layers were deposited on 800 nm sputtered Mo coated on soda-lime glass substrate. The electrical contact was permitted by local openings in the oxide layer made by a nano-imprint lithography process. Some samples were fabricated without openings for comparison. To conclude:

- 20 nm of ALD-Al_2O_3 and 50 nm of non annealed sol-gel TiO_2 were deposited on a Mo substrate.
- Some samples were nano-structured by nano-imprint lithography to create openings in the oxide layer. Different patterns were used. The pattern with the largest passivated surface has a 2-dimention arrays of 100 nm large square

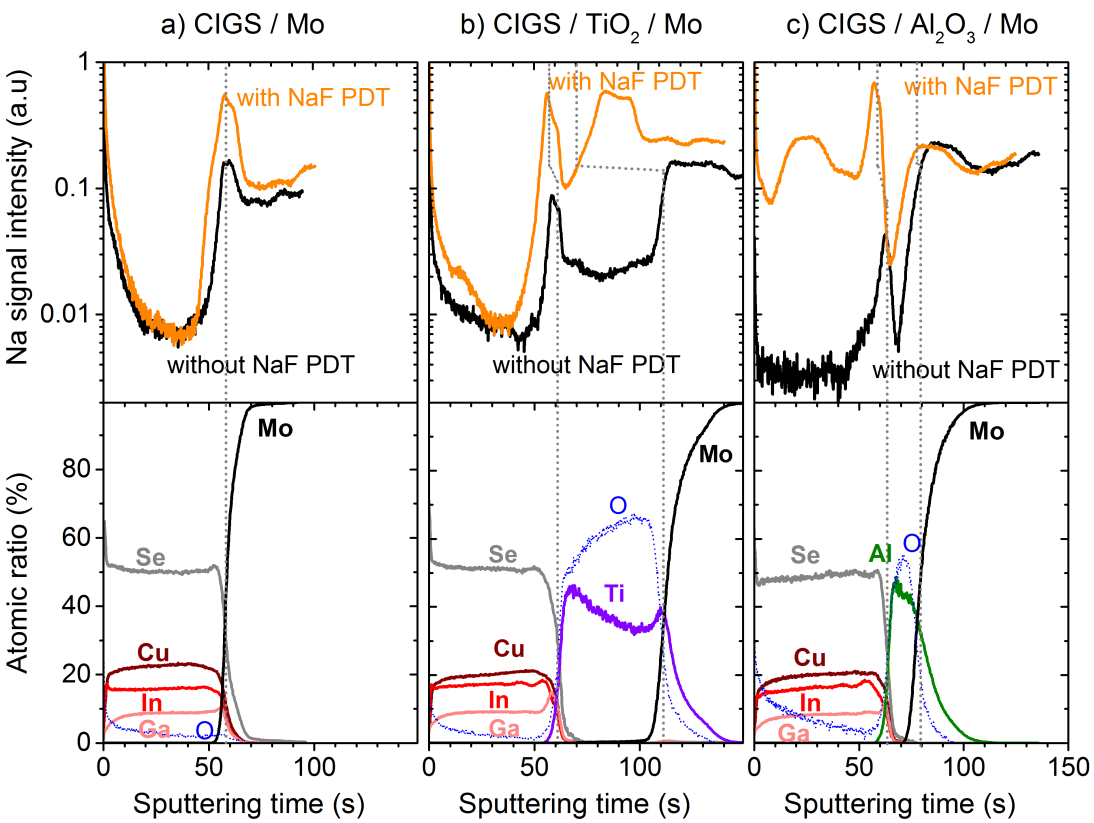

Figure 4.9.: GD-OES profile of the samples on Mo and Mo/oxide. At the top: Na signal intensity without correction. At the bottom: Atomic ratio quantification of the main elements.

openings spaced by 8 µm;

- The reflection at the Mo/oxide layer theoretically increase the cell photocurrent of 0.5 mA/cm² compared to the Mo back-contact;
- The CIGS growth (morphology and preferred orientation) on the oxide layers is very similar to the CIGS growth on the Mo layer. However the TiO_2 layer is permeable to Na whereas the Al_2O_3 layer acts as a Na barrier.
- Characteristics of the TiO_2 layer after the CIGS process, in particularly its doping type, are still under study.

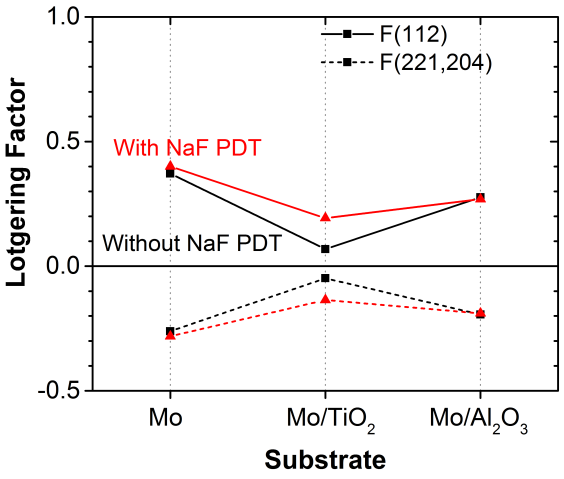

Figure 4.10.: Logtering factors of the main CIGS peak calculated according to the XRD patterns of the CIGS on different substrates.

4.4. Cell performances

The completed solar cells were characterized under AM1.5 100 mW/cm² illumination and in the dark.

For samples without NaF PDT, the cells were separated using the standard mechanical scribing. However, this method proved to be unadapted to samples with a Mo/oxide back-contact. In fact, most of the cells were either shunted or incompletely separated. As a consequence, the statistical significance of the result is low and it was not possible to compare the impact of the opening patterns on the cell performances. For each substrate, only the best cell is presented.

Based on these results, for samples with NaF PDT, the cells were separated using a chemical etching of the CIGS/front-window layers. This method leads to better results than the mechanical scribing. Cell performances with the different patterns are very similar and the number of cells is too low to conclude on the best pattern. Therefore, only the C100P8 pattern, which corresponds to the pattern with the larger passivated surface, is presented but does not necessarily leads to the higher efficiency.

4.4.1. Mo/TiO_2 substrate

The Tab. 4.2 summarized the I(V) parameters of the best cells for the samples on Mo, patterned- and unpatterned-/Mo/TiO_2. The corresponding I(V) curves and EQE are displayed in Fig. 4.11.

The reference cell on Mo reached an efficiency of 7.7% without NaF PDT and 8.5% with NaF PDT which is the expected performance for 380-390-nm-thick CIGS cells.

Surprisingly, without any openings in the TiO_2 film, an efficiency of 9.5 % was achieved on Mo/TiO_2 substrate. The V_{OC} is 625 mV and the J_{SC} is 21.4 mA/cm², which is respectively 25 mV and 1.1 mA/cm² higher than the reference cell on Mo. No change in FF is observed. This result means that an hole collection was achieved though the TiO_2 but the reason is still under discussion. The following explanations can be suggested:

1. A hole transport is achieved through the TiO_2 layer that becomes p-type after *in-situ* annealing at 500°C. The TiO_2 is stabilized in air at 110°C but is crystallized in vacuum at 500°C during the CIGS process. Since the p- or n-character depends on the equilibrium between oxygen vacancies, Ti interstitials and Ti vacancies, it is difficult to say what is the dominant charge carrier.
2. The TiO_2 is porous and is filled by a conducting phase allowing a contact with the Mo layer. According to previous studies of the TiO_2 [195], the layer should have a porosity of approximately 35%.

Table 4.2.: Best I(V) parameters under light illumination of samples on Mo and Mo/TiO_2 substrate. Samples were prepared in 2 separated CIGS/CdS/ZnO/ZnO:Al batches. *: low statistical significance.

		I(V) light				I(V) dark			
NaF PDT	Substrates	Efficiency (%)	J_{SC} (mA/cm²)	V_{OC} (mV)	FF (%)	J_{01} (mA/cm²)	J_{02} (mA/cm²)	R_{SH} (Ω.cm²)	R_S (Ω.cm²)
Without	Mo	7.7	19.6	574	69	-	-	-	-
	Mo/TiO_2 C0	not performed				-	-	-	-
	Mo/TiO_2 C500P4*	4.5	20.2	422	53	-	-	-	-
With	Mo	8.5	20.4	600	70	8.10^{-10}	8.10^{-5}	7.10^{2}	0.5
	Mo/TiO_2 C0	9.5	21.5	625	71	3.10^{-10}	1.10^{-6}	$> 1.10^{5}$	0.3
	Mo/TiO_2 C100P8	8.1	20.6	620	63	7.10^{-11}	2.10^{-5}	$> 1.10^{5}$	0.8

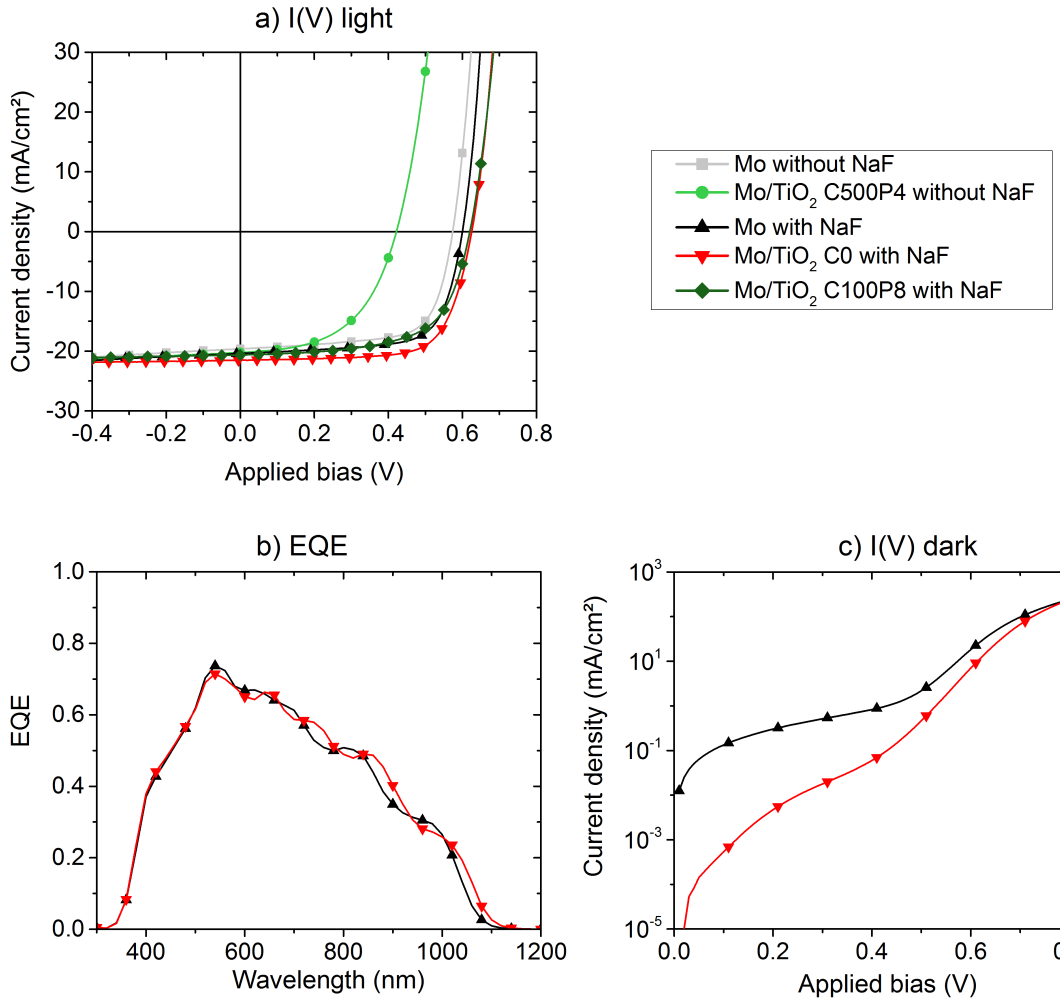

Figure 4.11.: Cell characterization of the samples on Mo, Mo/Al_2O_3 and Mo/TiO_2 with a NaF PDT.

The better V_{OC} is due to a decrease in both J_{01} and J_{02}. The influence of the J_{01} and J_{02} on the V_{OC} variation have been calculated according to the equations Appendix A. The variation of J_{01} and J_{02} equally contribute to the decrease in V_{OC}. We can therefore conclude on a small passivation effect of the back-contact (lower J_{01}) but also a better cell properties in the SCR (lower J_{02}).

Thus, nano-structuration of the TiO_2 is not necessary. CIGS on patterned-Mo/TiO_2 with NaF PDT leads to an efficiency of 8.1%. The cell still shows an improvement in the V_{OC} compared to the reference cell on Mo but suffers from a lower FF.

The dark I(V) curves clearly show that cells with the TiO_2 layer at the back-contact have higher shunt resistance with only Mo. The TiO_2 layer inhibits shunt paths through the CIGS layer.

However, without NaF PDT, an efficiency of only 4.5 % was achieved on a patterned-

Mo/TiO_2. The J_{SC} is close to the J_{SC} of the Mo reference cell without NaF. However, the V_{OC} decreases from 574 mV to 422 mV. As Na concentration in the CIGS is comparable to the Mo/CIGS samples according to the GD-OES measurements (see Fig. 4.9) , the low V_{OC} can be due to a high recombination at the TiO_2/CIGS interface. Moreover, the FF decreases from 69 % to 53 %.

4.4.2. Mo/Al_2O_3 substrate

The Tab. 4.3 summarized the I(V) parameters of the best cell for the samples on Mo and on the unpatterned- and patterned-Mo/Al_2O_3. The corresponding light and dark I(V), and EQEs are displayed in Fig. 4.11. The reference cell on Mo reached an efficiency of 7.7% without NaF PDT and 8.0% with NaF PDT.

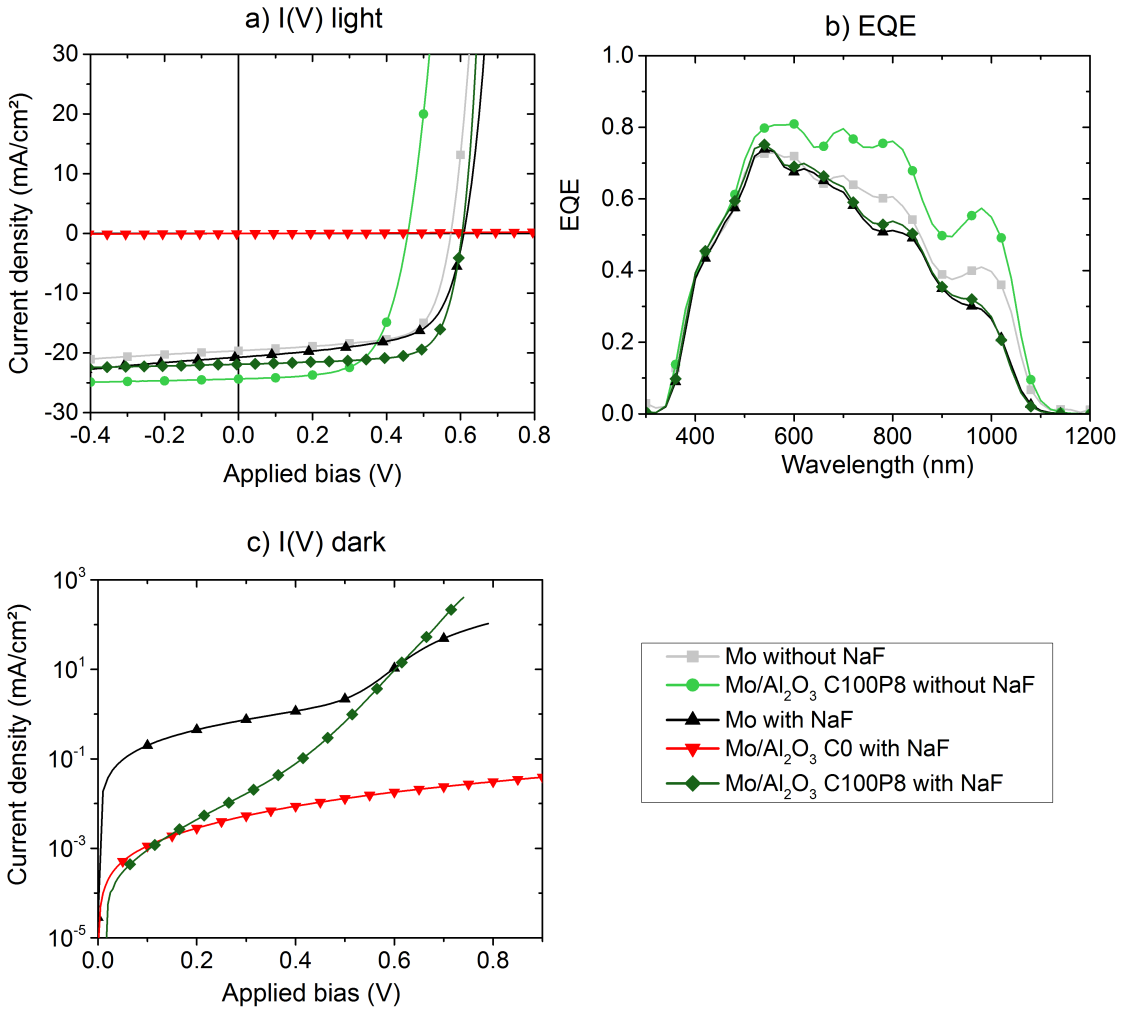

Figure 4.12.: Cell characterization of the samples on Mo and Mo/Al_2O_3

When Al_2O_3 layer is used at the back-contact without any openings (Mo/Al_2O_3 C0),

Table 4.3.: I(V) parameter for light illumination and in the dark of the best cells on Mo and Mo/Al_2O_3 samples. Samples were prepared in 2 separated CIGS/CdS/ZnO/ZnO:Al batch. *: low statistical significance.

		I(V) light				I(V) dark			
NaF PDT	Substrates	Efficiency (%)	J_{SC} (mA/cm^2)	V_{OC} (mV)	FF (%)	J_{01} (mA/cm^2)	J_{02} (mA/cm^2)	R_{SH} (Ω.cm^2)	R_S (Ω.cm^2)
Without	Mo	7.7	19.6	574	69	-	-	-	-
	Mo/Al_2O_3 C0	$\oslash$	< 0.01	< 50	25	-	-	-	-
	Mo/Al_2O_3 C100P8*	7.2	24.1	462	65	-	-	-	-
With	Mo	8.0	20.7	609	63	3.10^{-10}	6.10^{-5}	5.10^2	1.1
	Mo/Al_2O_3 C0	$\oslash$	< 0.01	< 50	25	$\oslash$	$\oslash$	$> 1.10^5$	$\oslash$
	Mo/Al_2O_3 C100P8	9.6	21.9	604	73	2.10^{-10}	4.10^{-5}	$> 1.10^5$	< 0.1

as expected no current collection was achieved. This also means that no deterioration of the Al_2O_3 appears during the CIGS deposition.

When Al_2O_3 layer is perforated, a current collection was achieved. The patterned-Mo/Al_2O_3 C100P8 without NaF PDT leads to an efficiency of 7.2 % with a J_{SC} of 24.1 mA/cm², V_{OC} of 462 mV and a FF of 65% (Tab. 4.3) . An efficient carrier collection is obtained though the openings. J_{SC} is 4.5 mA/cm² higher than the reference cell on Mo. The corresponding EQE (in Fig. 4.11b) shows an upward shift for all wavelength. As Na plays a role in the CIGS p-doping, the low Na concentration in this sample may enlarge the space charge region width through the whole CIGS thickness. For a back-contact with low recombination, this effect can lead to a better collection. Therefore this higher J_{SC} suggests a passivating effect of Al_2O_3 at the Mo/CIGS interface. However, the V_{OC} is 112 mV lower than the reference cell on Mo, surely due to the lower Na concentration that reduces the CIGS p-doping. Moreover the FF remains almost constant. The Al_2O_3 layer does not influence series resistance.

To get rid of the impact of the low Na concentration on the V_{OC}, the same measurements were carried out on the samples with a NaF PDT. The patterned-Mo/Al_2O_3 C100P8 with NaF PDT leads to an efficiency of 9.6% with a J_{SC} of 21.9 mA/cm², a V_{OC} of 604 mV and a FF of 73%. Once again, an efficient carrier collection is obtained though the openings. Compared to the Mo reference, the main change is due to the higher FF (+10%). The shunt resistance is very high, meaning that the Al_2O_3 layer prevents shunt paths through the CIGS layer. Moreover the series resistance is surprisingly low. The majority carrier collection is therefore not affected by the large lateral distance to reach the point contact. J_{SC} slightly increases compared to the Mo reference (+1.2 mA/cm²) but not the V_{OC}. An increase of 0.5 mA/cm² was expected with the Al_2O_3/Mo substrate due to the better interface reflection according to sec. 4.3.2.1. As a consequence, the change in J_{SC} and V_{OC} is much lower than the theoretical expectation of a passivation effect (approximately +200 mV according to the simulation Fig. 2.3 and +3 mA/cm² according to Fig. 3.3).

4.4.3. Conclusion

The study of the cells with a TiO_2 or Al_2O_3 layer inserted between the CIGS and the Mo layers leads to the following conclusion:

- Better performances were achieved with both Mo/TiO_2 and Mo/Al_2O_3 substrates compared to Mo substrate (respectively 9.5% and 9.6% compared to 8-8.5%).
- The 50 nm TiO_2 film deposited by sol-gel allows a hole conduction from the CIGS layer to the Mo layer. The reason is not clear and further investigations of the TiO_2 layer after the CIGS process are required (such as the determination of the doping type by capacitance spectroscopy and the element diffusion by XPS).

- The 20 nm Al_2O_3 film deposited by ALD is a hole blocking layer. However, a hole collection is possible through point contacts at least 8-µm spaced without loss in J_{SC} and without increase in the series resistance. In-depth investigations are required to explain this effect (such as electroluminescence measurements to observe the charge carrier diffusion length in a Mo/Al_2O_3 surface). This effect was also recently observed for contact-to-contact distance of 9 µm with Mo/Al_2O_3 and Mo/MgF_2 substrate by P. Casper *et al.* [188].
- The passivation effect of the TiO_2 and Al_2O_3 is not clear. In the case of TiO_2, the better V_{OC} compared to the unpatterned substrate is related to both lower recombination in the SCR and QNR. In the case of Al_2O_3 the Na concentration seems to be an important parameter. A fully depleted CIGS thickness greatly enhance the charge collection. However no increase in V_{OC} was observed and the best performance was mainly due to a reduction of the parallel conductivity.

For a better understanding of the passivation effect of TiO_2 and Al_2O_3, photoluminescence (PL) characterizations were performed.

4.5. Study of the passivation effect by photoluminescence

The PL-yield decreases under the influence of non-radiative recombination. For very thin CIGS thicknesses (below 500 nm), the charge-carriers are generated over the whole CIGS thickness. As a consequence, the PL signal is sensitive to the recombination at the back-contact. PL spectra were measured on non-patterned back-contact/CIGS/CdS stacks with a 532 nm laser.

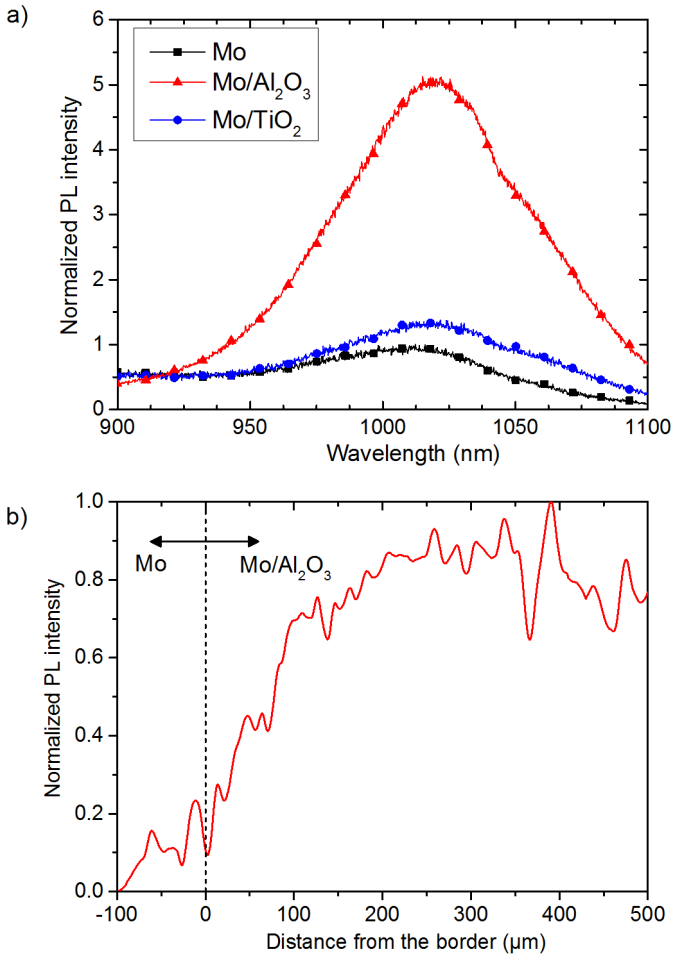

Figure 4.13.: Photoluminescence (PL) measurements of the CIGS on non-patterned substrates. a) PL spectra normalized with respect of the Mo sample, b) PL maximum intensity special profile across the Mo and Mo/Al_2O_3 border.

The measurements are presented in Fig. 4.13a. The spectra were normalized with respect of the PL maximum intensity of Mo/CIGS/CdS sample. For Mo/TiO_2 substrate, the signal is not significantly higher than on Mo substrate. As a consequence, the TiO_2 layer probably neither passivates nor deteriorates the Mo/CIGS interface.

For Mo/Al_2O_3 substrate the signal is 5 fold higher than the signal on the Mo substrate. This increase is too large to be only related to an optical effect and suggests a better interface properties obtained by a passivating effect of Al_2O_3.

To estimate its impact on the V_{OC} the PL-yield (Y_{PL}) is analyses. According to the Generalized Planck's Law, the PL-yield is given by:

$$Y_{PL} \propto \int_{E_G}^{\infty} E^2 \cdot \frac{dE}{\exp\left(\frac{E-\mu}{kT}\right) - 1} \tag{4.1}$$

with E the energy of the emitted light, μ the chemical potential of the electron-hole paire, E_g the CIGS band-gap, k the Boltzmann's constant and T the temperature. For decently illuminated solar cells, we can approximate $\left(\frac{E-\mu}{kT}\right) \gg 1$ and Eq. 4.1 can be analytically solved in:

$$Y_{PL} = C \cdot \exp\left(\frac{\mu}{kT}\right) \tag{4.2}$$

with C a constant that depends only on temperature and E_g.

As a consequence of Eq. 4.2, the increase of PL-yield due to the Al_2O_3 layer is related to an increase of the chemical potential ($\Delta\mu$) according to the relation in Eq. 4.3:

$$\Delta\mu = kT \cdot \ln\left(\frac{Y_{PL}^{Mo/Al_2O_3}}{Y_{PL}^{Mo}}\right) \tag{4.3}$$

Using a $Y_{PL}^{Mo/Al_2O_3}/Y_{PL}^{Mo}$ ratio of 5 as observed in Fig. 4.13a, $q.\Delta\mu$ is calculated at 40 mV. As μ is equal to the splitting of the quasi-Fermi level, $q\Delta\mu$ gives an upper limit of the V_{OC} increase when the Al_2O_3 layer is inserted between the Mo and CIGS layer. This increase was unfortunately not observed in Tab. 4.3.

An additional sample was fabricated on a substrate with a clear border between a bare-Mo region and a Mo/Al_2O_3 region. The PL maximum intensity spatial profile across this border is displayed Fig. 4.13b. Note that the PL spot is smaller than 5 µm and that the signal noise is due to spatial variations typically observed for coevaporated CIGS layer [196]. Away from the border, the signal intensity ratio between Mo and Mo/Al_2O_3 region is comparable to the values obtained in Fig. 4.13a. In between, the signal gradually increases over 200 µm in the Mo/Al_2O_3 region.

To explain this effect, the following reason can be suggested: when the CIGS is illuminated by the laser in Mo/Al_2O_3 region a voltage difference appears between

the illuminated area and the Mo region. As a consequence, the generated charges are drifted away and less recombination occur in the measurement area which leads to a reduction of the PL signal intensity. Away from the border in the Mo/Al_2O_3 region this voltage difference is reduced by a lateral resistance which limits the distance of the drift effect. Even if no quantitative value can be easily calculated with the PL profile, this measurements highlights that the bias voltage can be implemented over a large distance (order of magnitude of 100 µm) and therefore highlights a low lateral resistance in the Al_2O_3 /CIGS structure. This effect may explain the low series resistance obtained for cells on patterned-Mo/Al_2O_3 back-contact.

4.6. Conclusion of the chapter

In this chapter, we have compared two oxide films as passivation layer for the Mo/CIGS interface: Al_2O_3 and TiO_2. The following points can be highlighted:

- **Al_2O_3 layer is known to passivate Mo/CIGS interface** [87]: a chemical passivation by reducing the interface defects and a electical passivation due to negative fixed charge in Al_2O_3 bulk. In this work, 20 nm of ALD-Al_2O_3 was deposited on a Mo substrate. As hole cannot overpass the Al_2O_3 layer, point opening in the Al_2O_3 layer was created by physical etching of the Al_2O_3 layer with a nanoimprint lithography mask.
- **TiO_2 has been investigated at the CIGS back-contact for the first time.** In this work, 50 nm of sol-gel TiO_2 was deposited on a Mo substrate. The TiO_2 layer was also nano-structured by nano-imprint lithography. However it is difficult to predict the behavior of the TiO_2 at the interface between CIGS and Mo. Characteristics of the TiO_2 layer after the CIGS process, in particularly its doping type, are still under study.
- **The CIGS growth** (morphology and preferred orientation) on the oxide layers is very similar to the CIGS growth on the Mo layer. However the TiO_2 layer is permeable to Na whereas the **Al_2O_3 layer acts as a Na barrier**. A NaF PDT is therefore necessary.
- **Cell on Mo/TiO_2 back-contact with a 390-nm-thick CIGS reaches 9.5 %**, which is higher than the cell on standard Mo back-contact (8.5%). Surprisingly, **no opening in the TiO_2 layer was necessary**. To explain this effect, further investigations of the TiO_2 layer after the CIGS process (doping-content, nano-cracks) are required.
- **Cell on Mo/Al_2O_3 back-contact with a 390-nm-thick CIGS reaches 9.6 %**, which is higher than the cell on standard Mo back-contact (8.0%). Point opening through the Al_2O_3 layer was necessary to collect charges. In this case the point opening was 100-200 nm large and spaced by 8 µm. The increase of V_{OC}, which is expected for lower back-contact recombination, is not observed. The increase of J_{SC}, which is expected for lower collection loss, is observed only if the cell is poorly doped (possibly fully depleted). As a consequence, only a poor passivation effect was achieved. However, a **great attenuation of the parasitic resistance** is observed.
- **The PL measurements** of the back-contact/CIGS/CdS structures highlight **a better interface property in the case of Al_2O_3** back-contact compared to TiO_2 or Mo back-contact. On one hand, the increase in the PL-yield should lead to an increase of the V_{OC} up to 40 mV. On the other hand, it suggests the formation of a low lateral resistance in the Mo/Al_2O_3/CIGS structure.

To conclude this chapter, a slight passivation of the Mo/CIGS back contact was observed when an Al_2O_3 layer is inserted between the Mo and the CIGS layers.

The performance of ultra-thin CIGS can then be improved by replacing the Mo back-contact with the reflective back-contact developed in the previous chapter.

5. Ultra-thin CIGS solar cells on reflective and passivating back-contact

5.1. Introduction

We have seen in **Chapter 2**, that the Mo/CIGS back-interface is the main issue when making ultra-thin CIGS solar cell. This back-interface must be more reflecting and more passivating and should therefore be modified.

We have highlighted in **Chapter 3** the possibility to replace the Mo back-contact by a TCO. As the TCO is semi-transparent, a reflector can be added at the rear-side of the glass substrate. This way, we achieved solar cells with higher efficiencies than the one on Mo back-contact for CIGS thicknesses of 260 and 450 nm. However, this configuration suffers from:

- an optical loss due to the Glass/TCO absorption when light is reflected behind the glass;
- a collection loss due to high recombination at the TCO/CIGS interface, especially when the TCO used is SnO_2:F.

Moreover in **Chapter 4**, we have fabricated samples with a perforated Al_2O_3 layer between the CIGS and the Mo layer. This Al_2O_3 layer is stable during the CIGS process at high temperature, act as barrier for element and slightly passivates the Mo/CIGS back-interface.

At the light of the previous chapters, two advanced cell structures can be fabricated:

1. a cell on TCO back-contact with the perforated passivation Al_2O_3;
2. a cell with a Cu reflector encapsulated between the Mo and the Al_2O_3 layer.

The performances of these 2 structures are discussed in this chapter.

5.2. Passivated bifacial CIGS solar cells

This section explores the passivation of the TCO back-contact with a perforated Al_2O_3 layer. We proceed the same way as for the passivation of the Mo back-contact explained in Chapter 4.

This structure has also been investigated by W. Ohm et al. [93]. They developed a passivation alumina layer for the SnO_2:F/CIGS interface and they reached an efficiency of 10.1% for a 620-nm-thick-CIGS cell.

5.2.1. Samples preparation

For the cell fabrication, the CIGS was deposited on 3 different back-contacts on a soda-lime glass:

- a standard 800-nm-thick Mo back-contact.
- a commercial SnO_2:F back-contact.
- a 1100-nm-thick ZnO:Al substrate.

20 nm of ALD-Al_2O_3 was deposited on both TCO's surface. Openings were created through the Al_2O_3 following the recipe explained in Fig. 4.4.

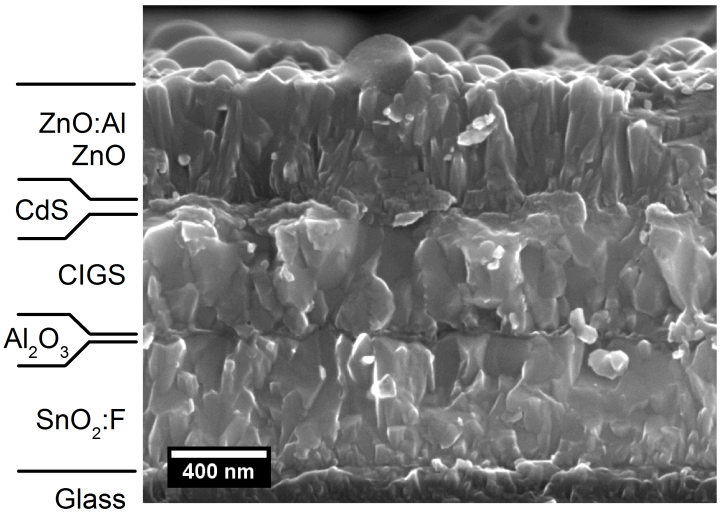

Figure 5.1.: Cross sectional SEM image of the CIGS cell on passivated SnO_2:F back-contact.

The CIGS was evaporated during 15 min by a 1-stage coevaporation process at a substrate temperature of approximately 500°C. The evaporation rate was kept constant to avoid a composition gradient. Subsequently to the CIGS deposition, a NaF post deposition treatment (NaF PDT) was performed: NaF was evaporated for 8 min at 300°C at a rate of 1-2 nm/min under Se atmosphere. The resulting CIGS

thickness, measured by profilometry, is 480 ± 20 nm and the resulting composition measured by XRF is CGI = 0.91 and GGI = 0.36.

Complete cells were competed using the standard front window CdS/ZnO/ZnO:Al detailed in sec. 2.2.2. The 3 samples were processed together in the same CIGS, CdS, ZnO, ZnO:Al batch. For each samples, 20 cells of 0.06 cm^2 were separated by chemical etching of the front-window/CIGS layers.

The cross sectional image of the cell structure is presented in Fig. 5.1. The different layers can be easily distinguish.

For the photoluminescence (PL) characterizations, specific samples were fabricated: a 5x5 cm^2 glass/TCO substrate with 20 nm of ALD-Al_2O_3 covering half of the surface. The same CIGS process used for cell fabrication was performed. A CdS layer was immediately deposited to prevent the formation of surface defects. This configuration allows a analysis of the impact of the Al_2O_3 passivating layer with exactly the same CIGS materials.

5.2.2. Performance of the passivated bifacial solar cells

Unfortunately, cells on the patterned-ZnO:Al/Al_2O_3 back-contact gave no results.

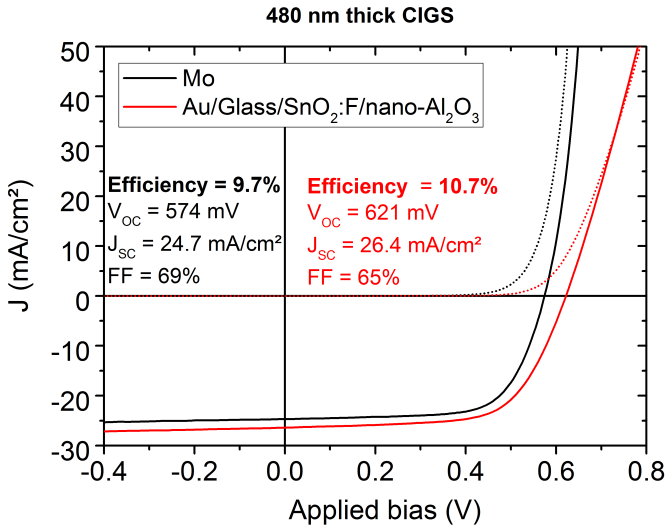

Figure 5.2.: I(V) curve of the best cell on patterned-SnO_2:F/Al_2O_3 back-contact and on Mo back-contact. The measurements were performed under illumination (solid line) and in the dark (dotted line).

Solar cells on patterned-SnO_2:F/Al_2O_3 back-contact was characterized under 1 sun illumination. A gold-reflector was placed at rear-side of the glass substrate to reflect the light. The I(V) and EQE curves are presented in Fig. 5.2 and Fig. 5.3. The cell was also measured in the dark and the dark-I(V) parameters fitted with a 2-diode

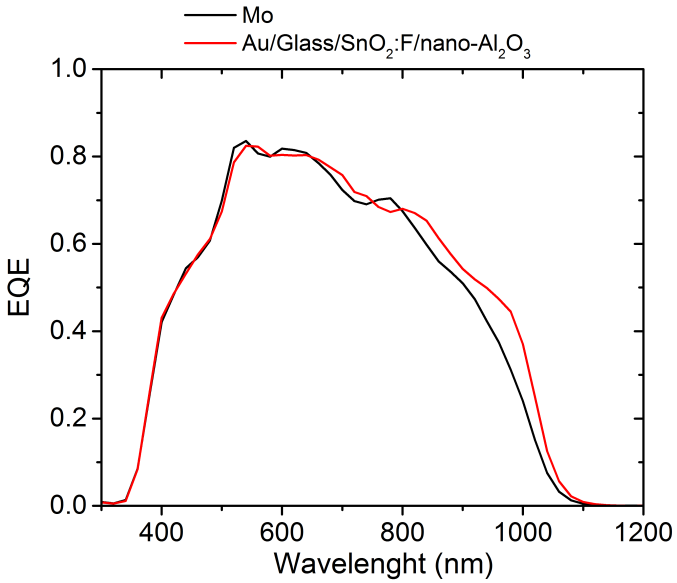

Figure 5.3.: EQE curves of the best cell on patterned-SnO_2:F/Al_2O_3 back-contact and on Mo back-contact.

model are shown in Tab. 5.1. The results are compared to the reference sample on Mo back-contact.

As observed in Fig. 5.2, we reached an efficiency of 10.7 % with the 480-nm-thick CIGS on the patterned-SnO_2:F/Al_2O_3 back-contact with an Au reflector. For comparison, the reference on Mo reached 9.7 %. We observe an increase in the J_{SC} (+1.7 mA/cm²) and in the V_{OC} (+47 mV).

The increase in J_{SC} is correlated to an upshift of the EQE curve in the wavelength above 800 nm (Fig. 5.3). However, this increase is lower than the increase observed for the 450-nm-thick CIGS without passivating layer in Tab. 3.8, but no light-soaking effect was observed. To explain this difference between the passivated and non-passivated cells, we suggest that the Al_2O_3 layer acts on the defects that are also passivated by light-soaking in the non-passivated cells (sec. 3.5).

The increase in V_{OC} is analyzed with the saturation currant J_{01} and J_{02} variations according to the equations detailed in Appendix A. The theoretical V_{OC} calculated directly from J_{01} and J_{02} in Tab. 5.1 is higher than the experimental V_{OC}, mainly due to the violation of the shifting approximation between the light- and dark-I(V) curves. We calculate that the lower J_{01}, observed for the cell on SnO_2:F/Al_2O_3 back-contact compared to Mo back-contact, is responsible of an increase in the V_{OC} of approximately 25 mV. This increase can be mainly related to lower recombination at the back-contact interface. Moreover, a lower J_{02} is also observed and is responsible for an increase in the V_{OC} of approximately 13 mV, probably related to lower recombination in the SCR because of a better CIGS bulk quality.

The FF of the cell on SnO_2:F/Al_2O_3 back-contact is slightly lower compared to the

Table 5.1.: I(V) dark parameters for one of the best cells. The curves are fitted with a two-diode model (J_{01} and J_{02}: saturation current for ideality factor of 1 and 2, R_{SH}: shunt resistance, R_S: series resistance). The measured V_{OC} under illumination (V_{OC} (exp)) is compared the theoretical V_{OC} calculated from J_{01} and J_{02} ($V_{OC}(J_{01}, J_{02})$). The V_{OC} variations related to J_{01} and J_{02} were calculated according to the equations in Appendix A.

Back-contact			Mo	SnO2:F/ nano-Al2O3
Dark I(V) parameters	J_{01}	(mA/cm²)	$6.6 \cdot 10^{-10}$	$5.3 \cdot 10^{-10}$
	J_{02}	(mA/cm²)	$5.5 \cdot 10^{-10}$	$7.7 \cdot 10^{-10}$
	R_S	(Ω.cm²)	0.2	4.3
	R_{SH}	(Ω.cm²)	$1 \cdot 10^5$	$4 \cdot 10^4$
V_{OC}	V_{OC}(exp)	(mV)	566	613
	$V_{OC}(J_{01}, J_{02})$	(mV)	622	658
V_{OC} variation compared to Mo	$\triangle V_{OC}(J_{01})$	(mV)		+25
	$\triangle V_{OC}(J_{02})$	(mV)		+13

cell on Mo back-contact: -4%abs (as observed in Fig. 5.2). According to the dark-IV fit parameters in Tab. 5.1, This decrease is mainly due to a high series resistance of 4.3 Ω.cm². Note that this increase of series resistance was however not observed in the case of the passivated Mo/Al_2O_3 back contact in sec. 4.4.2.

To conclude, a cell on with an efficient charge carrier collection on patterned-SnO_2:F/Al_2O_3 back-contact was achieved. However, other characterization techniques are required to validate the observation of a passivation effect of the Al_2O_3 layer.

5.2.3. In-depth back-contact recombination characterization

The recombination at the back-interface was characterized by 3 methods: analysis of the rear-illuminated EQE, analysis of the PL-yield and analysis of the time-resolved PL-decay.

5.2.3.1. Analysis of the rear-illuminated EQE

The best cell on patterned-SnO_2:F/Al_2O_3 back-contact was also characterized under rear-side illumination. The reflection at the rear-side was suppressed using a black-paper. The I(V) and the EQE curves are presented in Fig. 5.4 and Fig. 5.5.

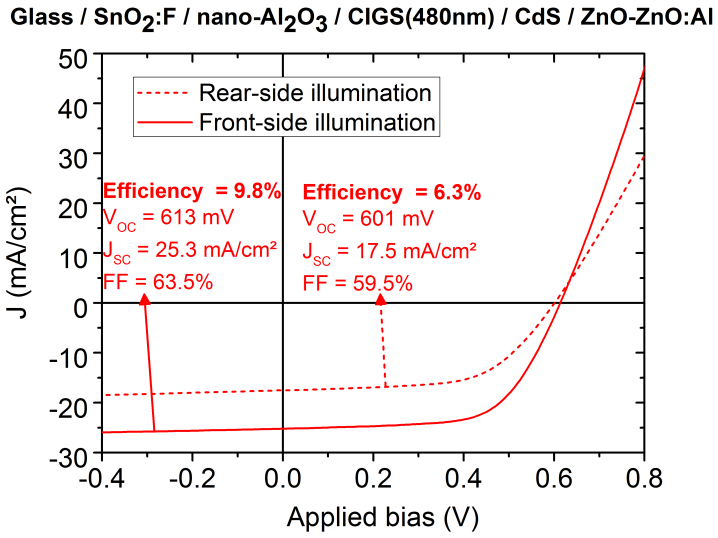

Figure 5.4.: I(V) curve for rear-side illumination of the best cell on patterned-SnO_2:F/Al_2O_3 back-contact.

As observed in Fig. 5.4, an efficiency of 6.3% was reached, which is lower than the efficiency for front-side illumination. This difference is mainly due to a much lower J_{SC}: 17.5 mA/cm² instead of 25.3 mA/cm². This lower J_{SC} is correlated to a weak EQE for all wavelengths (see Fig. 5.5). As explain in sec. 3.4.3.3, a high back-contact recombination can explain this effect.

The rear-side illuminated EQE of the sample on SnO_2:F back-contact can be simulated using the generation and collection model. The charge carrier generation is simulated with the Ray Transfer Method (see sec. 2.2.4.2). The light absorption profile in the CIGS layer was calculated for the following cell stack ZnO:Al(380nm) / ZnO(60nm) / CdS(45nm) / CIGS(450nm) / SnO_2:F(670nm) / Glass and for rear-side illumination. The charge carrier collection profile was calculated according to the model described in sec. 1.2.3.3 with h=0.95, w=250 nm and $S_{n,BC}$ varying from 10^3 to 10^7 cm/s.

The simulated EQE curves and the experimental rear-side illuminated EQE curve are presented in Fig. 5.5. From the qualitative comparison between the experiments and the simulations, $S_{n,BC}$ approximately ranges from 10^6 to 10^5 cm/s. For comparison, with non-passivated SnO_2:F back-contact, a $S_{n,BC}$ between 10^6 and 10^7 was found. This result highlights a slight passivation effect of the Al_2O_3 layer.

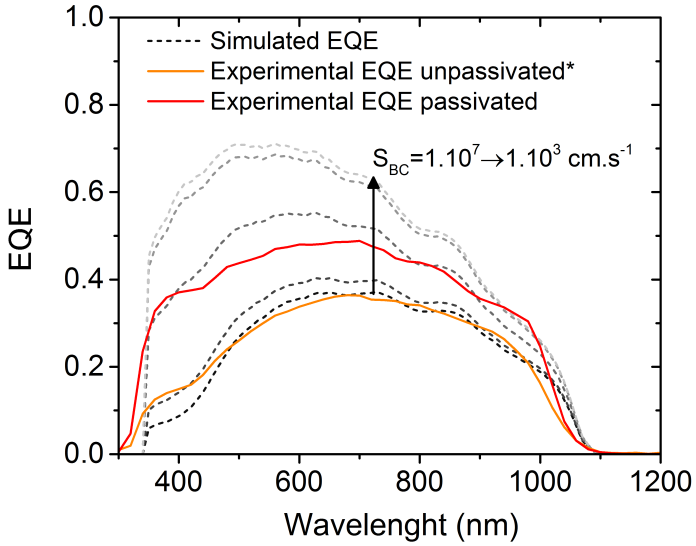

Figure 5.5.: Rear illuminated experimental EQE (solid line) and simulated EQE (dotted line). The 480-nm-thick CIGS cell on SnO_2:F/Al_2O_3 back-contact (passivated - red) is compared to the 450-nm-thick CIGS cell on SnO_2:F back-contact (unpassivated - orange) from Fig. 3.25. The collection model was set with a back-contact recombination velocity $S_{n,BC}$ varying from 10^3 to 10^7 cm/s, w=250 nm and h=0.95.

5.2.3.2. Analysis of the PL-yield

We also investigate the defects in the CIGS by PL. The PL-yield decreases under the influence of defect-related recombinations: bulk recombination, grain boundary recombination or surface recombination.

The PL measurements were performed in a HORIBA Scientist device with a 532 nm laser. The spot size was approximately 1 µm at the CIGS/CdS surface of the sample. We compared samples on ZnO:Al, ZnO:Al/Al_2O_3, SnO_2:F and SnO2:F/Al_2O_3.

The PL spectra are displayed in Fig. 5.6. We observe that the use of a Al_2O_3 layer at the interface between the TCO and the CIGS layer increases the PL signal approximately 5 folds the signal of CIGS on a bare TCO contact. A similar increases in the PL-yield was observed between the Mo and the Mo/Al_2O_3 back contact in sec. 4.5.

From such increase in PL-yield and according to the Generalized Planck's Law Eq. 4.1, a maximum V_{OC} increase of 40 mV is expected with the Al_2O_3 layer at the back-contact. This result highlights a reduction of the recombination in the CIGS layer.

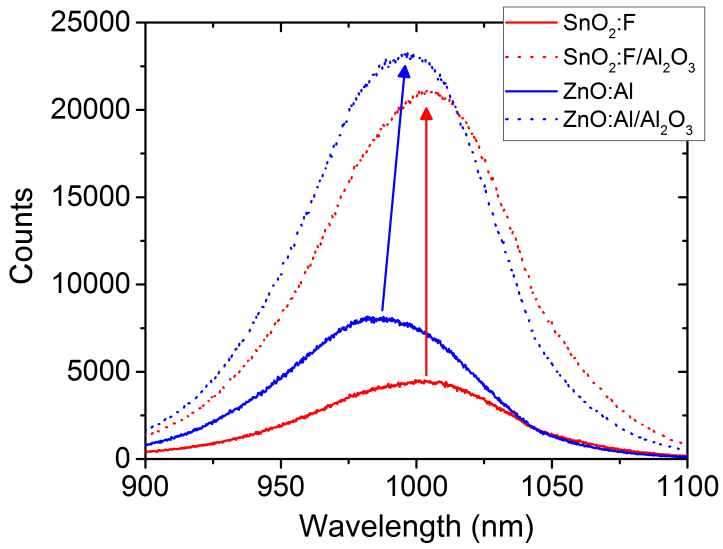

Figure 5.6.: Photoluminescence (PL) measurements of the CIGS on TCO back-contacts with and without the Al_2O_3 passivated layer.

5.2.3.3. Analysis of the PL-decay

For the time-resolved photoluminescence (TRPL) experiments, the excitation source is a *Fianium Supercontinuum* laser whose wavelength is selected using a *Photon Etc Laser Line Tunable Filter*. The laser was coupled into an optical fiber connected to a homemade microscope. The laser pulse duration was 6 ps and the repetition rate was set to 1 MHz. The sample was then excited using a Nikon objective with a numerical aperture $N.A. = 0.8$ on a spot size of approximately 1 µm. The selected pulsed excitation wavelength was 532 nm and the corresponding excitation intensity is equal to $1.8 \cdot 10^{15}$ photons/pulse/cm^2 which is in the high injection range. The detection of the PL decay dynamics was made using the time-correlated single-photon counting technique (TCSPC) giving a time resolution of approximately 100ps.

We observe in Fig. 5.7 that the PL-decay should be fitted by a double-exponential decay. The extraction of two lifetimes that governs the decay was was studied by G. El-Hajje *et al.* [197] in the case of CIGS: a short lifetime related to the direct recombination events *via* recombination centers (τ_{rec}) and a long lifetime related to trap states emission events (τ_{trap}) .

The TRPL decay was analyzed using the following expression:

$$I_{TRPL}(t) = A_{rec} \cdot \exp\left(-\frac{t}{\tau_{rec}}\right) + A_{trap} \cdot \exp\left(-\frac{t}{\tau_{trap}}\right) \tag{5.1}$$

with A_{rec} and A_{trap} the occurrence weight of the center-related recombination and the trap-state-related recombination.

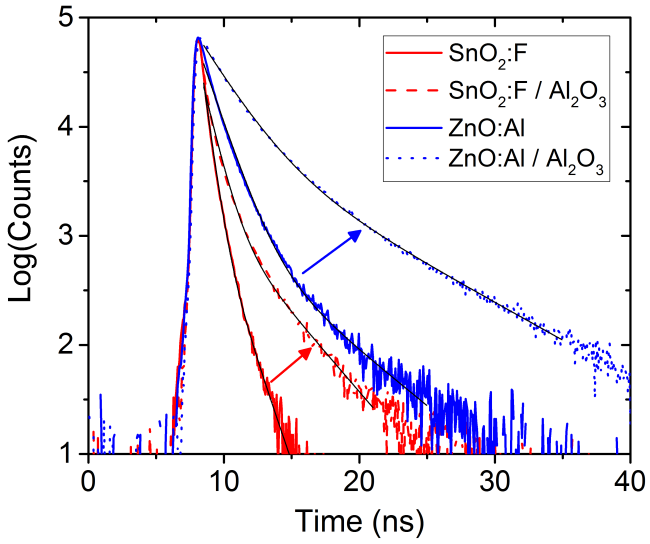

Figure 5.7.: Measured photoluminescence (PL) counts as a function of time for front-side excitation of the CIGS on TCO back-contacts with and without the Al_2O_3 passivated layer. The line in black correspond to the double-exponential fit the the PL decay.

Table 5.2.: Double-exponential fit of the normalized TRPL decay.

	A_{rec} (count)	τ_{rec} (ns)	A_{trap} (count)	τ_{trap} (ns)
SnO_2:F	0.37	0.5	0.03	1.2
SnO_2:F/Al_2O_3	0.34	0.8	0.03	3.0
ZnO:Al	0.56	1.2	0.02	4.3
ZnO:Al/Al_2O_3	0.75	2.0	0.11	6.3

The longer lifetimes is related to the presence of emission traps. They have a finite density of accessible states delaying the emission of the PL signal. Those traps start to reduce the effective recombination rate and gives to the data the appearance of a longer recombination lifetime than the actual recombination lifetime. However, under high injection regimes, the longer decay disappears and the decay becomes mono-exponential [198]. As a consequence, to reduce the influence of the emission traps on the minority carrier dynamic, a high injection regime was used to characterize the samples.

By fitting 5.1, we can extract the values of each of the occurrence weight (A_{rec} and A_{trap}) and the corresponding lifetime (τ_{rec} and τ_{trap}). The value are presented in Tab. 5.2. We observe that the ratio ($A_{rec}/(A_{rec} + A_{trap})$) is close to unity, therefore the recombinations are predominant over the trapping event [197]. As τ_{rec} is related

to the non-radiative recombination ($\tau_{rec}^{-1} = \tau_{\text{radiative}}^{-1} + \tau_{\text{non-radiative}}^{-1}$), this is the key parameter to probe the CIGS quality.

In Tab. 5.2, a higher τ_{rec} is found for TCO back-contact with the Al_2O_3 layer. This result highlights a better carrier dynamics quality, and hence, a better material quality. Moreover, τ_{rec} is higher in the case of ZnO:Al back-contact than with SnO_2:F meaning that a better passivation can be achieved with ZnO:Al.

5.2.3.4. Conclusion on the passivation effect of the TCO/CIGS interface

The better charge collection, measured from the EQE of the cell on TCO/Al_2O_3 back-contact, is correlated to an improvement of PL-yield and an improvement of the carrier life-time. We can conclude to a slight passivation effect of the Al_2O_3 layer that should be responsible for an increase in the V_{OC} of 40 mV maximum.

These results are consitant with the experimental improvement of V_{OC}. In Tab. 5.1, between the sample on non-passivated Mo back-contact and on passivated SnO_2:F back-contact, we observed an increase in the V_{OC} of 53 mV and we estimated that approximately 25 mV was related to the back-interface.

5.3. Encapsulated mirror

In the case with the nano-structured Al_2O_3 passivating layer, the electrical contact is only permitted by few percents of the surface. In this configuration, the main part of the interface can exhibit other properties. This surface can be a stack of material that achieves a good reflectivity. The only condition is that the last layer, in contact with CIGS, should be Al_2O_3.

In the literature, B. Vermang *et al.* [87] have inserted a 60-nm-thick MgF_2 layer between the Mo back-contact and the Al_2O_3 passivating layer. With this configuration, they reached an solar cell efficiency of 13.5% for 400-nm-thick CIGS.

We decided to insert a Cu layer between the Mo back-contact and the Al_2O_3 passivating layer. The insertion of the reflector directly under the Al_2O_3 layer should improve the light absorption in the CIGS compared to the reflector/glass/TCO configuration.

5.3.1. Samples preparation

The back-contact was prepared by a nano-imprint lithography with a combination of physical and chemical etching. A schematics of the resulting substrate is presented in Fig. 5.8. The fabrication process was:

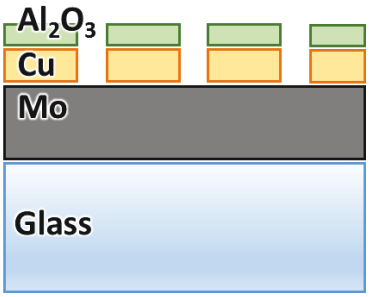

Figure 5.8.: Schematic of the Cu-encapsulated mirror on Mo back-contact.

1. Deposition of the 800-nm-thick Mo back-contact by magnetron sputtering. Thermal evaporation of a 100-nm-thick Cu layer. Deposition of a 20-nm-thick ALD-Al_2O_3layer;
2. Nano-patterning of the Al_2O_3 layer by nano-imprint lithography according to the process detailed in Fig. 4.4. The mask creates a square pattern 100 or 500 nm large and spaced by 2, 4 or 8 µm.
3. Physical etching of the Al_2O_3layer by Ion Beam Etching;
4. Chemical etching of the Cu layer with a 40:1:4 solution of de-ionized water, 97%wt sulfuric acid and 30%wt hydrogen peroxide;

5. The etching mask is removed by Reactive Ion Etching.

SEM images of the surface of the resulting substrate are presented in Fig. 5.9. Openings are created but they seems larger than initial template: for the upper SEM image in Fig. 5.9b, the opening appears almost 1.1 µm large instead of 100 nm and for the the lower SEM image in Fig. 5.9b, the opening appears almost 1.6 µm large instead of 500 nm. This can be due to an under-etching of the Cu layer during the Cu chemical etching. As a consequence, the openings in the Al_2O_3 layer is smaller than the openings in the Cu layer. The Al_2O_3 layer become in contact with the Mo layer, which seals the border of the opening and protects the Cu layer from the CIGS deposition.

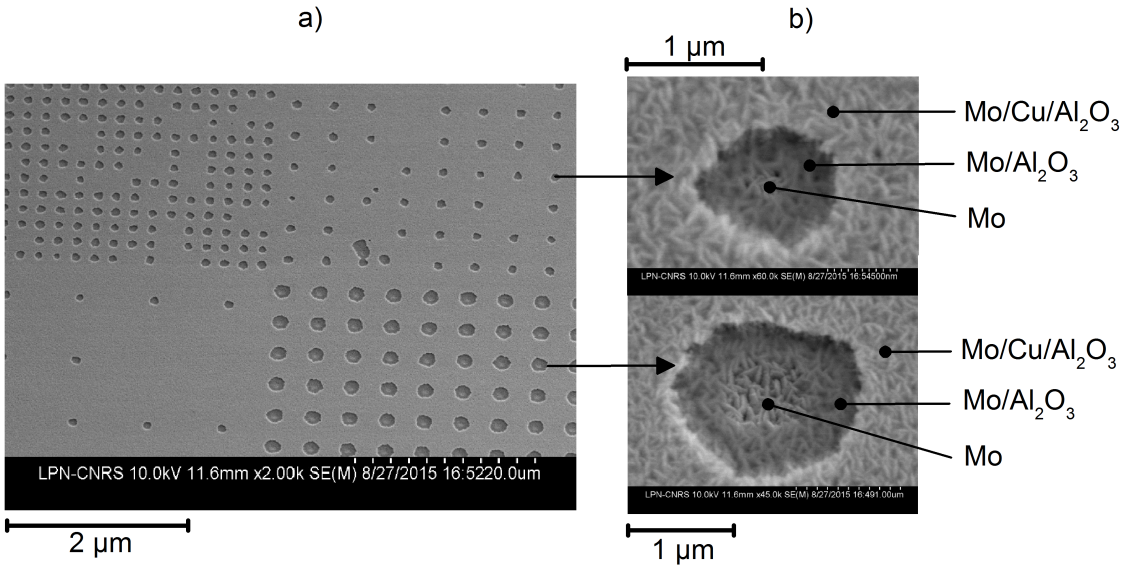

Figure 5.9.: SEM images of the nano-structured encapsulated Cu-mirror substrate: a) the different pattern used, b) details of the openings.

The CIGS was evaporated during 15 min by a 1-stage coevaporation process at a substrate temperature of approximately 450°C. This temperature is lower than the previous experiments to avoid cracks in the Cu or CIGS layers due to their different thermal expansions. The evaporation rate was kept constant to avoid a composition gradient. Subsequently to the CIGS deposition, a KF PDT was performed: KF was evaporated for 5 min at 300°C at a rate of 1-2 nm/min under Se atmosphere. The resulting CIGS thickness, measured by profilometry, is 280 ± 10 nm.

The structure after the CIGS deposition is presented in Fig. 5.10. From the observation of the cross sectional SEM image in Fig. 5.10a, no inter-diffusion between the CIGS and the Cu can be noticed. As observed in the SEM image of the CIGS surface in Fig. 5.10b, the CIGS appears darker at proximity of the perforation. This effect is probably due to a topological contrast in the secondary electron detection.

Complete cells were competed using the standard front window CdS/ZnO/ZnO:Al detailed in sec. 2.2.2. 20 cells of 0.1 cm^2 were separated by mechanical scribing of

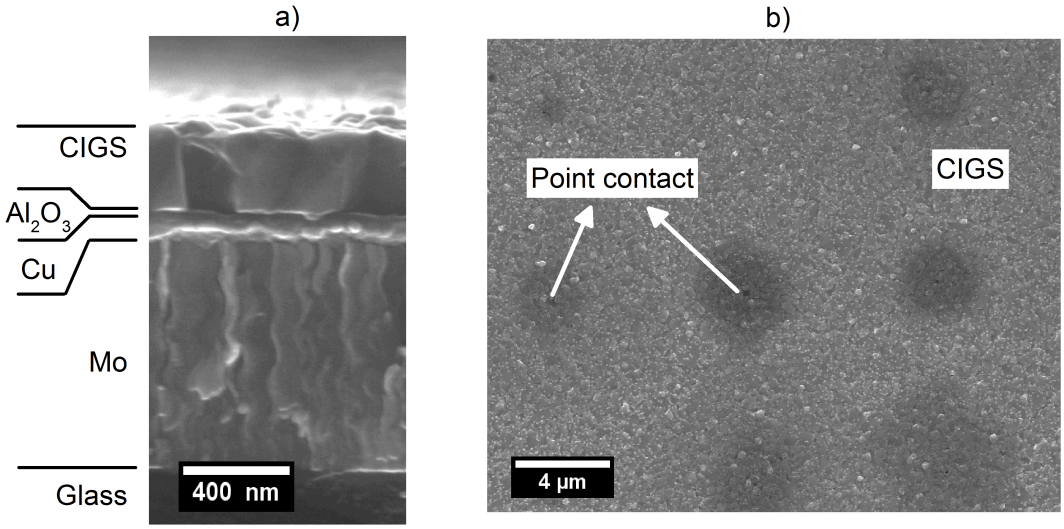

Figure 5.10.: SEM images of a) cross section of the CIGS deposited on the encapsulated Cu-mirror substrate. b) surface of the CIGS.

the front-window/CIGS layers.

5.3.2. Cell performance

The sample was characterized under illumination illumination. The I(V) curve is presented in Fig. 5.11. The reference sample on standard Mo back-contact has an efficiency of 6.3%.

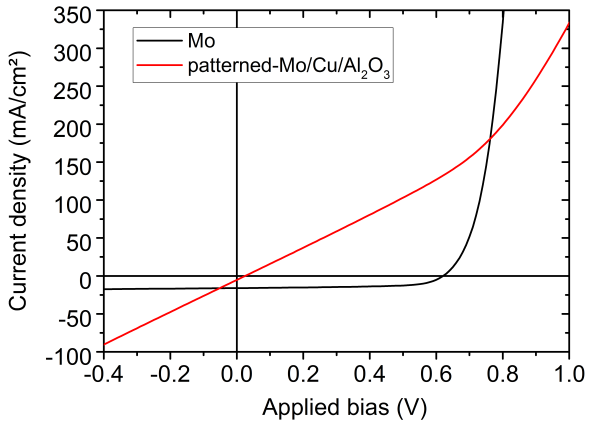

Figure 5.11.: I(V) curve of a cell on patterned-Mo/Cu/Al_2O_3 back-contact and on Mo back-contact.

As observed in Fig. 5.11, the cell unfortunately exhibits a strong shunt behavior. As

a consequence, the cell efficiency is very low (<0.5%) and cannot be analyzed. This shunt behavior can be due to:

- the mechanical scribing to separate the cell. The pin may shunt the cells. A chemical etching of the CIGS/front-contact layer is maybe more adapted;
- a rest of Cu layer that remains in the Cu/Al_2O_3 openings. The excess of Cu in the CIGS can form a $CuSe_x$ phase that shunts the cell.
- some cracks in the CIGS layer in the openings due to the variation of altitude. As a consequence, the CdS/ZnO/ZnO:Al may be in contact with Mo.

More experiments and analysis of the samples are required to discriminate the previous suggestions.

It should be noticed that a slight charge-carrier collection was nevertheless achieved.

5.4. Conclusion of the chapter

In this Chapter, we have fabricated and analyzed two advanced structures for ultra-thin CIGS solar cells:

A cell on TCO back-contact with the perforated passivation Al_2O_3:

- Cells with a CIGS thickness of 480 nm on patterned-SnO_2:F/Al_2O_3 back contact were fabricated. We achieved a maximum efficiency of 10.7%. This result is higher of 1% than the reference cell on Mo back-contact. Unfortunately, no cell was working on patterned-ZnO:Al/Al_2O_3 back contact.
- A slight passivation effect of the TCO/CIGS interface by the Al_2O_3 layer was demonstrated from the analysis of the cell EQE, the PL-yield, and the time-resolved PL-decay.
- This structure has the ability to become more efficient after optimization of the Al_2O_3 passivating layer (Al_2O_3 thickness and opening spacing) and after optimization of the CIGS process (multi-stage process). The beneficial effect of this back-contact would be clearer for even thinner CIGS thicknesses.

A cell with a perforated Cu reflector encapsulated between the Mo and the Al_2O_3 passivating layer:

- Substrates that combine Mo-back-contact / Cu-reflector / Al_2O_3-passivating-layer were successfully fabricated. The SEM images suggest that the chemical under-etching of the Cu layer allows for a protection of the Cu layer from reaction with the evaporated Se.
- Unfortunately, solar cells were not functioning due to a strong shunt effect. The explanation of the origin of this shunt requires further investigations.

Those advanced structures are promising for the fabrication of high-efficiency ultra-thin CIGS solar cells. More optimization of the different processes are required such as a multi-stage CIGS deposition, a control of the Al_2O_3 passivating effect or an optimum point-contact spacing.

General conclusion and perspectives

In this PhD thesis, we have worked on the development of ultra-thin CIGS solar cells with absorber thicknesses below 500 nm. Such solar cells demand lower metal quantity and can be fabricated faster. The industries can exploit these benefits to reduce their dependence to the international metal market and can reduce the module cost.

To achieve this goal, it is essential that the efficiency of the ultra-thin cells matches at least that of standard cells. A clear understanding of the physical mechanisms that limit the performance of ultra-thin CIGS cells have to be gathered. For that purpose, cells with various CIGS thicknesses were simulated on SCAPS and were fabricated to confront our results to some statements previously reported [76, 78, 73, 81, 77, 80] on role of the CIGS quality, light absorption or interfaces. We decided to avoid any composition gradients along the CIGS thickness to facilitates the analysis of the cells. We also set up a generation-collection model developed in collaboration with *Institut d'Optique* to confront the experimental results to physical parameters.

We observed that the CIGS materials was poorly impacted by the CIGS deposition duration (sec. 2.3.2.1): the main change was the decrease in the grain size, and therefore an increase in the grain boundary density. However, as previously observed in the literature, the efficiency of our cells dramatically decreased with the decreasing CIGS thickness (sec. 2.3.2.2). We found out that the J_{SC} was impacted by the non-absorption of photons in the CIGS layer, but also by the recombination at the Mo back-interface that reduces the charge-carrier collection in the Quasi Neutral Region (sec. 2.3.2.3). Moreover, the V_{OC} was slightly reduced for thin CIGS, whereas an inverse tendency was theoretically expected, related to a reduction total recombination in the cell (sec. 2.3.2.4). Therefore, we concluded that the quality of the CIGS remains the same but the increased impact of the back-contact recombination compensates the reduction of the bulk recombination.

Our efforts to improve the efficiency of ultra-thin CIGS cell by using advanced coevaporation depositions of the CIGS layer (composition gradient or multi-stage process) were not successful (**sec. 2.4**).

As a consequence, from the previous observations, we draw the following issue for our work:

> **The main issue in ultra-thin CIGS solar cells is the back-interface: the Mo/CIGS interface is weakly reflective and exhibits too high recombination velocity.**

In this PhD thesis, to address this issue, we decided to replace the Mo/CIGS back-interface by a more reflective and a more passivated interface.

Prior to the replacement of the back-contact, we first analyzed the influence of different growth conditions on the cell performances. The CIGS growth condition may change as a function of the back-contact used: a lower substrate temperature if the alternative back-interface is temperature sensitive or a Na supply if the alternative back-interface hinders the diffusion of Na from the glass. By using a full factorial design of experiment that exploits the substrate temperature, the diffusion of Na, an external supply of K and the formation of $MoSe_2$, we could clearly separate their impacts on the cell performances. Such compete analysis has not been performed before and allows us to accurately conclude that the substrate temperature should not be set **below 450°C** and that a **KF Post Deposition Treatment (PDT) can compensate the absence of Na** (sec. 2.5). In those conditions, we can fabricate CIGS material with the same quality that a standard CIGS.

The second step was to increase the photocurrent in the ultra-thin CIGS cells. For this purpose, we developed a simple alternative cell architecture: the substitution of the Mo by a transparent conducting oxide (TCO, SnO_2:F or ZnO:Al) back-contact. Indeed, the remaining light can be reflected by a mirror placed at the rear-side of the sample. We verified that this alternative back-contact fulfills the requirements for a device fabrication: **1/ we have simulated that it significantly improves the photocurrent**: a cell efficiency increase by +0.5% abs. for a 450-nm-thick CIGS and 1.5% abs. for a 250 nm thick CIGS can be achieved (sec. 3.2.4). **2/ we optimized the deposition of a high-quality CIGS** with an external Na supply by a NaF PDT (sec. 3.4). **3/ we achieved an ohmic contact with the CIGS.** From in-depth material characterization of the back-interface, we highlighted no *in-situ* phase formation at the ZnO:Al/CIGS interface, but a slight Cu-enrichment at the SnO_2:F/CIGS interface (sec. 3.4.2.2).

Finally, we realized cell efficiencies of **9.2% on a SnO_2:F back-contact** and **8.7% on a ZnO:Al back-contact** with a **260-nm-thick CIGS** with an Au-reflector (sec. 3.5), which are higher than the reference cell on Mo back-contact (7.0%). However, we have demonstrated that the TCO/CIGS surface recombination velocity is high, especially in the case of the SnO_2:F (sec. 3.4.3.3).

So, to achieve high efficiency ultra-thin CIGS cells, it is crucial to minimize the recombination at the back-contact. For this, we have compared TiO_2 and Al_2O_3 as passivation layers. For an easy cell fabrication and characterization, we first studied the passivation effect of these oxides on cells with Mo back-contact.

By using Mo/TiO_2 back-contact, developed for the first time for CIGS cells, we achieved a cell efficiency of **9.5% for a 390-nm-thick CIGS** (sec. 4.4.1). Surprisingly, openings in the TiO_2 layer were not necessary. This particularity need to be discussed more into details. In the case of Mo/Al_2O_3 back-contact, the cell fabrication required the realization of openings in the Al_2O_3 layer by nano-imprint lithography (sec. 4.4.2). The passivation effect is not clear, depending on the supply

of Na during the CIGS deposition process. However, we achieved a cell efficiency of **9.5% for a 390-nm-thick CIGS** with a surprisingly large spacing of the point-contacts (pitch of 8 µm, 98.5% of the back-contact covered by Al_2O_3). In particular, a **great attenuation of the parasitic resistances** was observed: a high shunt resistance (by removing of shunt path) and a low series resistance (that could be correlated to a lateral hole diffusion over long distances (sec. 4.5)).

Finally, in order to obtain high efficiency CIGS solar cells, we combined the effect of a reflective TCO back-contact and a slight passivation of the CIGS by using an an Al_2O_3 layer. To reach this goal, we have fabricated 2 advanced cell structures:

- **a cell on TCO back-contact with a perforated Al_2O_3 passivation layer (sec. 5.3).** From in depth characterization of the ZnO:Al/CIGS and SnO_2:F/CIGS interface by photoluminescence, we demonstrated a slight passivation effect of the Al_2O_3 layer at the TCO/CIGS interface. An efficiency of **10.7% was reached for a 480-nm-thick CIGS on SnO_2:F/Al_2O_3 back-contact**.
- **a cell with a Cu reflector encapsulated between the Mo and the Al_2O_3 layers (sec. 5.2).** The electrical contact between the CIGS and the Mo layer was made by openings in the Cu/Al_2O_3 stack. Unfortunately, the fabrication procedure has to be further optimized to obtain a cell without any shunt behavior.

To conclude, we proved in this PhD thesis that the efficiency of ultra-thin CIGS cells can be improved by using alternative back-contacts. The use of a passivated TCO back-contact is an example of a simple realization permitting to achieve this result.

However, the cell performances obtained in this PhD thesis remains lower than that of the cell we obtained with a thick CIGS layer: 14.0% for a 1-stage coevaporation process (obtained in Chapter 2) and 16.7% for a 3-stage coevaporation process (obtained by PhD thesis from T. Klinkert [97]). To reach such performances, we suggest to implement the following improvements:

- The improvement of the CIGS quality by the development of a fast 3-step process with a NaF incorporation;
- The control of the Al_2O_3 passivating effect by a control of the Al_2O_3 deposition and annealing;
- The optimization of the point-contact spacing to find an optimum between the passivation effect of the Al_2O_3 and the increase in the series resistance due to the distance required for hole collection;
- The optimization of the p-doping in the CIGS to enhance the benefit of the passivation of the back-contact.

To go further, the developments performed in this PhD thesis can be adapted for other cell architectures:

- a Lambertien reflector (such as white paint) as close a possible to the CIGS layer. Localized contacts would collect the current whereas the rest of the surface is passivated by an alumina layer and diffusive by the white paint. This configuration would lead to the best result but is complex to fabricate.
- a roof-top configuration, as suggested in [89], with an Al_2O_3-passivated SnO_2:F p-contact.
- the passivation of the front-contact, as suggested in [199, 200] and the replacement of the CdS/ZnO buffer layer by some more transparent materials such as Zn(O,S)/Zn(O,Mg), as suggested in [50].

In conclusion, we are confident that ultra-thin CIGS solar cells have the capability to reach the efficiency of a standard CIGS cell if an alternative back-interface is used. Theoretically, an optimized cell with around 500-nm-thick CIGS layer could even exceed the efficiency of a thick CIGS solar cell.

Appendix

A. V_{OC} analysis based on the 2-diode fit of the dark I(V) curves

The diode current $J(V)$ of a cell without photogeneration can be expressed formally as the sum of different recombination currents corresponding to different recombination mechanisms. The solar cell is then the contribution of 2 diodes (I_{01} and I_{02}) with ideality factors of respectively 1, related to the recombination in the interface and quasi-neutral region, and 2, related to the recombination in the space charge region [34].

The I(V) curves measured in the dark can therefore be fitted according to a model with two diodes in parallel, so called 2-diode model. This model is schematized in Fig. A.1.

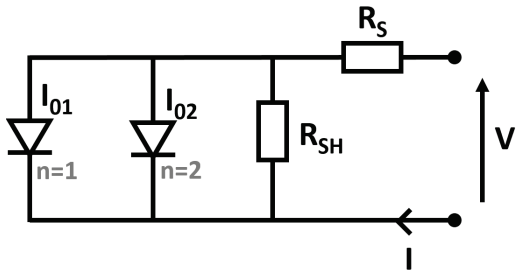

Figure A.1.: Equivalent circuit of the 2-diode model with ideality factor n of 1 and 2 for respectively the diode I_{01} and I_{02} .The parasitic shunt resistance (R_{SH}) and series resistance (R_S) are shown.

In this model, the diode current without parasitic resistance is expressed as:

$$J(V) = -J_{01}\left(\exp\left(\frac{qV}{kT}\right) - 1\right) - J_{02}\left(\exp\left(\frac{qV}{2kT}\right) - 1\right) \tag{A.1}$$

with q the charge of the electron, k the Boltzmann constant and T the temperature.

The complete expression of the diode current is:

$$J(V) = -J_{01}\left(\exp\left(\frac{q\,(V + J\cdot R_S)}{kT}\right) - 1\right) - J_{02}\left(\exp\left(\frac{q\,(V + J\cdot R_S)}{2kT}\right) - 1\right) - \frac{V + J\cdot R_S}{R_{SH}}$$

(A.2)

An example of I(V) dark fitting according to the 2-diode model is shown in Fig. A.2. The diode with ideality factor of 2 dominates at low voltage whereas the diode with ideality factor of 1 dominates at higher applied voltage.

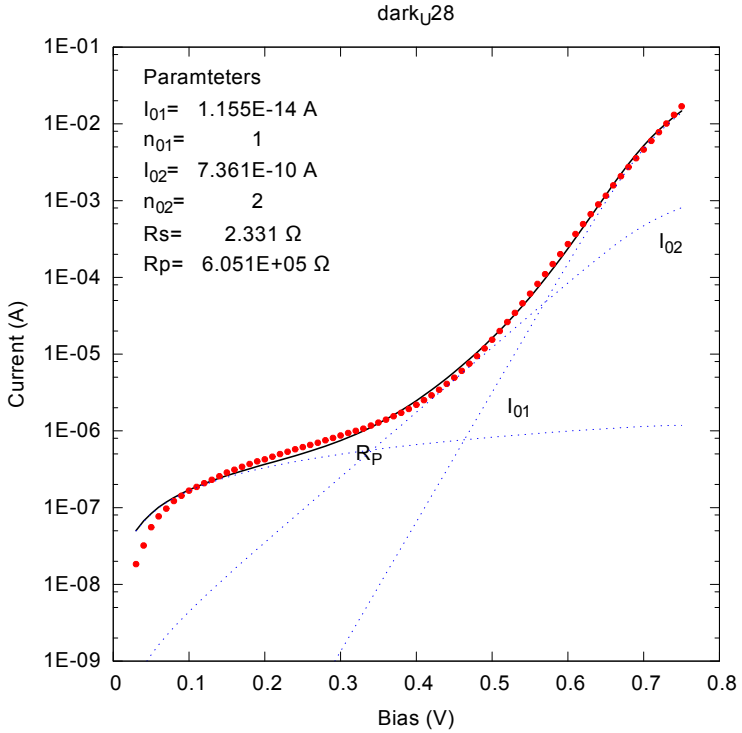

Figure A.2.: I(V) dark of a 1000-nm-thick CIGS on Mo substrate. Details of the 2-diode fitting is shown: I_{01} and I_{02} for the diodes with an ideality factor of 1 and 2, the shunt resistance (R_{SH}) and the series resistance (R_S).

The open circuit voltage, V_{OC}, corresponds to the voltage when no current flows. The V_{OC} is expressed in the 2-diode model without parasitic resistance by Eq. A.1:

$$V_{OC,\text{2-diode}} = \frac{2kT}{q} \cdot \ln\left(\frac{-J_{02} + \sqrt{J_{02}^2 + 4 \cdot J_{01} \cdot J_{SC}}}{2 \cdot J_{01}}\right) \tag{A.3}$$

from the resolution of the differential equation (from M. Pair thesis in [201]).

It is important to note that the V_{OC} experimentally obtained from the I(V) curves under illumination is not necessary the same than $V_{OC,\text{2-diode}}$. First, the superposition principle (i.e. the diode current in the light is the sum of the diode current in the dark and a voltage independent photocurrent) is generally not observed in the

CIGS solar cells. Second, the parasitic series and shunt resistance are not taken into account.

The current density J_0 for defect-related recombination of the CIGS cell can be expressed as:

$$J_{0i} = J_{00i} \cdot \exp\left(-\frac{E_a}{nkT}\right)$$

with i the region of the CIGS (SCR, QNR or IF), E_a the activation energy and n the ideality factor. The E_a and n parameters for the different regions can be approximated in simple values summerized in Tab. A.1.

Table A.1.: Simplified activation energy (E_a) and ideality factor (n) for the current density for defect related recombination in the different regions of the CIGS cell. From[34].

	condition	E_a	n
SCR	no tunneling	E_g	2
QNR	no tunneling	E_g	1
IF	no tunneling no fermi-level pinning	E_g	1

As the consequence, $J_{01}$is related to the QNR or IF recombination whereas J_{02} is related to the SCR recombination. Therefore, the I(V)-dark fit allows to separate the influence of the recombination occurring in the different regions. However, the $J_{01}$and J_{02} values also depends on the band-gap of the CIGS. If we compare two samples with two different band-gaps, it is not possible to determine the relative influence of the recombination in the different regions.

For this purpose, we consider $J_{01} = J_{001} \cdot \exp\left(-\frac{E_g}{kT}\right)$ and $J_{02} = J_{002} \cdot \exp\left(-\frac{E_g}{2kT}\right)$. The reference current density $J_{001}$and J_{002} are independent to the band-gap. With those values, Eq. A.3 is expressed as:

$$V_{OC,\text{2-diode}} = \frac{E_g}{q} + \frac{2kT}{q} \cdot \ln\left(\frac{-J_{002} + \sqrt{J_{002}^2 + 4 \cdot J_{001} \cdot J_{SC}}}{2 \cdot J_{001}}\right) \tag{A.4}$$

In order to calculate the relative influence of the QNR+IF and SCR recombinations on the V_{OC}, we compare the $V_{OC,\text{2-diode}}$ of the 2 samples (A and B) while changing the parameters one by one (J_{001}, J_{002} and E_g). Each parameter is changed while keeping the other parameters at the mean point between both samples.

- **Influence of the QNR and IF recombination on the V_{OC}**

$$\triangle V_{OC}(QNR, IF) = V_{OC,\text{2-diode}}(J^B_{001}) - V_{OC,\text{2-diode}}(J^A_{001})$$

with

$$J_{002} = 10^{\left(\frac{\log\left(J^A_{002}\right) + \log\left(J^B_{002}\right)}{2}\right)} \qquad \text{and} \qquad E^A_g = E^B_g$$

- **Influence of the SCR recombination on the V_{OC}**

  $$\triangle V_{OC}(SCR) = V_{OC,\text{2-diode}}(J^B_{002}) - V_{OC,\text{2-diode}}(J^A_{002})$$

with

$$J_{001} = 10^{\left(\frac{\log\left(J^A_{001}\right) + \log\left(J^B_{001}\right)}{2}\right)} \qquad \text{and} \qquad E^A_g = E^B_g$$

- **Influence of the band-gap on the V_{OC}**

  $$\triangle V_{OC}(E_g) = \frac{E^B_g - E^A_g}{q}$$

This treatment suffers of large approximations:

- Eq. A.4 cannot be lineased. Therefore, the sum of $\triangle V_{OC}(SCR)$, $\triangle V_{OC}(QNR, IF)$ and $\triangle V_{OC}(E_g)$ may varies from $\left[V^B_{OC,\text{2-diode}} - V^A_{OC,\text{2-diode}}\right]$.
- The values of E_a and n used for the calculations may be unadapted for some cells (such as tunneling effect, band-gap variation at the interface, high defect density at the front interface)

However, this calculation allows for a rough determination of the influence of the SCR, QNR and IF recombination on the V_{OC}.

B. CIGS analysis by ellispometry spectroscopy

This work has been performed by Institut Lavoisier of Versailles and have been recently published in reference [202]. The samples were fabricated at IRDEP in the same condition than the samples used in the PhD thesis.

Materials and methods

CIGS samples of different composition was fabricated. For all samples, the substrate was a 800-nm-thick Mo layer coated on a soda-lime glass. Approximately 600 nm of CIGS was deposited in a 1-stage coevaporation process in 30 min. The deposition was performed at an estimated temperature of 500°C. At the end of the process, the sample was annealed 5 min at 500°C under Se atmosphere. The evaporation rate was kept constant to avoid a composition gradient. To achieve different GGI, the In and Ga flux was changed between each sample while maintaining the same targeted CGI and thickness.

However, the accuracy of the spectroscopic ellipsometry is limited by the surface roughness and the chemical. Therefore, the CIGS surface was modifed by:

Surface flattening The surface flattening and CIGS thinning is processed thanks to a chemical engineering previously developed at ILV and described in reference [176]. An etching solution of HBr (0.2 mol·L^{-1}): Br_2 (0.02 mol·L^{-1}): H_2O is used for the dissolution process at room temperature using a rotating-disk system at 50 rpm, during 1min30s. After the etching, samples are rinsed in ultra-pure de-ionized water and dried with nitrogen flux. This chemical process allows a quasi layer by layer dissolution of the CIGS sample and leads to a spectacular decrease of its surface roughness.

Surface de-oxidation The surface was de-oxidazed by dipping the sample in HCl (1 mol·L-1) during at least 5 min. After the HCl treatment, the sample is rinsed in de-ionized ultra-pure water (18.2 MΩ) and dried under nitrogen (N_2) flux.

Surface morphology of CIGS surfaces was studied with a Digital Instruments/Veeco Dimension D3100 Atomic Force Microscope (AFM) and Nanoscope controller, using

contact mode. AFM image processing and rendering was analyzed with WsXM data analysis software.

The composition was measured by Energy Dispersion Spectroscopy (EDS) in a Scanning Electron Miscoscope (SEM) at the accelerating voltage of 15 kV.

The measurements were performed using a Phase Modulated Spectroscopic Ellipsometer, UVISEL from HORIBA Scientific. For this study, a 70° angle of incidence was used over a spectral range from 0.75 to 4 eV with a spot size diameter of 1 mm. The SE data analysis was performed with DeltaPsi2 software, using the Levenberg Marquadt linear regression method. Specifically, the optical constants and film structures are determined by minimization fitting error, calculated from the fitting error function.

The CIGS sample is described by 3 layers as presented in : the Mo substrate, an homogeneous CIGS layer, and a porous CIGS overlayer. The dielectric function of the overlayer is described using the BEMA (Bruggeman Effective Medium Approximation) with a mixture of 50% bulk layer and 50% void.

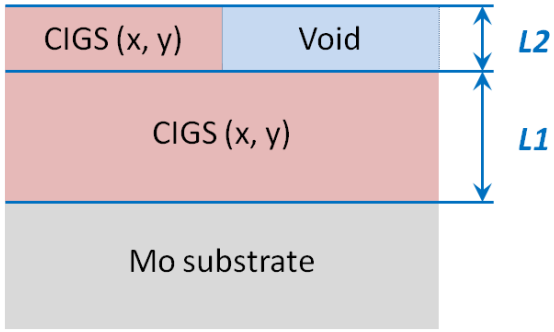

Figure B.1.: Model structure employed for SE analysis fittings: x and y refer to the constant GGI and CGI values everywhere inside the layer, L1 to the layer thickness and L2 to the overlayer thickness.

The optical constants of CIGS were modeled by combining the dispersion formula proposed by Adachi [203] with four Tauc-Lorentz oscillators [204]. Adachi formula is used to describe the fundamental absorption region. Adachi dispersion is well adapted for direct band gap semiconductor without anisotropic features. As we have polycrystalline layers with a random distribution of grains, the anisotropy contribution to optical properties associated to the monocrystalline CIGS can be neglected. So the Adachi formula can be used in approximation to describe the first critical points (CP) at low energies. The Tauc-Lorentz oscillators are used to express the higher photon energies. Using this procedure, we obtain very good agreement between measured and model-generated data. For all compositions, the fitting procedure gives rise to χ^2 lower than 5.

Materials analysis and ellipsometry measurement

The CIGS composition, roughness and the CIGS characteristic values extracted from the sprectroscopy ellipsometric (SE) model are summerized in Tab. B.1.

Table B.1.: CIGS characterization and CIGS characteristic values extracted from the sprectroscopy ellipsometric (SE) model. for the CIGS with different composition. The roughness values are obtained using the Root-Mean-Square (RMS) roughness analytical function on AFM. $L1$ is the SE CIGS bulk layer thickness. $L2$ is the SE CIGS overlayer thickness. E_0 is the fundamental transition. E_0, E_1 are deduced from Adachi model and E_2, E_3 from the two first Tauc-Lorentz oscillators. α is the absorption coefficient at 2 eV.

Sample	Materials characterization			SE model						
	CGI (EDS)	GGI (EDS)	RMS roughness Etched (nm)	$L1$ (nm)	$L2$ (nm)	E_0 (eV)	E_1 (eV)	E_2 (eV)	E_3 (eV)	α (cm^{-1}) (at 2 eV)
U119	0.89	0.15	7± 1	518 ± 2	4 ± 1	1.09 ± 0.01	1.30 ± 0.01	3.00 ± 0.01	3.77 ± 0.05	$7.01 \cdot 10^4$
U120	0.92	0.30	8± 1	445 ± 2	4 ± 1	1.18 ± 0.01	1.40 ± 0.01	3.03 ± 0.01	3.85 ± 0.05	$6.51 \cdot 10^4$
U121	0.90	0.42	8± 1	384 ± 2	4 ± 1	1.26 ± 0.01	1.50 ± 0.01	3.04 ± 0.01	3.96 ± 0.05	$6.70 \cdot 10^4$
U122	0.83	0.61	10± 1	569 ± 2	5 ± 1	1.39 ± 0.01	1.63 ± 0.01	3.09 ± 0.01	3.99 ± 0.05	$6.08 \cdot 10^4$

C. Ray Transfer Matrix method

The optical calculation in a stack of layers are based on the Ray Transfer Matrix (RTM) method [101, 102]. A code was developed on MATLAB at *Institut d'Optique Graduate school*, in the frame of the ANR UltraCIS^M [106, 205].

This method calculates the propagation of an electromagnetic wave across a stack of materials. It describes the electromagnetic field that enters and that exits each layer of the stack modeled by a 2x2 transfer matrix.

For the calculation, we made the following hypothesis:

- we consider only the transverse electromagnetic wave;
- each layer is homogeneous and isotropic;
- the incident angle of the ray is perpendicular to the stack (z-axis);
- each interface are flat (no scattering);
- the incident light in unpolarized. For this purpose, all calculations are performed with 2 orthogonal polarizations. The resulting optical parameters are the average of both calculations.

A schematic of the electromagnetic wave propagation though the layers is presented in Fig. C.1.

Determination of the transfer matrix

The transfer matrix associated to a layer m (M_m) of the stack is the matrix multiplication of a dynamic matrix (D_m) and a propagation matrix (P_m). D_m describes the wave propagation through the interface between the layers m and $m+1$. P_m describes the wave propagation though the bulk of the layer m.

The propagation of the electric field is described at an interface and in the bulk by D_m and P_m as:

$$\begin{pmatrix} E_m^+ \\ E_m^- \end{pmatrix} = D_m \begin{pmatrix} E_{m+1}^+ \\ E_{m+1}^- \end{pmatrix} \tag{C.1}$$

$$\begin{pmatrix} E_{m,top}^+ \\ E_{m,top}^- \end{pmatrix} = P_m \begin{pmatrix} E_{m,bottom}^+ \\ E_{m,bottom}^- \end{pmatrix} \tag{C.2}$$

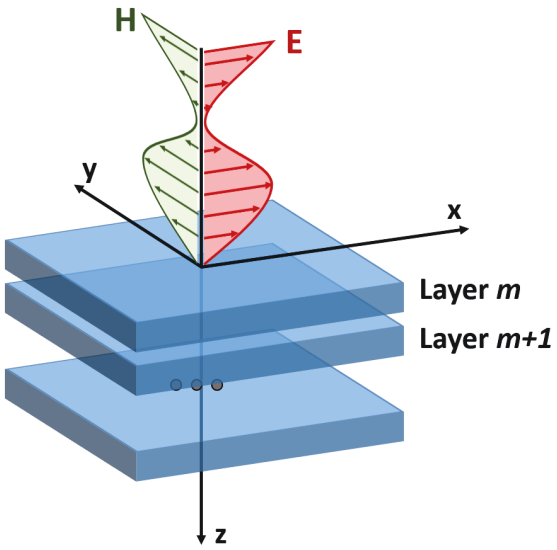

Figure C.1.: Schematics of the incident electromagnetic wave (electric field vector $\vec{E}$ and magnetic field vector $\vec{H}$) in the (xyz)-coordinate for a single polarization in a layer m of a thin-film stack.

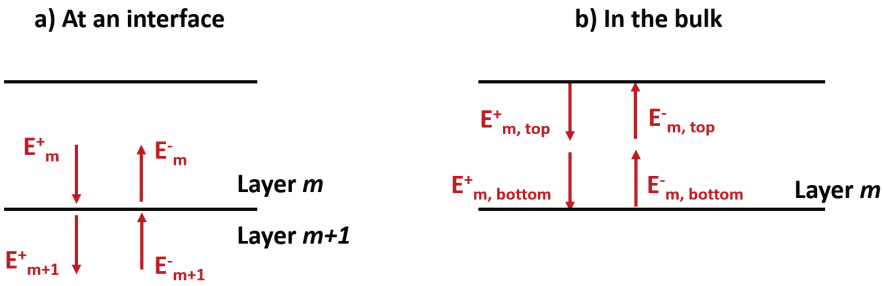

Figure C.2.: Schematics of the electric field amplitude distribution a) across an interface between the layers m and $m+1$ and b) through the material bulk of the layer m.

with the notation indicated in Fig. C.3a at the layer interface and in Fig. C.3b in the layer bulk.

Finally, the transfer matrix M_m for one layer m is:

$$M_m = D_m \cdot P_m \tag{C.3}$$

We set the wavenumber (k_m) direction along z for the layer m:

$$k_m = \frac{2\Pi}{\lambda} \cdot \tilde{n}_m$$

with $\tilde{n}_m$ the complex refractive index of the layer m, and λ the wavelength of the incident wave.

The propagation of the electromagnetic wave depends on its polarization. We define the wavenumber Q as:

- Polarization of the electric field $\overrightarrow{E}$ along the x-axis: $Q = k$
- Polarization of the electric field vector $\overrightarrow{E}$ along the y-axis: $Q = \frac{k}{\tilde{n}^2}$

At an interface between 2 layers. The incident wave is separated in 2 components directed upward and downward that are different in module and phase: the reflection (r) and the transition (t). The reflection and transmission coefficient are calculated according to the Fresnel equations Eq. C.4 and Eq. C.5:

$$r = \frac{Q_m - Q_{m+1}}{Q_m + Q_{m+1}} \tag{C.4}$$

$$t = \frac{2 \cdot Q_m}{Q_m + Q_{m+1}} \tag{C.5}$$

Finally, at the interface between the layer m and $m+1$, the dynamic matrix is:

$$D_m = \frac{1}{t^*} \begin{pmatrix} 1 & r \\ r & 1 \end{pmatrix} \tag{C.6}$$

In the bulk . The incident wave is attenuated by the absorption of the material. The attenuation factor in the layer m is defined by:

$$\Phi = k_m \cdot d_m$$

with k_m the wavenumber in the layer m, and d_m the thickness of the layer m.

Finally, in the layer m , the propagation matrix is:

$$P_m = \begin{pmatrix} \exp(-i\Phi) & 0 \\ 0 & \exp(-i\Phi) \end{pmatrix} \tag{C.7}$$

The transfer matrix M corresponding to the wave propagation in the layer stack is calculated by the matrix multiplication of the transfer matrix of each layers:

$$M = D_1 \prod_{m=2}^{end} P_m \cdot D_m \tag{C.8}$$

This transfer matrix is used to calculate the total reflectance and transmittance of the stack.

Determination of the reflectance, transmitance and layer absorption

We consider a incident electromagnetic wave that propagate downward and enter into the layer stack from the top. The interesting optical parameters of the stack are:

- the reflectance (R): the percentage of the incident power that propagates upward, on the top of the stack;
- the transmittance (T): the percentage of the incident power that propagates downward, on the bottom of the stack;
- the absorption in a layer m (A_m): the percentage of the incident power that is attenuated in the layer m.

The power flow of the electromagnetic wave is defined by real part of the time-averaged Pointing Vector through a surface, noted S in Eq. C.9:

$$S = \frac{1}{2} \cdot \mathrm{Re}\left(\vec{E} \times \vec{H}^*\right) \tag{C.9}$$

with $\times$ the cross product of the vectors, and * the complex conjugate.

We will now determine the power flow at the different interfaces.

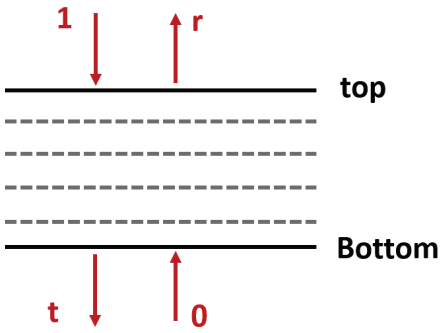

Figure C.3.: Schematic of the electric field amplitude that enters and that exits the layer stack. r is the total reflection and t is the total transmission.

The transfer matrix M of the layer stack, calculated in Eq.C.8, can be noted as Eq.C.10:

$$\begin{pmatrix} E_1^+ \\ E_1^- \end{pmatrix} = \begin{pmatrix} a & b \\ c & d \end{pmatrix} \begin{pmatrix} E_{end}^+ \\ E_{end}^- \end{pmatrix} \tag{C.10}$$

We note r the electric field amplitude that is reflected at the top of the stack and t the electric field amplitude that is transmitted through the stack along the z-axis. As displayed in Fig. C.3, electric field coordinate are $E_1^+ = 1$, $E_1^- = r$, $E_{end}^+ = t$ and $E_{end}^- = 0$.

The coordinates of the transfer matrix (a,b, c and d) were calculated from the optical parameter of each materials. Therefore, r and t can be calculated as Eq.C.11:

$$\begin{cases} r = c/a \\ t = 1/a \end{cases} \tag{C.11}$$

The electric field vector $\overrightarrow{E}$ and the magnetic field $\overrightarrow{H}$ vector in the (x,y,z) for one polarization are:

$$\begin{cases} \text{Incident light: } E_{inc} = (0,1,0) & H_m = (Q_1 \cdot 1, 0, 0) \\ \text{Reflected light: } E_r = (0,r,0) & H_r = (Q_1 \cdot r, 0, 0) \\ \text{Transmitted light: } E_t = (0,t,0) & H_t = (Q_{end} \cdot t, 0, 0) \\ \text{At the interface: } E_m = (0, A+B, 0) & H_m = (Q_m \cdot (A-B), 0, 0) \end{cases} \tag{C.12}$$

with A and B in Eq. C.12 the solution of the relation Eq. C.13 :

$$\begin{pmatrix} A \\ B \end{pmatrix} = \frac{1}{M_m} \cdot \begin{pmatrix} 1 \\ r \end{pmatrix} \cdot 1 \tag{C.13}$$

The reflectance, transmittance and absorbance for one polarization (p) are then calculated from the Pointing vectors:

$$\begin{cases} R_p = \frac{S_r}{S_{inc}} \\ T_p = \frac{S_t}{S_{inc}} \\ A_{p,m} = \frac{S_{m+1} - S_m}{S_{inc}} \end{cases} \tag{C.14}$$

With the parameters of C.12 and Eq. C.9, the Eq. C.14 leads to Eq. C.15:

$$\begin{cases} R_p = rr^* \\ T_p = \mathrm{Re}\left(\frac{Q_{end}}{Q_1}\right) \cdot tt^* \\ A_{p,m} = \frac{S_{m+1} - S_m}{S_{inc}} \end{cases} \tag{C.15}$$

The same calculations are performed with the other polarization.

Finally, R, T and A_m correspond to the mean value of R_p, T_p and $A_{p,m}$ of Eq. C.15 for both polarization.

D. SCAPS model for a CIGS cell

Table D.1.: Materials parameters for the SCAPS baseline model of the CIGS with a band-gap of 1.2 eV.

Parameters	Value used					
	Front contact	ZnO:Al	ZnO	CdS	CIGS	Mo contact
d (µm)	–	0.4	0.05	0.05	0.1 - 2	–
E_g (eV)	–	3.5	3.3	2.4	1.2	–
χ(eV)	–	4.65	4.450	4.2	4.4	–
ε_r	–	9.0	9	10	13.6	–
N_C / N_V (cm^{-3})	–	10^{18} / 10^{19}	10^{18} / 10^{19}	10^{18} / 10^{19}	10^{18} / 10^{19}	–
μ_e /μ_h (cm^2.(V.s)$^{-1}$)	–	100 / 25	100 / 25	100 / 25	100 / 25	–
N_D (cm^{-3})	–	$7.5 \cdot 10^{20}$	$1 \cdot 10^{17}$	$1 \cdot 10^{17}$	1	–
N_A (cm^{-3})	–	1	1	1	5.10^{15}	–
N_d (cm^{-3})	–	2.10^{16}	2.10^{16}	2.10^{17}	8.10^{13}	–
σ_e / σ_h (cm^2)	–	10^{-12} / 10^{-12}	10^{-12} / 10^{-12}	10^{-13} / 10^{-13}	10^{-13} / 10^{-15}	–
L_n / L_h (µm)	–	–	–	–	1.8 / 9	–
α (cm^{-1}.eV$^{\frac{1}{2}}$)	–	'Numo ZnO'	'Numo ZnO'	'Numo CdS'	$4.10^4.\sqrt{E - E_g}$	–
S_n / S_h (cm/s)	10^7 / 10^7	–	–	–	–	10^7 / 10^7
WF (eV)	4.45	–	–	–	–	Flat-bands
Reflection	10 %	–	–	–	–	20 %

E. Optimization of NaF PDT on different substrate

This appendix is complementary to sec. 3.4.3 which deals with the understanding of the substitution of the Mo back-contact with alternative back-contact (ZnO:Al and SnO_2:F). In the following we detail the effect of different NaF PDT on the cell performances.

Materials and methods

First, we indicate the experimental details:

Different NaF PDT condition was tested on 250 nm and 450 nm thick CIGS absorber. In each experiment, the CIGS is coevaporated in 1-stage at a temperature of 500-550°C. No composition gradient was intentionally implemented. Subsequently to the CIGS deposition, NaF is evaporated at around 1 nm/min under a Se flux. For the different samples, the NaF PDT duration were varied between 4 and 12 min and the substrate temperature during the NaF PDT were varied between 250 and 350 °C.

A soda-lime glass substrate was used. The four different back contacts we compared are:

- a sputtered 800 nm thick Mo layer as control sample;
- a commercial SnO_2:F (650 nm thick, R_{sheet}=7 Ω/square). The samples are washed with 5% RBS, ethanol, acetone and concentrated nitric acid prior to the CIGS deposition; ;
- an RF sputtered ZnO:Al (1100 nm thick, R_{sheet}=8 Ω/square) ;
- a sputtered 800 nm thick Mo layer deposited on a glass substrate coated with a 300 nm thick Al_2O_3. The Al_2O_3 layer, deposited by atomic layer deposition, hinder the Na diffusion from the glass during the CIGS deposition.

In total, 10 batches were prepared: for 2 CIGS thicknesses (250 nm and 450 nm) and the 5 NaF PDT condition variations (see Fig. 3.12b). In each batch, the 4 different substrates were processed together. A KCN treatment was carried out prior to the characterizations and the cell fabrication. The solar cells were completed with

the standard chemical bath deposited CdS (50 nm) / rf-sputtered ZnO (60nm) / rf-sputtered ZnO:Al (350 nm) stack detailed in sec. 2.2.2.

For the Mo, Al_2O_3/Mo and ZnO:Al back-contact cells of 0.1 cm^2 were mechanical separated by scribbling. For the SnO_2:F back-contact, cells of 0.1 cm^2 were chemically separated according to the procedure detailed in Appendix XX.

The I(V) measurements were performed with a simulated AM1.5G spectrum at 25°C. As the cells on SnO_2:F and ZnO:Al back-contact are semi- transparent, the samples were characterized with a black paper placed at the rear side of the glass substrate to prevent from light reflection on the substrate holder.

The I(V)measurements were also performed in the dark and were fitted according to the 2-diode model that calculates J_{01} and J_{02} (saturation current for ideality factor of 1 and 2), R_{SH} (shunt resistance) and R_S (series resistance).

450 nm thick CIGS

The I(V) parameters in the light and in the dark of the bast cell for each NaF PDT condition for cells with 450 nm thick CIGS on the different back-contacts are displayed in Fig. E.1 and Fig. E.2.

Samples on Mo in Fig. E.1a (Na is provided from both the substrate and the NaF PDT). The cell efficiency slightly varies for the different NaF PDT conditions and a maximum efficiency of 9.9% is reached for the process that incorporates the lower amount of Na (4 min at 250°C). This optimum is the result of opposite trends in J_{SC}, V_{OC} and FF. The V_{OC} is inversely proportional to t and T, and is driven by the variation of J_{02} related to the recombination in the SCR (Fig. E.2a). The J_{SC} on the opposite, varies with t and T. This observation is inconsistent with the expected effect of an increased p-doping concentration in the CIGS with the Na concentration: higher V_{OC} and lower J_{SC} for high p-doping. Therefore, enough Na concentration is provided by diffusion whereas the excess of Na provided by NaF PDT is detrimental for the cell performance..

Samples on Al_2O_3/Mo in Fig. E.1b (Na is provided only from the NaF PDT). A maximum efficiency of 9.9% is reached for the NaF PDT at 300°C for 8 min whereas the lowest efficiency (8.0%) is reached for the condition that incorporates the least of Na (4 min at 250°C). The NaF PDT for 12 min at 350°C leads to a slightly lower efficiency (9.6%). The J_{SC} increases with the increasing T. V_{OC} increases with T but decreases against t due the variation of J_{02}. This effect highlight the beneficial effect of Na up to an optimum Na concentration. The efficiency reached is similar to the best cell on Mo without Na barrier meaning that the NaF PDT successfully compensates the absence of Na. The different behavior of the cells is nevertheless observed different according to comparison of the J_{01} and J_{02} (Fig. E.2b). For the cell on Al_2O_3/Mo, J_{01} is negligible and J_{02} is higher than the cell on Mo. This

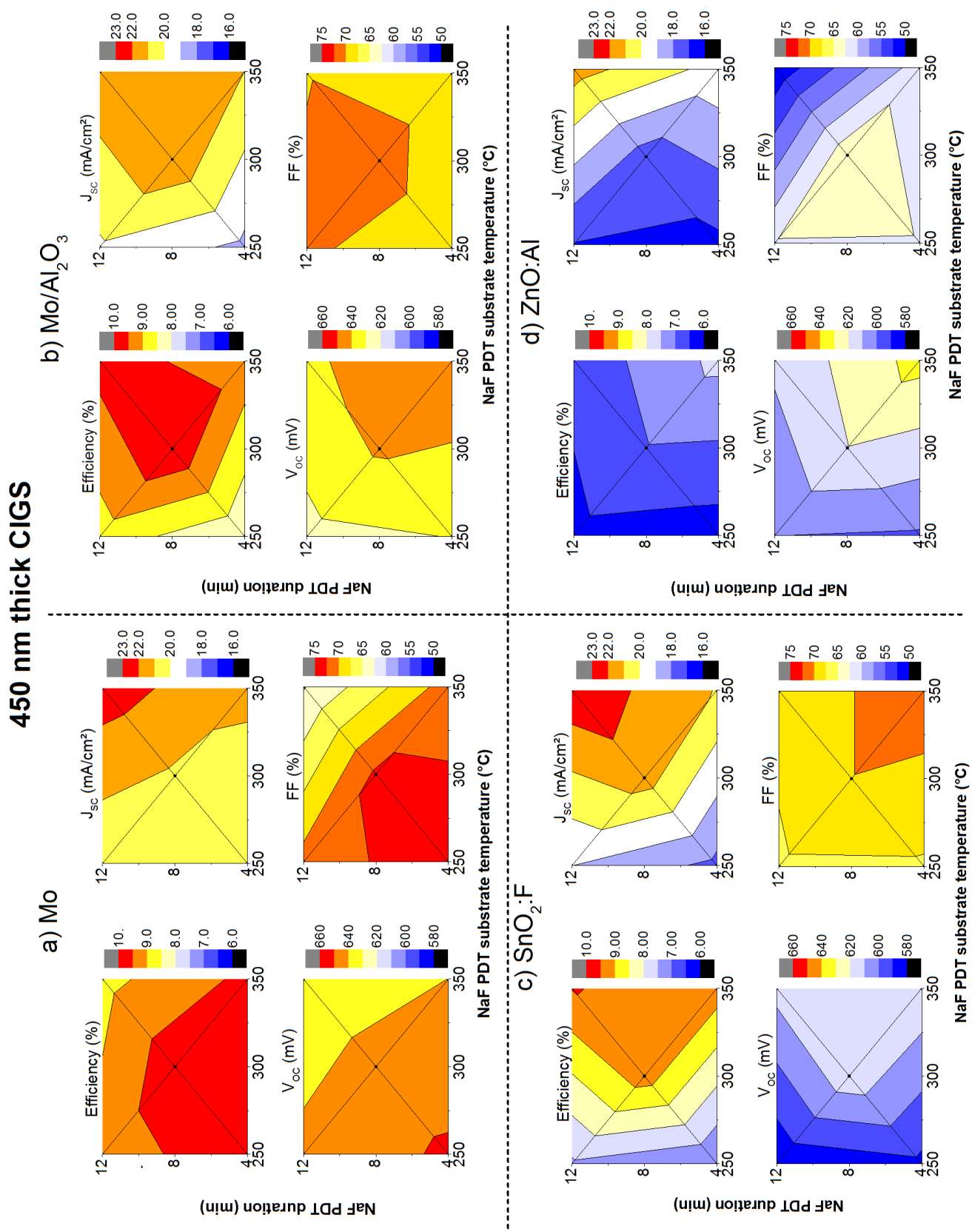

Figure E.1.: Efficiency, J_{SC}, V_{OC} and FF of the cells with 450 nm of CIGS processed with different NaF PDT. The CIGS layer were deposited on: a) a standard Mo back-contact, b) a Mo coated on the Al_2O_3 barrier layer back-contact, c) a SnO_2:F back-contact and d) a ZnO:Al back-contact.

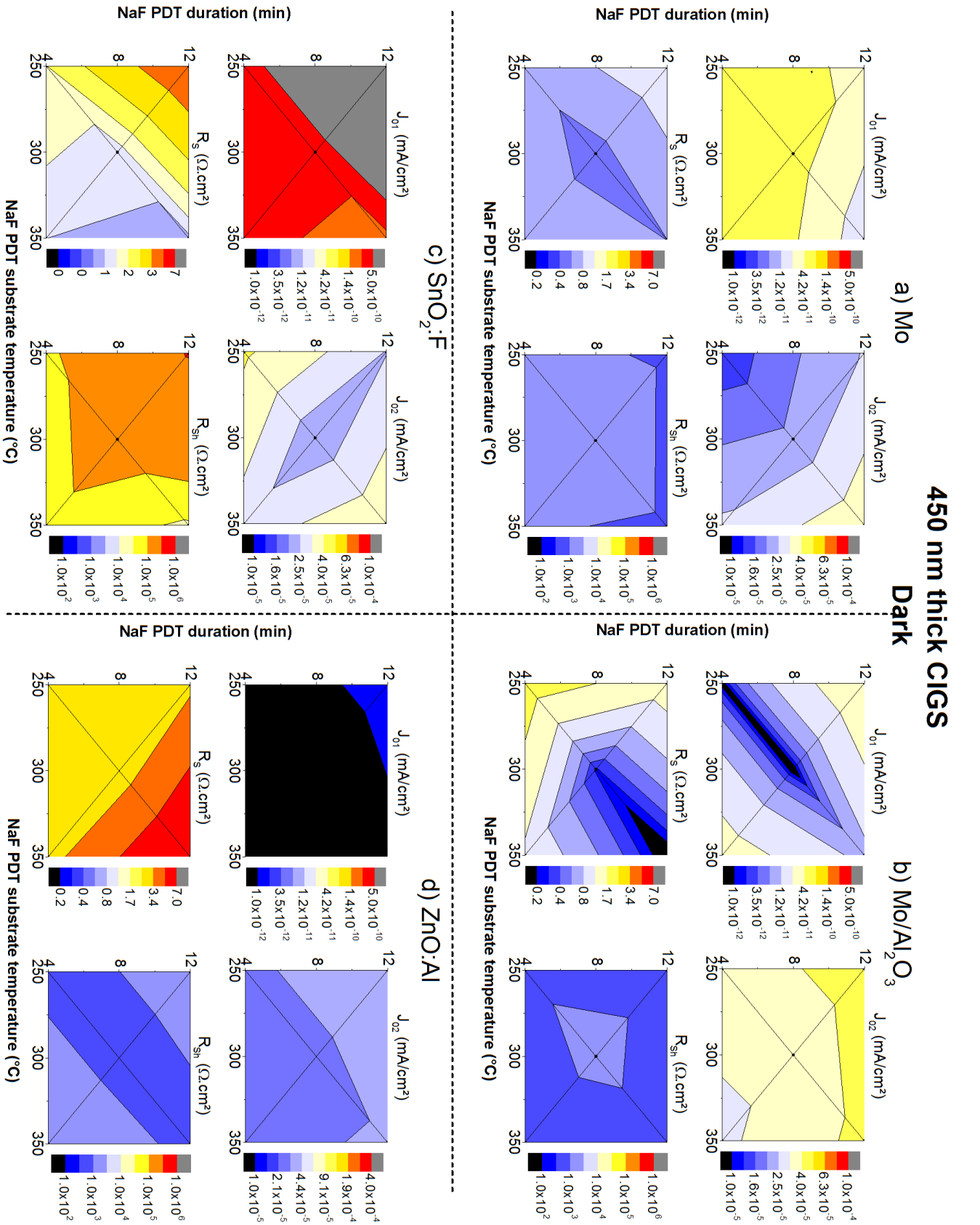

Figure E.2.: IV dark fitting parameters of the cells with 450 nm of CIGS processed with different NaF PDT. The CIGS layer were deposited on: a) a standard Mo back-contact, b) a Mo coated on the Al_2O_3 barrier layer back-contact, c) a SnO_2:F back-contact and d) a ZnO:Al back-contact.

change can be related to a change in the recombination process: lower QNR and interface recombination (generally associated to J_{01}) and higher recombination in the SCR (generally associated to J_{02}) for the cell on Al_2O_3/Mo back-contact. It could be explained by the small passivation of the back-contact due to the NaF PDT observed by [174] and some defects in the CIGS bulk that are not passivated by the Na incorporated by NaF PDT. The FF of the cells on Al_2O_3/Mo back-contact is also lower than cells on Mo. Dark I(V) curves show a low R_{SH} that may be due to some shunt paths created during the mechanical scribbing procedure.

Samples on SnO_2:F in Fig. E.1c. As for the process on Al_2O_3/Mo back contact, the Na in provided only from the NaF PDT but does not diffuse in the substrate and seems to be accumulated at the interface (see Fig. 3.16c). The cell efficiency increases from 7.0% to 9.5% when t increases from 4 min to 12 min and T increases from 250°C to 350°C. The trends in J_{SC} and V_{OC} are similar to the cells on Al_2O_3/Mo back-contact meaning that the NaF PDT has the same beneficial effect on SnO_2:F back-contact. However, the V_{OC} of the cells on SnO_2:F back-contact (590-620 mV) is much lower than the V_{OC} of the cells on Al_2O_3/Mo (630-650 mV) and is related to a much larger J_{01}. Large interface recombination at the SnO_2:F/CIGS interface can explain this effect. The FF increases with T due to a decrease of R_S. For the best NaF PDT condition, the R_S is comparable to the R_S of the cells on Mo or Al_2O_3/Mo back-contact, meaning that a low resistance ohmic contact was achieved at the SnO_2:F/CIGS back-contact. The shunt resistance R_{SH} is also much higher than the cells on Mo or Al_2O_3/Mo back-contact surely due to the chemical cell isolation procedure.

Samples on ZnO:Al in Fig. E.1d. As for the cells on SnO2:F and Mo/Al2O3, Na is provided only from the NaF PDT and accumulated at the back-contact, but in addition, the ZnO:Al is likely to be degraded at high temperature. The efficiency increase from 6.2% the NaF PDT at 250°C for 4 or 12 min to 7.5% for the NaF PDT at 350°C for 4 min . Unlike the cells on Mo/Al2O3 and SnO2:F, the NaF PDT at 350°C for 12 min does not lead to the best efficiency (only 6.6%) due to a large series resistance R_S =6.5 Ω.cm². Therefore a suitable Na incorporation at high temperature is required but a too long process leads to the formation a resistive layer CIGS/ZnO:Al interface. This result was observed on the contact resistance calculation on a ZnO:Al/CIGS/Au device (see Fig. 3.22b). According to the dark I(V), the J_{01} is negligible independently to the NaF PDT. Therefore, as J_{01} refer to the interface recombination, the ZnO:Al/CIGS contact has probably better properties than the SnO2:F/CIGS contact (considering similar QNR recombination).

To conclude, an optimal NaF PDT were found for each different substrates. This optimal NaF PDT is a balance between the beneficial effect of the increasing amount of Na which is incorporated in the CIGS, the annealing of the sample at high temperature and the degradation of the TCO at high temperature.

300 nm thick CIGS

The I(V) parameters in the light and in the dark of the best cells with the 250 nm thick CIGS, processed with the different NaF PDT and on the different back-contact are displayed in Fig. E.3 and X.

First, the samples with the NaF PDT at 350°C for 12 min on Mo and Mo/Al2O3 were unstable in water. The CIGS layer delaminates from the Mo layer. This effect was already absorbed before [110]. The Na concentration is surely too high at the Mo/CIGS interface leading to a dissolution of the interface layer in water. On SnO2:F and ZnO:Al, no delamination was observed but the efficiency was very low (<1%). Moreover, very low shunt resistance was observed for cells on ZnO:Al and was probably due to the mechanical scribbing procedure.

Samples on Mo. The tendency is different than for the cells with 450 nm thick CIGS. The efficiency increases from 5.2% to 7.2%, the J_{SC} from 15.2 to 17.6 mA/cm² and the V_{OC} from 509 to 620 mV and are all maximum for the NaF PDT at 300°C for 8 min. The result highlights that a supply of Na in addition of the Na diffusing from the glass is beneficial.

On the opposite, the cells on Mo/Al2O3, SnO2:F and ZnO:Al exhibits the same tendencies in the J_{SC}, V_{OC} and FF than the 450 nm thick CIGS if we do not consider the samples for the NaF PDT at 350°C for 12 min. Compared to the 450 nm thick CIGS, the optimum NaF PDT condition for Mo/Al2O3, SnO2:F and ZnO:Al is shifted to a shorter process but still at high temperature (4 min at 350°C). The main difference between the samples with 300 nm and 450 nm thick CIGS is that the optimum NaF PDT condition is much more narrow. Therefore an optimization of the NaF PDT process is crucial to reach high cell performance.

Samples on Mo/Al2O3. The efficiency increases from 4.6 % for the NaF PDT of 4 min at 250°C to 6.3 % for NaF PDT of 4 min at 350°C. This efficiency is lower than the cell on Mo and probably means than an higher Na incorporation is required. The J_{SC} increases from 14.3 to 16.5 mA/cm² with T. The V_{OC} increases from 587 to 604 mV with T due to a large decrease in J_{01} and J_{02} and can be explained by either the p-doping of the CIGS and the passivation of the back-contact by Na. FF increase from 54% to 63 % with T and t due to a decrease ofR_S.

Samples on SnO2:F. The efficiency increases from 4.7 % for the NaF PDT of 4 min at 250°C to 7.5 % for NaF PDT of 4 min at 350°C which is higher than the Mo reference. The J_{SC} increases from 15.1 to 16.6 mA/cm² with T. A high V_{OC} (590-615 mV) comparable to the V_{OC} of the cells on Mo is achieved whatever the NaF PDT. The FF increases from 52% to 69% with T and t mainly due to a decrease in R_S.

Samples on ZnO:Al. An efficiency of 6.8% was obtained with the NaF PDT of 4 min at 350°C. This is the only decently working cell so no conclusion in the influence of the NaF PDT can be made.

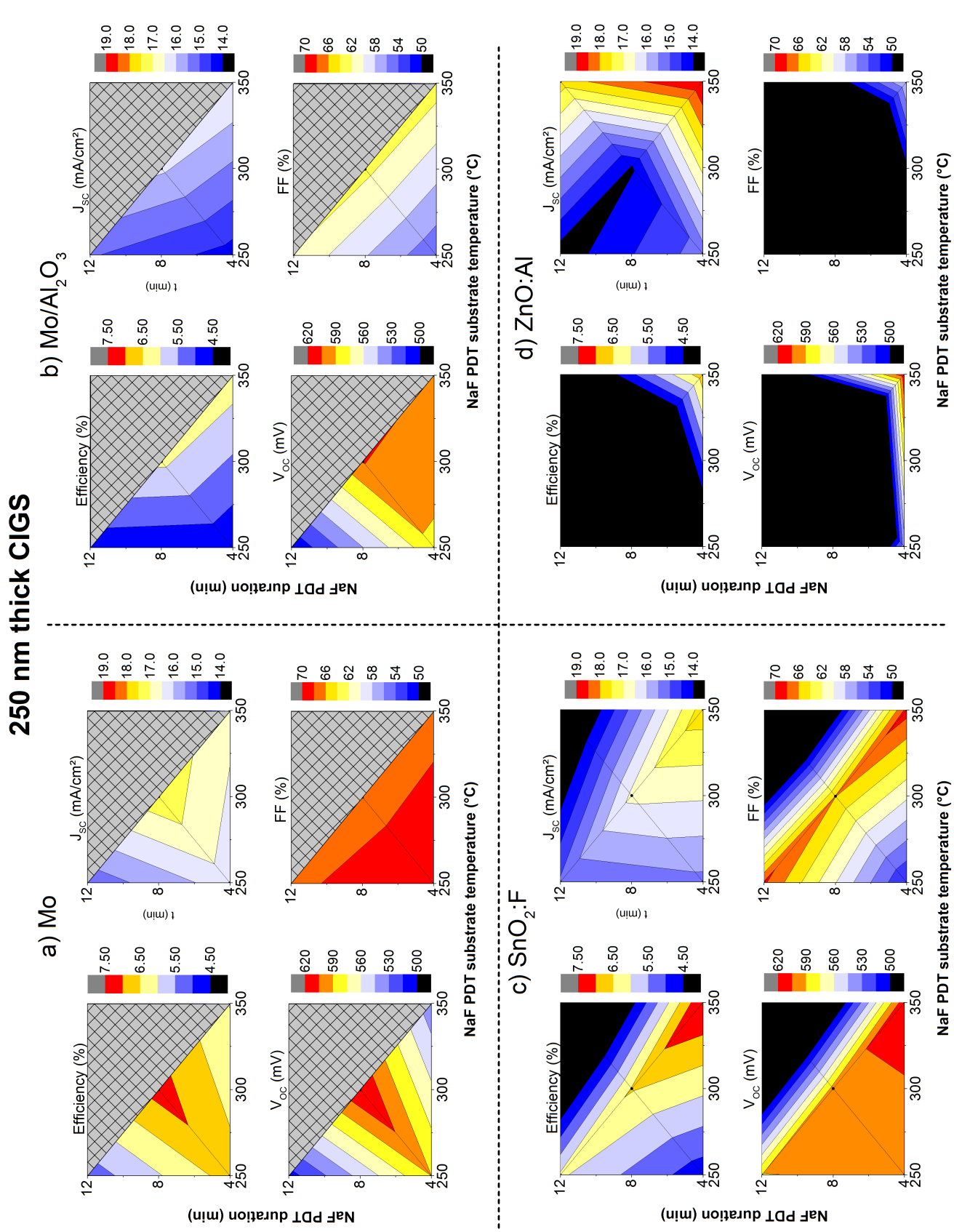

Figure E.3.: Efficiency, J_{SC}, V_{OC} and FF of the cells with 300 nm of CIGS processed with different NaF PDT. The CIGS layer were deposited on: a) a standard Mo back-contact, b) a Mo coated on the Al_2O_3 barrier layer back-contact, c) a SnO_2:F back-contact and d) a ZnO:Al back-contact. Some samples delaminated (grey mask) or was strongly shunted (efficiency <1% out of the scale).

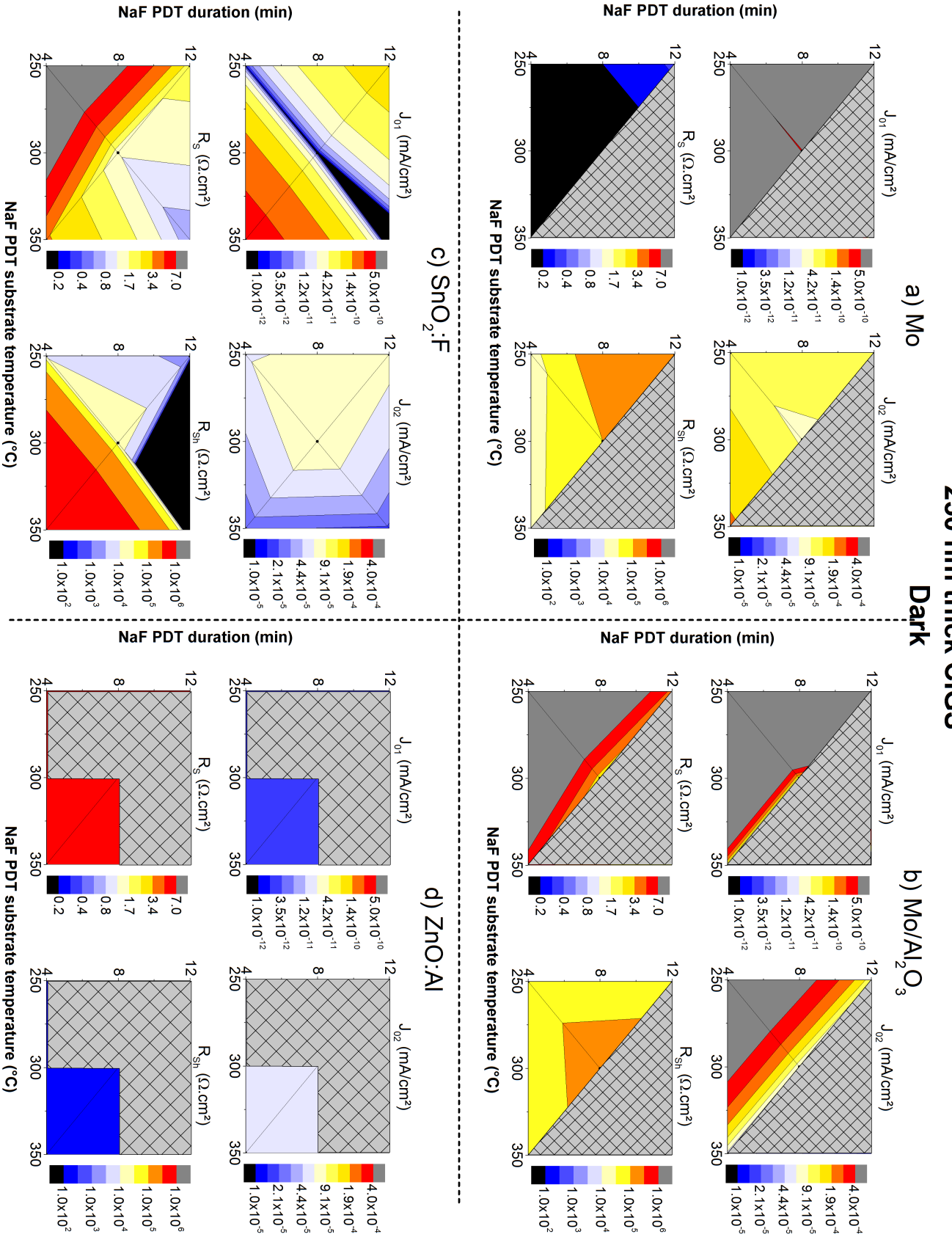

Figure E.4.: IV dark fitting parameters of the cells with 450 nm of CIGS processed with different NaF PDT. The CIGS layer were deposited on: a) a standard Mo back-contact, b) a Mo coated on the Al_2O_3 barrier layer back-contact, c) a SnO_2:F back-contact and d) a ZnO:Al back-contact.

To conclude, the optimal NaF PDT is more difficult to find for each different substrates on the 300 nm thick CIGS than on the 450 nm thick CIGS. This optimal NaF PDT is a balance between a the beneficial effect of the Na incorporation and the deterioration of the CIGS layer due to a too large amount of Na.

Best condition

Table E.1.: I(V) light parameters for the samples on the different substrates with the best NaF PDT. Light I(V) parameters are given as mean ± standard deviation of the 10 best cells (one sample contains 20 cells).

Experiments			Light I(V) parameters			
CIGS thickness	Substrate	NaF PDT	Efficiency (%)	J_{SC} (mA/cm²)	V_{OC} (mV)	FF (%)
450 nm	Mo	4 min / 250°C	**9.8**±0.3	**21.4**±0.2	**648**±3	**71**±2
	Mo/Al_2O_3	8 min / 300°C	**10.0**±0.3	**22.7**±0.3	**641**±3	**68**±2
	SnO_2:F	12 min / 350°C	**9.8**±0.2	**23.5**±0.6	**611**±3	**68**±1
	ZnO:Al	4 min / 350°C	**8.6**±0.2	**23.1**±0.3	**628**±4	**59**±1
250 nm	Mo	8 min / 300°C	**6.8**∓ 0.4	**17.7**∓ 0.2	**605** ∓ 13	**63**∓ 3
	Mo/Al_2O_3	4 min / 350°C	**6.3**∓ 0.2	**16.8**∓ 0.4	**601**∓ 6	**62**∓ 1
	SnO_2:F	4 min / 350°C	**7.6**∓ 0.1	**18.2**∓ 0.2	**614**∓ 3	**68**∓ 2
	ZnO:Al	4 min / 350°C	**6.8**∓ 0.4	**20.8**∓ 0.5	**601**∓ 10	**54**∓ 3

F. Refractive indices

	ZnO:Al		ZnO		CdS		Mo		SnO_2:F	
(nm)	n	k	n	k	n	k	n	k	n	k
350	2,09	5,1E-02	2,20	4,6E-01	2,48	4,6E-01	1,73	2,0E+00	1,64	2,1E-02
360	2,06	3,7E-02	2,27	4,8E-01	2,48	4,6E-01	1,75	2,0E+00	1,63	1,8E-02
370	2,03	2,8E-02	2,42	4,5E-01	2,49	4,5E-01	1,77	2,0E+00	1,63	1,6E-02
380	2,01	2,1E-02	2,51	2,3E-01	2,50	4,4E-01	1,79	2,0E+00	1,63	1,4E-02
390	1,99	1,7E-02	2,41	8,7E-02	2,51	4,4E-01	1,80	2,1E+00	1,62	1,3E-02
400	1,97	1,3E-02	2,31	2,2E-02	2,53	4,2E-01	1,82	2,1E+00	1,62	1,1E-02
410	1,96	1,1E-02	2,24	2,4E-03	2,54	4,1E-01	1,83	2,1E+00	1,61	1,0E-02
420	1,94	8,5E-03	2,20	0,0E+00	2,56	3,9E-01	1,85	2,1E+00	1,61	9,4E-03
430	1,93	7,0E-03	2,17	0,0E+00	2,58	3,7E-01	1,87	2,2E+00	1,61	8,7E-03
440	1,92	5,7E-03	2,15	0,0E+00	2,60	3,5E-01	1,89	2,2E+00	1,60	8,1E-03
450	1,91	4,8E-03	2,13	0,0E+00	2,61	3,2E-01	1,92	2,2E+00	1,60	7,6E-03
460	1,90	4,1E-03	2,12	0,0E+00	2,63	2,9E-01	1,94	2,3E+00	1,59	7,2E-03
470	1,89	3,5E-03	2,10	0,0E+00	2,64	2,5E-01	1,97	2,3E+00	1,59	6,9E-03
480	1,88	3,1E-03	2,10	0,0E+00	2,65	2,0E-01	2,01	2,3E+00	1,59	6,6E-03
490	1,88	2,7E-03	2,09	0,0E+00	2,64	1,5E-01	2,04	2,4E+00	1,58	6,4E-03
500	1,87	2,5E-03	2,08	0,0E+00	2,61	9,7E-02	2,08	2,4E+00	1,58	6,2E-03
510	1,86	2,3E-03	2,08	0,0E+00	2,57	6,7E-02	2,12	2,4E+00	1,58	6,1E-03
520	1,85	2,2E-03	2,07	0,0E+00	2,54	5,3E-02	2,16	2,4E+00	1,57	6,0E-03
530	1,85	2,1E-03	2,07	0,0E+00	2,51	4,5E-02	2,21	2,4E+00	1,57	5,9E-03
540	1,84	2,0E-03	2,06	0,0E+00	2,49	4,0E-02	2,24	2,4E+00	1,57	5,9E-03
550	1,83	2,0E-03	2,06	0,0E+00	2,47	3,7E-02	2,26	2,4E+00	1,56	5,9E-03
560	1,83	2,0E-03	2,05	0,0E+00	2,46	3,4E-02	2,28	2,4E+00	1,56	5,9E-03
570	1,82	2,0E-03	2,05	0,0E+00	2,44	3,2E-02	2,30	2,4E+00	1,56	6,0E-03
580	1,81	2,1E-03	2,05	0,0E+00	2,43	3,0E-02	2,31	2,4E+00	1,55	6,1E-03
590	1,81	2,1E-03	2,05	0,0E+00	2,42	2,8E-02	2,32	2,5E+00	1,55	6,2E-03
600	1,80	2,2E-03	2,04	0,0E+00	2,41	2,7E-02	2,33	2,5E+00	1,54	6,3E-03
610	1,80	2,3E-03	2,04	0,0E+00	2,40	2,6E-02	2,34	2,5E+00	1,54	6,4E-03
620	1,79	2,4E-03	2,04	0,0E+00	2,39	2,5E-02	2,35	2,5E+00	1,54	6,6E-03
630	1,78	2,5E-03	2,04	0,0E+00	2,38	2,4E-02	2,37	2,5E+00	1,53	6,7E-03
640	1,78	2,6E-03	2,03	0,0E+00	2,37	2,3E-02	2,38	2,5E+00	1,53	6,9E-03
650	1,77	2,8E-03	2,03	0,0E+00	2,37	2,2E-02	2,40	2,5E+00	1,53	7,1E-03
660	1,77	2,9E-03	2,03	0,0E+00	2,36	2,2E-02	2,41	2,5E+00	1,52	7,4E-03
670	1,76	3,1E-03	2,03	0,0E+00	2,36	2,1E-02	2,43	2,6E+00	1,52	7,6E-03
680	1,75	3,2E-03	2,03	0,0E+00	2,35	2,1E-02	2,44	2,6E+00	1,51	7,9E-03
690	1,75	3,4E-03	2,03	0,0E+00	2,35	2,0E-02	2,45	2,6E+00	1,51	8,1E-03
700	1,74	3,6E-03	2,03	0,0E+00	2,34	1,9E-02	2,46	2,6E+00	1,50	8,4E-03
710	1,74	3,8E-03	2,02	0,0E+00	2,34	1,9E-02	2,48	2,6E+00	1,50	8,7E-03
720	1,73	4,0E-03	2,02	0,0E+00	2,33	1,9E-02	2,49	2,6E+00	1,50	9,0E-03
730	1,73	4,3E-03	2,02	0,0E+00	2,33	1,8E-02	2,50	2,6E+00	1,49	9,4E-03
740	1,72	4,5E-03	2,02	0,0E+00	2,32	1,8E-02	2,50	2,6E+00	1,49	9,7E-03
750	1,71	4,8E-03	2,02	0,0E+00	2,32	1,7E-02	2,51	2,6E+00	1,48	1,0E-02
760	1,71	5,1E-03	2,02	0,0E+00	2,32	1,7E-02	2,51	2,6E+00	1,48	1,1E-02

	ZnO:Al		ZnO		CdS		Mo		SnO_2:F	
(nm)	n	k	n	k	n	k	n	k	n	k
770	1,70	5,3E-03	2,02	0,0E+00	2,31	1,7E-02	2,51	2,6E+00	1,47	1,1E-02
780	1,69	5,7E-03	2,02	0,0E+00	2,31	1,6E-02	2,51	2,6E+00	1,47	1,1E-02
790	1,69	6,0E-03	2,02	0,0E+00	2,31	1,6E-02	2,51	2,6E+00	1,46	1,2E-02
800	1,68	6,3E-03	2,02	0,0E+00	2,31	1,6E-02	2,51	2,6E+00	1,46	1,2E-02
810	1,68	6,7E-03	2,01	0,0E+00	2,30	1,5E-02	2,50	2,6E+00	1,45	1,3E-02
820	1,67	7,1E-03	2,01	0,0E+00	2,30	1,5E-02	2,49	2,6E+00	1,45	1,3E-02
830	1,66	7,5E-03	2,01	0,0E+00	2,30	1,5E-02	2,48	2,6E+00	1,44	1,4E-02
840	1,66	7,9E-03	2,01	0,0E+00	2,30	1,5E-02	2,47	2,6E+00	1,44	1,4E-02
850	1,65	8,4E-03	2,01	0,0E+00	2,29	1,4E-02	2,46	2,6E+00	1,43	1,5E-02
860	1,64	8,9E-03	2,01	0,0E+00	2,29	1,4E-02	2,44	2,7E+00	1,43	1,5E-02
870	1,64	9,4E-03	2,01	0,0E+00	2,29	1,4E-02	2,43	2,7E+00	1,42	1,6E-02
880	1,63	1,0E-02	2,01	0,0E+00	2,29	1,4E-02	2,41	2,7E+00	1,42	1,7E-02
890	1,62	1,1E-02	2,01	0,0E+00	2,29	1,4E-02	2,39	2,7E+00	1,41	1,7E-02
900	1,62	1,1E-02	2,01	0,0E+00	2,28	1,3E-02	2,37	2,7E+00	1,40	1,8E-02
910	1,61	1,2E-02	2,01	0,0E+00	2,28	1,3E-02	2,35	2,7E+00	1,40	1,9E-02
920	1,60	1,3E-02	2,01	0,0E+00	2,28	1,3E-02	2,33	2,7E+00	1,39	1,9E-02
930	1,60	1,3E-02	2,01	0,0E+00	2,28	1,3E-02	2,31	2,8E+00	1,39	2,0E-02
940	1,59	1,4E-02	2,01	0,0E+00	2,28	1,3E-02	2,30	2,8E+00	1,38	2,1E-02
950	1,58	1,5E-02	2,01	0,0E+00	2,28	1,2E-02	2,28	2,8E+00	1,38	2,2E-02
960	1,57	1,6E-02	2,01	0,0E+00	2,28	1,2E-02	2,26	2,8E+00	1,37	2,2E-02
970	1,57	1,7E-02	2,01	0,0E+00	2,27	1,2E-02	2,25	2,9E+00	1,36	2,3E-02
980	1,56	1,8E-02	2,01	0,0E+00	2,27	1,2E-02	2,23	2,9E+00	1,36	2,4E-02
990	1,55	1,9E-02	2,01	0,0E+00	2,27	1,2E-02	2,21	2,9E+00	1,35	2,5E-02
1000	1,54	2,0E-02	2,01	0,0E+00	2,27	1,2E-02	2,20	3,0E+00	1,34	2,6E-02
1010	1,54	2,1E-02	2,01	0,0E+00	2,27	1,1E-02	2,18	3,0E+00	1,34	2,7E-02
1020	1,53	2,2E-02	2,00	0,0E+00	2,27	1,1E-02	2,17	3,0E+00	1,33	2,8E-02
1030	1,52	2,3E-02	2,00	0,0E+00	2,27	1,1E-02	2,16	3,1E+00	1,32	2,9E-02
1040	1,51	2,4E-02	2,00	0,0E+00	2,27	1,1E-02	2,15	3,1E+00	1,32	3,0E-02
1050	1,50	2,6E-02	2,00	0,0E+00	2,26	1,1E-02	2,14	3,2E+00	1,31	3,1E-02
1060	1,50	2,7E-02	2,00	0,0E+00	2,26	1,1E-02	2,14	3,2E+00	1,30	3,2E-02
1070	1,49	2,9E-02	2,00	0,0E+00	2,26	1,1E-02	2,13	3,2E+00	1,30	3,3E-02
1080	1,48	3,0E-02	2,00	0,0E+00	2,26	1,1E-02	2,12	3,3E+00	1,29	3,4E-02
1090	1,47	3,2E-02	2,00	0,0E+00	2,26	1,0E-02	2,12	3,3E+00	1,28	3,5E-02
1100	1,46	3,3E-02	2,00	0,0E+00	2,26	1,0E-02	2,11	3,3E+00	1,27	3,7E-02
1110	1,45	3,5E-02	2,00	0,0E+00	2,26	1,0E-02	2,11	3,4E+00	1,27	3,8E-02
1120	1,44	3,7E-02	2,00	0,0E+00	2,26	1,0E-02	2,10	3,4E+00	1,26	3,9E-02
1130	1,43	3,9E-02	2,00	0,0E+00	2,26	1,0E-02	2,10	3,5E+00	1,25	4,1E-02
1140	1,43	4,1E-02	2,00	0,0E+00	2,26	9,9E-03	2,10	3,5E+00	1,24	4,2E-02
1150	1,42	4,3E-02	2,00	0,0E+00	2,26	9,8E-03	2,10	3,5E+00	1,23	4,4E-02
1160	1,41	4,5E-02	2,00	0,0E+00	2,26	9,7E-03	2,10	3,6E+00	1,23	4,5E-02
1170	1,40	4,7E-02	2,00	0,0E+00	2,25	9,6E-03	2,10	3,6E+00	1,22	4,7E-02
1180	1,39	4,9E-02	2,00	0,0E+00	2,25	9,5E-03	2,09	3,6E+00	1,21	4,8E-02

	ZnO:Al		ZnO		CdS		Mo		SnO_2:F	
(nm)	n	k	n	k	n	k	n	k	n	k
1190	1,38	5,1E-02	2,00	0,0E+00	2,25	9,4E-03	2,10	3,7E+00	1,20	5,0E-02
1200	1,37	5,3E-02	2,00	0,0E+00	2,25	9,3E-03	2,10	3,7E+00	1,19	5,2E-02
1210	1,36	5,5E-02	2,00	0,0E+00	2,25	9,2E-03	2,10	3,8E+00	1,18	5,3E-02
1220	1,35	5,8E-02	2,00	0,0E+00	2,25	9,2E-03	2,10	3,8E+00	1,17	5,5E-02
1230	1,34	6,0E-02	2,00	0,0E+00	2,25	9,1E-03	2,10	3,8E+00	1,17	5,7E-02
1240	1,33	6,3E-02	2,00	0,0E+00	2,25	9,0E-03	2,10	3,9E+00	1,16	5,9E-02
1250	1,32	6,5E-02	2,00	0,0E+00	2,25	8,9E-03	2,11	3,9E+00	1,15	6,1E-02
1260	1,31	6,8E-02	2,00	0,0E+00	2,25	8,8E-03	2,11	3,9E+00	1,14	6,3E-02
1270	1,30	7,1E-02	2,00	0,0E+00	2,25	8,7E-03	2,12	4,0E+00	1,13	6,5E-02
1280	1,28	7,4E-02	2,00	0,0E+00	2,25	8,7E-03	2,13	4,0E+00	1,12	6,8E-02
1290	1,27	7,7E-02	2,00	0,0E+00	2,25	8,6E-03	2,13	4,0E+00	1,11	7,0E-02
1300	1,26	8,0E-02	2,00	0,0E+00	2,25	8,5E-03	2,14	4,1E+00	1,10	7,2E-02
1310	1,25	8,3E-02	2,00	0,0E+00	2,25	8,4E-03	2,15	4,1E+00	1,09	7,5E-02
1320	1,24	8,6E-02	2,00	0,0E+00	2,25	8,4E-03	2,15	4,1E+00	1,08	7,7E-02
1330	1,23	8,9E-02	2,00	0,0E+00	2,25	8,3E-03	2,16	4,2E+00	1,07	8,0E-02
1340	1,21	9,3E-02	2,00	0,0E+00	2,24	8,2E-03	2,16	4,2E+00	1,06	8,3E-02
1350	1,20	9,6E-02	2,00	0,0E+00	2,24	8,2E-03	2,17	4,2E+00	1,05	8,6E-02
1360	1,19	1,0E-01	2,00	0,0E+00	2,24	8,1E-03	2,18	4,3E+00	1,04	8,9E-02
1370	1,18	1,0E-01	2,00	0,0E+00	2,24	8,0E-03	2,18	4,3E+00	1,02	9,2E-02
1380	1,16	1,1E-01	2,00	0,0E+00	2,24	8,0E-03	2,19	4,3E+00	1,01	9,5E-02
1390	1,15	1,1E-01	2,00	0,0E+00	2,24	7,9E-03	2,19	4,4E+00	1,00	9,8E-02
1400	1,14	1,2E-01	2,00	0,0E+00	2,24	7,8E-03	2,20	4,4E+00	0,99	1,0E-01
1410	1,13	1,2E-01	2,00	0,0E+00	2,24	7,8E-03	2,20	4,4E+00	0,98	1,1E-01
1420	1,11	1,2E-01	2,00	0,0E+00	2,24	7,7E-03	2,21	4,4E+00	0,97	1,1E-01
1430	1,10	1,3E-01	2,00	0,0E+00	2,24	7,6E-03	2,21	4,5E+00	0,95	1,1E-01
1440	1,08	1,3E-01	2,00	0,0E+00	2,24	7,6E-03	2,22	4,5E+00	0,94	1,2E-01
1450	1,07	1,4E-01	2,00	0,0E+00	2,24	7,5E-03	2,23	4,5E+00	0,93	1,2E-01
1460	1,06	1,4E-01	2,00	0,0E+00	2,24	7,5E-03	2,23	4,6E+00	0,92	1,3E-01
1470	1,04	1,5E-01	2,00	0,0E+00	2,24	7,4E-03	2,24	4,6E+00	0,90	1,3E-01
1480	1,03	1,6E-01	2,00	0,0E+00	2,24	7,4E-03	2,24	4,6E+00	0,89	1,4E-01
1490	1,01	1,6E-01	2,00	0,0E+00	2,24	7,3E-03	2,25	4,7E+00	0,88	1,4E-01
1500	0,99	1,7E-01	2,00	0,0E+00	2,24	7,3E-03	2,25	4,7E+00	0,86	1,5E-01

	CIGS							
	GGI=0.15		GGI=0.30		GGI=0.42		GGI=0.61	
(nm)	n	k	n	k	n	k	n	k
350	2,83	1,0E+00	2,85	1,0E+00	2,89	1,0E+00	2,88	1,0E+00
360	2,83	1,0E+00	2,84	9,9E-01	2,89	1,0E+00	2,89	1,0E+00
370	2,83	1,0E+00	2,85	1,0E+00	2,90	1,0E+00	2,93	1,0E+00
380	2,85	1,0E+00	2,88	1,0E+00	2,94	1,1E+00	2,99	1,1E+00
390	2,89	1,0E+00	2,94	1,0E+00	3,01	1,1E+00	3,06	1,0E+00
400	2,96	1,0E+00	3,02	1,0E+00	3,09	1,0E+00	3,14	9,8E-01
410	3,04	1,0E+00	3,10	9,8E-01	3,17	9,8E-01	3,20	9,1E-01
420	3,11	9,6E-01	3,16	9,2E-01	3,22	9,0E-01	3,24	8,3E-01
430	3,16	8,9E-01	3,20	8,3E-01	3,25	8,1E-01	3,25	7,4E-01
440	3,19	8,2E-01	3,22	7,5E-01	3,26	7,3E-01	3,24	6,7E-01
450	3,20	7,4E-01	3,21	6,8E-01	3,25	6,6E-01	3,23	6,1E-01
460	3,19	6,8E-01	3,20	6,2E-01	3,23	6,0E-01	3,21	5,5E-01
470	3,18	6,2E-01	3,18	5,6E-01	3,21	5,5E-01	3,19	5,1E-01
480	3,16	5,7E-01	3,16	5,2E-01	3,18	5,2E-01	3,16	4,8E-01
490	3,14	5,3E-01	3,14	4,9E-01	3,16	4,8E-01	3,14	4,5E-01
500	3,12	5,0E-01	3,12	4,6E-01	3,14	4,6E-01	3,12	4,2E-01
510	3,10	4,8E-01	3,10	4,4E-01	3,12	4,4E-01	3,10	4,0E-01
520	3,09	4,5E-01	3,08	4,2E-01	3,10	4,2E-01	3,09	3,9E-01
530	3,07	4,4E-01	3,06	4,0E-01	3,09	4,0E-01	3,07	3,7E-01
540	3,05	4,2E-01	3,05	3,9E-01	3,07	3,9E-01	3,06	3,6E-01
550	3,04	4,1E-01	3,03	3,8E-01	3,06	3,8E-01	3,05	3,5E-01
560	3,03	4,0E-01	3,02	3,7E-01	3,05	3,7E-01	3,04	3,4E-01
570	3,02	3,9E-01	3,01	3,6E-01	3,04	3,6E-01	3,03	3,3E-01
580	3,01	3,8E-01	3,00	3,5E-01	3,03	3,5E-01	3,02	3,2E-01
590	3,00	3,7E-01	3,00	3,4E-01	3,02	3,4E-01	3,02	3,2E-01
600	2,99	3,7E-01	2,99	3,4E-01	3,02	3,4E-01	3,01	3,1E-01
610	2,99	3,6E-01	2,98	3,3E-01	3,01	3,3E-01	3,01	3,0E-01
620	2,98	3,5E-01	2,98	3,3E-01	3,01	3,3E-01	3,00	3,0E-01
630	2,98	3,5E-01	2,97	3,2E-01	3,00	3,2E-01	3,00	2,9E-01
640	2,97	3,4E-01	2,97	3,2E-01	3,00	3,1E-01	3,00	2,8E-01
650	2,97	3,4E-01	2,97	3,1E-01	3,00	3,1E-01	3,00	2,8E-01
660	2,97	3,3E-01	2,97	3,1E-01	3,00	3,0E-01	3,00	2,7E-01
670	2,96	3,3E-01	2,96	3,0E-01	3,00	3,0E-01	3,00	2,6E-01
680	2,96	3,3E-01	2,96	3,0E-01	2,99	2,9E-01	3,00	2,5E-01
690	2,96	3,2E-01	2,96	2,9E-01	2,99	2,9E-01	3,00	2,5E-01
700	2,96	3,2E-01	2,96	2,9E-01	2,99	2,8E-01	3,00	2,4E-01
710	2,96	3,1E-01	2,96	2,8E-01	2,99	2,8E-01	3,00	2,3E-01
720	2,96	3,1E-01	2,96	2,8E-01	2,99	2,7E-01	3,00	2,2E-01
730	2,96	3,1E-01	2,96	2,8E-01	2,99	2,6E-01	2,99	2,1E-01
740	2,96	3,0E-01	2,96	2,7E-01	3,00	2,6E-01	2,99	2,1E-01
750	2,96	3,0E-01	2,96	2,7E-01	3,00	2,5E-01	2,99	2,0E-01
760	2,96	2,9E-01	2,96	2,6E-01	3,00	2,4E-01	2,99	1,9E-01

	CIGS							
	GGI=0.15		GGI=0.30		GGI=0.42		GGI=0.61	
(nm)	n	k	n	k	n	k	n	k
770	2,96	2,9E-01	2,97	2,6E-01	3,00	2,4E-01	2,99	1,8E-01
780	2,97	2,8E-01	2,97	2,5E-01	3,00	2,3E-01	2,99	1,7E-01
790	2,97	2,8E-01	2,97	2,4E-01	3,00	2,2E-01	2,99	1,6E-01
800	2,97	2,7E-01	2,97	2,4E-01	3,00	2,2E-01	2,99	1,5E-01
810	2,97	2,7E-01	2,97	2,3E-01	3,00	2,1E-01	2,99	1,4E-01
820	2,97	2,6E-01	2,98	2,3E-01	3,00	2,0E-01	2,99	1,3E-01
830	2,97	2,6E-01	2,98	2,2E-01	3,01	1,9E-01	2,98	1,2E-01
840	2,98	2,5E-01	2,98	2,1E-01	3,01	1,8E-01	2,98	1,1E-01
850	2,98	2,5E-01	2,98	2,0E-01	3,01	1,7E-01	2,98	1,0E-01
860	2,98	2,4E-01	2,98	1,9E-01	3,00	1,6E-01	2,97	9,3E-02
870	2,98	2,4E-01	2,99	1,8E-01	3,00	1,5E-01	2,97	8,3E-02
880	2,98	2,3E-01	2,98	1,7E-01	3,00	1,5E-01	2,96	7,4E-02
890	2,99	2,2E-01	2,98	1,6E-01	3,00	1,4E-01	2,95	6,5E-02
900	2,99	2,2E-01	2,98	1,6E-01	3,00	1,3E-01	2,95	5,8E-02
910	2,99	2,1E-01	2,97	1,5E-01	2,99	1,2E-01	2,94	5,1E-02
920	2,99	2,0E-01	2,97	1,5E-01	2,99	1,1E-01	2,93	4,5E-02
930	2,99	1,9E-01	2,97	1,4E-01	2,99	1,1E-01	2,92	4,1E-02
940	3,00	1,9E-01	2,97	1,4E-01	2,99	9,9E-02	2,91	3,7E-02
950	3,00	1,8E-01	2,97	1,3E-01	2,98	9,1E-02	2,91	3,3E-02
960	3,00	1,7E-01	2,97	1,2E-01	2,98	8,2E-02	2,90	2,9E-02
970	2,99	1,6E-01	2,97	1,2E-01	2,98	7,3E-02	2,89	2,6E-02
980	2,99	1,5E-01	2,97	1,1E-01	2,97	6,4E-02	2,89	2,3E-02
990	2,99	1,4E-01	2,97	1,0E-01	2,97	5,6E-02	2,88	2,1E-02
1000	2,99	1,4E-01	2,97	9,7E-02	2,96	4,8E-02	2,88	1,9E-02
1010	2,98	1,3E-01	2,97	8,9E-02	2,95	3,8E-02	2,87	1,7E-02
1020	2,98	1,3E-01	2,97	7,9E-02	2,95	3,0E-02	2,87	1,5E-02
1030	2,98	1,2E-01	2,97	6,9E-02	2,94	2,4E-02	2,86	1,4E-02
1040	2,98	1,2E-01	2,97	5,7E-02	2,93	1,9E-02	2,86	1,2E-02
1050	2,98	1,1E-01	2,97	4,4E-02	2,92	1,5E-02	2,86	1,1E-02
1060	2,98	1,0E-01	2,96	2,9E-02	2,92	1,2E-02	2,85	1,0E-02
1070	2,98	9,8E-02	2,95	1,4E-02	2,91	9,2E-03	2,85	9,3E-03
1080	2,98	9,1E-02	2,93	7,9E-03	2,90	7,3E-03	2,84	8,4E-03
1090	2,98	8,4E-02	2,92	2,6E-03	2,90	5,4E-03	2,84	7,6E-03
1100	2,98	7,6E-02	2,91	1,1E-03	2,89	4,0E-03	2,84	6,9E-03
1110	2,98	6,7E-02	2,90	0,0E+00	2,89	2,7E-03	2,83	6,3E-03
1120	2,98	5,7E-02	2,90	0,0E+00	2,88	1,6E-03	2,83	5,7E-03
1130	2,97	4,6E-02	2,89	0,0E+00	2,88	7,3E-04	2,83	5,1E-03
1140	2,97	3,4E-02	2,89	0,0E+00	2,88	3,3E-04	2,83	4,6E-03
1150	2,96	2,2E-02	2,88	0,0E+00	2,87	0,0E+00	2,82	4,1E-03
1160	2,95	1,4E-02	2,87	0,0E+00	2,87	0,0E+00	2,82	3,7E-03
1170	2,94	6,0E-03	2,87	0,0E+00	2,87	0,0E+00	2,82	3,3E-03
1180	2,93	3,3E-03	2,87	0,0E+00	2,86	0,0E+00	2,82	2,9E-03

	CIGS							
	GGI=0.15		GGI=0.30		GGI=0.42		GGI=0.61	
(nm)	n	k	n	k	n	k	n	k
1190	2,92	6,2E-04	2,86	0,0E+00	2,86	0,0E+00	2,81	2,6E-03
1200	2,91	0,0E+00	2,86	0,0E+00	2,86	0,0E+00	2,81	2,3E-03
1210	2,91	0,0E+00	2,85	0,0E+00	2,85	0,0E+00	2,81	2,0E-03
1220	2,90	0,0E+00	2,85	0,0E+00	2,85	0,0E+00	2,81	1,7E-03
1230	2,90	0,0E+00	2,85	0,0E+00	2,85	0,0E+00	2,80	1,4E-03
1240	2,89	0,0E+00	2,84	0,0E+00	2,84	0,0E+00	2,80	1,2E-03
1250	2,89	0,0E+00	2,84	0,0E+00	2,84	0,0E+00	2,80	9,4E-04
1260	2,88	0,0E+00	2,84	0,0E+00	2,84	0,0E+00	2,80	7,2E-04
1270	2,88	0,0E+00	2,84	0,0E+00	2,84	0,0E+00	2,80	5,2E-04
1280	2,87	0,0E+00	2,83	0,0E+00	2,84	0,0E+00	2,80	3,3E-04
1290	2,87	0,0E+00	2,83	0,0E+00	2,83	0,0E+00	2,79	1,3E-04
1300	2,87	0,0E+00	2,83	0,0E+00	2,83	0,0E+00	2,79	7,2E-05

Optimisation de cellules solaires ultra-minces à base de Cu(In,Ga)Se_2 avec contact arrière alternatif

Introduction

Les énergies renouvelables sont essentielles pour respecter l'Accord de Paris 2015 qui vise à répondre à la menace du changement climatique [1]. Les technologies photovoltaïques (PV) sont un élément clé de l'électricité décarbonée, qui exploite l'énergie quasi-illimitée du soleil et qui, de plus, est en passe de devenir compétitive par rapport à d'autres sources d'énergie.

Le photovoltaïque est aujourd'hui dominé par la technologie du silicium cristallin. Parmi les alternatives, la technologie en couche mince Cu(In,Ga)Se_2 (CIGS) est l'une des plus avancées et des plus efficaces [2]. Celle-ci est déjà mature, avec une efficacité record en 2016 de 22,6% pour une surface de 0,5 cm^2 [3] et une efficacité pour les modules de 16,5%. Pour être plus compétitive, le coût du module CIGS, calculé par le *Levelized Cost of Electricity*, doit encore être réduit. Cela passe par une diminution du coût de fabrication du module, une augmentation de la production, une amélioration de l'efficacité du module et une plus faible dégradation du module avec le temps [4].

Cette thèse vise à réduire le coût de fabrication du module et à augmenter l'efficacité du module en réduisant l'épaisseur de l'absorbeur CIGS. Cette stratégie permettrait (1) d'augmenter le débit d'une usine en réduisant le temps de dépôt de CIGS, (2) de réduire la consommation de matière, notamment l'indium et le gallium identifiés comme matières premières critiques par un rapport de 2014 de la Commission Européenne [5] et (3) d'augmenter l'efficacité de conversion de puissance du dispositif en minimisant les pertes électriques dans l'absorbeur de CIGS.

Cependant, des études antérieures ont montée que l'amincissement de l'épaisseur de l'absorbeur CIGS de 2 - 2,5 μm (cellules standard à haut rendement) , à moins de 500 nm (cellules ultra-minces), a un impact négatif sur l'efficacité des cellules [6]. Le coefficient d'absorption CIGS est insuffisant pour garantir une absorption de lumière à travers moins de 500 nm de matériaux. De plus, la couche de molybdène absorbe de manière excessive et la recombinaison des porteurs de charges à l'interface arrière est amplifiée. Un changement de paradigme est nécessaire : nous devons faire paraître les matériaux «électriquement minces mais optiquement épais».

Dans cette thèse de doctorat, nous avons cherché à développer une interface arrière appropriée à la cellule solaire CIGS ultra-mince permettant une génération et une collecte efficace des porteurs de charge.

Motivation de l'étude et compréhension des mécanismes de pertes dans les cellules CIGS ultra-minces

Une cellule solaire standard CIGS est schématisée dans la Figure F.1. Expliqué simplement, la cellule est composée d'une couche de Cu(In,Ga)Se_2 de type p, qui est le principal absorbeur de lumière. L'énergie des rayonnement du soleil est convertie en énergie chimique par la création de pair électron-trou au sein de cette couche. Le CIGS est en contact avec une couche CdS de type n pour former une jonction p-n. Cette jonction forme un champ électrique dans la couche de CIGS et améliore la collecte des porteurs de charges. A l'avant, une électrode transparente, généralement une bicouche ZnO / ZnO : Al, collecte les électrons. À l'arrière, une électrode en molybdène collecte les trous.

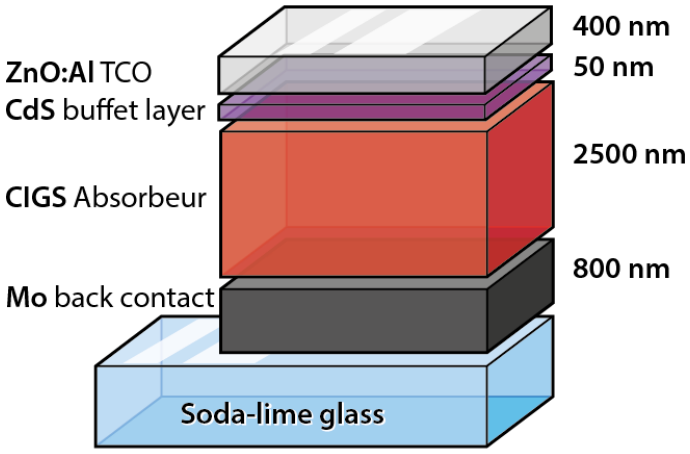

Figure F.1. : Schema d'une cellule solaire à base de CIGS.

Le développement de cellules solaires CIGS ultra-minces (c'est-à-dire avec une épaisseur de CIGS inférieure à 500 nm) présente plusieurs avantages industriels par rapport aux cellules solaires CIGS standards (c'est-à-dire avec une épaisseur de CIGS entre 2,0 et 2,5 μm). Cela rend les industries moins dépendant du marché international du métal. Il pourrait également réduire le coût du module en diminuant

la consommation de matière et en augmentant le débit de l'usine. Avec un calcule approximatif, nous pouvons montrer que la réduction des coups pour un module de 14% de rendement est de au moins 30 €/kW (sur un coup total de 500 €/kW [4]). En retour, l'efficacité des cellules ultra-minces doit, au minimum, être identique à celle des cellules standards. En effet, une variation de 1% du rendement correspond à une variation de 35 €/kW de coût.

Cependant, il a été trouvé dans la littérature, que l'amincissement de la couche CIGS conduit à une réduction de l'efficacité des cellules, en particulier pour les épaisseurs CIGS en-dessous de 1 μm. Nous avons simulé le comportement d'une cellule solaire en fonction de l'épaisseur par 2 méthodes : électrique et optique.

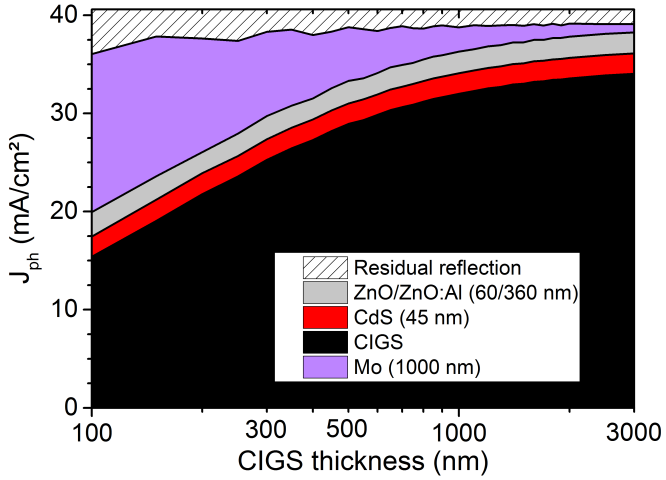

Figure F.2. : Simulation du photocourrant J_{ph} absorbé par les différentes couches de l'empilement lors d'une illumination de la cellule sous condition standard (AM1.5 1000W/m²). Le photocourrant est calculé à partir des courbes absorptions simulé par le méthode de transfert matriciel.

Optique La simulation optique a été effectué avec un logiciel développé sur *Matlab*. Le logiciel permet de calculer le comportement optique d'un empilement de couches minces en utilisant la méthode de transfert matriciel. Chaque couche est simulé par son indice de réfraction complexe en fonction de la longueur d'onde obtenu par ellipsometrie. L'absorption des différentes couches d'un CIGS en fonction de l'épaisseur est présenté dans Figure F.2. Nous pouvons remarquer la prédominance de l'absorption de la couche de Mo au détriment de la couche de CIGS. Le coefficient d'absorption du CIGS ne permet pas d'absorber toute la lumière sur une faible épaisseur tandis que le Mo absorbe fortement toute la lumière restante.

Électrique La simulation électrique a été effectuée en utilisant le logiciel SCAPS, developpé par Prof. Burgelman *et al.* de l'université de Gent [59, 60].

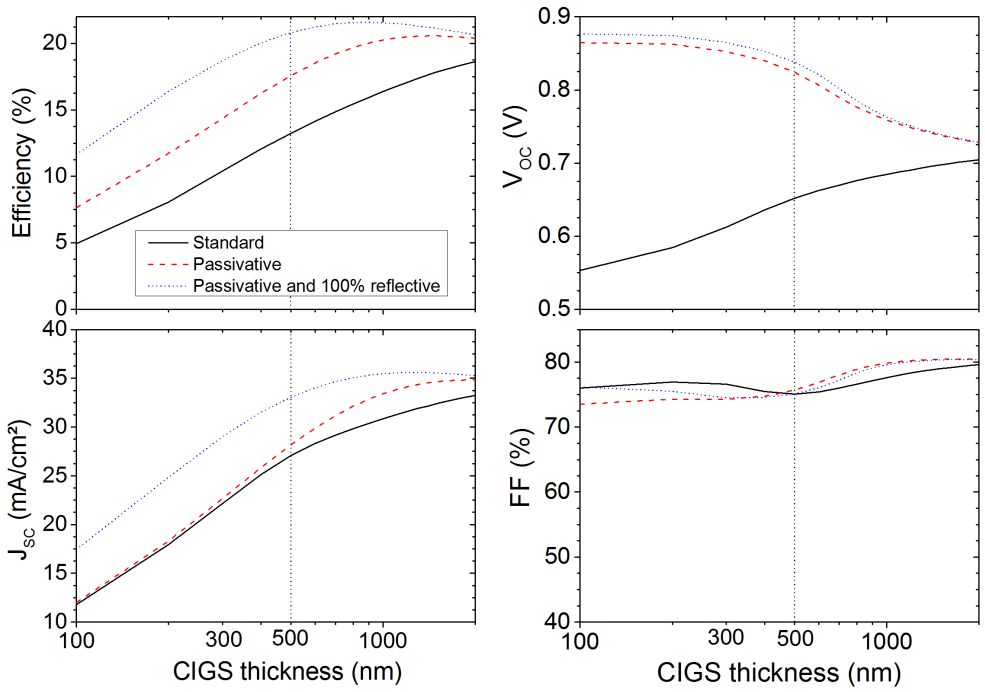

Figure F.3. : Simulation des paramètres I(V) d'une cellule CIGS standard sur le contact arrière en Mo en fonction de l'épaisseur de CIGS. Les paramètres du CIGS sont considérés comme indépendants de son épaisseur. Différentes propriétés du contact arrière ont été simulées.

Ce programme calcule en 1 dimension les caractéristiques électriques des cellules solaires à hétérojonction en couches minces. Le résultat de la simulation est présenté dans la Figure F.3 pour 3 cas : (1) le contact arrière est recombinant et faiblement réfléchissant, (2) le contact arrière est passivé et faiblement refléchissant, (3) le contact arrière est passivé et réfléchissant. Une forte diminution du rendement est observée dans le cas (1). En revanche le V_{OC} croit lorsque le contact arrière est passivé dans le cas (2). En effet, la réduction de matériaux se traduit par une diminution du taux de recombinaison total dans la cellules. De plus, le J_{SC} est augmenté lorsque le conctact arrière est réfléchissant. On observe une que le rendement est même supérieur pour 600 nm d'épaisseur que pour 2000 nm dans le cas (3). La passivation et la reflectivité du contact arrière sont donc des points cruciaux pour fabriquer des CIGS ultra-minces de hauts rendements.

Pour analyser l'effet de la diminution de l'épaisseur sur nos échantillons, nous avons fabriqué des échantillons avec des épaisseurs différentes de CIGS par coevaporation des éléments Cu, In, Ga et Se sur un substrat de verre/Mo à une température de 550°C. La coévaporation s'est effectuée en 1 étape, sans variation du taux d'évaporation. Cela permet d'éviter les gradient de composition pour une analyse plus aisée des caractéristiques électriques.

Nous avons montré que la couche de CIGS en elle-même est faiblement impactée par le changement d'épaisseur du CIGS jusqu'à 250 nm : le changement principal est la diminution de la taille des grains et donc une augmentation de la densité des joins de grains. Les autres paramètres des matériaux, tels que la cristallinité, sont restés inchangés. Une épaisseur de 80 nm a aussi été déposée, couvrant convenablement le substrats, et présentant aussi une couche de $MoSe_2$ à l'interface, mais présentant des cristallites très fines.

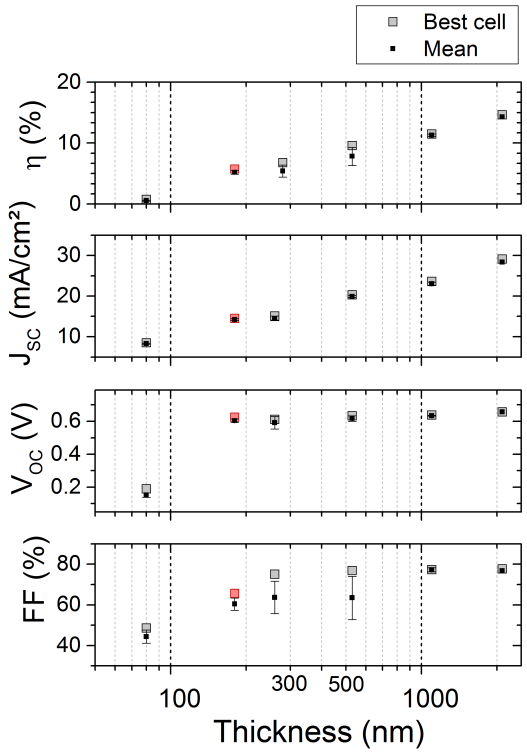

Figure F.4. : Paramètres des cellules solaires sous illumination en fonction de l'épaisseur de la couche de CIGS.

Des cellules solaires ont été réalisées après dépôt du contact avant CdS/ZnO/ZnO :Al. Les cellules solaires ont été caractérisées et le résultat des paramètres courant tension I(V) est présentée dans la Figure F.4. Nous observons que l'efficacité des cellules diminue considérablement lorsque l'épaisseur diminue, principalement à cause d'une diminution du J_{SC} et du V_{OC}.

Nous avons soigneusement analysé cette tendance décroissante du J_{SC} en utilisant en place un modèle de collection des porteurs de charge. La génération des porteurs de charge est simulée au sein de toute l'épaisseur du CIGS en utilisant l'outil de simulation optique par transfert matriciel. Puis la collecte est simulée en utilisant une fonction de collecte f_c. Cette fonction de collecte est la probabilité de collecté une charge générée en fonction de la position dans l'épaisseur z du CIGS. f_c dans la

zone de charge d'espace (SCR) et dans la zone quasi-neutre (QNR) est donnée par [34] :

$$\begin{cases} f_c^{SCR} = h \\ f_c^{QNR} = h.\dfrac{\left(\frac{1}{Ln}\right)\cosh\left(\frac{z-d}{Ln}\right)-\left(\frac{S_{n,BC}}{D_n}\right)\sinh\left(\frac{z-d}{Ln}\right)}{\left(\frac{S_{n,BC}}{D_n}\right)\cosh\left(\frac{d-w}{Ln}\right)-\left(\frac{1}{Ln}\right)\sinh\left(\frac{d-w}{Ln}\right)} \end{cases} \tag{F.1}$$

avec h, une constante associée aux pertes dans la SCR (défauts dans le CIGS ou à l'interface avant), L_n dans longueur de diffusion des électrons, D_n la constante de diffusion, d l'épaisseur du CIGS, w l'épaisseur de la SCR et $S_{n,BC}$ la vitesse de recombinaisons des électrons à l'interface Mo/CIGS.

Le résultat est donné dans la Figure F.5a. Le J_{SC} est affecté non-seulement par la non-absorption de photons dans la couche CIGS, mais aussi par les recombinaisons à l'interface arrière en Mo qui réduisent la collecte dans la Région Quasi-Neutre (QNR).

Nous avons également soigneusement analysé la tendance décroissante du V_{OC} en décomposant l'équation :

$$V_{OC} = \frac{nkT}{q}\ln\left(\frac{f_c(V_{OC}).J_{SC}}{J_0}\right) \tag{F.2}$$

avec n le facteur d'idéalité de la diode, k la constante de Boltzman, T la temperature, q la charge de l'électron, f_c la fonction de collecte en fonction du voltage, J_0 le courant de saturation de la diode.

Le résultat est donné dans la Figure F.5b. Le V_{OC} diminue légèrement avec l'épaisseur CIGS. Ce cas correspond au cas où le contact arrière est fortement recombinant d'après les simulations SCAPS (voir Figure F.3). Cela signifie que la diminution des recombinaison lié à la diminution de la couche de CIGS est compensée par une QNR fortement influencée par les recombinations en face arrière.

Nos efforts pour améliorer l'efficacité des cellules CIGS ultra-minces en utilisant un dépôt de coévaporation plus complexe de la couche CIGS (gradient de composition ou processus à plusieurs étapes) n'ont pas aboutit autant qu'attendu. En conséquence, nous tirons la conclusion suivante :

La réalisation de cellules solaires en CIGS ultra-mince à haut rendement pose principalement le problème de l'interface arrière : l'interface Mo/CIGS est trop faiblement réfléchissante et génère trop de recombinaison de porteurs de charges.

Afin de résoudre ces problèmes, nous envisageons dans ce travail de remplacer le contact arrière en Mo par un oxyde transparent conducteur (TCO) couplé avec un réflecteur. Ce système a l'avantage d'être simple à mettre en place.

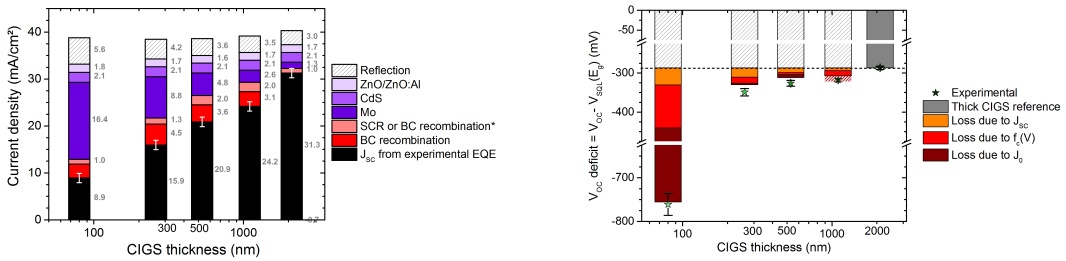

(a) Analyse de la diminution du J_{SC} en fonction de l'épaisseur du CIGS. Les différentes contributions optiques sont indiquées en nuance de violets et les différentes contribution électrique sont indiquées en nuance de rouge.

(b) Analyse de la diminution du déficit en V_{OC} en fonction de l'épaisseur du CIGS. La contribution du courant de saturation J_0, du J_{SC} et de la fonction de collecte dépendant du voltage f_c sont indiquées.

Figure F.5. : Analyse de la diminution du rendement des cellules CIGS en fonction de l'épaisseur du CIGS.

Nous avons simuler avec notre modèle de génération-collection l'augmentation du J_{SC} pour différentes architectures de cellules : avec une TCO et avec différents réflecteurs. Le résultat des simulations est présenté dans la Figure F.6.

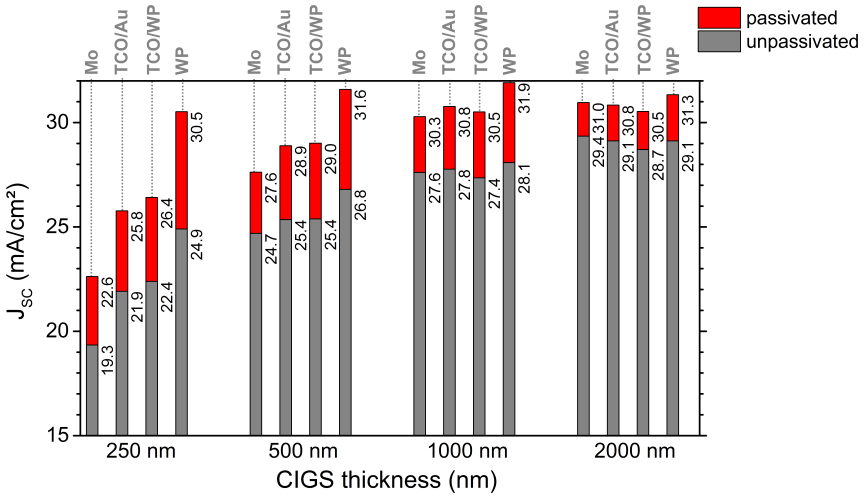

Figure F.6. : Simulation de J_{SC} pour des CIGS de différentes épaisseurs et pour 4 contacts arrières différents : Mo, 500 nm ZnO : Al / Au (TCO / Au), 500 nm ZnO : Al / peinture blanche (TCO / WP) et CIGS directement en contact avec la peinture blanche (WP).

Un contact arrière TCO/Au permet une forte augmentation du J_{SC} pour les faible épaisseur de CIGS (de 22.6 mA/cm² à 25.8 mA/cm² dans le cas de contact passivé). L'utilisation d'une peinture diffusante à la place de Au ne change pas le résultat car l'effet de diffusion est perdu par les variations d'indices optiques de l'empilement. Les calculs montrent également que le contrôle de la passivation est importante car les variations de J_{SC} associée sont grandes comparé au gain permis par le nouveau

contact arrière.

Conclusion. L'interface Mo/CIGS doit être remplacée par une interface plus réfléchissante et plus passivée. Pour obtenir ce changement, nous devons d'abord : 1/ analyser l'influence de différentes conditions de croissance sur les performances cellulaires, 2/ augmenter le photocourant par la substitution de la couche Mo par un oxyde conducteur transparent (TCO) couplé avec un réflecteur et 3/ minimiser les recombinaison au contact arrière en utilisant des couches d'oxyde de passivation.

Réalisation de contacts arrières passivés et réfléchissants

Influence des conditions de croissance du CIGS

Nous avons avant tout analysé l'influence de différentes conditions de croissance sur les performances des cellules solaires. Les conditions de croissance du CIGS peuvent changer en fonction du contact arrière : une faible température de substrat si le contact arrière alternatif est sensible à la température ou un apport en Na si il empêche la diffusion du Na du verre vers le CIGS.

En utilisant un plan complet d'expérience qui prend en compte la température du substrat, la diffusion de Na, un apport externe de K et la formation de $MoSe_2$, nous pouvons séparer avec précision leurs impacts sur les performances des cellules. L'influence de la température et des alkalins décorrelés de la formation de $MoSe_2$, est présentée dans la Figure F.7.

Nous avons conclu que traitement post-déposition KF (PDT) compense l'absence de Na et permet d'atteindre des rendements de cellules équivalent. De plus, la température du substrat ne doit pas être inférieure à 450°C pour éviter la formation de défauts qui réduisent le V_{OC}.

Remplacement du contact arrière en Mo par un TCO

Nous avons ensuite modifié le contact arrière en Mo et utilisé un TCO. En particulier, nous avons utilisé de l'oxyde de zinc dopé à l'aluminium (ZnO :Al) et l'oxyde d'étain dopé au fluor (SnO_2 :F). Avec un tel contact arrière semi-transparent, un reflecteur (Cu ou Au) peut-être placé sur la face arrière de la cellule, en contact avec le verre. Si l'on prend en compte la résistivité du TCO, une l'épaisseur du TCO doit être optimiser pour combiner transparence et conduction de la couche. Nous avons simulé qu'une augmentation de l'efficacité cellulaire de +0,5% abs . pour un CIGS de 450 nm d'épaisseur et +1,5% d'abs. pour un CIGS de 250 nm d'épaisseur peut-être atteinte.

Nous avons ensuite analysé et optimisé le dépôt CIGS sur les contact arrière en SnO_2 :F et ZnO :Al. Nous avons réalisé ces dépôts à 500°C avec un apport externe de Na par un post-traitement au NaF (NaF PDT). Il faut noter que la croissance du

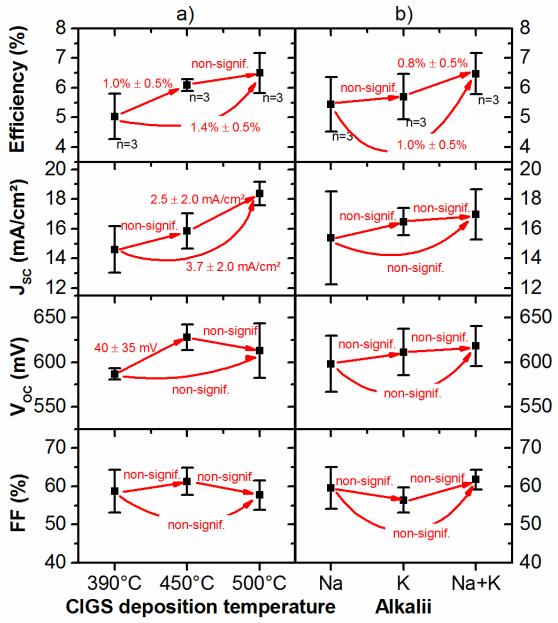

Figure F.7. : Comparaison des paramètres de cellules a) pour les échantillons avec diffusion de Na, K provenant d'un post-traitement au KF, ou avec à la fois Na et K, et b) pour des échantillons fabriqués à différentes températures de substrat. Les données, sous forme de moyenne ± écart-type (n échantillons), sont en noir. La variation moyenne ± intervalle de confiance est indiqué en rouge et a été calculée par ANOVA à 2 niveau avec un test de Fisher apparié pour la comparaison de la moyenne avec un risque de 10% d'erreur. «Non signif» signifie que la variation moyenne n'est pas significative (valeur p> 0,1).

CIGS, analysée en diffraction des rayonx X, ne se fait pas selon la même orientation cristalline sur les différents contacts arrières.

La caractérisation approfondie des éléments à l'interface arrière a été réalisé par spectroscopie de photoelectron induit par rayon-X (XPS) et par nano-spectroscopie Auger (nano-AES). Les resultats sont montrés dans la Figure F.8. Contrairement à la littérature sur l'interface ZnO/CIGS [164], aucune phase intermédiaire comme GaO_x n'est mise en évidence. Par contre, à l'interface SnO_2 :F/CIGS, nous avons remarqué un enrichissement en cuivre mais nous ne sommes pas capable d'identifier la phase correspondante. Les mesures utilisant un GD-OES (Glow-Discharge Optical Emission Spectroscopy) montrent également un enrichissement au Na des deux interfaces ZnO :Al/CIGS et SnO_2 :F/CIGS.

Le contact électrique a également été analysé. Pour cela, nous avons remplacé la fenêtre avant par une couche d'Au. Comme le contact CIGS/Au a une faible résistance, les caractéristiques I(V) de cette structure dépendent principalement de la résistance du contact arrière. Le résultat des mesures est indiqué dans la Figure F.9. Les deux contacts arrières en TCO présentent un comportement ohmique, ce qui est approprié pour la fabrication de cellules. Néanmoins, la résistivité est plus élevée que pour le contact Mo/CIGS, en particulier pour le contact CIGS/ZnO :Al.

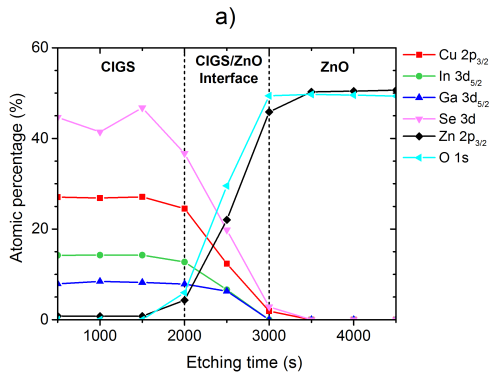

(a) Analyse XPS de l'interface ZnO :Al/CIGS. Aucune phase intermédiaire n'est remarquée.

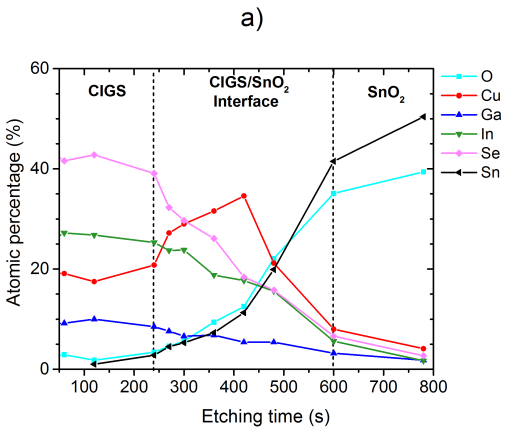

(b) Analyse nano-AES de l'interface SnO_2 :F/CIGS. Le pointage est repositionné entre chaque mesure. Le cuivre semble s'accumuler à l'interface.

Figure F.8. : Pourcentage atomique en fonction de l'abrasion sous flux d'argon.

Enfin, les cellules solaires ont été fabriquées et étudiées. Les courbes I(V) correspondantes sont présentées dans la Figure F.10. Le réflecteur métallique permet une large augmentation du J_{SC} comme attendu par les simulations. Néanmoins, le réflecteur diffusant ne permet pas d'atteindre une augmentations de J_{SC} supérieure à celle du réflecteur métallique. Nous avons pu obtenir des cellules solaires avec des performances supérieures aux cellules standards sur un contact en Mo. Au final, des efficacités de 9,2% sur un contact arrière en SnO_2 :F et de 8,7% sur un contact arrière en ZnO :Al avec un CIGS de 260 nm avec un réflecteur Au ont été obtenues (comparé à 7.0% sur Mo).

Cependant, l'analyse poussée des courbes de rendement quantique a permis de montrer que la vitesse de recombinaison du contact arrière est élevée : environ $10^5 - 10^6$ cm/s dans le cas du ZnO :Al et 10^7 cm/s dans le cas du SnO_2 :F. Cela réduit le profit du réflecteur. Un contrôle de la passivation est donc nécessaire comme proposé par B. Vermang *et al.* [88].

Contôle de la passivation du contact arrière

Ce travail a été réalisé et adapté pour nos échantillons. Nous avons déposé le CIGS par coévaporation en 1 étape, sans gradient de composition, à 500°C sur un substrat Mo/oxyde. Nous avons comparé les couches TiO_2 et Al_2O_3 comme couches de passivation pour l'interface Mo/CIGS.

Al_2O_3 Des études ont déjà démontré que l'ALD-Al_2O_3 conduit à une excellente passivation de l'interface Mo/CIGS [107][187]. Comme aucun transport de trous ne peut être réalisé à travers la couche Al_2O_3, des contacts

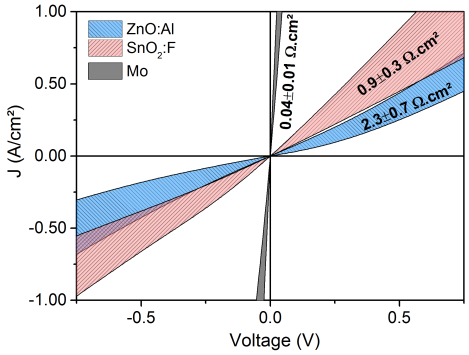

Figure F.9. : Caractéristiques de courant-tension I(V) de la structure de contact/CIGS/Au. La résistance de contact à 0V est indiquée par la moyenne ± écart-type.

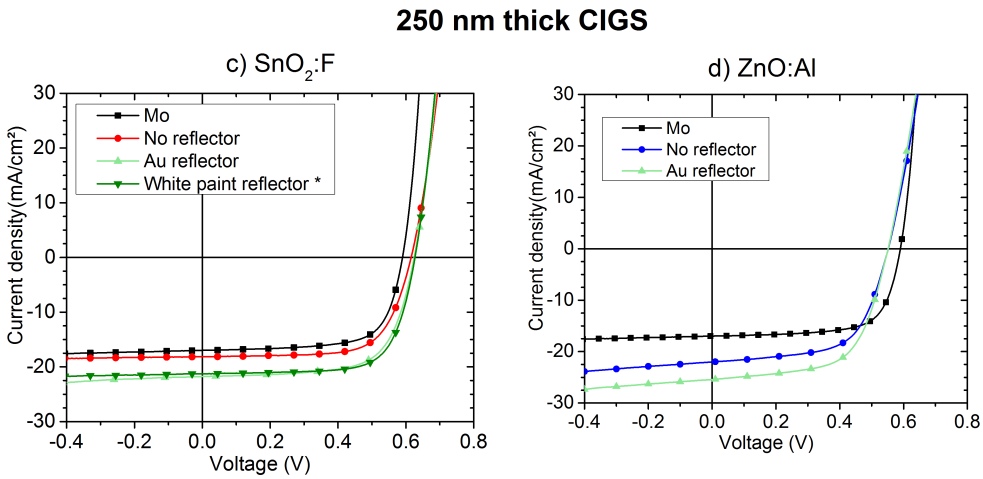

Figure F.10. : Courbes I(V) des meilleurs cellules sur différents contacts passivés.

ponctuels entre la couche CIGS et la couche Mo sont nécessaires. La lithographie par nano-impression a donc été utilisée pour créer les contacts ponctuels.

TiO_2 En raison des caractéristiques uniques et variées du TiO_2 [193], il est difficile de prédire le comportement du TiO_2 à l'interface entre CIGS et Mo. Il s'agit donc d'une étude exploratoire sur l'impact du TiO_2 sur la performance de la cellule et sa passivation à l'interface arrière. Nous avons choisi un sol-gel TiO_2 pour sa technique de dépôt simple par spin-coating. La couche peut également être nano-structurée par une lithographie par nano-impression.

Une analyse matériaux de la couche de CIGS par diffraction des rayon X et par GD-OES a montré que la croissance de CIGS sur les films TiO_2 ou Al_2O_3 est pratiquement similaire à la croissance des couches Mo. La principale différence est que l'Al_2O_3 agit comme couche bloquante pour la diffusion du Na.

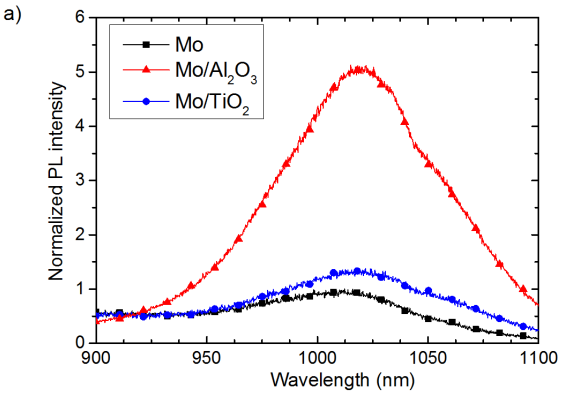

Figure F.11. : Analyse de la photoluminescence du CIGS excité avec un laser de 532 nm. L'intensité du signal dépend du taux de recombinaison non radiative et donc de la qualité du contact arrière.

Des mesures de photoluminescences (PL) ont été effectuées. Puisque le rendement de PL dépend de la quantité relative de recombination radiative et non-radiative, les mesures mettent en évidence la présence de défauts. Les mesures sont présentée dans la Figure F.11 et mettent en évidence une amélioration des propriétés de l'interface arrière lorsque l'Al_2O_3 est utilisée. En revanche, aucune amélioration n'est observé dans le cas de TiO_2.

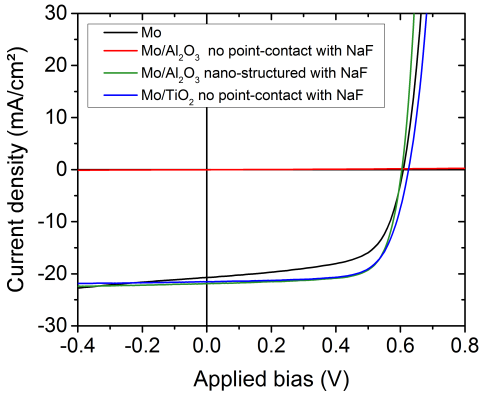

Figure F.12. : Courbes I(V) des meilleures cellules sur différents contacts passivés.

Les courbes I(V) des meilleures cellules sur contact arrière passivé Mo/TiO_2 et Mo/Al_2O_3 sont présentées sur Figure F.12.

Avec un contact arrière en Mo/TiO_2, développé pour la première fois pour les cellules CIGS, nous avons obtenu une efficacité de 9,5% pour un CIGS de 390 nm d'épaisseur. De façon surprenante, des ouvertures dans la couche TiO_2 ne sont pas nécessaires pour avoir un contact électrique. Des analyses de la couche de TiO_2 plus poussées sont nécessaires pour expliquer ce phénomène.

Dans le cas du contact arrière en Mo/Al_2O_3, la fabrication des cellules nécessite absolument la réalisation d'ouvertures dans la couche d'Al_2O_3 (carrés de 100 nm de large par pas de 8 μm : 99.98% du contact arrière couvert par l'Al_2O_3). Sans ouverture, la couche bloque la collecte. A partir de ces échantillons, nous avons montré que : d'une part, la passivation par le contact arrière Mo/Al_2O_3 n'est pas claire et semble dépendre de l'apport de Na pendant le dépôt CIGS ; et d'autre part, on a obtenu un rendement 9,5% pour un CIGS de 390 nm d'épaisseur avec un espacement étonnamment grand de 8 µm entre les contacts ponctuels. En particulier, une grande atténuation des résistances parasites a été observée : une résistance parallèle élevée (annulation des court-circuits) et une faible résistance série (qui pourrait être corrélée à une diffusion latérale de trous sur de longues distances). Un tel résultat ouvre la voie vers un meilleur contrôle des propriétés de l'interface arrière.

Pour résumer, nous avons mis en œuvre un contact arrière réfléchissant en utilisant un réflecteur métallique et une légère passivation du CIGS en utilisant une couche d'Al_2O_3.

Combinaison de l'effet de réflexion et de passivation

Afin d'obtenir des cellules solaires CIGS à haut rendement, ces effets ont été combinés. A cet effet, une structure avancée de cellule a été fabriquées : une cellule avec 470 nm de CIGS sur contact arrière en TCO avec une couche de passivation d'Al_2O_3 perforée.

Pour cet échantillon, le CIGS a été évaporé pendant 15 minutes par un procédé de co-évaporation à 1 étage à une température du substrat d'environ 500°C. La vitesse d'évaporation a été maintenue constante pour éviter un gradient de composition. Après le dépôt CIGS, on a effectué un traitement de NaF pendant 8 min à 300 ° C à une vitesse de 1-2 nm / min sous atmosphère de Se. La composition atteinte est de CGI = 0,91 et GGI = 0,36.

Le schéma et la structure de la cellule observée par microscopie électronique à balayage sont présentées dans la figure Figure F.13.

Nous avons analysé en détail la passivation à l'interface $TCO/Al_2O_3/CIGS$. Pour cela nous avons comparé plusieurs techniques de caractérisation : (1) l'analyse du rendement quantique externe (EQE) mesuré depuis la face arrière. Cet EQE peut être simulé par notre modèle de génération-collection, ce qui permet de remonter à une estimation de la valeur de la vitesse de recombinaison au contact arrière. (2) l'analyse de l'intensité de photoluminescence (PL) après excitation avec un laser de 532 nm. L'intensité du signal dépend du taux de recombinaisons non-radiatives dans la couche. (3) l'analyse résolue en temps de la décroissance du signal de photoluminescence. La concentration de défauts réduit le temps de vie des porteurs. Les mesures sont présentées dans Figure F.14.

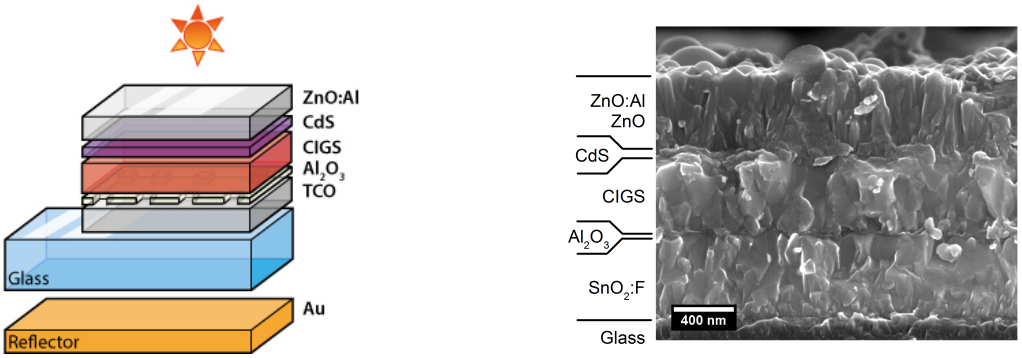

(a) Schema

(b) Image MEB en tranche

Figure F.13. : Structure de la cellule complète avec un CIGS sur un contact arrière de SnO_2 :F passivé.

L'EQE plus élevé de la cellule sur la couche TCO/Al_2O_3 (meilleure collecte), est corrélée à une amélioration du rendement de PL (moins de recombinaison non radiative) et à un allongement de la durée du signal de PL (temps de vie des porteurs plus long). On peut donc conclure à un léger effet de passivation de la couche Al_2O_3. Cela devrait être responsable d'une augmentation du V_{OC} d'environ 40 mV.

Les performances de la cellule solaire sur contact arrière en SnO_2 :F passivé (Al_2O_3 nano-structuré) ont été également mesurées. Une efficacité de 10,7% a été atteinte pour un CIGS de 470 nm d'épaisseur, ce qui est supérieur au rendement de l'échantillon sur Mo (9.7%). La nouvelle interface arrière permet une amélioration du J_{SC} et du V_{OC}. On observe une augmentation du V_{OC} de 53 mV et on a estimé qu'approximativement 25 mV étaient liés à l'interface, ce qui est proche de l'augmentation attendu d'après les mesures de PL.

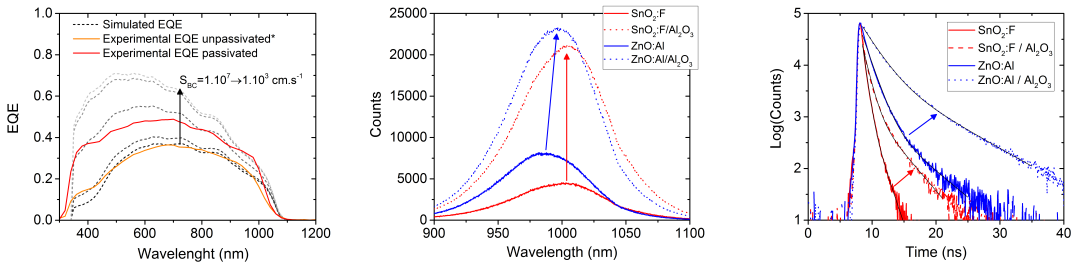

(a) Mesure de l'EQE en face arrière pour l'échantillon sur SnO_2 :F/Al_2O_3 structuré. La mesure est comparée avec l'EQE simulé selon le modèle optico-électrique mis en place pendant la thèse en fonction de la vitesse de recombinaisons en face arrière (S_n).

(b) Mesure de photoluminescence du CIGS sur les différents substrats. La couche de CIGS est excitée avec un laser de 532 nm. L'intensité dépend du taux de recombinaisons non-radiatives dans la couche.

(c) Mesure résolue en temps du signal de photoluminescence sur les différents substrats. La couche de CIGS est excitée avec un laser de 532 nm. Le temps de vie est limité par les recombinaisons dans le CIGS.

Figure F.14. : Analyse de la passivation en Al_2O_3 avec un contact arrière en TCO.

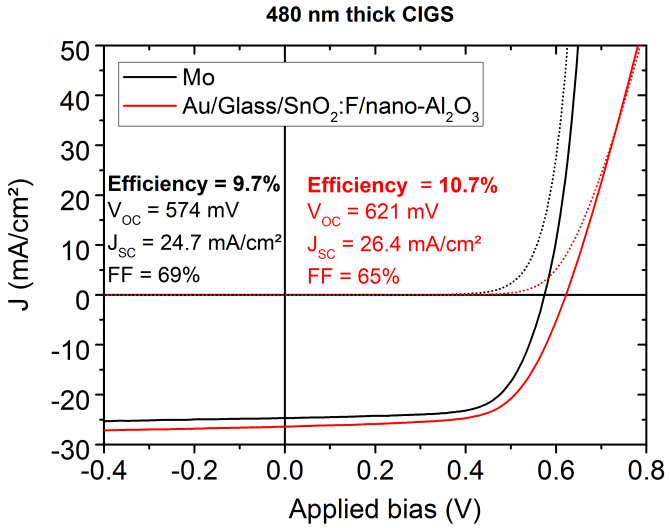

Figure F.15. : Mesures de la meilleur cellule solaire sur un contact arrière en SnO_2 :F passivé comparé à la mesure sur contact arrière en Mo.

Conclusion et perspectives

Dans ce travail de thèse, nous avons réalisé des cellules CIGS ultra-minces sur des contacts arrières alternatifs composés d'une couche TCO couplée à une couche de passivation perforée d'Al_2O_3 à l'interface TCO/CIGS et d'un réflecteur métallique placé derrière le contact semi-transparent.

Nous avons montré que l'efficacité de ces cellules est plus élevée que celle des cellules de référence sur le contact arrière Mo pour les mêmes épaisseurs de CIGS. Nous avons obtenu une cellule à 10,7% pour une épaisseur de CIGS de 470 nm.

Cependant, ces performances sont inférieures à celles des cellules obtenues avec une couche de CIGS épaisse (>2000 nm) : 14,0% pour un dépôt de coévaporation en 1 étape et 16,7% pour un dépôt en 3 étapes (obtenue par thèse de T. Klinkert [97]). Pour obtenir de telles performances, d'autres améliorations doivent être mises en œuvre, telles que :

- L'amélioration de la qualité CIGS par le développement d'un dépôt rapide du CIGS en 3 étapes avec incorporation de NaF ;
- Le contrôle de l'effet de passivation de la couche Al_2O_3 par un contrôle du dépôt et du recuit de l'Al_2O_3 ;
- L'optimisation de l'espacement entre les contacts ponctuels pour trouver un optimum entre l'effet de passivation de l'Al_2O_3 et l'augmentation de la résistance en série due à la distance requise pour la collecte de trous ;
- L'optimisation du dopage p dans le CIGS pour augmenter l'avantage donné par la passivation du contact arrière.

De plus, nous pouvons proposer d'autres améliorations, actuellement en cours de développement sur des cellules solaires standards de CIGS. Par exemple, nous pourrions utiliser un réflecteur Lambertian (tel que de la peinture blanche) directement en contact avec le CIGS. Cette configuration est complexe à mettre en place car il faut pouvoir récupérer le courant avec des contacts poncuels.

En conclusion, nous sommes confiants que les cellules solaires ultra-minces CIGS ont la capacité d'atteindre l'efficacité d'une cellule CIGS standard si un contact arrière autre que le Mo est utilisé. Théoriquement, une cellule optimisée avec une couche CIGS d'environ 600 nm d'épaisseur pourrait même dépasser l'efficacité d'une cellule solaire CIGS épaisse.

Bibliography

[1] "Paris Agreement, FCCC/CP/2015/L.9/Rev.1, United Nations," tech. rep., Framework Convention on Climate Change (FCCC), Dec. 2015.

[2] J. Palm, Schneider, K. Kushiya, L. Stolt, A. N. Tiwari, E. Niemi, K. M. Beck, c. Eberspacher, P. Wohlfart, A. Bayman, U. Schoop, K. Ramanathan, B. Wieting, B. Dimmler, C. Kuhn, S. Whitelegg, U. Rühle, D. Lincot, N. Naghavi, T. Walter, M. C. Lux-Steiner, R. Schatmann, A. Kuypers, B. Szyszka, S. Siebentritt, P. Lechner, M. Powalla, R. Noufi, and H.-W. Schock, "White paper for CIGS thin film solar cell technology, WWW.CIGS-PV.NET," 2016.

[3] P. Jackson, R. Wuerz, D. Hariskos, E. Lotter, W. Witte, and M. Powalla, "Effects of heavy alkali elements in Cu(In,Ga)Se_2 solar cells with efficiencies up to 22.6%," *physica status solidi (RRL) - Rapid Research Letters*, Aug. 2016.

[4] K. A. Horowitz and M. Woodhouse, "Cost and potential of monolithic CIGS photovoltaic modules," in *Photovoltaic Specialist Conference (PVSC), 2015 IEEE 42nd*, pp. 1–6, IEEE, 2015.

[5] "Report on critical row materials for the EU," tech. rep., European Commision, May 2014.

[6] Z. Jehl Li Kao, *Elaboration of Ultrathin Indium Gallium Diselenide Based Solar Cells*. PhD thesis, University Paris Sud-Orsay, 2012.

[7] "Renewables 2016 Global Status Report," tech. rep., REN21, 2016.

[8] "Key World Energy Trends 2016," tech. rep., International Energy Agency (IEA), 2016.

[9] "Climate Change 2014: Mitagation of Climate Change," tech. rep., Intergovernmental Panel on Climate Change, 2014.

[10] "Photovoltaics Report," tech. rep., Fraunhofer ISE, June 2016.

[11] "Current and Future Cost of Photovoltaics," tech. rep., Agora Energiewende, Fraunhofer ISE, Feb. 2015.

[12] "Dubai Shatters all Records for Cost of Solar with Earth's Largest Solar Power Plant," May 2016.

[13] K. P. Bhandari, J. M. Collier, R. J. Ellingson, and D. S. Apul, "Energy payback time (EPBT) and energy return on energy invested (EROI) of solar photovoltaic systems: A systematic review and meta-analysis," *Renewable and Sustainable Energy Reviews*, vol. 47, pp. 133–141, July 2015.

[14] "Levelized cost of electricity renewable energy technology," tech. rep., Fraunhofer ISE, Nov. 2013.

[15] F. Kessler, D. Herrmann, and M. Powalla, "Approaches to flexible CIGS thin-film solar cells," *Thin Solid Films*, vol. 480-481, pp. 491–498, June 2005.

[16] J. L. Shay, S. Wagner, and H. M. Kasper, "Efficient $CuInSe_2$/CdS solar cells," *Applied Physics Letters*, vol. 27, no. 2, p. 89, 1975.

[17] D. Rudmann, D. Brémaud, A. da Cunha, G. Bilger, A. Strohm, M. Kaelin, H. Zogg, and A. Tiwari, "Sodium incorporation strategies for CIGS growth at different temperatures," *Thin Solid Films*, vol. 480-481, pp. 55–60, June 2005.

[18] J. Hedström, H. Ohlsén, M. Bodegârd, A. Kylner, L. Stolt, D. Hariskos, M. Ruckh, and H.-W. Schock, "ZnO/CdS/Cu(In,Ga)Se_2 thin film solar cells with improved performance," in *Photovoltaic Specialists Conference, 1993., Conference Record of the Twenty Third IEEE*, pp. 364–371, IEEE, 1993.

[19] A. Chirilă, P. Reinhard, F. Pianezzi, P. Bloesch, A. R. Uhl, C. Fella, L. Kranz, D. Keller, C. Gretener, H. Hagendorfer, D. Jaeger, R. Erni, S. Nishiwaki, S. Buecheler, and A. N. Tiwari, "Potassium-induced surface modification of Cu(In,Ga)Se_2 thin films for high-efficiency solar cells," *Nature Materials*, vol. 12, pp. 1107–1111, Nov. 2013.

[20] F. Kessler and D. Rudmann, "Technological aspects of flexible CIGS solar cells and modules," *Solar Energy*, vol. 77, pp. 685–695, Dec. 2004.

[21] MiaSolé., "MiaSolé - Home. http://miasole.com/," 2016.

[22] A. Gerthoffer, F. Roux, F. Emieux, P. Faucherand, H. Fournier, L. Grenet, and S. Perraud, "CIGS solar cells on flexible ultra-thin glass substrates: Characterization and bending test," *Thin Solid Films*, vol. 592, pp. 99–104, Oct. 2015.

[23] N. Kohara, S. Nishiwaki, Y. Hashimoto, T. Negami, and T. Wada, "Electrical properties of the Cu(In,Ga)Se_2/$MoSe_2$/Mo structure," *Solar Energy Materials and Solar Cells*, vol. 67, no. 209-215, pp. 209–215, 2001.

[24] D. Abou-Ras, G. Kostorz, D. Bremaud, M. Kälin, F. Kurdesau, A. Tiwari, and M. Döbeli, "Formation and characterisation of MoSe₂ for Cu(In,Ga)Se₂ based solar cells," *Thin Solid Films*, vol. 480-481, pp. 433–438, June 2005.

[25] M. Tomassini, *Synthèse de couches minces de molybdène et application au sein des cellules solaires à base de Cu(In,Ga)Se_2 co-évaporé*. PhD thesis, Université de Nantes, 2013.

[26] J.-H. Yoon, J.-H. Kim, W. M. Kim, J.-K. Park, Y.-J. Baik, T.-Y. Seong, and J.-h. Jeong, "Electrical properties of CIGS/Mo junctions as a function of $MoSe_2$ orientation and Na doping: Electrical properties of CIGS/Mo junctions," *Progress in Photovoltaics: Research and Applications*, vol. 22, pp. 90–96, Jan. 2014.

[27] R. Caballero, M. Nichterwitz, A. Steigert, A. Eicke, I. Lauermann, H. Schock, and C. Kaufmann, "Impact of Na on $MoSe_2$ formation at the CIGSe/Mo interface in thin-film solar cells on polyimide foil at low process temperatures," *Acta Materialia*, vol. 63, pp. 54–62, Jan. 2014.

[28] K. Orgassa, H. Schock, and J. Werner, "Alternative back contact materials for thin film Cu(In,Ga)Se_2 solar cells," *Thin Solid Films*, vol. 431-432, pp. 387–391, May 2003.

[29] T. Klinkert, *Comprehension and optimisation of the co-evaporation deposition of Cu(In,Ga)Se_2 absorber layers for very high efficiency thin film solar cells.* PhD thesis, Université Pierre et Marie Curie-Paris VI, 2015.

[30] T. Klinkert, M. Jubault, F. Donsanti, D. Lincot, and J.-F. Guillemoles, "Differential in-depth characterization of co-evaporated Cu(In,Ga)Se_2 thin films for solar cell applications," *Thin Solid Films*, vol. 558, pp. 47–53, May 2014.

[31] P. D. Paulson, R. W. Birkmire, and W. N. Shafarman, "Optical characterization of $CuIn_{1-x}Ga_xSe_2$ alloy thin films by spectroscopic ellipsometry," *Journal of Applied Physics*, vol. 94, no. 2, p. 879, 2003.

[32] M. Alonso, M. Garriga, C. Durante Rincón, E. Hernández, and M. León, "Optical functions of chalcopyrite $CuGa_xIn_{1-x}Se_2$ alloys," *Applied Physics A: Materials Science & Processing*, vol. 74, pp. 659–664, May 2002.

[33] M. A. Contreras, L. M. Mansfield, B. Egaas, J. Li, M. Romero, R. Noufi, E. Rudiger-Voigt, and W. Mannstadt, "Wide bandgap Cu(In,Ga)Se_2 solar cells with improved energy conversion efficiency: Wide bandgap Cu(In,Ga)Se_2 solar cells," *Progress in Photovoltaics: Research and Applications*, vol. 20, pp. 843–850, Nov. 2012.

[34] R. Scheer and H.-W. Schock, *Chalcogenide Photovoltaics : Physics, Technologies, and Thin Film Devices.* Wiley-VCH, 2011.

[35] S. Siebentritt, M. Igalson, C. Persson, and S. Lany, "The electronic structure of chalcopyrites-bands, point defects and grain boundaries," *Progress in Photovoltaics: Research and Applications*, vol. 18, pp. 390–410, Sept. 2010.

[36] S. B. Zhang, S.-H. Wei, A. Zunger, and H. Katayama-Yoshida, "Defect physics of the $CuInSe_2$ chalcopyrite semiconductor," *Physical Review B*, vol. 57, no. 16, p. 9642, 1998.

[37] S. Siebentritt, L. Gütay, D. Regesch, Y. Aida, and V. Deprédurand, "Why do we make Cu(In,Ga)Se_2 solar cells non-stoichiometric?," *Solar Energy Materials and Solar Cells*, vol. 119, pp. 18–25, Dec. 2013.

[38] J. E. Granata, J. R. Sites, S. Asher, and R. J. Matson, "Quantitative incorporation of sodium in $CuInSe_2$ and Cu(In,Ga)Se_2 photovoltaic devices," in *Photovoltaic Specialists Conference, 1997., Conference Record of the Twenty-Sixth IEEE*, pp. 387–390, IEEE, 1997.

[39] A. Rockett, M. Bodegard, K. Granath, and L. Stolt, "Na incorporation and diffusion in $CuIn_{1-x}Ga_xSe_2$," in *Photovoltaic Specialists Conference, 1996., Conference Record of the Twenty Fifth IEEE*, pp. 985–987, IEEE, 1996.

[40] S.-H. Wei, S. B. Zhang, and A. Zunger, "Effects of Na on the electrical and structural properties of $CuInSe_2$," *Journal of Applied Physics*, vol. 85, no. 10, p. 7214, 1999.

[41] A. Chirilă, S. Buecheler, F. Pianezzi, P. Bloesch, C. Gretener, A. R. Uhl, C. Fella, L. Kranz, J. Perrenoud, S. Seyrling, R. Verma, S. Nishiwaki, Y. E. Romanyuk, G. Bilger, and A. N. Tiwari, "Highly efficient $Cu(In,Ga)Se_2$ solar cells grown on flexible polymer films," *Nature Materials*, vol. 10, pp. 857–861, Sept. 2011.

[42] U. Rau, K. Taretto, and S. Siebentritt, "Grain boundaries in $Cu(In,Ga)(Se,S)_2$ thin-film solar cells," *Applied Physics A*, vol. 96, pp. 221–234, July 2009.

[43] C. Persson and A. Zunger, "Anomalous Grain Boundary Physics in Polycrystalline $CuInSe_2$: The Existence of a Hole Barrier," *Physical Review Letters*, vol. 91, Dec. 2003.

[44] D. Abou-Ras, C. Koch, V. Küstner, P. van Aken, U. Jahn, M. Contreras, R. Caballero, C. Kaufmann, R. Scheer, T. Unold, and H.-W. Schock, "Grain-boundary types in chalcopyrite-type thin films and their correlations with film texture and electrical properties," *Thin Solid Films*, vol. 517, pp. 2545–2549, Feb. 2009.

[45] D. Abou-Ras, N. Schäfer, T. Rissom, M. N. Kelly, J. Haarstrich, C. Ronning, G. S. Rohrer, and A. D. Rollett, "Grain-boundary character distribution and correlations with electrical and optoelectronic properties of $CuInSe_2$ thin films," *Acta Materialia*, vol. 118, pp. 244–252, Oct. 2016.

[46] W. Metzger, I. Repins, M. Romero, P. Dippo, M. Contreras, R. Noufi, and D. Levi, "Recombination kinetics and stability in polycrystalline $Cu(In,Ga)Se_2$ solar cells," *Thin Solid Films*, vol. 517, pp. 2360–2364, Feb. 2009.

[47] H. Mönig, Y. Smith, R. Caballero, C. A. Kaufmann, I. Lauermann, M. C. Lux-Steiner, and S. Sadewasser, "Direct Evidence for a Reduced Density of Deep Level Defects at Grain Boundaries of $Cu(In,Ga)Se_2$ Thin Films," *Physical Review Letters*, vol. 105, Sept. 2010.

[48] W.-J. Yin, Y. Wu, R. Noufi, M. Al-Jassim, and Y. Yan, "Defect segregation at grain boundary and its impact on photovoltaic performance of CuInSe2," *Applied Physics Letters*, vol. 102, no. 19, p. 193905, 2013.

[49] R. Baier, C. Leendertz, D. Abou-Ras, M. C. Lux-Steiner, and S. Sadewasser, "Properties of electronic potential barriers at grain boundaries in $Cu(In,Ga)Se_2$ thin films," *Solar Energy Materials and Solar Cells*, vol. 130, pp. 124–131, Nov. 2014.

[50] R. Kamada, T. Yagoika, S. Adachi, A. Handa, K. Fai Tai, T. Kato, and H. Sugimoto, "New World Record Cu(In,Ga)(Se,S)$_2$ Thin Film Solar Cell Efficiency Beyond 22%," *Proceedings of the 43th IEEE Photovoltaic Specialist Conference*, pp. 1287–1291, 2016.

[51] C. Broussillou, C. Viscogliosi, A. Rogee, S. Angle, P. P. Grand, S. Bodnar, C. Debauche, J. L. Allary, B. Bertrand, C. Guillou, and others, "Statistical Process Control for Cu(In,Ga)(S,Se)$_2$ electrodeposition-based manufacturing process of 60x120cm2 modules up to 14, 0% efficiency," in *Photovoltaic Specialist Conference (PVSC), 2015 IEEE 42nd*, pp. 1–5, IEEE, 2015.

[52] D. Schmid, M. Ruckh, F. Grunwald, and H. W. Schock, "Chalcopyrite/defect chalcopyrite heterojunctions on the basis of CuInSe$_2$," *Journal of Applied Physics*, vol. 73, no. 6, p. 2902, 1993.

[53] N. Naghavi, D. Abou-Ras, N. Allsop, N. Barreau, S. Bücheler, A. Ennaoui, C.-H. Fischer, C. Guillen, D. Hariskos, J. Herrero, R. Klenk, K. Kushiya, D. Lincot, R. Menner, T. Nakada, C. Platzer-Björkman, S. Spiering, A. Tiwari, and T. Törndahl, "Buffer layers and transparent conducting oxides for chalcopyrite Cu(In,Ga)(S,Se)$_2$ based thin film photovoltaics: present status and current developments," *Progress in Photovoltaics: Research and Applications*, vol. 18, pp. 411–433, Sept. 2010.

[54] R. Scheer, L. Messmann-Vera, R. Klenk, and H.-W. Schock, "On the role of non-doped ZnO in CIGSe solar cells: Non-doped ZnO in CIGSe solar cells," *Progress in Photovoltaics: Research and Applications*, vol. 20, pp. 619–624, Sept. 2012.

[55] T. Nakada, Y. Hirabayashi, T. Tokado, D. Ohmori, and T. Mise, "Novel device structure for Cu(In,Ga)Se$_2$ thin film solar cells using transparent conducting oxide back and front contacts," *Solar Energy*, vol. 77, no. 6, pp. 739–747, 2004.

[56] T. Dalibor, P. Eraerds, M. Grave, M. Algasinger, S. Visbeck, T. Niesen, and J. Palm, "Advanced PVD Buffers on the Road to GW-scale CIGSSe Production," *Photovoltaic Specialist Conference (PVSC), 2016 IEEE 43nd*, pp. 1433–1437, 2016.

[57] T. Feurer, P. Reinhard, E. Avancini, B. Bissig, J. Löckinger, P. Fuchs, R. Carron, T. P. Weiss, J. Perrenoud, S. Stutterheim, S. Buecheler, and A. N. Tiwari, "Progress in thin film CIGS photovoltaics - Research and development, manufacturing, and applications: Progress in thin film CIGS photovoltaics," *Progress in Photovoltaics: Research and Applications*, 2016.

[58] M. A. Green, K. Emery, Y. Hishikawa, W. Warta, and E. D. Dunlop, "Solar cell efficiency tables (version 48): Solar cell efficiency tables (version 48)," *Progress in Photovoltaics: Research and Applications*, vol. 24, pp. 905–913, July 2016.

[59] M. Burgelman, P. Nollet, and S. Degrave, "Modelling polycrystalline semiconductor solar cells," *Thin Solid Films*, vol. 361–362, pp. 527–532, 2000.

[60] M. Burgelman, J. Verschraegen, S. Degrave, and P. Nollet, "Modeling thin-film PV devices," *Progress in Photovoltaics: Research and Applications*, vol. 12, no. 2-3, pp. 143–153, 2004.

[61] L. Lombez, D. Ory, M. Paire, A. Delamarre, G. El Hajje, and J. Guillemoles, "Micrometric investigation of external quantum efficiency in microcrystalline CuInGa(S,Se)$_2$ solar cells," *Thin Solid Films*, vol. 565, pp. 32–36, Aug. 2014.

[62] M. Richter, M. Hammer, T. Sonnet, and J. Parisi, "Bandgap extraction from quantum efficiency spectra of Cu(In,Ga)Se$_2$ solar cells with varied grading profile and diffusion length," *Thin Solid Films*, Aug. 2016.

[63] M. Nichterwitz, R. Caballero, C. A. Kaufmann, H.-W. Schock, and T. Unold, "Generation-dependent charge carrier transport in Cu(In,Ga) Se$_2$/CdS/ZnO thin-film solar-cells," *Journal of Applied Physics*, vol. 113, no. 4, p. 044515, 2013.

[64] M. A. Green, "Do built-in fields improve solar cell performance?," *Progress in Photovoltaics: Research and Applications*, vol. 17, pp. 57–66, Jan. 2009.

[65] W. W. Gärtner, "Depletion-Layer Photoeffects in Semiconductors," *Physical Review*, vol. 116, pp. 84–87, Oct. 1959.

[66] Z. Jehl, M. Bouttemy, D. Lincot, J. F. Guillemoles, I. Gerard, A. Etcheberry, G. Voorwinden, M. Powalla, and N. Naghavi, "Insights on the influence of surface roughness on photovoltaic properties of state of the art copper indium gallium diselenide thin films solar cells," *Journal of Applied Physics*, vol. 111, no. 11, p. 114509, 2012.

[67] T. Dullweber, O. Lundberg, J. Malmström, M. Bodeg\a ard, L. Stolt, U. Rau, H.-W. Schock, and J. H. Werner, "Back surface band gap gradings in Cu(In,Ga)Se$_2$ solar cells," *Thin Solid Films*, vol. 387, no. 1, pp. 11–13, 2001.

[68] A. Nicmegeers, M. Burgelman, R. Herberholz, U. Rau, D. Hariskos, and H. W. Schock, "Model for Electronic Transport in Cu(In,Ga)Se$_2$ Solar Cells," *Progress in Photovoltaics: Research and Applications*, vol. 6, pp. 407–421, 1998.

[69] W. Shockley and H. J. Queisser, "Detailed Balance Limit of Efficiency of p-n Junction Solar Cells," *Journal of Applied Physics*, vol. 32, no. 3, p. 510, 1961.

[70] "Mineral comodity summaries 2016," tech. rep., U.S. Geological Survey, 2016.

[71] "Annex V to the Report on critical row materials for the EU," tech. rep., European Commision.

[72] M. Edoff, S. Schleussner, E. Wallin, and O. Lundberg, "Technological and economical aspects on the influence of reduced Cu(In,Ga)Se$_2$ thickness and Ga grading for co-evaporated Cu(In,Ga)Se$_2$ modules," *Thin Solid Films*, vol. 519, pp. 7530–7533, Aug. 2011.

[73] B. Vermang, V. Fjällström, J. Pettersson, P. Salomé, and M. Edoff, "Development of rear surface passivated Cu(In,Ga)Se_2 thin film solar cells with nano-sized local rear point contacts," *Solar Energy Materials and Solar Cells*, vol. 117, pp. 505–511, Oct. 2013.

[74] Shafarman, Birkmire, Marsillac, Marudachalam, Orbey, and Russel, "Effect of reduced deposition temperature, time and thickness on Cu(In,Ga)Se_2 films and devices," 1997.

[75] T. Negami, S. Nishiwaki, Y. Hashimoto, and N. Kohara, "Effect of absorber thickness on perfomance of Cu(In,Ga)Se_2 solar cells," *2nd world conference and exhibition on photovoltaic solar energy conversion, Vienna (Austria)*, pp. 1181–1184, 1998.

[76] Z. Jehl, F. Erfurth, N. Naghavi, L. Lombez, I. Gerard, M. Bouttemy, P. Tran-Van, A. Etcheberry, G. Voorwinden, B. Dimmler, W. Wischmann, M. Powalla, J. Guillemoles, and D. Lincot, "Thinning of CIGS solar cells: Part II: Cell characterizations," *Thin Solid Films*, vol. 519, pp. 7212–7215, Aug. 2011.

[77] E. Jarzembowski, M. Maiberg, F. Obereigner, K. Kaufmann, S. Krause, and R. Scheer, "Optical and electrical characterization of Cu(In,Ga)Se_2 thin film solar cells with varied absorber layer thickness," *Thin Solid Films*, vol. 576, pp. 75–80, Feb. 2015.

[78] N. Dahan, Z. Jehl, T. Hildebrandt, J.-J. Greffet, J.-F. Guillemoles, D. Lincot, and N. Naghavi, "Optical approaches to improve the photocurrent generation in Cu(In,Ga)Se_2 solar cells with absorber thicknesses down to 0.5 μm," *Journal of Applied Physics*, vol. 112, no. 9, p. 094902, 2012.

[79] Z. J. Li-Kao, N. Naghavi, F. Erfurth, J. F. Guillemoles, I. Gérard, A. Etcheberry, J. L. Pelouard, S. Collin, G. Voorwinden, and D. Lincot, "Towards ultrathin copper indium gallium diselenide solar cells: proof of concept study by chemical etching and gold back contact engineering," *Progress in Photovoltaics: Research and Applications*, vol. 20, pp. 582–587, Aug. 2012.

[80] O. Lundberg, M. Bodeg\aard, J. Malmström, and L. Stolt, "Influence of the Cu(In,Ga)Se_2 thickness and Ga grading on solar cell performance," *Progress in Photovoltaics: Research and Applications*, vol. 11, no. 2, pp. 77–88, 2003.

[81] J. Pettersson, T. Torndahl, C. Platzer-Bjorkman, A. Hultqvist, and M. Edoff, "The Influence of Absorber Thickness on Cu(In,Ga)Se_2 Solar Cells With Different Buffer Layers," *IEEE Journal of Photovoltaics*, vol. 3, pp. 1376–1382, Oct. 2013.

[82] M. Gloeckler and J. R. Sites, "Potential of submicrometer thickness Cu(In,Ga)Se_2 solar cells," *Journal of Applied Physics*, vol. 98, no. 10, p. 103703, 2005.

[83] G. Yin, V. Brackmann, V. Hoffmann, and M. Schmid, "Enhanced performance of ultra-thin Cu(In,Ga)Se_2 solar cells deposited at low process temperature," *Solar Energy Materials and Solar Cells*, vol. 132, pp. 142–147, Jan. 2015.

[84] E. Leonard, *Cellule Solaires à Base de Couche Mince de CIGSe submicrométrique : Opimisation des Performances par Ingénierie Optique et Electronique*. PhD thesis, Université de Nantes, 2013.

[85] J. Pettersson, T. Torndahl, C. Platzer-Bjorkman, A. Hultqvist, and M. Edoff, "The Influence of Absorber Thickness on Cu(In,Ga)Se_2 Solar Cells With Different Buffer Layers," *IEEE Journal of Photovoltaics*, vol. 3, pp. 1376–1382, Oct. 2013.

[86] K. Ramanathan, R. Noufi, B. To, D. L. Young, R. Bhattacharya, M. A. Contreras, R. G. Dhere, and G. Teeter, "Processing and properties of sub-micron CIGS solar cells," in *Photovoltaic Energy Conversion, Conference Record of the 2006 IEEE 4th World Conference on*, vol. 1, pp. 380–383, IEEE, 2006.

[87] B. Vermang, J. T. Wätjen, V. Fjällström, F. Rostvall, M. Edoff, R. Kotipalli, F. Henry, and D. Flandre, "Employing Si solar cell technology to increase efficiency of ultra-thin Cu(In,Ga)Se $_2$ solar cells: Employing Si solar cell technology," *Progress in Photovoltaics: Research and Applications*, vol. 22, pp. 1023–1029, Oct. 2014.

[88] B. Vermang, J. T. Watjen, C. Frisk, V. Fjallstrom, F. Rostvall, M. Edoff, P. Salome, J. Borme, N. Nicoara, and S. Sadewasser, "Introduction of Si PERC Rear Contacting Design to Boost Efficiency of Cu(In,Ga)Se_2 Solar Cells," *IEEE Journal of Photovoltaics*, vol. 4, pp. 1644–1649, Nov. 2014.

[89] J. K. Larsen, H. Simchi, P. Xin, K. Kim, and W. N. Shafarman, "Backwall superstrate configuration for ultrathin Cu(In,Ga)Se_2 solar cells," *Applied Physics Letters*, vol. 104, p. 033901, Jan. 2014.

[90] H. Simchi, B. E. McCandless, T. Meng, and W. N. Shafarman, "Structure and interface chemistry of MoO_3 back contacts in Cu(In,Ga)Se_2 thin film solar cells," *Journal of Applied Physics*, vol. 115, p. 033514, Jan. 2014.

[91] E. Jarzembowski, B. Fuhrmann, H. Leipner, W. Fränzel, and R. Scheer, "Ultrathin Cu(In,Ga)Se_2 solar cells with point-like back contact in experiment and simulation," *Thin Solid Films*, Nov. 2016.

[92] C. van Lare, G. Yin, A. Polman, and M. Schmid, "Light Coupling and Trapping in Ultrathin Cu(In,Ga)Se_2 Solar Cells Using Dielectric Scattering Patterns," *ACS Nano*, vol. 9, pp. 9603–9613, Oct. 2015.

[93] W. Ohm, W. Riedel, U. Aksunger, D. Greiner, C. A. Kaufmann, M. C. Lux-Steiner, and S. Gledhill, "Bifacial Cu(In,Ga)Se_2 solar cells with submicron absorber thickness: back-contact passivation and light management," in *Photovoltaic Specialist Conference (PVSC), 2015 IEEE 42nd*, pp. 1–5, IEEE, 2015.

[94] J. Posada, M. Jubault, and N. Naghavi, "Ultra-thin Cu(In,Ga)Se_2 solar cells prepared by an alternative hybrid co-sputtering/evaporation process," *Thin Solid Films*, Aug. 2016.

[95] "ZSW Sets New World Record for Thin-film Solar Cells," May 2016.

[96] "Dr. Eberl MBE-Komponenten GmbH, www.mbe-komponenten.de." www.mbe-komponenten.de.

[97] T. Klinkert, *Comprehension and optimisation of the co-evaporation deposition of Cu(In,Ga)Se_2 absorber layers for very high efficiency thin film solar cells.* phdthesis, Université Pierre et Marie Curie - Paris VI, 2015.

[98] M. Burgelman, K. Decock, S. Khelifi, and A. Abass, "Advanced electrical simulation of thin film solar cells," *Thin Solid Films*, vol. 535, pp. 296–301, May 2013.

[99] J. Pettersson, M. Edoff, and C. Platzer-Björkman, "Electrical modeling of Cu(In,Ga)Se_2 cells with ALD-Zn1-xMgxO buffer layers," *Journal of Applied Physics*, vol. 111, no. 1, p. 014509, 2012.

[100] M. Gloeckler, A. L. Fahrenbruch, and J. R. Sites, "Numerical modeling of CIGS and CdTe solar cells: setting the baseline," in *Photovoltaic Energy Conversion, 2003. Proceedings of 3rd World Conference on*, vol. 1, pp. 491–494, IEEE, 2003.

[101] F. Abelès, "La théorie générale des couches minces," *J. Phys. Radium*, vol. 11, no. 7, pp. 307–309, 1950.

[102] P. Yeh, *Optical waves in layered media.* Wiley-Interscience, 2005.

[103] N. Ehrmann and R. Reineke-Koch, "Ellipsometric studies on ZnO:Al thin films: Refinement of dispersion theories," *Thin Solid Films*, vol. 519, pp. 1475–1485, Dec. 2010.

[104] S. Ninomiya and S. Adachi, "Optical properties of wurtzite CdS," *Journal of Applied Physics*, vol. 78, no. 2, p. 1183, 1995.

[105] K. M. McPeak, S. V. Jayanti, S. J. P. Kress, S. Meyer, S. Iotti, A. Rossinelli, and D. J. Norris, "Plasmonic Films Can Easily Be Better: Rules and Recipes," *ACS Photonics*, vol. 2, pp. 326–333, Mar. 2015.

[106] N. Dahan, Z. Jehl, J. F. Guillemoles, D. Lincot, N. Naghavi, and J.-J. Greffet, "Using radiative transfer equation to model absorption by thin Cu(In,Ga)Se_2 solar cells with Lambertian back reflector," *Optics express*, vol. 21, no. 3, pp. 2563–2580, 2013.

[107] W.-W. Hsu, J. Y. Chen, T.-H. Cheng, S. C. Lu, W.-S. Ho, Y.-Y. Chen, Y.-J. Chien, and C. W. Liu, "Surface passivation of Cu(In,Ga)Se_2 using atomic layer deposited Al_2O_3," *Applied Physics Letters*, vol. 100, no. 2, p. 023508, 2012.

[108] T. Schlenker, H.-W. Schock, and J. Werner, "Initial growth behavior of CIGSe on Mo substrates," *Journal of Crystal Growth*, vol. 258, p. 47, 2008.

[109] T. Schlenker, M. Luis Valero, H. W. Schock, and J. Werner, "Grain growth studies of thin CIGSe films," *Journal of Crystal Growth*, vol. 264, p. 178, 2004.

[110] P. Salomé, Viktor Fjällström, P. Szaniawski, J. Leitao, U. Zimmermann, A. da Cunha, and M. Edoff, "A comparision between thin film solar cells made from co-evaporated CIGSe using one-stage versus a three-stage process," 2014.

[111] J. Kessler, C. Chityuttakan, J. Lu, J. Schöldström, and L. Stolt, "Cu(In,Ga)Se_2 thin films grown with a Cu-poor/rich/poor sequence: growth model and structural considerations," *Progress in Photovoltaics: Research and Applications*, vol. 11, no. 5, pp. 319–331, 2003.

[112] R. Caballero, C. A. Kaufmann, V. Efimova, T. Rissom, V. Hoffmann, and H. W. Schock, "Investigation of Cu(In,Ga)Se_2 thin-film formation during the multi-stage co-evaporation process: CIGSe thin-film formation multi-stage co-evaporation process," *Progress in Photovoltaics: Research and Applications*, vol. 21, pp. 30–46, Jan. 2013.

[113] T. Wada, N. Kohara, T. Negami, and M. Nishitani, "Growth of $CuInSe_2$ crystals in Cu-rich Cu–In–Se thin films," *Journal of Materials Research*, vol. 12, no. 06, pp. 1456–1462, 1997.

[114] N. Barreau, T. Painchaud, F. Couzinié-Devy, L. Arzel, and J. Kessler, "Recrystallization of CIGSe layers grown by three-step processes: A model based on grain boundary migration," *Acta Materialia*, vol. 58, pp. 5572–5577, Oct. 2010.

[115] F. Couzinie-Devy, E. Cadel, N. Barreau, L. Arzel, and P. Pareige, "Na distribution in Cu(In,Ga)Se_2 thin films: Investigation by atom probe tomography," *Scripta Materialia*, vol. 104, pp. 83–86, 2015.

[116] C.-S. Jiang, R. Noufi, K. Ramanathan, J. A. AbuShama, H. R. Moutinho, and M. M. Al-Jassim, "Does the local built-in potential on grain boundaries of Cu(In,Ga)Se_2 thin films benefit photovoltaic performance of the device?," *Applied Physics Letters*, vol. 85, no. 13, p. 2625, 2004.

[117] D. Azulay, O. Millo, I. Balberg, H.-W. Schock, I. Visoly-Fisher, and D. Cahen, "Current routes in polycrystalline $CuInSe_2$ and Cu(In,Ga)Se_2 films," *Solar Energy Materials and Solar Cells*, vol. 91, pp. 85–90, Jan. 2007.

[118] D. Abou-Ras, S. S. Schmidt, R. Caballero, T. Unold, H.-W. Schock, C. T. Koch, B. Schaffer, M. Schaffer, P.-P. Choi, and O. Cojocaru-Mirédin, "Confined and Chemically Flexible Grain Boundaries in Polycrystalline Compound Semiconductors," *Advanced Energy Materials*, vol. 2, pp. 992–998, Aug. 2012.

[119] E. J. Friedrich, R. Fernández-Ruiz, J. M. Merino, and M. León, "X-ray diffraction data and Rietveld refinement of $CuGa_xIn_{1-x}Se_2$ (x=0.15 and 0.50)," *Powder Diffraction*, vol. 25, pp. 253–257, Sept. 2010.

[120] S. Chaisitsak, A. Yamada, and M. Konagai, "Preferred orientation control of Cu (In1-xGax) Se2 (x? 0.28) thin films and its influence on solar cell characteristics," *Japanese Journal of Applied Physics*, vol. 41, no. 2R, p. 507, 2002.

[121] C. Rincón and F. J. Ramírez, "Lattice vibrations of $CuInSe_2$ and $CuGaSe_2$ by Raman microspectrometry," *Journal of Applied Physics*, vol. 72, no. 9, p. 4321, 1992.

[122] W. Witte, R. Kniese, and M. Powalla, "Raman investigations of $Cu(In,Ga)Se_2$ thin films with various copper contents," *Thin Solid Films*, vol. 517, pp. 867–869, Nov. 2008.

[123] G. Sakr, I. Yahia, M. Fadel, S. Fouad, and N. Romčević, "Optical spectroscopy, optical conductivity, dielectric properties and new methods for determining the gap states of CuSe thin films," *Journal of Alloys and Compounds*, vol. 507, pp. 557–562, Oct. 2010.

[124] B. Minceva-Sukarova, M. Najdoski, I. Grozdanov, and C. J. Chunnilall, "Raman spectra of thin solid films of some metal sulfides," *Journal of Molecular Structure*, vol. 410, pp. 267–270, June 1997.

[125] J. Weszka, P. Daniel, A. M. Burian, A. Burian, M. Elechower, and A. T. Nguyen, "Raman scattering in amorphous films of $In_{1-x}Se_x$ alloys," *Journal of non-crystalline solids*, vol. 315, no. 3, pp. 219–222, 2003.

[126] S. Jandl and C. Carlone, "Raman spectrum of crystalline InSe," *Solid State Communications*, vol. 25, no. 1, pp. 5–8, 1978.

[127] C. Rincón, S. M. Wasim, G. Marı?n, J. M. Delgado, J. R. Huntzinger, A. Zwick, and J. Galibert, "Raman spectra of the ordered vacancy compounds $CuIn_3Se_5$and $CuGa_3Se₅$," *Applied Physics Letters*, vol. 73, no. 4, p. 441, 1998.

[128] S. Nomura, S. Ouchi, and S. Endo, "Raman Spectra of Ordered Vacancy Compounds in the Cu-In-Se System," *Japanese Journal of Applied Physics*, vol. 36, no. 8B, pp. 1075–1077, 1997.

[129] P. Tonndorf, R. Schmidt, P. Böttger, X. Zhang, J. Börner, A. Liebig, M. Albrecht, C. Kloc, O. Gordan, D. R. Zahn, and others, "Photoluminescence emission and Raman response of monolayer MoS_2, $MoSe_2$, and WSe_2," *Optics express*, vol. 21, no. 4, pp. 4908–4916, 2013.

[130] C. Paorici, L. Zanotti, N. Romeo, G. Sberveglieri, and L. Tarricone, "Crystal growth and properties of $CuGa_xIn_{1-x}Se_2$ chalcopyrite compound," *Solar Energy Materials*, vol. 1, no. 1-2, pp. 3–9, 1979.

[131] S. Jung, S. Ahn, J. H. Yun, J. Gwak, D. Kim, and K. Yoon, "Effects of Ga contents on properties of CIGS thin films and solar cells fabricated by co-evaporation technique," *Current Applied Physics*, vol. 10, no. 4, pp. 990–996, 2010.

[132] T. Klinkert, T. Hildebrandt, M. Jubault, F. Donsanti, J.-F. Guillemoles, and N. Naghavi, "Adaptation of the surface-near Ga content in co-evaporated $Cu(In,Ga)Se_2$ for CdS versus Zn(S,O)-based buffer layers," *Thin Solid Films*, vol. 582, pp. 295–299, 2015.

[133] L. Weinhardt, O. Fuchs, D. Groß, G. Storch, E. Umbach, N. G. Dhere, A. A. Kadam, S. S. Kulkarni, and C. Heske, "Band alignment at the CdS/Cu(In,Ga)S_2 interface in thin-film solar cells," *Applied Physics Letters*, vol. 86, no. 6, p. 062109, 2005.

[134] T. M. Friedlmeier, P. Jackson, A. Bauer, D. Hariskos, O. Kiowski, R. Menner, R. Wuerz, and M. Powalla, "High-efficiency Cu(In,Ga)Se_2 solar cells," *Thin Solid Films*, Aug. 2016.

[135] R. Herberholz, V. Nadenau, U. Rühle, C. Köble, H. W. Schock, and B. Dimmler, "Prospects of wide-gap chalcopyrites for thin film photovoltaic modules," *Solar Energy Materials and Solar Cells*, vol. 49, no. 1, pp. 227–237, 1997.

[136] G. Hanna, A. Jasenek, U. Rau, and H.-W. Schock, "Influence of the Ga-content on the bulk defect densities of Cu(In,Ga)Se_2," *Thin Solid Films*, vol. 387, pp. 71–73, 2001.

[137] P. Jackson, D. Hariskos, E. Lotter, S. Paetel, R. Wuerz, R. Menner, W. Wischmann, and M. Powalla, "New world record efficiency for Cu(In,Ga)Se_2 thin-film solar cells beyond 20%," *Progress in Photovoltaics: Research and Applications*, vol. 19, pp. 894–897, Nov. 2011.

[138] T. Eisenbarth, T. Unold, R. Caballero, C. Kaufmann, D. Abou-Ras, and H.-W. Schock, "Origin of defects in $CuIn_{1-x}Ga_xSe_2$ solar cells with varied Ga content," *Thin Solid Films*, vol. 517, pp. 2244–2247, Feb. 2009.

[139] B. Huang, S. Chen, H.-X. Deng, L.-W. Wang, M. A. Contreras, R. Noufi, and S.-H. Wei, "Origin of Reduced Efficiency in Cu(In,Ga)Se_2 Solar Cells With High Ga Concentration: Alloy Solubility Versus Intrinsic Defects," *IEEE Journal of Photovoltaics*, vol. 4, pp. 477–482, Jan. 2014.

[140] F. Pianezzi, P. Reinhard, A. Chirilă, B. Bissig, S. Nishiwaki, S. Buecheler, and A. N. Tiwari, "Unveiling the effects of post-deposition treatment with different alkaline elements on the electronic properties of CIGS thin film solar cells," *Physical Chemistry Chemical Physics*, vol. 16, no. 19, p. 8843, 2014.

[141] A. Rockett, J. S. Britt, T. Gillespie, C. Marshall, M. M. Al Jassim, F. Hasoon, R. Matson, and B. Basol, "Na in selenized Cu(In,Ga)Se_2 on Na-containing and Na-free glasses: distribution, grain structure, and device performances," *Thin Solid Films*, vol. 372, no. 1, pp. 212–217, 2000.

[142] M. Lammer, U. Klemm, and M. Powalla, "Sodium co-evaporation for low temperature CIGSe deposition," vol. 387, pp. 33–36, 2001.

[143] M. Kim, J. Lee, Y. Lee, J.-h. Jeong, and K.-B. Lee, "Structural and compositional analyses of Cu(In,Ga)Se_2 thin film solar cells with different cell performances," *Journal of Vacuum Science & Technology B, Nanotechnology and Microelectronics: Materials, Processing, Measurement, and Phenomena*, vol. 34, p. 03H121, May 2016.

[144] Braunger, Bilger, Rau, and Schock, "Influence of sodium on the grownth of polycrystalline CIGSE thin films," *Thin Solid Films*, vol. 361-362, pp. 161–166, 2000.

[145] K. Granath, M. Bodeg\aard, and L. Stolt, "The effect of NaF on Cu(In,Ga)Se_2 thin film solar cells," *Solar energy materials and solar cells*, vol. 60, no. 3, pp. 279–293, 2000.

[146] B. Fleutot, D. Lincot, M. Jubault, Z. J. Li Kao, N. Naghavi, J.-F. Guillemoles, and F. Donsanti, "GaSe Formation at the Cu(In,Ga)Se_2/Mo Interface-A Novel Approach for Flexible Solar Cells by Easy Mechanical Lift-Off," *Advanced Materials Interfaces*, vol. 1, pp. n/a–n/a, July 2014.

[147] S. Sugai and T. Ueda, "High-pressure Raman spectroscopy in the layered materials 2 H-MoS_2, 2 H-$MoSe_2$, and 2 H-$MoTe_2$," *Physical Review B*, vol. 26, no. 12, p. 6554, 1982.

[148] "Minitab 17 statistical Software," 2010.

[149] J. F. Wager and D. A. Keszler, "Novel Materials Development for polycristalline thin film solar cells," tech. rep., NREL, 2008.

[150] R. Caballero, C. Kaufmann, T. Eisenbarth, M. Cancela, R. Hesse, T. Unold, A. Eicke, R. Klenk, and H. Schock, "The influence of Na on low temperature growth of CIGS thin film solar cells on polyimide substrates," *Thin Solid Films*, vol. 517, pp. 2187–2190, Feb. 2009.

[151] S. Nishiwaki, S. Siebentritt, P. Walk, and others, "A stacked chalcopyrite thin-film tandem solar cell with 1.2 V open-circuit voltage," *Progress in Photovoltaics: Research and Applications*, vol. 11, no. 4, pp. 243–248, 2003.

[152] J. H. Choi, K. Kim, Y.-J. Eo, J. H. Park, J. Gwak, S.-K. Ahn, A. Cho, S. Ahn, J.-S. Cho, K. Shin, K. Yoon, S. H. Kong, J.-H. Yun, and J. Yoo, "Wide-bandgap $CuGaSe_2$ thin film solar cell fabrication using ITO back contacts," *Vacuum*, vol. 120, pp. 42–46, Oct. 2015.

[153] R. Caballero, K. Sakurai, C. A. Kaufmann, M. C. Lux-Steiner, and others, "CGS-Thin Films Solar Cells on Transparent Back Contact," in *2006 IEEE 4th World Conference on Photovoltaic Energy Conference*, vol. 1, pp. 479–482, IEEE, 2006.

[154] G. Quesada, D. Rousse, Y. Dutil, M. Badache, and S. Hallé, "A comprehensive review of solar facades. Transparent and translucent solar facades," *Renewable and Sustainable Energy Reviews*, vol. 16, pp. 2643–2651, June 2012.

[155] C. G. Granqvist, "Transparent conductors as solar energy materials: A panoramic review," *Solar Energy Materials and Solar Cells*, vol. 91, pp. 1529–1598, Oct. 2007.

[156] R. G. Gordon, "Criteria for choosing transparent conductors," *MRS bulletin*, vol. 25, no. 08, pp. 52–57, 2000.

[157] D.-S. Liu, C.-S. Sheu, C.-T. Lee, and C.-H. Lin, "Thermal stability of indium tin oxide thin films co-sputtered with zinc oxide," *Thin Solid Films*, vol. 516, pp. 3196–3203, Mar. 2008.

[158] M. Wimmer, F. Ruske, S. Scherf, and B. Rech, "Improving the electrical and optical properties of DC-sputtered ZnO:Al by thermal post deposition treatments," *Thin Solid Films*, vol. 520, pp. 4203–4207, Apr. 2012.

[159] T. Nakada, T. Kume, T. Mise, and A. Kunioka, "Superstrate-type Cu(In,Ga)Se_2 thin film solar cells with ZnO buffer layers," *Japanese journal of applied physics*, vol. 37, no. 5A, p. L499, 1998.

[160] M. Heinemann, F. Ruske, D. Greiner, A. Jeong, M. Rusu, B. Rech, R. Schlatmann, and C. Kaufmann, "Advantageous light management in Cu(In,Ga)Se2 superstrate solar cells," *Solar Energy Materials and Solar Cells*, vol. 150, pp. 76–81, June 2016.

[161] P. Rostan, J. Mattheis, G. Bilger, U. Rau, and J. Werner, "Formation of transparent and ohmic ZnO:Al/$MoSe_2$ contacts for bifacial Cu(In,Ga)Se_2 solar cells and tandem structures," *Thin Solid Films*, vol. 480-481, pp. 67–70, June 2005.

[162] M. Terheggen, H. Heinrich, G. Kostorz, F.-J. Haug, H. Zogg, and A. N. Tiwari, "Ga_2O_3 segregation in Cu(In,Ga)Se_2/ZnO superstrate solar cells and its impact on their photovoltaic properties," *Thin Solid Films*, vol. 403 - 404, pp. 212–215, 2002.

[163] F.-J. Haug, D. Rudmann, H. Zogg, and A. Tiwari, "Light soaking effects in Cu(In,Ga)Se_2 superstrate solar cells," *Thin Solid Films*, vol. 431-432, pp. 431–435, May 2003.

[164] M. D. Heinemann, V. Efimova, R. Klenk, B. Hoepfner, M. Wollgarten, T. Unold, H.-W. Schock, and C. A. Kaufmann, "Cu(In,Ga)Se_2 superstrate solar cells: prospects and limitations: Cu(In,Ga)Se_2 superstrate solar cells," *Progress in Photovoltaics: Research and Applications*, vol. 23, pp. 1228–1237, Oct. 2015.

[165] S. Seyrling, S. Calnan, S. Bücheler, J. Hüpkes, S. Wenger, D. Brémaud, H. Zogg, and A. Tiwari, "$CuIn_{1-x}Ga_xSe_2$ photovoltaic devices for tandem solar cell application," *Thin Solid Films*, vol. 517, pp. 2411–2414, Feb. 2009.

[166] J. Mattheis, P. Rostan, U. Rau, and J. Werner, "Carrier collection in Cu(In,Ga)Se_2 solar cells with graded band gaps and transparent ZnO:Al back contacts," *Solar Energy Materials and Solar Cells*, vol. 91, pp. 689–695, May 2007.

[167] F.-J. Haug, D. Rudmann, G. Bilger, H. Zogg, and A. N. Tiwari, "Comparison of structural and electrical properties of Cu(In, Ga)Se_2 for substrate and superstrate solar cells," *Thin Solid Films*, vol. 403, pp. 293–296, 2002.

[168] T. Nakada, Y. Hirabayashi, and T. Tokado, "$CuIn_{1-x}Ga_xSe_2$-based thin film solar cells using transparent conducting back contacts," *Japanese Journal of Applied Physics*, vol. 41, no. 11A, p. L1209, 2002.

[169] D. L. Young, J. Abushama, R. Noufi, X. Li, J. Keane, T. A. Gessert, J. S. Ward, M. Contreras, M. Symko-Davies, and T. J. Coutts, "A new thin-film $CuGaSe_2$/Cu (In, Ga) Se_2 bifacial, tandem solar cell with both junctions formed simultaneously," in *Photovoltaic Specialists Conference, 2002. Conference Record of the Twenty-Ninth IEEE*, pp. 608–611, IEEE, 2002.

[170] E. Yablonovitch, "Statistical ray optics," *JOSA*, vol. 72, no. 7, pp. 899–907, 1982.

[171] B. Theys, T. Klinkert, F. Mollica, E. Leite, F. Donsanti, M. Jubault, and D. Lincot, "Revisiting Schottky barriers for CIGS solar cells: Electrical characterization of the Al/Cu(InGa)Se $_2$ contact: Revisiting Schottky barriers for CIGS solar cells," *physica status solidi (a)*, vol. 213, pp. 2425–2430, Sept. 2016.

[172] J.-F. Guillemoles, L. Kronik, D. Cahen, U. Rau, A. Jasenek, and H.-W. Schock, "Stability Issues of Cu(In,Ga)Se $_2$ -Based Solar Cells," *The Journal of Physical Chemistry B*, vol. 104, pp. 4849–4862, May 2000.

[173] M. Bodegard, K. Granath, and L. Stolt, "Growth of $Cu(In,Ga)Se_2$ thin films by coevaporation using alkaline precursors," *Thin Solid Films*, vol. 361, pp. 9–16, 2000.

[174] E. Jarzembowski, F. Syrowatka, K. Kaufmann, W. Fränzel, T. Hölscher, and R. Scheer, "The influence of sodium on the molybdenum/$Cu(In,Ga)Se_2$ interface recombination velocity, determined by time resolved photoluminescence," *Applied Physics Letters*, vol. 107, p. 051601, Aug. 2015.

[175] M. D. Heinemann, D. Greiner, T. Unold, R. Klenk, H.-W. Schock, R. Schlatmann, and C. A. Kaufmann, "The Importance of Sodium Control in CIGSe Superstrate Solar Cells," *IEEE Journal of Photovoltaics*, vol. 5, pp. 378–381, Jan. 2015.

[176] M. Bouttemy, P. Tran-Van, I. Gerard, T. Hildebrandt, A. Causier, J. Pelouard, G. Dagher, Z. Jehl, N. Naghavi, G. Voorwinden, B. Dimmler, M. Powalla, J. Guillemoles, D. Lincot, and A. Etcheberry, "Thinning of CIGS solar cells: Part I: Chemical processing in acidic bromine solutions," *Thin Solid Films*, vol. 519, pp. 7207–7211, Aug. 2011.

[177] D. Mercier, M. Bouttemy, J. Vigneron, P. Chapon, and A. Etcheberry, "GD-OES and XPS coupling: A new way for the chemical profiling of photovoltaic absorbers," *Applied Surface Science*, vol. 347, pp. 799–807, Aug. 2015.

[178] M. D. Heinemann, "CIGSe superstrate solar cells," 2016.

[179] F.-J. Haug, D. Rudmann, G. Bilger, H. Zogg, and A. N. Tiwari, "Comparison of structural and electrical properties of $Cu(In,Ga)Se_2$ for substrate and superstrate solar cells," *Thin Solid Films*, vol. 403, pp. 293–296, 2002.

[180] J. Mattheis, P. Rostan, U. Rau, and J. Werner, "Carrier collection in Cu(In,Ga)Se_2 solar cells with graded band gaps and transparent ZnO:Al back contacts," *Solar Energy Materials and Solar Cells*, vol. 91, pp. 689–695, May 2007.

[181] A. McEvoy, T. Markvart, L. Castaner, T. Markvart, and L. Castaner, *Practical Handbook of Photovoltaics: Fundamentals and Applications*. Elsevier, Oct. 2003. Google-Books-ID: E2BAosEwDfQC.

[182] J. A. Giesecke, M. Kasemann, and W. Warta, "Determination of local minority carrier diffusion lengths in crystalline silicon from luminescence images," *Journal of Applied Physics*, vol. 106, no. 1, p. 014907, 2009.

[183] M. Nerat, "Copper–indium–gallium–selenide (CIGS) solar cells with localized back contacts for achieving high performance," *Solar Energy Materials and Solar Cells*, vol. 104, pp. 152–158, Sept. 2012.

[184] B. Vermang, J. T. Wätjen, V. Fjällström, F. Rostvall, M. Edoff, R. Gunnarsson, I. Pilch, U. Helmersson, R. Kotipalli, F. Henry, and D. Flandre, "Highly reflective rear surface passivation design for ultra-thin Cu(In,Ga)Se_2 solar cells," *Thin Solid Films*, vol. 582, pp. 300–303, May 2015.

[185] G. Dingemans and W. M. M. Kessels, "Status and prospects of Al_2O_3-based surface passivation schemes for silicon solar cells," *Journal of Vacuum Science & Technology A: Vacuum, Surfaces, and Films*, vol. 30, no. 4, p. 040802, 2012.

[186] J. Joel, B. Vermang, J. Larsen, O. Donzel-Gargand, and M. Edoff, "On the assessment of CIGS surface passivation by photoluminescence," *physica status solidi (RRL)-Rapid Research Letters*, vol. 9999, 2015.

[187] R. Kotipalli, B. Vermang, J. Joel, R. Rajkumar, M. Edoff, and D. Flandre, "Investigating the electronic properties of Al_2O_3/Cu(In,Ga)Se_2 interface," *AIP Advances*, vol. 5, p. 107101, Oct. 2015.

[188] P. Casper, R. Hünig, G. Gomard, O. Kiowski, C. Reitz, U. Lemmer, M. Powalla, and M. Hetterich, "Optoelectrical improvement of ultra-thin Cu(In,Ga)Se_2 solar cells through microstructured MgF_2 and Al_2O_3 back contact passivation layer," *physica status solidi (RRL) - Rapid Research Letters*, vol. 10, pp. 376–380, May 2016.

[189] F. A. Kröger and H. J. Vink, "Relations between the Concentrations of Imperfections in Crystalline Solids," in *Solid State Physics* (F. S. a. D. Turnbull, ed.), vol. 3, pp. 307–435, Academic Press, 1956.

[190] T. Bak, J. Nowotny, M. Rekas, and C. Sorrell, "Defect chemistry and semiconducting properties of titanium dioxide: II. Defect diagrams*," *Journal of Physics and Chemistry of Solids*, vol. 64, pp. 1057–1067, July 2003.

[191] F. Hossein-Babaei, M. Keshmiri, M. Kakavand, and T. Troczynski, "A resistive gas sensor based on undoped p-type anatase," *Sensors and Actuators B: Chemical*, vol. 110, pp. 28–35, Sept. 2005.

[192] A. Hazra, B. Bhowmik, K. Dutta, V. Manjuladevi, R. K. Gupta, and P. Bhattacharyya, "Low Temperature Methanol Sensing by p-Type Nano-titania: Correlation with Defects States and Schottky Barrier Model," *IEEE Transactions on Nanotechnology*, vol. 14, pp. 187–195, Jan. 2015.

[193] M. Nowotny, P. Bogdanoff, T. Dittrich, S. Fiechter, A. Fujishima, and H. Tributsch, "Observations of p-type semiconductivity in titanium dioxide at room temperature," *Materials Letters*, vol. 64, pp. 928–930, Apr. 2010.

[194] D. O. Scanlon, C. W. Dunnill, J. Buckeridge, S. A. Shevlin, A. J. Logsdail, S. M. Woodley, C. R. A. Catlow, M. J. Powell, R. G. Palgrave, I. P. Parkin, G. W. Watson, T. W. Keal, P. Sherwood, A. Walsh, and A. A. Sokol, "Band alignment of rutile and anatase TiO_2," *Nature Materials*, vol. 12, pp. 798–801, July 2013.

[195] J. D. Bass, D. Grosso, C. Boissiere, and C. Sanchez, "Pyrolysis, Crystallization, and Sintering of Mesostructured Titania Thin Films Assessed by in Situ Thermal Ellipsometry," *Journal of the American Chemical Society*, vol. 130, pp. 7882–7897, June 2008.

[196] T. Jürgens, L. Gütay, and G. Bauer, "Photoluminescence, open circuit voltage, and photocurrents in Cu(In,Ga)Se_2 solar cells with lateral submicron resolution," *Thin Solid Films*, vol. 511-512, pp. 678–683, July 2006.

[197] G. El-Hajje, D. Ory, M. Paire, J.-F. Guillemoles, and L. Lombez, "Contactless characterization of metastable defects in Cu(In,Ga)Se_2 solar cells using time-resolved photoluminescence," *Solar Energy Materials and Solar Cells*, vol. 145, pp. 462–467, Feb. 2016.

[198] G. El-Hajje, D. Ory, J.-F. Guillemoles, and L. Lombez, "Local transport properties investigation by correlating hyperspectral and confocal luminescence images," p. 97430C, Mar. 2016.

[199] J. Keller, F. Gustavsson, L. Stolt, M. Edoff, and T. Törndahl, "On the beneficial effect of Al2o3 front contact passivation in Cu(In,Ga)Se2 solar cells," *Solar Energy Materials and Solar Cells*, vol. 159, pp. 189–196, Jan. 2017.

[200] P. Reinhard, B. Bissig, F. Pianezzi, H. Hagendorfer, G. Sozzi, R. Menozzi, C. Gretener, S. Nishiwaki, S. Buecheler, and A. N. Tiwari, "Alkali-Templated Surface Nanopatterning of Chalcogenide Thin Films: A Novel Approach Toward Solar Cells with Enhanced Efficiency," *Nano Letters*, vol. 15, pp. 3334–3340, May 2015.

[201] M. Paire, *Highly efficient solar cells in low dimensionality based on Cu(In,Ga)Se_2 chalcopyrite materials*. PhD thesis, Paris 6, Jan. 2012.

[202] A. Loubat, C. Eypert, F. Mollica, M. Bouttemy, N. Naghavi, D. Lincot, and A. Etcheberry, "Optical Properties of Ultrathin CIGS Films Studied by Spectroscopic Ellipsometry assisted by Chemical Engineering," *Applied Surface Science*, Oct. 2016.

[203] S. Adachi, "Model dielectric constants of GaP, GaAs, GaSb, InP, InAs, and InSb," *Physical review B*, vol. 35, no. 14, p. 7454, 1987.

[204] G. E. Jellison and F. A. Modine, "Parameterization of the optical functions of amorphous materials in the interband region," *Applied Physics Letters*, vol. 69, no. 3, p. 371, 1996.

[205] N. Dahan, Z. Jehl, J.-F. Guillemoles, D. Lincot, N. Naghavi, and J.-J. Greffet, "Lambertian back reflector in Cu(InGa)Se_2 solar cell: optical modeling and characterization," p. 862019, Mar. 2013.